

University of St Andrews



Full metadata for this thesis is available in
St Andrews Research Repository
at:

<http://research-repository.st-andrews.ac.uk/>

This thesis is protected by original copyright

**Tape Casting, Co-firing
and Electrical Characterisation**

of a

Novel design Solid Oxide Fuel Cell:

SOFCRoll

A thesis submitted for the title of Ph.D.

By

Fran G. E. Jones

University of St Andrews

Supervised by Prof. John T. S. Irvine

**Project Sponsor:
Scottish Enterprise**

Submitted September 2005



Th F100

DECLARATION

I, Fran G. E. Jones hereby certify that this thesis, which is approximately 50,000 words in length, has been written by me, that it is the record of work carried out by me and that it has not been submitted in any previous application for a higher degree.

date ..29/8/05. signature of candidate .

I was admitted as a research student in March 2001 and as a candidate for the degree of Doctor of Philosophy in March 2001; the higher study for which this is a record was carried out in the University of St Andrews between 2001 and 2004.

date ..29/8/05. signature of candidate

I hereby certify that the candidate has fulfilled the conditions of the Resolution and Regulations appropriate for the degree of Doctor of Philosophy in the University of St Andrews and that the candidate is qualified to submit this thesis in application for that degree.

date ..29/8/05... signature of supervisor

In submitting this thesis to the University of St Andrews I wish access to it to be subject to the following conditions:

for a period of 3 years [maximum 5] from the date of submission, the thesis shall be

- (a) withheld from use;
- (b) made available for use only with the consent of the Head of the School in which the work was carried out
(delete one clause)

I understand, however, that the title and abstract of the thesis will be published during this period of restricted access; and that after the expiry of this period the thesis will be made available for use in accordance with the regulations of the University Library for the time being in force, subject to any copyright in the work not being affected thereby, and a copy of the work may be made and supplied to any *bona fide* library or research worker.

date ..29/8/05... signature of candidate

Acknowledgements

This work is dedicated to my man Dave, who if hadn't decided to pursue science in Scotland, who knows what I'd be doing right now – certainly wouldn't have put myself through this that's for sure! ☺. His support and encouragement have been never faltering. Special mention also goes to my parents and the rest of the ever growing family for continued love and support in everything I do.

Big thanks must of course be passed on to my supervisor, John Irvine, without whom this PhD and SOFCRoll would never have been. Opportunities to partake in international conferences, constant new ideas and research support has been inspirational. Additionally thanks must be extended to the 'SOFCRoll team' past and present (in no particular order): Julie Nairn, Jim Rennie, Paul Connor, Alan Feighery, Jochen Wolff, Gabriel Piou, Marie Karlsson and Eduarda Caivallio.

A huge thanks goes to Eric Twinane (formally of Mistler Inc, currently of ESL Electro-Science Ltd) for never failing to answer email pleas for help in areas of tape casting his book hadn't covered, John Bradley and Angela Kruth for their a.c. impedance and XRD wizardry respectively, Sylvia Williamson and Ross Blackley for all their technical help and Paul Milner & Jürgen Blumm (Netzsch Instruments) for their advice and suggestions. Finally, thanks to Jon Foreman (Nextech Ltd) and Gorden Bennett (Unitec Ceramics Ltd) for their freebies.

Scottish Enterprise – thanks for the money!

To everyone past and present in the JTISI group... I shan't mention any names – you know who you all are, it's been memorable – you'll be missed! I wish you all the very best for the future.

ABSTRACT

This study has focused on the implementation of a novel design of solid oxide fuel cell (SOFC). Stumbling blocks for the commercialisation of SOFCs are based on durability and cost. The new SOFC design aims to reduce the cost of production, by firstly utilising a cheap, easily scalable production technique: tape casting, together with co-firing all components, in one single step. It further combines the advantages of the planar (high power density) and tubular (high unit strength, no sealing problems) fuel cells.

Tape casting is a well known, cheap technique for the production of dense films. It is easily adapted to add porosity by variation of organic additives and addition of pyrolysable particles, the latter of which was the primary method used in this investigation. The main challenge of this project was the achievement of the desired microstructures whilst obtaining a matching shrinkage profile for each component. Additionally the ideal sintering temperatures for each component varied greatly, with a high sintering temperature required for adequate densification of the electrolyte and a low sintering temperature required to prevent undesirable reactions between electrolyte and cathode.

Sintering temperatures were initially investigated to obtain a dense electrolyte, which formed the basis for the electrode formulations. Powder reactions performed between the YSZ and LSM of varying A-site deficiencies showed $(\text{La}_{0.8}\text{Sr}_{0.2})_{0.95}\text{MnO}_3$ to have a sufficient A-site deficiency to prevent the formation of the pyrochlore $\text{La}_2\text{Zr}_2\text{O}_7$ at sintering temperatures of both 1300°C and 1350°C.

Increasing the NiO to YSZ ratio in the anode decreased the high temperature shrinkage, which was counteracted at lower NiO to YSZ ratios by the addition of graphite particles to increase the porosity. A-site deficient LSM had increased high

temperatures shrinkages, which could be reduced by increasing the YSZ to LSM ratio in the cathode. Adequate cathode conductivity with desired shrinkages was achieved with a 2-layer system: YSZ- $(\text{La}_{0.8}\text{Sr}_{0.2})_{0.95}\text{MnO}_3$ composite and 100% $(\text{La}_{0.8}\text{Sr}_{0.2})\text{MnO}_3$.

The maximum power, 0.58W at 925°C was achieved with a high Ni content anode current collector for a 5g cell (includes seal weighing approximately 1g). The OCV, series resistance and polarisation resistances of this cell were 0.94V, 0.21Ω and 0.19Ω respectively. Typical results obtained at 800°C were a maximum power of 0.33W at an OCV of 0.97V, and series and polarisation resistances of 0.42Ω and 0.40Ω respectively.

Contents Page

	Page no
1 Introduction	
1.1 Fuel Cells	1
1.2 Thermodynamics	5
1.3 Why Solid Oxide Fuel Cells?	9
1.4 Component Materials	12
1.4.1 Electrolyte	12
1.4.2 Anode	20
1.4.3 Cathode	25
1.4.4 Interconnect	28
1.5 Different Design Geometry	34
1.5.1 Planar Geometry	34
1.5.2 Tubular Geometry	38
1.5.3 Monolithic Geometry	42
1.6 Aim of this work	43
1.7 References	46
2 Experimental	
2.1 Overview	52
2.2 Powder preparation	52
2.3 Powder characterisation	54
2.3.1 BET surface area analysis	54
2.3.2 SEM analysis	55
2.3.3 X-ray Diffraction (XRD)	55
2.3.3.1 Particle Size	57
2.3.3.2 Evaluation of A-site deficiency	58
2.3.3.3 Examination of presence of pyrochlore	59
2.4 Tape Casting	61
2.4.1 Particle Dispersion	63
2.4.2 Slip Viscosity	66
2.4.2.1 Theory	66
2.4.2.2 Procedure used in this investigation	70
2.5 Thermal Gravimetric Analysis	72
2.6 Shrinkage analysis	72
2.6.1 Measuring rectangle samples	73
2.6.2 Dilatometer measurements	74
2.6.3 Rate controlled sintering	76
2.7 Density Measurements	78
2.8 Microstructure evaluation – SEM analysis	79
2.8.1 Instrument Lay-out	79
2.8.1.1 Generation of electron beam	79
2.8.1.2 Interaction with sample and data collection	87
2.8.2 Sample preparation	92
2.9 Homogeneity – EDS Analysis	93
2.9.1 Theory	94

2.9.2	Procedure used in this investigation	97
2.10	Fuel cell Production	98
2.11	Performance Testing	102
2.11.1	I-V Curves	105
2.11.2	a.c. impedance	107
2.12	References	112

3 Processing

3.1	Introduction	114
3.2	Tape Casting	115
3.2.1	Particle Characterisation of Ceramic Powders	115
3.2.1a	Production of A-site deficient LSM	120
3.2.2	Particle Characterisation of Pore Formers	127
3.2.3	Dispersion Settling Tests	130
3.2.3.1	YSZ (Pi-Kem Ltd) only	130
3.2.3.2	YSZ (Pi-Kem Ltd) and graphite grade 615 (Griffin & George Ltd)	132
3.2.3.3	NiO (Aldrich Ltd), YSZ (Pi-Kem Ltd) and graphite -325 (Aldrich Ltd)	138
3.2.3.4	LSM (Praxair Ltd, Nextech Ltd), YSZ (Unitec Ceramics Ltd) and graphite -325 (Aldrich Ltd)	142
3.2.4	Dispersion Properties of the Binder	147
3.2.4.1	Microstructure	147
3.2.4.2	Slurry Viscosities	150
3.2.5	Summary	155
3.2.5.1	Single Component Slurry	155
3.2.5.2	Multi-component Slips	156
3.3	Electrolyte Sintering	157
3.3.1	Sintering Temperature on Microstructure	157
3.3.2	Sintering Times on Microstructure	159
3.3.3	Shrinkage Profile	162
3.4	Production of Porous Films (YSZ)	167
3.4.1	Addition of a Pore Former	167
3.4.2	Particle Size/Shape of Pore Former	167
3.4.3	Ceramic Particle Size	169
3.4.4	Binder/Plasticizer Concentration	172
3.4.5	Summary	173
3.5	Anode Production	175
3.5.1	No Pore Former	175
3.5.1.1	Microstructure	176
3.5.1.2	Shrinkage	179
3.5.2	Use of Pore Former	181
3.5.2.1	Microstructure	181
3.5.2.2	Shrinkage	187
3.5.3	Varying NiO Content	192
3.5.3.1	Microstructure	193
3.5.3.2	Shrinkage	198
3.5.4	Summary	201

3.6	Cathode Production	202
3.6.1	Pyrochlore Analysis	202
3.6.2	100% LSM (Porous)	208
3.6.2.1	Microstructure	209
3.6.2.2	Shrinkage	215
3.6.3	LSM & YSZ Composite	221
3.6.3.1	Microstructure	222
3.6.3.2	Shrinkage	224
3.6.4	100% LSM (Dense)	227
3.6.4.1	Microstructure	227
3.6.4.2	Shrinkage	229
3.6.5	Summary	229
3.7	Sintering of multi-layers	231
3.7.1	Introduction	231
3.7.2	Rate Controlled Sintering (RCS) of fuel cell components	232
3.8	Summary	238
3.9	References	239
4	Fuel Cell Testing	
4.1	Introduction	242
4.2	Testing methods	246
4.2.1	Material Resistance	246
4.2.1.1	Electrode-steel contact & Steel corrosion	246
4.2.1.2	Deterioration with time	247
4.2.2	Open circuit voltages	250
4.2.2.1	Gas flow rate	251
4.2.2.2	Sealing	251
4.2.3	SEM cross-sectional analysis	252
4.2.3.1	Damage to cell after testing when removing steel inlet tubes	254
4.2.3.2	Damage to cell due to epoxy cure	254
4.3	Anode Current Collection	257
4.3.1	Sintering Temperature: 1300°C vs 1350°C	257
4.3.2	Electrolyte thickness	261
4.3.3	Addition of high Ni content current collector layer	261
4.4	Heating Rates	270
4.4.1	Sintering temperature of 1350°C	270
4.4.2	Sintering temperature of 1300°C	280
4.4.3	Summary	290
4.5	References	291
5	Conclusions	292

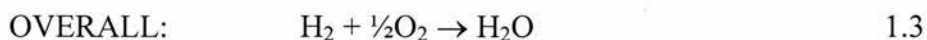
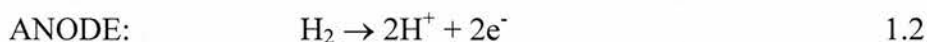
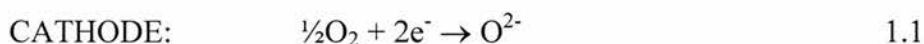
1 Introduction

1.1 Fuel Cells

A fuel cell is an electrochemical cell, which converts chemical energy into electrical energy. Chemicals are supplied continuously to the electrodes, where they undergo reactions to give an electric current^[1,2].

A fuel cell is made up from the following components: anode, cathode and electrolyte, as shown schematically in figure 1.1. The cathode or air electrode is supplied with O₂, either as pure O₂ or as air: a cheaper O₂ source. The anode or fuel electrode is supplied with the fuel, which is a hydrogen source. The fuel can be a variety of different hydrogen containing chemicals limited by the type of fuel cell for example H₂, CH₄ or CH₃OH.

At the cathode, electrons are taken from the external circuit and the O₂ is reduced to form O²⁻ ions as in equation 1.1. The anode oxidises the hydrogen to form H⁺ ions, releasing electrons into the external circuit as in equation 1.2. The electrolyte is an ionic conductor and allows O²⁻, OH⁻ or H⁺ ions (depending on the type of fuel cell) to travel through to meet the other reactants giving the overall reaction as shown in equation 1.3.



The above equation 1.3 shows that using hydrogen as a fuel, the overall reaction yields water. This offers a distinct advantage over current fossil fuel energy sources, which produce harmful products such as CO, CO₂, VOCs (volatile organic

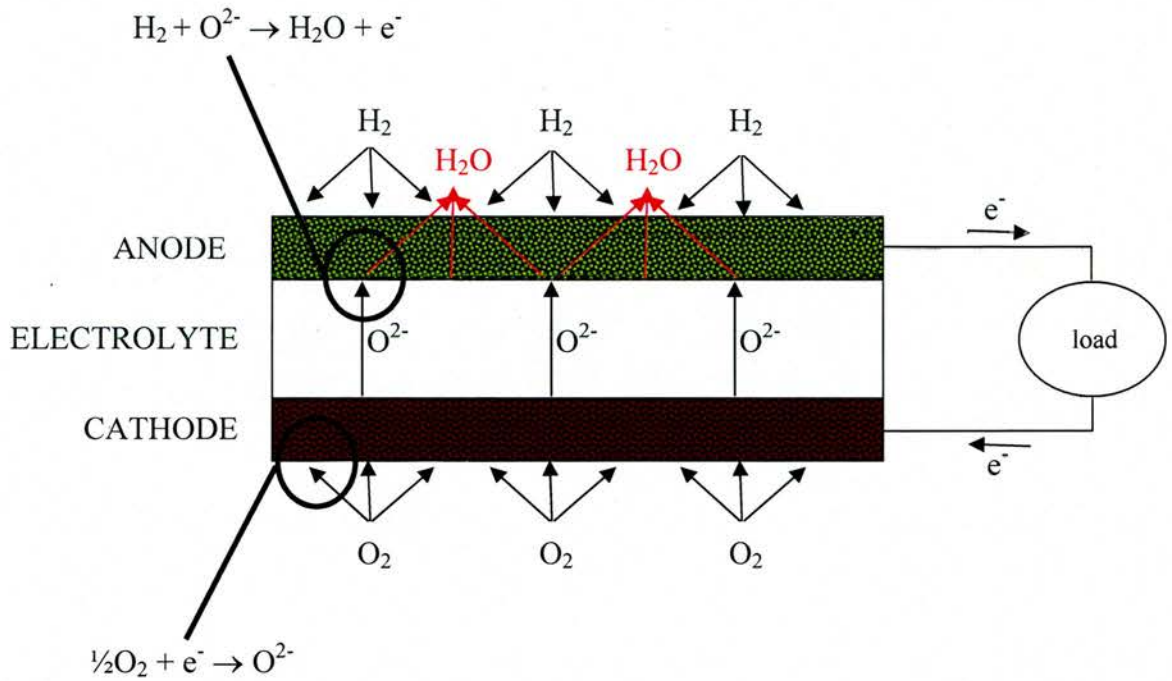


Figure 1.1: Schematic diagram of the fuel cell – specifically an SOFC (solid oxide fuel cell) with an oxide ion conducting electrolyte.

Energy Carrier	Form of Storage	Energy density	
		/kWhkg ⁻¹	/kWhl ⁻¹
Hydrogen	Gas (20MPa)	33.3	0.53
	Gas (24.8MPa)	33.3	0.64
	Gas (30MPa)	33.3	0.75
	Liquid (-253°C)	33.3	2.36
	Metal hydride	0.58	3.18
Natural gas	Gas (20MPa)	13.9	2.58
	Gas (24.8MPa)	13.9	3.01
	Gas (30MPa)	13.9	3.38
	Liquid (-162°C)	13.9	5.8
LPG (Propane)	Liquid	12.9	7.5
Methanol	Liquid	5.6	4.42
Gasoline	Liquid	12.7	8.76
Diesel	Liquid	11.6	9.7

Table 1.1: Energy densities of hydrogen and other selected hydrogen based fuels^[3]

compounds), SO_x (oxides of sulphur) and NO_x (oxides of nitrogen). It is important to note that currently, the majority of hydrogen is obtained from fossil fuels^[4], thereby continuing to contribute to the greenhouse gases and depletion of fossil fuels. Hydrogen would ideally be produced cleanly from electrolysis of water (from other renewable systems such as solar and wind power^[5]), a good method of storing energy when supply exceeds demand. However, there are drawbacks of using hydrogen as a fuel: hydrogen has a high energy per unit mass, but since it is the lightest gas, has a low energy per unit volume shown in table 1.1. In order to improve the energy density, the gas can be pressurized, cooled or stored as metal hydrides, which in turn increases cost and weight (from heavy canisters/cylinders or heating of metal hydrides for H₂ release^[4]).

The use of other fuels such as hydrocarbons or methanol rather than hydrogen as a fuel would be advantageous, as the existing infrastructure for fuel supply could be used^[2, 6-7]. In addition, hydrocarbons have a higher energy density than H₂ shown in table 1.1, which reduces the volume of gas storage required for the same energy^[8]. The low carbon to hydrogen ratio fuels can be used directly in some fuel cells reducing the CO, SO_x and NO_x pollutants to very low levels^[9]. Disadvantages occur when external reformers are required (of particular importance with the low operating temperature fuel cells) adding cost – and this can still involve the use of fossil fuels.

If the hydrocarbons were ‘carbon neutral fuels’, that is renewable hydrocarbons such as biogas^[10] (anaerobic decomposition of organic material, composed primarily of methane, carbon dioxide, and hydrogen sulfide) collected from landfill sites and farms^[11], there would be no net increase in CO₂ release into the atmosphere. Since, per mole, CH₄ is a more effective greenhouse gas than CO₂^[12], the removal of CH₄ from such areas would actually serve to benefit the environment.

Other possibilities would be combination of hydrogen (produced cleanly by electrolysis of water) together with CO₂ taken directly from existing power plants or from the atmosphere to produce short chain hydrocarbons^[13]. This would improve the fuel energy density as described above and allow the existing infrastructure to be used. The CO₂ waste gases released would merely equal that taken from the atmosphere originally, thereby having no net increase in CO₂ emissions, that is they are 'carbon neutral'.

1.2 Thermodynamics

The efficiency of fossil fuel combustion to produce steam in order to drive a turbine or generator for the production of electrical energy is limited thermodynamically, described by the Carnot Limit (η)^[1, 6] as shown in equation 1.4. The Carnot limit is the maximum efficiency possible from an ideally reversible heat engine, working between two temperature limits T_2 and T_1 where $T_2 > T_1$.

$$\eta = \frac{T_2 - T_1}{T_2} \quad 1.4$$

Figure 1.2 shows that in order to increase the efficiency of a combustion engine, the difference between T_1 and T_2 must be maximised. The highest T_2 achievable is limited by materials used, which reduces the maximum theoretical efficiencies achievable to below 50%^[1]. Further reductions in efficiencies occur due to friction caused by moving parts, loss of steam and incomplete fuel combustion. The optimum efficiencies of power stations using steam turbines is 45%, diesel and petrol powered generators are 30% and 20% respectively^[14], with efficiencies of above 40% rarely being obtained^[15].

Fuel cells convert fuel into electricity utilising the chemical energy through the electrochemical cell. The maximum efficiency possible would be if all the chemical energy (defined as the change in Gibbs free energy of formation between reactants: H_2 , O_2 and products: H_2O) was converted to electrical energy. This would give efficiencies of 100%, but in practice some energy is released as heat. In order to compare the fuel cell efficiency with other technologies which burn the fuel to release energy, the maximum efficiency is quoted as shown in equation 1.5^[6]. Since $\Delta \bar{g}_f$ and

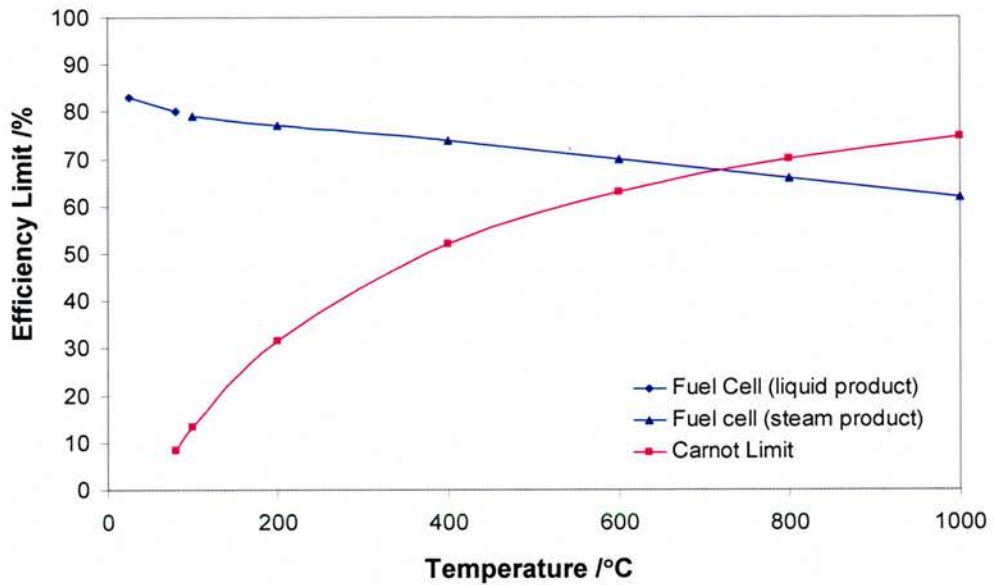


Figure 1.2^[6]: Variation of efficiency of the combustion engine as determined by the Carnot Limit with T_2 when T_1 is fixed at 50°C as determined by equation 1.4, and the HHV and LHV efficiencies of a hydrogen fuel cell with temperature $T < 100^\circ\text{C}$ and $T > 100^\circ\text{C}$ respectively as determined by equation 1.5.

$\Delta \bar{h}_f$ are both dependent on temperature, this maximum efficiency depends on the fuel cell operating temperature. Temperatures below 100°C give a liquid water product, and above 100°C would give a steam water product, which affects the $\Delta \bar{h}_f$ values due to the enthalpy of water vapourisation, so fuel cell efficiencies are quoted as LHV or HHV when the product is steam or water respectively.

$$Efficiency_{\max} = \frac{\Delta \bar{g}_f}{\Delta \bar{h}_f} \times 100 \quad 1.5$$

Figure 1.2 shows a steady decrease in the hydrogen fuel cell efficiency with increasing temperature, with theoretical efficiencies higher than combustion engines at temperatures lower than 700°C. At the higher temperatures, combustion methods give the better theoretical efficiencies, but for reasons described above, T_2 and hence efficiencies never get this high in practice.

Real efficiencies of fuel cells are of course lower than shown in figure 1.2 due to energy losses attributed to activation polarisation (energy required to promote reactions at the electrodes), internal currents and fuel cross-over (electrolyte allowing electron transfer and fuel to permeate), ohmic losses and concentration losses^[6]. However, these losses are relatively low in comparison to friction and noise in a combustion energy source – not applicable to fuel cells due to the lack of moving parts, allowing the efficiency of a fuel cell to approach the maximum value. An important point to note regarding efficiencies of fuel cells is the fuel utilisation. The partial pressures of reactants and products affect the voltages resulting in the fuel utilisation rarely reaching 100% which reduces fuel cell efficiency. The degree to which this reduces fuel cell system efficiency depends on the type of fuel cell (see section 1.3).

The maximum theoretical voltage obtainable from a hydrogen fuel cell is given by equation 1.6, (where E is the cell emf, and F is the Faraday constant). The Gibbs free energy of formation given in equation 1.6 is at standard pressure and temperature, however, as seen above, operating temperature affects the Gibbs free energy of formation and so the maximum cell emf according to equation 1.7 for the reaction of H₂ and O₂ is 0.92V at 1000°C, 1.18V at 80°C^[6]. The pressure of the gases also affect the cell emf and increasing the partial pressures result in an increase in cell voltage as shown by the Nernst equation 1.7.

$$E^{\circ} = -\frac{\overline{\Delta g}_f}{2F} \quad 1.6$$

$$E = E^{\circ} + \frac{RT}{2F} \ln \left(\frac{P_{H_2} \cdot P_{O_2}^{\frac{1}{2}}}{P_{H_2O}} \right) \quad 1.7$$

The actual voltage obtained is lower for reasons such as activation polarisation mentioned above, and so in order to produce a useful voltage, the fuel cells are connected in series, separated by an interconnect to form a stack. The interconnect is an electronic conductor, allowing electrons to flow from the anode to the cathode via the external circuit, preventing mixing of the hydrogen and oxygen, and allowing the gases to flow to their respective electrodes.

1.3 Why Solid Oxide Fuel Cell?

There are various different types of fuel cell as shown in table 1.2. They take their name from the electrolyte they use, and operate at various different temperatures. There are various advantages associated with the solid oxide fuel cell (SOFC) over the other types of fuel cell.

Advantages occur due to the high operating temperature: it reduces the activation polarisation losses^[6] allowing efficiencies to approach theoretical values, it allows carbon based fuels to be used directly as a fuel, without the requirement of an external reformer^[2, 9] hence reducing the cost, and the cost is furthermore reduced as non-precious metal catalysts can be used in the electrodes. Whilst these advantages are relevant to all high temperature fuel cells, the solid electrolyte in the SOFC removes problems associated with liquid electrolytes which are often corrosive and difficult to handle. In addition the solid nature of the electrolyte allows different shaped fuel cells to be produced to improve performance^[2, 16].

Finally, the SOFC has high tolerance to impurities in the gas stream^[2, 17-18], which is the downfall of the lower temperature fuel cells which easily become poisoned and so require high purity gasses adding to the cost. With the SOFC, no adverse effects are reported at impurity levels up to 2ppm of SO₂^[9] present in the air flow, up to 5000ppm NH₃^[9] or up to 1ppm HCl^[9] in the fuel gas. As little as 1ppm of H₂S in the fuel does however reduce the voltage by 10% after 24 hours^[9], but this effect has been shown to be reversible, as the voltage recovers once the H₂S is removed from the fuel.

The SOFC currently shows the highest electrical conversion efficiencies of any type of fuel cell^[19] at 50-60% for normal fuel cell operations – much higher than

Fuel Cell Type	Alkaline Fuel Cell (AFC)	Proton Exchange Membrane Fuel Cell (PEM)	Phosphoric Acid Fuel Cell (PAFC)	Molten Carbonate Fuel Cell (MCFC)	Solid Oxide Fuel Cell (SOFC)
Typical Electrolyte Material	KOH	polymer	Concentrated Phosphoric Acid	$\text{Li}_2\text{CO}_3/\text{K}_2\text{CO}_3$	YSZ
Electrolyte state	Liquid	Solid	Immobilized liquid	Immobilized liquid	Solid
Fuel	H_2	$\text{H}_2, \text{CH}_3\text{OH}$	H_2, CH_4	$\text{H}_2, \text{CH}_4, \text{CO}$	H_2, CH_4
Mobile Ion	OH^-	H^+	H^+	CO_3^{2-}	O^{2-}
Cathode Reaction	$\text{O}_2 + 2\text{H}_2\text{O} + 4\text{e}^- \rightarrow 4\text{OH}^-$	$\text{O}_2 + 4\text{H}^+ + 4\text{e}^- \rightarrow 2\text{H}_2\text{O}$	$\text{O}_2 + 4\text{H}^+ + 4\text{e}^- \rightarrow 2\text{H}_2\text{O}$	$\text{O}_2 + 2\text{CO}_2 + 4\text{e}^- \rightarrow 2\text{CO}_3^{2-}$	$\text{O}_2 + 4\text{e}^- \rightarrow 2\text{O}^{2-}$
Active Cathode catalyst	Pt	Pt (on Carbon support)	Pt	NiO	Strontium doped Lanthanum Manganite (LSM)
Anode Reaction	$2\text{H}_2 + 4\text{OH}^- \rightarrow 4\text{H}_2\text{O} + 4\text{e}^-$	$2\text{H}_2 \rightarrow 4\text{H}^+ + 4\text{e}^-$	$2\text{H}_2 \rightarrow 4\text{H}^+ + 4\text{e}^-$	$2\text{H}_2 + 2\text{CO}_3^{2-} \rightarrow 2\text{H}_2\text{O} + 2\text{CO}_2 + 4\text{e}^-$	$2\text{H}_2 + 2\text{O}^{2-} \rightarrow 2\text{H}_2\text{O} + 4\text{e}^-$
Active Anode catalyst	Pd/Ag with Ni catalyst for fuel reforming	Pt/Ru (on Carbon support)	Pt	Ni	Ni
Operating Temperature /°C	50-250	50-100	220	650	500-1000
Applications	Transport Used in space missions	Transport Replaced AFC for space missions Low power CHP	Co-generation systems	Dispersed/co-generation systems	Dispersed/co-generation systems
Disadvantages	CO_2 in fuel/air block pores, degrading performance	Humidification of gases CO and S problems	CO and S problems	Requires CO_2 cycling	Ceramic materials
Advantages	Easy to start up from cold	Easy to start up from cold CH_3OH – alternative fuel	CH_4 – alternative fuel	CO and CH_4 – alternative fuels	CH_4 – alternative fuel Tolerance to fuel impurities

Table 1.2^[2, 6, 17, 19]: Table of different fuel cell systems

is thermodynamically achievable from the conventional combustion systems described in section 1.2, especially when considering all but the very largest of systems. The high operating temperature allows the heat by-product to be used in combined heat and power systems, which further increases the efficiency^[6, 16-17], with efficiencies of up to 70% reported for the combined cycle pressurised turbine SOFC system and in excess of 90% with heat recovery^[2, 18].

Whilst high temperature operation gives many advantages, it also has corresponding disadvantages. The effects of high temperature and exposure to oxidising and reducing environments on the chemical stabilities of the fuel cell components reduce the fuel cell lifetime^[18] and therefore a lot of research is centred on reducing operating temperatures. Lower temperatures has the added advantage that a cheaper stainless steel interconnect material can be used, which would corrode at the higher temperatures. Two main methods of reducing the operating temperature is either to reduce the thickness of the electrolyte, thereby lowering the ionic resistance enabling it to give reasonable performances at lower temperatures, or to use different materials making a solid proton conducting electrolyte fuel cell. Solid oxide ion conducting fuel cells are less developed than MCFC, but offer greater potential efficiencies^[16], and it is this type of fuel cell which is considered in this report.

1.4 Component Materials

The components of a solid oxide fuel cell: anode, cathode, electrolyte and interconnect place various chemical and physical requirements on the materials^[9, 16]. They must be stable, chemically and structurally, at both operating and construction temperatures, and in operating environments of oxidising and/or reducing atmospheres. They must be chemically compatible with the other components, and also have similar thermal expansion co-efficients to avoid warping and cracking of the fuel cell. Each component must possess the correct conductivity and have adequate density/porosity. Additionally it is advantageous for the materials to have high strength, toughness, ease of handling and low cost^[16].

1.4.1 Electrolyte

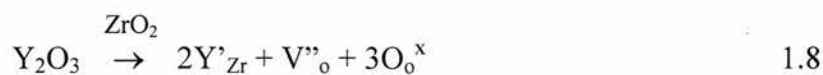
The electrolyte has the following requirements:

- Nearly 100% ionic conductivity
- Stability in both oxidising and reducing atmospheres
- Non-reactive with cathode and anode at both operating and production temperatures
- A thermal expansion close to other fuel cell components
- Gas tight to prevent direct combination of fuel and oxidant

The electrolyte material is generally composed of doped zirconia; pure zirconia isn't used, as its ionic conductivity is too low for fuel cell use^[15, 20] and the crystal structure changes with temperature (shown in figure 1.4). During the transformation to tetragonal, a large volume decrease of 3-5% occurs, which reverses at ~900-1000°C on cooling and causes the ZrO_2 to fracture^[16, 21]. This is a big processing problem, as although this transition occurs above the fuel cell operating

temperature, the sintering of the ceramics occurs above this transition temperature. The addition of cubic oxides such as Y_2O_3 , CaO and Sc_2O_3 can stabilize the cubic fluorite structure of ZrO_2 between room temperature and its melting point and increases the oxygen ion conductivity^[15-16, 20]. The crystal structure of the doped ZrO_2 is an imperfect fluorite structure.

Doping replaces some Zr^{4+} ions with Y^{3+} , Sc^{3+} or Ca^{2+} (depending on the dopant), leading to oxygen vacancies, which occur to restore the electrical charge balance of the system^[22]. It is by these oxygen vacancies which the O^{2-} ions travel; a migration process through the electrolyte^[15]. The higher the dopant concentration the greater the number of oxygen ion vacancies as shown by the Kröger-Vink notation in equation 1.8. In terms of ionic conductivity, however, increasing the number of oxygen vacancies only increases the ionic conductivity to a point, as seen in figure 1.3, which is believed to occur due to the clustering of oxygen vacancies with high dopant concentration^[16, 23-25]. At high oxygen vacancy concentration, coulombic forces are thought to cause V''_o to form a complex with the Y^{3+} , which ‘ties up’ the V''_o , preventing them from contributing to conduction^[24-25]. This model is certainly valid for ceria systems, which are cubic over the full range of doping concentrations. It is important to remember however, that at low level doping for zirconia systems, the tetragonal phase becomes more favourable. At doping levels below that required for maximum conductivities, it typically exists as a two phase mixture of tetragonal and cubic^[26-29], as shown in the phase diagram of yttria doped zirconia in figure 1.4.



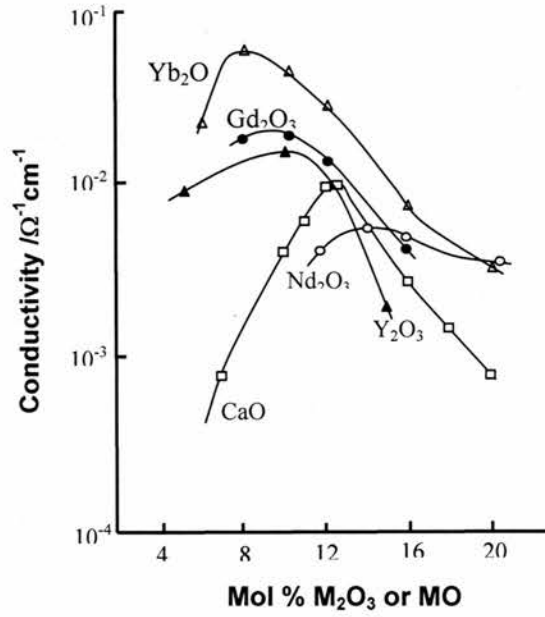


Figure 1.3^[16]: Variation of ionic conductivity of ZrO_2 with dopant concentration (Temperature: $807^\circ C$)

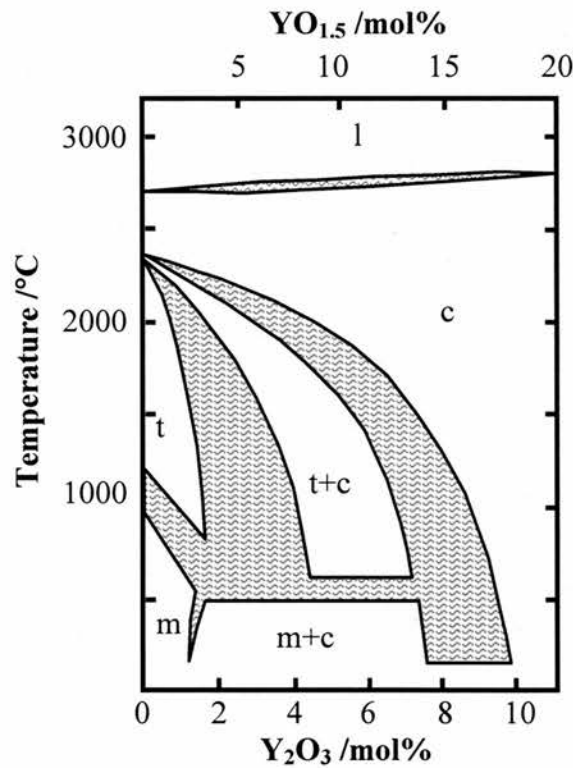


Figure 1.4: ZrO_2 - Y_2O_3 phase diagram for the ZrO_2 rich region. The shaded areas depict the range of phase boundary lines reported in the literature^[26].

As is evident from figure 1.3, doping with Y_2O_3 doesn't achieve the highest ionic conductivity possible for doped zirconia, however it is the most commonly used dopant for electrolyte material due to its relative cost. The most common material used for the oxide conducting electrolyte is yttria stabilised zirconia (YSZ).

The highest ionic conductivity achieved of YSZ is with a doping level of approximately 8mol% giving reported conductivities of up to 0.18Scm^{-1} ^[18, 30] at an operating temperature of 1000°C , with negligible electron conductivity. Discrepancies in reported measured conductivities are likely to be due to differences in grain size, densities, sample impurities and synthesis methods^[27, 30] (see figure 1.5a). At 800°C , the conductivity is reduced to approximately 0.05Scm^{-1} ^[18, 30-31], which unless the electrolyte is very thin, is too low an ionic conductivity for a fuel cell electrolyte.

Whilst YSZ is stable in both reducing and oxidising environments^[15-16], the 8mol% YSZ is not completely stabilised at fuel cell temperatures and the conductivity reduces with time^[18, 27, 30]. TEM evidence suggests this occurs due to re-arrangement of the dopant by cation diffusion to give tetragonal (low dopant concentration) and cubic (high dopant concentration) phases^[21, 23, 32]. The initial drop in conductivity is high and slows down with time, which was explained by a reduction in concentration gradients^[21, 23]. Other work shows aging without evidence of precipitates^[27, 33], indicating the presence of a second mechanism such as short range oxygen ion vacancies ordering to the Zr, or trapping of the oxygen vacancies by the Zr to relax the anisotropy of the lattice distortion^[23, 33-34].

Discrepancies in the reported minimum yttria dopant concentration required to fully stabilise the cubic fluorite structure is demonstrated in figure 1.4, however it is

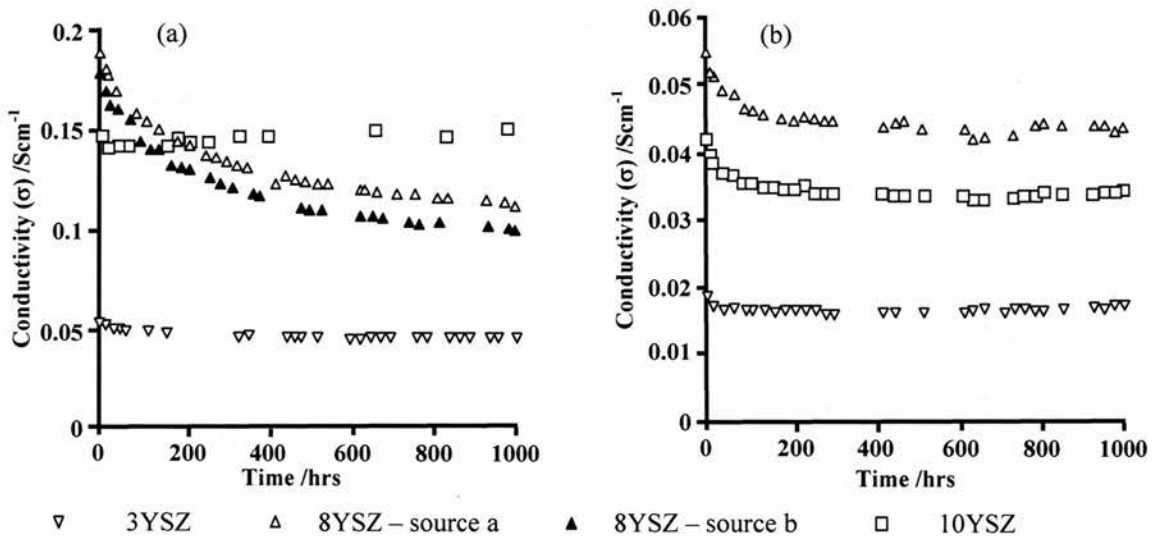


Figure 1.5^[23]: Aging effects on the conductivity of YSZ (a) at 1000°C, and (b) at 800°C (note the two different sources a and b for 8YSZ)

accepted that an yttria dopant concentration of 9mol% fully stabilises the cubic structure at 1000°C, dramatically reducing the loss of conductivity with time^[21, 26]. Increasing yttria content in excess of 8.5mol% also has the effect of severely reducing the ionic conductivity, as seen in figure 1.3. Again, as seen for the 8mol% YSZ discrepancies in the literature exist on the measured conductivities due to synthesis route, impurity, grain size and density differences: the highest measured at 1000°C being 0.165Scm⁻¹ and 0.135Scm⁻¹ for 9mol% and 10mol% respectively^[18, 21, 33].

Figure 1.5a demonstrates, that sacrificing initial conductivity by using fully stabilised zirconia is beneficial in the long run. In this study^[23], after a prolonged period >200hrs at 1000°C, the 10mol% YSZ has a higher conductivity than the 8mol% YSZ, and for this reason 10mol% YSZ is sometimes used as the electrolyte material (see section 1.5.2). In addition, it is worth noting that should the fuel cell be operated at a lower temperature of 800°C, both 8mol% and 10mol% YSZ have significant aging problems^[23], shown in figure 1.5b.

The electrolyte needs to be as uniformly thin as possible to reduce ohmic losses. A thickness of less than 40µm is desirable, with reported thicknesses of as low as 3µm being obtained^[35], allowing a lower operating temperature to be used. A high density is crucial, as any open pores present allow the gases to meet resulting in reduced fuel cell performance. The density should be >94%^[36] and any porosity present should be only closed pores, which don't contribute to any gas cross-flow. For YSZ, this means a high production temperature is required, which can lead to problems with the 'state of the art' cathode, detailed in section 1.4.3.

The strength, toughness and thermal shock resistance of the cubic phase zirconia is low^[21]. 8mol% YSZ has a toughness of 2-3MPa·m^{1/2} at room temperature^[16]. This is of sufficient strength for the electrolyte supported planar fuel

cell design described in section 1.5.1, where the electrolyte has a thickness of $>200\mu\text{m}$. Since thin electrolyte layers are preferential for reduced ohmic losses, tetragonal 2.5-3mol% YSZ can be used^[37], which has a much higher strength of approximately $6.5\text{Mpa}\cdot\text{m}^{1/2}$ ^[16, 21] at room temperature (but with reduced ionic conductivities of 0.056Scm^{-1} ^[21, 23] as seen in figure 1.4). Additionally, the 8mol% YSZ can be strengthened by adding Al_2O_3 dopant^[16, 22]. This has the added effect of reacting with any SiO_2 impurity present (which sits at grain boundaries, increasing the grain boundary resistivity^[38-39]), thereby reducing its associated problems^[21, 39-40], but can lead to reaction with electrode materials such as LSM.

Using high purity YSZ powders eliminates the undesirable properties caused by impurities. However, manganese migration into the electrolyte from the LSM cathode during high temperature fuel cell production (an effect exaggerated when using A-site deficient LSM – see section 1.4.3) is an important consideration for the electrolyte. Manganese ions in YSZ have the effect of increasing the number of oxygen vacancies, stabilising the cubic phase of zirconia with yttria contents as low as 7.5mol% Y_2O_3 ^[41]. Similar to $>8.5\text{mol}\%$ YSZ, where the number of oxygen vacancies are higher, manganese doping has the effect of decreasing the ionic conductivity^[26, 42] and at dopant concentrations of $>2\text{mol}\%$ Mn, reducing the rate of deterioration^[26]. In fact, studies have shown^[26], the high stability of 5mol% Mn 7.9mol% YSZ gives a constant conductivity: retaining 0.11Scm^{-1} after 2000hrs at 1000°C , higher than corresponding samples of lower Mn content. This could suggest that a purposeful addition of Mn to YSZ (if Mn were unavoidable) would be beneficial, not only improving long term stability but also compatibility with the LSM^[41]. However, conversely, at lower operating temperatures of 850°C , even high levels (5mol% Mn)

doping didn't stabilise the YSZ enough to off-set the effect of the huge initial drop in conductivity^[26].

The microstructure of the electrolyte has been shown to affect the ionic conductivity. Smaller particle size increases the sintering reactivity, and so lowers processing temperatures, or reduces sintering time needed. Increased sintering times leads to larger grain size, which reduces the resistance associated with grain boundaries but decreases the mechanical strength of the material. At the high operating temperatures of the solid oxide fuel cell (800°C-1000°C), the grain boundary is shown to have negligible effect on the ionic conductivity^[16, 30].

1.4.2 Anode

The anode has the following requirements:

- High electronic conductivity
- Stability in reducing atmospheres
- Non-reactive with electrolyte and interconnect at both operating/production temperatures and environments
- A thermal expansion close to other fuel cell components
- Sufficient porosity to allow transport of the fuel gas to the electrolyte/electrode interface

The most common anode for SOFCs is the Ni/YSZ cermet, the active catalyst for the oxidation of hydrogen to water being nickel. Addition of YSZ provides three main functions: to reduce the anode thermal expansion coefficient, prevent the sintering of Ni particles at operating temperature^[16] and to increase the triple-phase boundary^[43-44].

The triple phase boundary, shown schematically in figure 1.6, is the region where gas, electrolyte ion conductor and electrode catalyst come together. It is important to have a large triple phase boundary area in the electrode, as this is where the oxide ion and hydrogen gas are brought together and reacted at the nickel site^[37]. In addition, there must be good nickel-nickel particle contact to allow the transport of electrons to the electrical circuit contacts. A Ni to YSZ ratio of 3:7 by volume is close to the limit for percolation of the nickel particles, and as a result the measured conductivities vary significantly depending on relative particle sizes and porosities^[45-47]. Particle size and particle size distribution of the YSZ and Ni in the anode determine to a large extent the anode performance^[31]. It has been shown that when

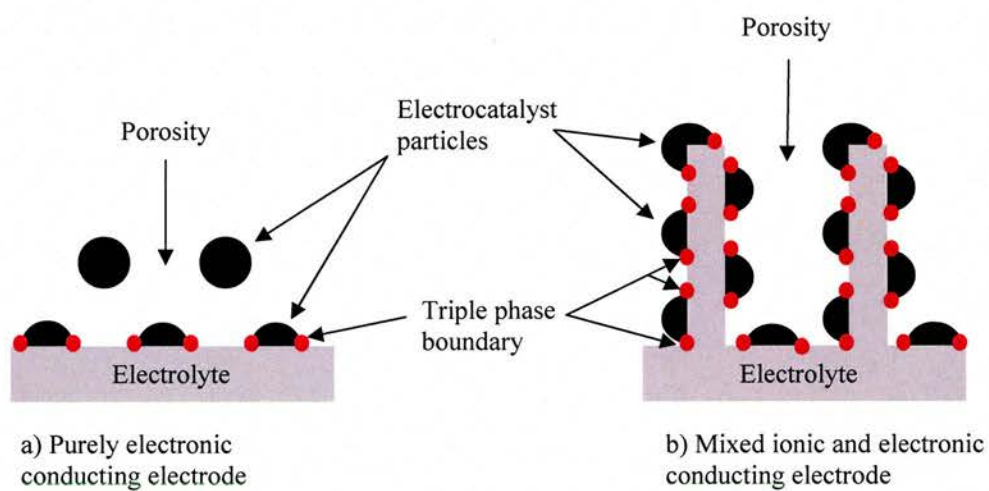


Figure 1.6: Schematic showing the increased triple phase boundary when electrolyte material is mixed in with the electrode material.

2/3 fine YSZ particles ($<2\mu\text{m}$) and 1/3 coarser YSZ particles ($2\text{-}20\mu\text{m}$) are used in the fabrication of the anode, the stability and electrode performance are increased^[47-50]. Percolation has been achieved with lower Ni to YSZ ratios obtained by low Ni to YSZ particle size ratios^[49], using Ni coated YSZ^[51] or using Ni coated pore formers^[52]. Despite this, a nickel content of 30vol%-40vol% is commonly used^[18], giving conductivities of between 0.2Scm^{-1} ^[45] and 600Scm^{-1} ^[46] for 30vol% (relative to YSZ content) and between 200Scm^{-1} ^[45] and 3000Scm^{-1} ^[46] for 40vol% Ni (relative to YSZ content), depending on relative particle size and distributions and porosities.

The anode is typically produced by making a film of NiO/YSZ ceramic. The NiO is then reduced in situ, typically up to temperatures between 800°C - 1000°C in an atmosphere of H_2 . A volume change of 41% is associated with the reduction of NiO to Ni metal, which serves to introduce porosity into the system. At temperatures as low as the fuel cell operating temperature of 1000°C , the nickel particles can sinter together^[53], which reduces both the active catalyst surface area, triple phase boundary, and porosity^[16, 37] and so producing a YSZ/NiO anode first is not only an effective way of introducing porosity to the electrode but allows the YSZ to sinter to form a skeleton framework at high temperatures preventing the nickel particles sintering during production.

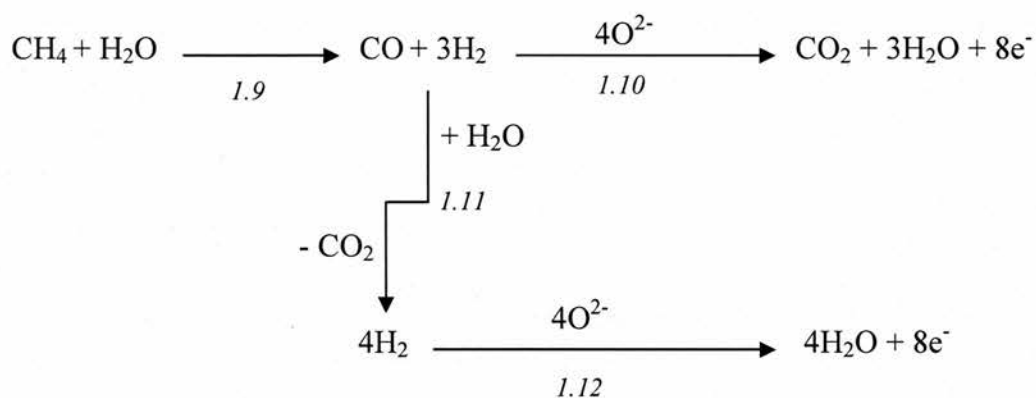
The thermal expansion co-efficient of YSZ and Ni are approximately $10.5 \times 10^{-6}\text{K}^{-1}$ ^[16] and $14.5 \times 10^{-6}\text{K}^{-1}$ ^[16] respectively and the difference in thermal expansion would cause warping and cracking of components during processing and during heating to operating temperature. The thermal expansion co-efficient of the anode is linearly reduced with increasing YSZ content^[16], and so a medium must be achieved without sacrificing the electronic conduction of the anode. The coefficient of thermal expansion (CTE) is quoted as $12 \times 10^{-6}\text{K}^{-1}$ and $12.5 \times 10^{-6}\text{K}^{-1}$ for 30vol% and

40vol% nickel respectively^[16]. In the pre-reduced state, the CTE is also affected by the NiO to YSZ particle size ratios^[54].

During operation of a fuel cell, it is feasible that the anode will be exposed to oxidising atmospheres at high temperatures, for example during a failure in fuel supply. Whilst the volume change when NiO is reduced to Ni aids with the production of porosity in the anode, the volume change associated with re-oxidation leads to the formation of micro-cracks^[55], reducing performance and resulting in problems for long term operation of Ni/YSZ anodes regarding redox stability. This is of particular importance when the anode is the support component of the fuel cell, as the electrolyte is very thin and easily cracked by the anode volume changes. Studies have shown that the initial reduction of NiO to Ni occurs without a change in length of the bulk ceramic, however, subsequent oxidation causes cracking in electrolyte and a significant increase in anode volume of 5-10% (from its reduced form)^[53]. One theory why this volume change occurs after re-oxidation rather than during the initial reduction is that during initial reduction and subsequent fuel cell operation, a small degree of Ni-Ni particle sintering occurs, thereby increasing the Ni size. This would therefore have a greater effect on the YSZ framework when increasing in volume due to oxidation^[53]. This theory is further supported by studies which showed the higher initial sintering temperatures of the anode (hence larger initial NiO size due to increased sintering^[55]) or increased initial NiO particle size lead to lower tolerance to redox cycles, with larger bulk anode volume changes and increased anode resistance from formation of cracks in the YSZ framework^[55].

The use of hydrocarbons as a fuel has advantages as described in section 1.1, however whilst nickel is a good reforming catalyst, the carbon has an affinity for nickel depositing on the catalyst, blocking pores and reducing the electrode

performance^[56]. It is possible to remove the deposited carbon reasonably efficiently by burning^[56], but this comes at a cost due to the poor redox stability of the Ni/YSZ anode and during filament formation, the nickel particles are actually lifted from their support causing irreversible damage to the anode^[57]. For methane to be used as a fuel with this anode, the internal reforming requires an excess of steam (2 moles of steam to every mole of methane) to ensure complete oxidation of the carbon^[57-58] according to equations 1.9-1.12. However, the dilution of fuel in this way decreases the open circuit potential as described in section 1.2 thereby reducing the fuel cell performance.



- 1.9 Methane reforming
- 1.10 Fuel cell reaction utilising both H₂ and CO as a fuel
- 1.11 Shift reaction
- 1.12 Fuel cell reaction utilising H₂ only as a fuel

1.4.3 Cathode

The cathode has the following requirements:

- High electronic conductivity
- Stability in oxidising atmospheres
- Non-reactive with electrolyte and interconnect at both operating/production temperatures and environments
- A thermal expansion close to other fuel cell components
- Sufficient porosity to allow transport of the fuel gas to the electrolyte/electrode interface

The most commonly used material for the solid oxide fuel cell cathode is doped LaMnO₃. Lanthanum manganite is a p-type perovskite oxide, and the electronic conduction occurs by the hopping of electron holes between the Mn³⁺ and Mn⁴⁺ states^[9, 16]. Doping with strontium to give: $La_{1-x}^{3+}Sr_x^{2+}Mn_{1-x}^{3+}Mn_x^{4+}O_3$ (LSM) causes some La³⁺ ions to be replaced by Sr²⁺ ions, which increases the Mn⁴⁺ content, decreases the activation energy (E_a) and increases the electronic conductivity^[16].

The electronic conductivity is not affected by changes in oxygen partial pressures between 1 and 10⁻¹⁰ atm^[16]. At lower oxygen partial pressures, the conductivity falls very quickly due to decomposition of the LaMnO₃. The range of acceptable oxygen partial pressures decreases with increasing strontium dopant levels, however increasing the strontium content increases the electronic conductivity, giving a maximum at La_{0.5}Sr_{0.5}MnO₃^[59]. The conductivity is stable at temperatures above 700°C^[16].

The thermal expansion co-efficient of the LaMnO₃ is higher than YSZ at 11.2x10⁻⁶K⁻¹, which increases with dopant concentration to 12.8x10⁻⁶K⁻¹ at x=0.3 Sr content^[16]. As with the anode, the difference in thermal expansion can be reduced by

addition of YSZ into the cathode, which also serves to increase the triple phase boundary^[60], reduce polarisation losses^[31] and increase adherence of the cathode to the electrolyte^[37, 60]. Since this has the effect of reducing the electronic conductivity, it is common in the electrode to have a multilayer composite cathode^[61], with high YSZ content near to the electrolyte and decreasing YSZ content until at the opposite side to the electrolyte it is 100% LSM to give the high conductivity required for the fuel cell.

One major problem associated with using the strontium doped lanthanum manganite as a cathode material is its tendency to react with the YSZ electrolyte. Two insulating phases are formed at high temperatures, typically in excess of 1200°C^[62-63]: the pyrochlore lanthanum zirconate $\text{La}_2\text{Zr}_2\text{O}_7$ (LZO)^[64] and perovskite strontium zirconite SrZrO_3 (SZO)^[16, 63]. These insulating phases act as a barrier layer to O^{2-} transport, the ionic conductivity of the LZO is much lower than that of the YSZ electrolyte – by about 2.5 orders of magnitude^[16, 62], increasing the ohmic losses and thereby reducing the performance of the fuel cell. The amount of LZO formed has been shown to decrease with the increasing strontium doping content allowing the use of increased production temperatures before the formation of any deleterious phase is seen, however, it is in the highly doped systems of $\text{La}_{1-x}\text{Sr}_x\text{MnO}_3$ with $x \geq 0.3$ when the SZO begins to form^[16, 64] exclusively forming at $x \geq 0.5$ ^[59]. Generally the pyrochlore formation is due to the high mobility of the manganese ion at processing temperatures. The manganese ion readily diffuses into the electrolyte^[16, 18] at high temperatures: processing temperatures are therefore kept below 1400°C to minimise the Mn diffusion, whereas at fuel cell operating temperatures of 1000°C the migration is negligible^[16]. The loss of manganese into the electrolyte results in a lanthanum excess in the LSM unit cell, leading to La_2O_3 precipitation, which then readily reacts

with the YSZ to form the pyrochlore LZO^[64]. The reaction then progresses by lanthanum diffusion through the reaction layer giving rise to Kirkendall voids and cathode-electrolyte de-lamination with thick LZO layers^[62-63].

A known and well researched method of reducing the LZO formation is to increase the manganese to lanthanum/strontium ratio, producing an A-site deficient LSM structure^[63-66]. This has the effect of increasing the 'induction period' the period of time where the manganese ions are diffusing into the electrolyte, but not to a high enough extent to lead to La₂O₃ precipitation and hence LZO formation. Using A-site deficient LSM therefore allows increased processing temperatures and/or times to be used severely reducing or even eliminating the formation of the insulating LZO. Conversely however, the migration of the manganese ions increases with increasing lanthanum deficiency^[17, 65], which affects the ionic conductivity of the YSZ electrolyte as detailed in section 1.4.1.

Finally, the LSM cathode material also reacts with the interconnect material: doped LaCrO₃ at high temperature to form (Sr,La)₃Mn₂O₇ and (Ca,La)₃Mn₂O₇, which occurs due to Cr and Sr migration and more importantly Cr volatilisation^[16].

1.4.4 Interconnect

The interconnect has the following requirements:

- Nearly 100% electronic conductivity ($>1\text{Scm}^{-1}$)^[67]
- Stability in both oxidising and reducing atmospheres
- Non-reactive with cathode and anode at both operating and production temperatures
- Thermal expansion close to other fuel cell components
- Gas tight to prevent direct combination of fuel and oxidant.

In the past, the most commonly used material for the high temperature solid oxide fuel cell interconnect is doped LaCrO_3 ^[2, 16, 22, 67- 68] and whilst high temperature steels (detailed later in this section) are becoming increasingly more commonplace some compatibility issues of the LaCrO_3 is relevant to the high temperature steels. Whilst doped LaCrO_3 is the best oxide available in terms of stability and high conductivity in both oxidising and reducing atmospheres and non-reactivity with other fuel cell components, there is however, one major challenge associated with this material: namely obtaining gas tight ceramics^[16, 67, 69].

The LaCrO_3 perovskite is a p-type conductor due to the holes in the 3d band of the chromium atoms. Similarly to the doped LaMnO_3 cathode material, in oxidising atmospheres, doping with a lower valence ion such as Sr or Ca (which replaces some La ions) or Mg, Fe, Ni, Cu, or Co (which replace some Cr ions) causes a charge compensation transition of Cr^{3+} to Cr^{4+} , increases the p-type electronic conductivity^[16, 68-69]. However, in reducing atmospheres, such as those experienced at the anode, charge compensation occurs by generation of oxygen vacancies resulting in a decrease in electronic conductivity^[68-70] by approximately 3 orders of magnitude^[16]. This results in a conductivity gradient across the interconnect during operation of the fuel

cell^[67]. However, as long as the operating temperature of the fuel cell remains above 800°C, the electronic conductivity of LaCrO₃ is sufficient for use as an interconnect material^[71].

As already mentioned above, doping with lower valence ions causes an increase in conductivity in oxidising atmospheres, however it also causes an increase in oxygen vacancies with the same reducing atmospheres when compared to the stoichiometric LaCrO₃ which affects the thermal expansion^[67] (and chemical expansion coefficient caused by the change in unit cell size with generation of oxygen vacancies in reducing atmospheres^[69, 72-74]) and thereby causing stresses and possible warping in the fuel cell stacks. In addition, increasing the doping content can increase the strength degradation associated with the interconnect in reducing atmospheres^[67]. Increased oxygen vacancies in reducing atmospheres leads to a higher oxygen permeability, which leads to a degree of oxygen transport from the cathode to the anode thereby reducing the fuel cells performance^[75].

The most commonly used dopant is strontium^[69], being favoured over other dopants due to its smaller effect on thermal expansion, allowing a higher degree of doping and hence increased conductivity^[67]. The thermal expansion of La_{0.9}Sr_{0.1}CrO₃ is $10.7 \times 10^{-6} \text{K}^{-1}$ ^[16, 67], which is very close to that of the electrolyte: $10.5 \times 10^{-6} \text{K}^{-1}$. The greatest challenge with this material is obtaining dense films; Cr(VI) is volatile at high sintering temperatures in oxidising atmospheres^[16, 67], resulting in thin layers of Cr₂O₃ forming at the interparticle neck at the initial sintering stages^[16, 67, 76]. Sintering under reduced oxygen partial pressures have been used to achieve high density films at temperatures in excess of 1700°C^[16, 77]. Lower temperature sintering has been investigated by increasing strontium doping levels and introducing A-site deficiency^[16] or slight B-site deficiency^[74]. Two strontium chromate phases SrCrO₄

and $\text{Sr}_{2.67}(\text{CrO}_4)_2$ were formed during sintering, which melted and aided densification, producing densities $>90\%$ when sintered at 1600°C for just 2hrs^[16, 78]. However, this was achieved when high strontium contents were used, which results in increased chemical expansion and hence can lead to structural failure of fabricated films. Further methods for reducing the sintering temperature below 1600°C include highly reactive powders (high surface area), sintering aids, for example strontium vanadate reduced the sintering temperature required to 1550°C ^[69] and modification of processing techniques, for example the use of microwave processing^[16].

Because of the difficulties described above in obtaining dense films of the doped LaCrO_3 material and because of the current movement towards researching lower operating temperature fuel cells ($500\text{-}800^\circ\text{C}$), typically for the planar solid oxide fuel cell (see section 1.5.1), which renders the doped LaCrO_3 useless due to its inadequate electronic conductivity at this temperature, there has been increased interest and research in high temperature alloys^[2, 16, 67, 79-80]. Although the thermal expansion of metals is generally higher than that of the YSZ^[22] $10.5 \times 10^{-6} \text{ K}^{-1}$, there is a greater tolerance to thermal expansion mismatch when using metallic interconnects as they are more flexible in accommodating associated stresses^[81-82]. In addition to the possibility of reduced temperature operation and less restraint on thermal expansion, metallic interconnects also have the advantages of electrical and thermal conductivity, stability and easy and low cost manufacture^[67, 80-81]. However, the challenges with using metallic interconnectors are connected to their oxidation at high temperature. This leads to the following requirements^[81-82]:

- Growth rate of oxide scale in both oxidising and reducing atmospheres are slow as possible
- Oxide scale is strongly adhered to the metal substrate without spallation or delamination during thermal cycling
- Oxide scale is dense, homogeneous in thickness and microstructure
- Oxide scale is a good conductor at the desired operating temperature

The alloys investigated for the interconnect material fall into three main categories^[81]: chromium based alloys, iron based alloys^[80] or nickel based superalloys^[79, 82], all of which have some level of chromium content; the Cr₂O₃ formed at fuel cell operating temperatures has a relatively low resistivity^[67, 82] and higher scaling temperature than the fuel cell operating temperature^[67]. The iron based alloys or nickel based superalloys are favoured over the chromium based alloys due to their lower cost and better long-term performance^[67, 80-81].

The oxidation process is a diffusion-controlled process which can be simplified by equation 1.13, where x is the scale thickness, K_p is the parabolic rate factor and t is time^[67-68, 79, 81-82]. Other factors which particularly affect the scale growth of chromium based alloys are gas transport through the scale due to the formation of microvoids and microcracks^[68].

$$x^2 = K_p t \quad 1.13$$

This has been noted with studies of scale growth in fuel cell cathode and anode environments. The partial pressure of oxygen typically seen in the fuel atmosphere in the fuel cell ranges between 10^{-22} and 10^{-17} atm: orders of magnitude higher than the Cr/Cr₂O₃ equilibrium of oxygen partial pressure of 10^{-28} atm (at 800°C)^[81-82], causing the formation of Cr₂O₃. Indeed, whilst not fully understood, the degree of scaling seen on the anode side is greater than that of the cathode side^[79, 81]. This is thought to

be due to the presence of water vapour, causing a porous scale to be formed^[81], thereby increasing the gas transport to the substrate as described above.

$$ASR = \tau_s l_s + 2\tau_o l_o \quad 1.14$$

The scale has a much lower conductivity than that of the alloy, increasing the area specific resistance (ASR) as determined by equation 1.14^[81] where τ_o and τ_s are the resistivity of the scale and alloy substrate respectively and l_o and l_s corresponds to the scale and alloy substrate thickness. Hence the requirement for a slow oxide growth rate to prolong the life-time of the interconnect material. The growth rate of Cr_2O_3 however is quite fast^[67], which can be retarded by addition of a small quantity of reactive elements^[79, 82] such as Y, La, Zr. They also have the effect of increasing adherence of the scale to the substrate, thereby reducing the likelihood for spallation of the scale and changing the thermal expansion co-efficient^[67].

As with the ceramic interconnect described above, the metallic interconnects suffer from the high volatility of Cr (VI) in fuel cell operating conditions^[67]. This can lead to poisoning of the cathode by deposits of Cr_2O_3 at the cathode-electrolyte interface and in the pores^[81] and reaction with the LSM to form Cr_2MnO_4 spinel^[83]. In addition, during fuel cell start-up, the NiO in the anode can react to form Ni-Cr spinels, which are consequently reduced with the NiO, this can lead to deposits of large Cr_2O_3 crystals in the anode^[81].

Research is on-going to coat the metallic interconnect with an oxide which retards the chromium diffusion, whilst remaining electronically conductive and possessing all other necessary physical properties such as matching thermal expansion and stability. Positive results have been obtained with the Mn coating of a nickel-based superalloy Haynes 230, which had the effect of forming $MnCr_2O_4$, improving

the electrical conductivity of the scale^[84-85]. Other examples of other coatings investigated are La, LSC, LSM and LSCo (Sr doped lanthanum cobalt).^[22, 81, 85]

1.5 Different Design Geometry

The two main, most developed fuel cell geometries are the planar and tubular geometries detailed in the following sections. Each has their associated advantages and disadvantages: no requirement for seals and high unit strength (tubular advantages over planar design), and cheap manufacturing techniques and short current paths (planar advantages over tubular design).

1.5.1 Planar Geometry

The planar design, shown in figure 1.7 was the first fuel cell design and is the simplest. Due to the brittle nature of ceramic materials, the strength of this design is obtained by a 'support' layer. Figure 1.7 shows an electrolyte supported design, whereby the thickness of the electrolyte is much larger than that of the other components^[31], typically in excess of $200\mu\text{m}$ ^[16]. This was the original support for the planar cell, but with research now aiming for reduced operating temperature electrolytes as thick as this have much too high an ohmic resistance^[31] and so the support is now generally the anode. Naturally any component could feasibly be used as the support material, but high cost prevents the use of the cathode or interconnect material. Having the anode as the support material allows the electrolyte thickness to be greatly reduced. Various thicknesses have been reported, with the anode thickness ranging from $200\mu\text{m}$ ^[49, 86] to $1500\mu\text{m}$ ^[87] as the support, with the electrolyte thickness reduced to between $6\mu\text{m}$ ^[86] and $20\mu\text{m}$ ^[87].

The interconnect material is a bi-polar plate, which can be arranged in a co-flow or crossflow design. The cross flow system is shown in figure 1.7, whereby the fuel and air are supplied at different faces (in the co-flow system the fuel and air are both supplied at the same edge). The bipolar plate allows the interconnect to make

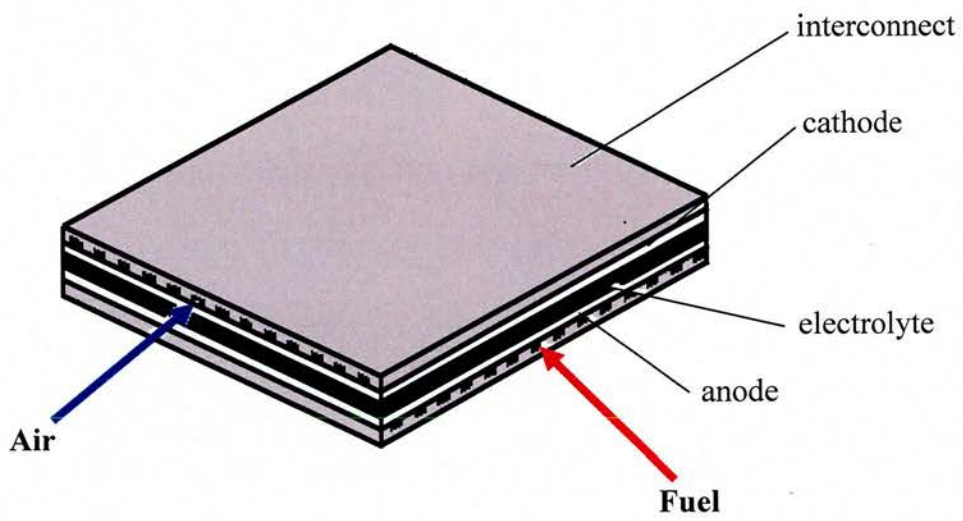


Figure 1.7: Cross-flow electrolyte supported planar design

good connection with both the cathode and anode material, whilst allowing adequate gas flow^[6]. A balance needs to be obtained between good gas flow into the fuel cell without sacrificing the electrical connection between the electrodes and interconnect.

The ease of producing flat sheets means a variety of many processing techniques for the production of each component is available, allowing the cheapest processing technique to be chosen without sacrificing the component quality^[2, 16]. Typical processing techniques for each component are as follows: electrodes – slurry casting, screen printing and plasma spraying, electrolyte – tape casting, and interconnect – tape casting or hot pressing^[16]. This is one of the greatest advantages of this design, as one of the major problems with fuel cells is the high cost. One other great advantage of the planar design is the short current path. The current path is merely the cross-section of the fuel cell before it reaches the interconnect material, and is transported to the external circuit.

There are of course disadvantages associated with this and with every design. The planar cell requires a thicker support material, which already touched on has problems with reduced efficiency (increased ohmic losses associated with the electrolyte supported design), reduced lifetime (poor redox stability associated with the anode supported design) and increased cost (with the cathode supported design).

A major concern of the planar design is the need for high temperature seals, another driving force for the reduced temperature operation of fuel cells^[88]. As the importance of having an air tight electrolyte, high temperature seals are required around the plate edges to prevent the fuel and oxidant coming into contact in any other way than by the electrochemical reaction in the fuel cell to yield high efficiencies. Different seals can be used, each with their own associated problems^[16]. Compressive seals can lead to cracking of the plates due to the uneven stress

distribution it imposes on the fuel cell and cement and glass seals react with the fuel cell components at the high operating temperatures and are brittle in nature. A variation of the planar design produced by Sulzer-Hexis Ltd has limited sealing concepts allowing un-used fuel and oxidant to come into contact and combust, providing heat^[6], similar to the tubular design reducing some of these problems.

A further problem occurs with the stacking of the planar fuel cell design. As described in section 1.2, each fuel cell can only achieve a maximum voltage of just over 1V, and so many cells must be stacked together in order to be a useful electrical source. The planar design isn't very mechanically strong, and as the cells are stacked one on top of the other, the weight of the stack often causes cracks in the ceramics, leading to reduced performances. Stresses in the fuel cell due to thermal expansion mismatches cause bending of the flat plates during heating (which is more pronounced after NiO reduction), leading to loss of electrical contact between electrodes and current collectors and when constrained by seals and interconnects and so on lead to formation of cracks, reducing performance^[89].

Power densities obtained are high, with typical cell performance of 0.7V, with a current density of $260\text{mA}\cdot\text{cm}^{-2}$ ^[16]. Ceramic Fuel Cell Ltd have produced 25kW stacks, and plan demonstrations of a 100kW stack^[6].

1.5.2 Tubular Geometry

The tubular design (figure 1.8) answered two of the main disadvantages associated with the planar design: the removal of high temperature seals^[22], and increased strength as the basic tubular geometry has a high unit strength. Figure 1.9 shows the tube is open at one end only, and air is fed down the centre of the cell through a thin alumina tube^[6]. The oxidant gas is introduced at room temperature, and so the only seal associated with the tubular cell is not at high temperatures and is therefore easily sealed. The air is heated as it travels down the tube, so when it reaches the bottom (closed end) it has reached operating temperatures. The air then flows back up the tube, in contact with the air electrode. Any un-reacted oxygen reaching the top of the tube meets with un-reacted fuel, combusting to provide heat which serves to warm incoming gases^[6]. The imperfect, non-gas tight seals allow the product (steam) to enter the fuel allowing internal reforming of the fuel.

As for the planar cell, the tubular cell requires a thicker support material which leads to higher cost or loss of performance as detailed above in section 1.5.1. The cathode is generally the support, which consists of over 90% of the fuel cell weight^[9], having a typical porosity of 35%^[16].

Unlike the planar cell, the more complex design of the tubular cell limits the techniques available for processing each component, and therefore the processing costs are higher than that of the planar cell. The cathode is produced by an extrusion process^[16, 22], after which the interconnect is deposited by EVD (electrochemical vapor deposition)^[16, 22], or plasma spraying^[16], in the form of a strip along the length of the tube. The interconnect strip is typically 85 μ m thick^[9, 22] and 9mm wide^[9, 16]. The electrolyte layer is deposited on top of the cathode, also by the EVD process to

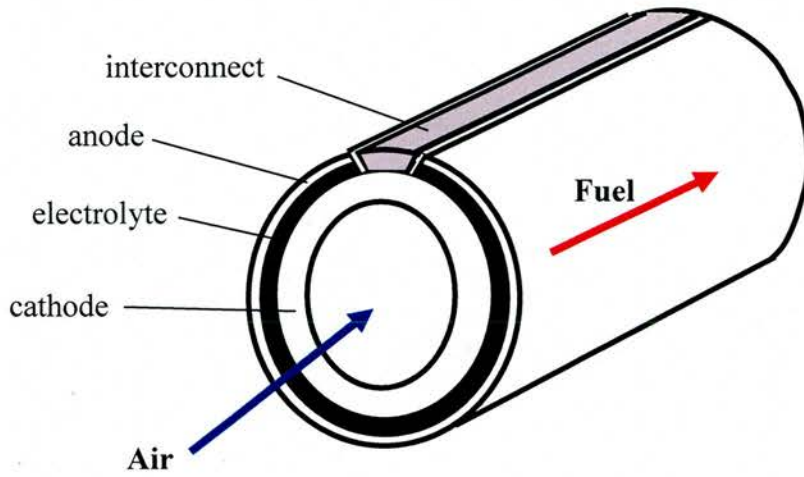


Figure 1.8: Cathode supported tubular design

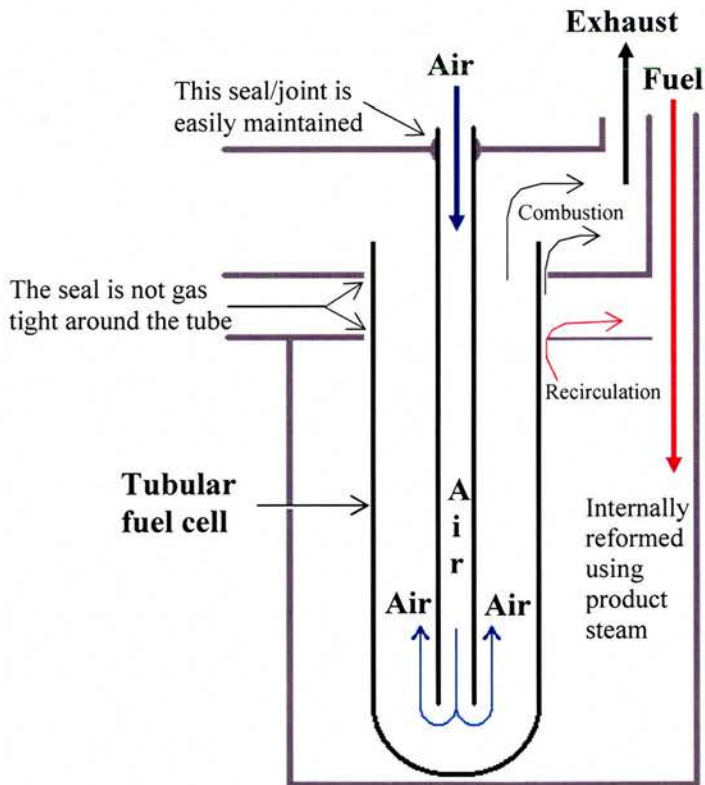


Figure 1.9: Schematic of the tubular fuel cell in operation

form a dense layer, approximately $40\mu\text{m}$ thick^[16, 22]. Siemens-Westinghouse produce tubular cells using 10mol% YSZ electrolyte^[6], favoured over the higher conductivity of 8mol% YSZ, due to its longer lifetime (see section 1.4.1). The anode is deposited in a two-stage process. Firstly the cell is dipped in a nickel slurry and secondly the YSZ is added by the EVD process^[9]. An alternative method of depositing the anode material is to use a Ni/YSZ slurry, depositing the cermet in one step^[9]. This process has proved to produce anodes of a similar standard, and as EVD is a high cost processing technique, reduces the cost of fabrication. The anode layer thickness is between $100\text{-}150\mu\text{m}$ ^[9, 16, 22], and it doesn't cover the entire electrolyte layer, to ensure that no connection is made with the interconnect, preventing cell shorting. Nickel is plated on top of the interconnect strip to provide electrical contact^[16].

The fuel cells are stacked together in series, as shown in figure 1.10 and in parallel, joined as in series, by nickel felt^[16]. In order to reduce the cost associated with the support cathode tube, in the past a porous support tube of calcia stabilised zirconia has been used in order to reduce cost, but the long current path associated with the tubular cell shown in figure 1.10, has led to this being discarded.

The tubular design (produced initially by Siemens Westinghouse) is currently the most advanced at present in the solid oxide fuel cell market. Typical dimensions of the tubes manufactured by Siemens-Westinghouse are 150cm long with a diameter of 2.2cm ^[6] and work is ongoing to achieve tubes with a length greater than 2m ^[16]. Typical cell performance is 0.68V at 250mAcm^{-2} , using a 89% H_2 , 11% H_2O fuel mix, with approximately 85% fuel utilisation^[16].

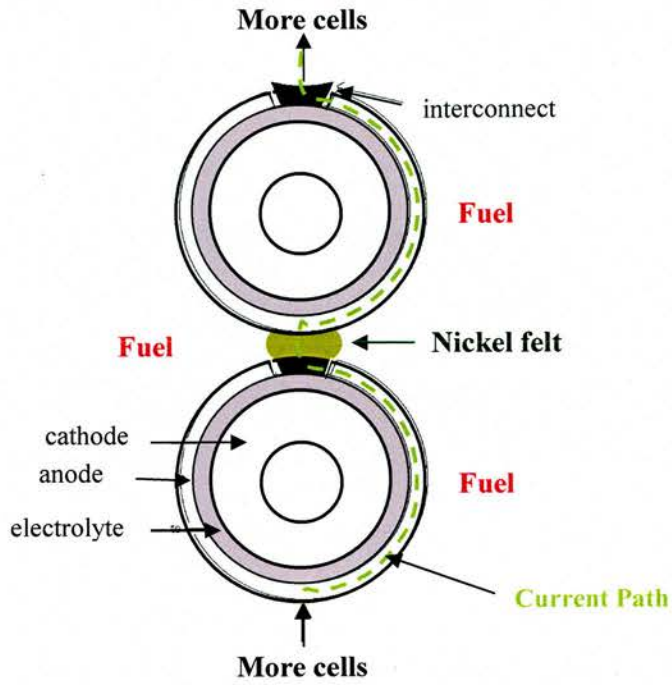


Figure 1.10: Stacking of the tubular cells

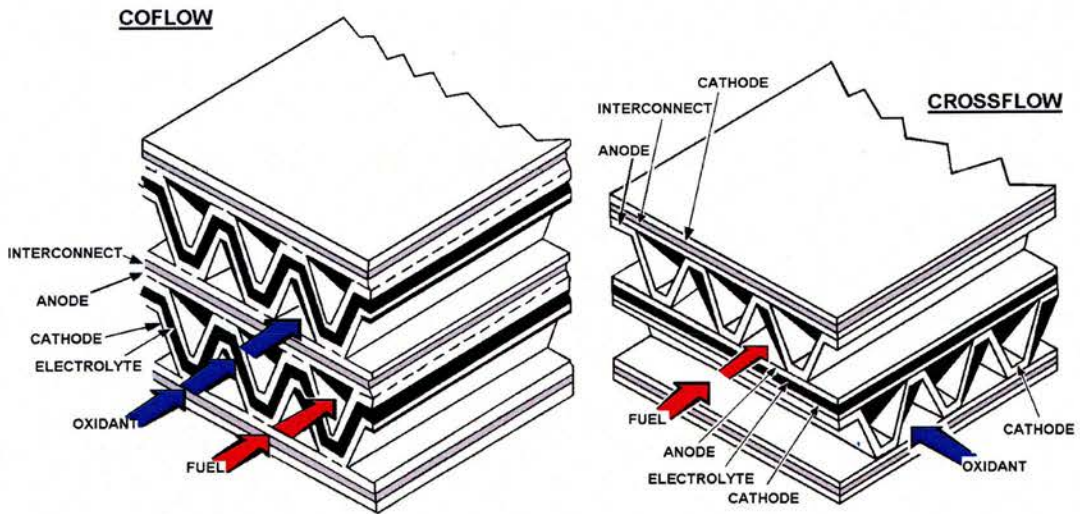


Figure 1.11: Monolithic fuel cell – co flow and cross flow arrangements

1.5.3 Monolithic Fuel Cell

The monolithic fuel cell, shown in figure 1.11, is fabricated by tape casting and tape calendaring^[16]. The fuel cell is produced in the green state, and then fired, all together, with component thicknesses of approximately $100\mu\text{m}$ ^[16]. The co-firing offers advantages in reduction of production time (which differs from other designs, where each layer is deposited and sintered before the next layer is deposited).

In addition to the reduced production costs, the monolithic fuel cell has other advantages such as a small cell size and high power density^[16]. The cell is much lighter than other designs, which is achieved by eliminating the need for supports, such as in the anode/electrolyte supported planar fuel cell design. The small cell size allows higher current densities approximately 2.2Acm^{-2} (with H_2 fuel and air as the O_2 source)^[16] to be achieved due to lower activation polarisation losses and increased active surface area, and power densities are calculated to be 8kWkg^{-1} , or 4kWl^{-1} ^[22].

The two different designs – co-flow and cross-flow have their own associated advantages. The co-flow design, whereby the fuel and air flow in parallel achieves a higher power density,^[16] and the cross-flow design, whereby the fuel and air-flow are perpendicular to each other, approaching the cell from different sides, is much easier to manage the incoming and outgoing gases^[16].

1.6 Aim of this Work

A new design of fuel cell: the SOFCRoll shown in figure 1.12 has been proposed at the University of St Andrews^[90]. This design offers a number of advantages over existing designs as follows. The production technique of all components is tape casting (similar to the monolithic design, section 1.5.3) a cheap and easily scalable manufacturing technique, all components being produced, laminated and co-fired in a single step. The need for the LaCrO₃ based high temperature interconnect material is removed (similar to the planar design, section 1.5.1). There is therefore a large reduction in production cost: with the removal of expensive interconnect materials, with the utilization of a cheap production technique for all layers, and co-firing shortening production time and cost with only one high temperature sintering step required. It also has the unit strength associated with the tubular fuel cell, with the spirals around the central tubes giving the fuel cell high mechanical strength. Since each spiral layer is in contact with the next giving the high strength, the need for a thicker component for support (as described in sections 1.5.1 and 1.5.2) is eliminated, further reducing cost.

The gases are introduced through the loops in the centre and flow down the length of each tube in the same way as the tubular design and additionally flow around the spirals as shown in figure 1.13. This is another important advantage of this cell: the SOFCRoll support (the spiral layers) are active layers, making use of the entire fuel cell and thereby giving the fuel cell a high power density^[90]. However, in order to get good gas transport through the spirals, the porosity of the electrode layers must be higher than is necessary for the other fuel cell designs – approximately 50% porosity in contrast to 30%, which is satisfactory for other fuel cell designs. In a

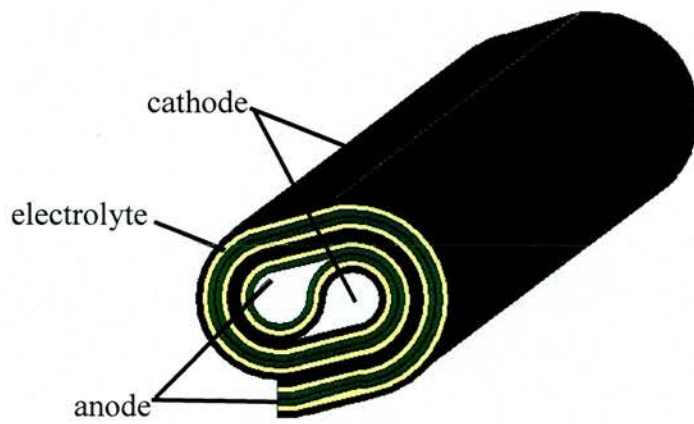


Figure 1.12: The SOFCRoll design

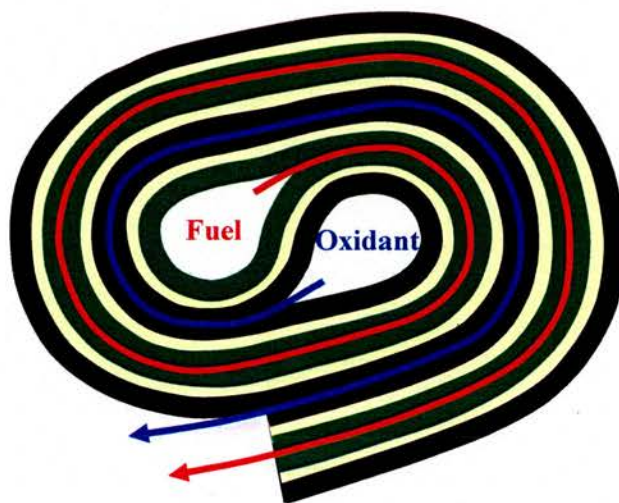


Figure 1.13: Gas flow around the spirals of the SOFCRoll design

similar manner to that of the tubular design, high temperature seals are not a problem; the tubes are easily sealed with electrolyte material during the initial processing stage.

The electrical connections to the cell are made by inserting steel tubes into the gas inlet holes. These tubes will both act as a current collector and method for introducing the gases to the fuel cell. Since the tubes (interconnect material) will only be at one end of the fuel cell (and not down the entire length as the tubular design section 1.5.2) the majority of the fuel cell can be at a high temperature thus increasing the performance with the use of YSZ electrolyte and LSM cathode (see sections 1.4.1 and 1.4.3).

The aim of this project was to produce this design via the tape casting technique with the 'standard' fuel cell materials: YSZ electrolyte, LSM cathode and Ni/YSZ anode for a proof of concept. The tape casting technique is good for the production of dense films, methods of introducing adequate porosity for the desired microstructure were needed for the electrodes. One of the most challenging areas of this project regarding production is matching the shrinkage profile of each component, whilst maintaining their desired microstructure. However, this is vitally important to ensure that minimal strain is put on the system during co-firing, giving good mechanical strength for the fuel cells with a fault-free electrolyte.

1.7 References

- 1 A. McDougall, "Fuel Cells" London: The MacMillan Press Ltd, **1976**
- 2 A. B. Stambouli, E. Traversa, "Solid oxide fuel cells (SOFCs): a review of an environmentally clean and efficient source of energy", *Renewable and Sustainable Energy Reviews*, *6*, **2002**, 433-455
- 3 W. Zittel, R. Wurster, L. Bolkow, "Hydrogen in the Energy Sector", Systemtechnik, Gmbitt, **1996**
- 4 J. J. Romm, "The Hype about Hydrogen", Washington: Island Press, **2004**
- 5 P. Hoffmann, "Tomorrow's Energy Hydrogen, Fuel Cells, and the prospects for a Cleaner Planet", London: The MIT Press, **2002**
- 6 J. Larminie, A. Dicks, "Fuel Cell Systems Explained", Chichester: John Wiley & Sons Ltd, **2001**
- 7 T. Stephenson, "Key Issues for Building a Hydrogen Infrastructure", Shell Global Solutions (UK). *Presented at a Fuel Cell Seminar, Edinburgh UK: 'Hydrogen/Fuel Cells – The New Energy Economy in the Scottish Context'* 10 October **2001**
- 8 C. E. G. Padró, V. Putsche, "Survey of the Economies of Hydrogen Technologies", Technical Report, NREL/TP-570-27079, NREL National Renewable Energy Laboratory, Golden, Colorado 80401-3393, **1999**
- 9 S. C. Singhal, "Advances in Solid Oxide Fuel Cell Technology", *Solid State Ionics*, **2000**, *135*, 305-313
- 10 J. Stainiforth, M. Ormerod, "Running fuel cells on biogas – a renewable fuel", *Green Chemistry*, **2001**, G61-63
- 11 "Farm looks to fuel cells to help with the chores", ENN, September 18 **2000**
- 12 C. Baird, "Environmental Chemistry", 2nd edition, NY: W. H. Freeman and Company, **1998**
- 13 B. Eliasson, U. Bossel, "The Future of the Hydrogen Economy: Bright or Bleak?", in: M. Nurdin (Eds), *Proceedings of the International Conference with Exhibition The Fuel Cell World*, Lucerne, Switzerland, 1-5 July **1999**, 367-382
- 14 W. Vielstich, "Fuel Cells, Modern Processes for the Electrochemical Production of Energy", Chichester: Wiley-Interscience, **1970**
- 15 K. R. Williams, "An introduction to Fuel Cells". Ed by Keith R. Williams, Amsterdam London: Elsevier, **1966**
- 16 N. Q. Minh, "Ceramic Fuel Cells", *J. Am. Ceram. Soc.*, *76* (3), **1993**, 563-588
- 17 K. V. Kordesch, G. R. Simader, "Environmental Impact of Fuel Cell Technology". *Chem. Revs.*, *95* (1), **1995**, 191-207
- 18 S. P. Badwal, "Stability of Solid Oxide Fuel Cell Components", *Solid State Ionics*, *143*, **2001**, 39-46

- 19 A. C. Fisher "Examples of Fuel Cells", University of Cambridge, Department of Chemical engineering, April **2005**, at: <http://www.cheng.cam.ac.uk/research/groups/electrochem/JAVA/electrochemistry/ELEC/110html/main.html>
- 20 M. M. Nasrallah, D. L. Douglas, "Ionic and Electronic Conductivity in Y₂O₃ doped monoclinic ZrO₂", J. Electrochem. Soc., *121* (2), **1974**, 255-262
- 21 S. P. S. Badwal, "Zirconia-based solid electrolytes: microstructure, stability and ionic conductivity", Solid State Ionics, *52*, **1992**, 23-32
- 22 O. Yamamoto, "Solid oxide fuel cells: fundamental aspects and prospects", Electrochim. Acta, *45*, **2000**, 2423-2435
- 23 J. Kondoh, T. Kawashima, S. Kikuchi, Y. Tomii, Y. Ito, "Effect of Aging on Yttria-stabilised zirconia I: A study of its electrochemical properties", J. Electrochem. Soc., *145* (5), **1998**, 1527-1536
- 24 J. A. Kilner, R. J. Brook, "A study of oxygen ion conductivity in doped nonstoichiometric oxides", Solid State Ionics, *6*, **1982**, 237-252
- 25 V. N. Chebotin, V. A. Mezrin, "Ordering of defects, thermodynamic and transport-properties of solid oxide electrolytes with fluorite structure", Phys. Status Solidi A, *89* (1), **1985**, 199-211
- 26 C. C. Appel, N. Bonanos, A. Horsewell, S. Linderorth, "Ageing behaviour of zirconia stabilised by yttria and manganese oxide", J. Mat. Sci., *36*, **2001**, 4493-4501
- 27 I. R. Gibson, G. P. Dransfield, J. T. S. Irvine, "Influence of yttria concentration upon electrical properties and susceptibility to ageing of yttria-stabilised zirconias", J. Eur. Ceram. Soc. *18*, **1998**, 661-667
- 28 I. R. Gibson, J. T. S. Irvine, "Qualitative X-ray Diffraction Analysis of Metastable Tetragonal (t') Zirconia", J. Am. Ceram. Soc. *84*(3), **2001**, 615-618
- 29 H. G. Scott, "Phase relationships in the zirconia-yttria system", J. Mat. Sci., *10*, **1975**, 1527-1535
- 30 F. T. Ciacchi, K. M. Crane, S. P. S. Badwal, "Evaluation of commercial zirconia powders for solid oxide fuel cells", Solid State Ionics, *73*(1-2), **1994**, 49-61
- 31 J. P. P. Huijsmans, "Ceramics in solid oxide fuel cells", Current Opinion in Solid State and Materials Science, *5*, **2001**, 317-323
- 32 S. Linderorth, N. Bonanos, K. V. Jensen, J. B. Bilde-Sørensen, "Effect of NiO-to-Ni Transformation on Conductivity and Structure of Yttria-Stabilized ZrO₂", J. Am. Ceram. Soc., *84*(11), **2001**, 2652-56
- 33 J. Kondoh, S. Kikuchi, Y. Tomii, Y. Ito, "Effect of aging on yttria-stabilised zirconia. II A study of the effect of the microstructure on conductivity", J. Electrochem. Soc., *145* (5), **1998**, 1536-1550
- 34 J. Kondoh, S. Kikuchi, Y. Tomii, Y. Ito, "Effect of aging on yttria-stabilized zirconia III. A study of the effect of local structures on conductivity", J. Electrochem. Soc., *145*, **1998**, 1550-1560

- 35 C. Wang, W. L. Worrell, S. Park, J. M. Vohs and R. J. Gorte, "Fabrication and Performance of Thin Film YSZ Solid Oxide Fuel Cells", *J. Electrochem. Soc.*, *148* (8), **2001**, 864-868
- 36 H. Ohri, T. Matsushima, T. Hirai, "Performance of a solid oxide fuel cell fabricated by co-firing", *J. Power Sources*, *71*, **1998**, 185-189
- 37 E. Ivers-Tiffée, A. Weber, D. Herbstritt, "Materials and technologies for SOFC-componenets", *J. Eur. Ceram. Soc.*, *21*, **2001**, 1805-1811
- 38 M. Aoki, Y. M. Chiang, I. Kosacki, I. J. R. Lee, H. Tuller, Y. P. Liu, "Solute segregation and grain-boundary impedance in high-purity stabilized zirconia", *J. Am. Ceram. Soc.*, *79*(5), **1996**, 1169-1180
- 39 J. G. Li, T. Ikegami, J. H. Lee, T. Mori, "Low-temperature fabrication of transparent yttrium aluminium garnet (YAG) ceramics without additives", *J. Am. Ceram. Soc.* *83*(4), **2000**, 961-963
- 40 J. H. Lee, T. Mori, J. G. Li, T. Ikegami, M. Komatsu, H. Haneda, "The influence of alumina distributions upon scavenging highly resistive grain-boundary phase of 8 mol% yttria-stabilized zirconia", *Electrochemistry*, *68*(6), **2000**, 427-432
- 41 C. C. Appel, G. A. Botton, A. Horsewell and W. M. Stobbs, "Chemical and Structural Changes in Manganese-Doped Yttria-Stabilized Zirconia Studied by Electron Energy Loss Spectroscopy Combined with Electron Diffraction", *J. Am. Ceram. Soc.*, *82* (2), **1999**, 429-435
- 42 T. Kawada, N. Sakai, H. Yokokawa, M. Dokiya, "Electrical properties of transition metal-doped YSZ", *Solid State Ionics*, *53-56*, **1992**, 418-425
- 43 C. W. Tanner, K. Fung, A. V. Virkar, "The Effect of Porous Composite Electrode Structure on Solid Oxide Fuel Cell Performance", *J. Electrochem. Soc.*, *144* (1), **1997**, 21-30
- 44 R. J. Gorte, S. Park, J. M. Vohs, C. Wang, "Anodes for Direct Oxidation of Dry Hydrocarbons in a Solid Oxide Fuel Cell" *Adv. Mater.*, *12* (19), **2000**, 1465-1469
- 45 D. W. Dees, T. D. Claar, T. E. Easler, D. C. Fee, F. C. Mrazek, "Conductivity of Porous Ni/ZrO₂-Y₂O₃ Cermets", *J. Electrochem. Soc.*, *134* (9), **1987**, 2141-2146
- 46 S. K. Pratihari, R. N. Basu, S. Mazumder, H. S. Maiti, "Electrical Conductivity and Microstructure of Ni-YSZ Anode Prepared by Liquid Dispersion Method", in: S. C. Singhal, M. Dokiya (Eds), *Proceedings of the Sixth International Symposium on Solid Oxide Fuel Cells (SOFC-VI)*, Honolulu, Hawaii, 17-22 October **1999**, 513
- 47 S. P. Jiang, P. J. Callus, S. P. S. Badwal, "Fabrication & Performance of Ni/3mol% Y₂O₃-ZrO₃ cermet anodes for Solid Oxide Fuel Cells", *Solid State Ionics*, *132*, **2000**, 1-14
- 48 B. de Boer, M. Gonzalez, H. J. M. Bouwmeester, H. Verweij, "The Effect of the Presence of fine YSZ Particles on the Performance of Porous Nickel Electrodes", *Solid State Ionics*, *127*, **2000**, 269-276

- 49 P. Charpentier, P. Fragnaud, D. M. Schleich, E. Gehain, "Preparation of Thin Film Solid Oxide Fuel Cells working at Reduced Temperature", *Solid State Ionics*, *135*, **2000**, 373-380
- 50 H. Itoh, T. Yamamoto, M. Mori, T. Horita, N. Sakai, H. Yokokawa, M. Dokiya, "Configurational and Electrical Behaviour of Ni-YSZ Cermet with Novel Microstructure for Solid Oxide Fuel Cell Anodes", *J. Electrochem. Soc.*, *144(2)*, **1997**, 641-646
- 51 S. K. Pratihari, A. Das Sharma, R. N. Basu, H. S. Maiti, "Preparation of nickel coated YSZ powder for application as an anode for solid oxide fuel cells", *J. Power Sources*, *129*, **2004**, 138-142
- 52 S. F. Corbin, X. Qiao, "Development of Solid Oxide Fuel Cell Anodes Using Metal-Coated Pore-Forming Agents", *J. Am. Ceram. Soc.*, *86(3)*, **2003**, 401-406
- 53 M. Cassidy, G. Lindsay, K. Kendall, "The reduction of nickel-zirconia cermet anodes and the effects on supported thin electrolytes", *J. Power Sources*, *61*, **1996**, 189-192
- 54 A. C. Müller, D. Herbstritt, E. Ivers-Tiffée, "Development of a multilayer anode for solid oxide fuel cells", *Solid State Ionics*, *152-153*, **2002**, 537-542
- 55 D. Fouquet, A. C. Müller, A. Weber, E. Ivers-Tiffée, "Kinetics of Oxidation and Reduction of Ni/YSZ Cermets" in J. Huijismans (Ed), *Proceedings of the 5th European Solid Oxide Fuel Cell Forum, Vol 1*, Lucerne, Switzerland, July 1-5, **2002**, 467-474
- 56 J.-H. Koh, Y.-S. Yoo, J.-W. Park, H. C. Lim, "Carbon deposition and cell performance of Ni-YSZ anode support SOFC with methane fuel", *Solid State Ionics*, *149*, **2002**, 157-166
- 57 S. McIntosh, R. J. Gorte, "Direct Hydrocarbon Solid Oxide Fuel Cells", *Chem. Revs.*, *104 (10)*, **2004**, 4845-4865
- 58 D. L. Trimm, Z. I. Önsan, "Onboard fuel conversion for hydrogen-fuel-cell-driven vehicles", *Catalysis Reviews*, *43(1&2)*, **2001**, 31-84
- 59 H-K. Lee, "Electrochemical characteristics of $\text{La}_{1-x}\text{Sr}_x\text{MnO}_3$ for solid oxide fuel cell", *Mat. Chem. Phys.*, *77*, **2002**, 639-646
- 60 S. Wang, Y. Jiang, Y. Zhang, J. Yan, W. Li, "Promoting Effect of YSZ on the Electrochemical Performance of YSZ and LSM Composite Electrodes" *Solid State Ionics*, *113-115*, **1998**, 291-303
- 61 P. Holtappels, C. Bagger, "Fabrication and performance of advanced multi-layer SOFC cathodes", *J. Euro. Ceram. Soc.* *22*, **2002**, 41-48
- 62 C. Brugnoli, U. Decati, M. Scagliotti, "SOFC cathode/electrolyte interface. Part I: Reactivity between $\text{La}_{0.85}\text{Sr}_{0.15}\text{MnO}_3$ and $\text{ZrO}_2\text{-Y}_2\text{O}_3$ ", *Solid State Ionics*, *76*, **1995**, 177-182
- 63 J. A. M. van Roosmalen, E. H. P. Cordfunke, "Chemical reactivity and interdiffusion of $(\text{La,Sr})\text{MnO}_3$ and $(\text{Zr,Y})\text{O}_2$, solid oxide fuel cell cathode and electrolyte materials", *Solid State Ionics*, *52*, **1992**, 303-312

- 64 A. Mitterdorfer, L. J. Gauckler, "La₂Zr₂O₇ formation and oxygen reduction kinetics of the La_{0.85}Sr_{0.15}Mn_yO₃, O₂ (g)|YSZ system", *Solid State Ionics*, *111*, **1998**, 185-218
- 65 C. Clausen, C. Bagge, J. B. Bilde-Sørensen, A. Horsewell, "Microstructural and Microchemical Characterization of the Interface between La_{0.85}Sr_{0.15}MnO₃ and Y₂O₃-stabilized ZrO₂", *Solid State Ionics*, *70/71*, **1994**, 59-64
- 66 A. Weber, R. Männer, B. Jobst, M. Schiele, H. Cerva, R. Waser, E. Ivers-Tiffée, "The influence of A-site deficiency on the performance of Strontium doped Lanthanum-manganate perovskite type SOFC-cathodes" in: Poulsen, Bonanos, Linderoth, Mogensen, Christiansen, (Ed.), *Proceedings on the 17th Risoe International Symposium on Materials Science: High Temperature Electrochemistry: Ceramics and Metals* Risoe National Laboratory, Roskilde, Denmark, **1996**, 473-478
- 67 W. Z. Zhu, S. C. Deevi, "Development of interconnect materials for solid oxide fuel cells", *Mater. Sci Eng.*, *A348*, **2003**, 227-243
- 68 K. Hilpert, W. J. Quadackers, L. Singheiser, Chapter 74 "Interconnects" in: "Handbook of Fuel Cells – Fundamentals, Technology and Applications", Ed. W. Vielstich, A. Lamm, H. A. Gasteiger, Chichester: John Wiley & Sons Ltd, **2003**
- 69 S. P. Simner, J. S. Hardy, J. W. Stevenson, T. R. Armstrong, "Sintering of Lanthanum Chromite using Strontium Vanadate", *Solid State Ionics*, *128*, **2000**, 53-63
- 70 D. B. Meadowcroft, "Some properties of strontium-doped lanthanum chromite", *J. Phys. D: App. Phys.*, *2 (9)*, **1969**, 1225-1233
- 71 N. Q. Minh, T. Takahashi, "Science and Technology of Ceramic Fuel Cells", Elsevier, Amsterdam, **1995**
- 72 T. R. Armstrong, J. W. Stevenson, L. R. Pederson, P. E. Raney, "Dimensional Instability of Doped Lanthanum Chromite", *J. Electrochem. Soc.*, *143 (9)*, **1996**, 2919
- 73 W. Paulik, S. Baskaran, T. R. Armstrong, "Mechanical properties of calcium- and strontium-substituted lanthanum chromite", *J. Mater. Sci.*, *33 (9)*, **1998**, 2397-2404
- 74 N. Sakai, T. Kawada, H. Yokokamo, M. Dokiya, T. Iwata, "Thermal expansion of some chromium deficient lanthanum chromites", *Solid State Ionics*, *40/41*, **1990**, 394-397
- 75 N. Sakai, T. Horita, H. Yokokawa, M. Dokiya, T. Kawada, K. Hiwatashi, A. Ueno, M. Aizawa, "Electrochemical Oxygen Permeation through Lanthanum Chromite Interconnects," in: B. Thorstensen (ed.), *Proceedings of the 2nd European Solid Oxide Fuel Cells*, May 6-10 **1996**, Oslo, Norway, *Vol. 2*, 531-541
- 76 H. Yokokawa, N. Sakai, M. Dokiya, "Chemical Thermodynamic Considerations in Sintering of LaCrO₃ based perovskites", *J. Electrochem. Soc.*, *138 (4)*, **1991**, 1018-
- 77 L. Group, H. U. Anderson, "The Influence of Oxygen Activity on Sintering of Sr-Doped Lanthanum Chromite", *J. Am. Ceram. Soc.* *59(9-10)*, **1976**, 449-354
- 78 S. P. Simner, J. S. Hardy, J. W. Stevenson, T. R. Armstrong, "Sintering mechanisms in strontium doped lanthanum chromite", *J. Mater. Sci.* *34(23)*, **1999**, 5721-5732

- 79 D. M. England, A. V. Virkar, "Oxidation Kinetics of Some Nickel-Based Superalloy Foils in Humidified Hydrogen and Electronic Resistance of the Oxide Scale Formed, Part II", *J. Electrochem. Soc.*, *148(4)*, **2001**, A330-338
- 80 Z. Yang, M. S. Walker, P. Singh, J. W. Stevenson, "Anomalous Corrosion Behaviour of Stainless Steels under SOFC Interconnect Exposure Conditions", *Electrochem. Solid St.*, *6(10)*, **2003**, B35-37
- 81 W. Z. Zhu, S. C. Deevi, "Opportunity of metallic interconnects for solid oxide fuel cells: a status on contact resistance", *Mat. Res. Bull.*, *38*, **2003**, 957-972
- 82 D. M England, A. V. Virkar, "Oxidation Kinetics of Some Nickel-Based Superalloy Foils and Electronic Resistance of the Oxide Scale Formed in Air, Part I", *J. Electrochem. Soc.*, *146(9)*, **1999**, 3196-3202
- 83 D. Dulieu, J. Cotton, H. Greiner, "Development of Interconnector Materials for Intermediate Temperature SOFC's" in: P. Stevens (Ed.), *Proceedings of Third European Solid Oxide Fuel Cell Forum, Nantes, France, June 2-5 1998*, 447-458
- 84 A. V. Virkar, D. M. England, Solid Oxide Fuel Cell Interconnector, US Pat. 6053231
- 85 T. J. Armstrong, M. A. Homer, A. V. Virkar, "Evaluation of Metallic interconnects for use in Intermediate Temperature SOFC" in S. C. Singhal, M. Dokiya (Ed), *Proceedings of the International Symposium SOFC VIII, Vol 2003-07, Paris, France, April 2003*, 841-850
- 86 J. Van Herle, R. Ihringer, R. Vasquez Cavieres, L. Constantin, O. Bucheli, "Anode Supported Solid Oxide Fuel Cells with Screen-Printed Cathodes", *J. Eur. Ceram. Soc.*, *21*, **2001**, 1855-1859
- 87 D. Simwonis, H. Thülen, R. J. Dias, A. Naoumidis, D. Stöver, "Properties of Ni/YSZ Porous Cermets of Solid Oxide Fuel Cell anode substrates prepared by Tape Casting and Coat-mix® Process", *J. Mater. Proc. Tech.*, *92-93*, **1999**, 107-111
- 88 S.-B. Sohn, S.-Y. Choi, G.-H. Kim, H.-S. Song, G.-D. Kim, "Stable sealing glass for planar solid oxide fuel cell", *J. Non-Cryst Solids*, *297*, **2002**, 103-112
- 89 J. Matzbender, T. Wakui, R. W. Steinbrech, L. Singheiser, "Deflection of Planar Solid Oxide Fuel Cells during Sealing and Cooling of Stacks" in M. Mogensen (Ed), *Proceedings of the 6th European Solid Oxide Fuel Cell Forum, Vol 1, Lucerne, Switzerland, June 28-July 2, 2004*, 329-338
- 90 J. T. S. Irvine, F. G. E. Jones and P. A. Connor, University Court of the University of St Andrews. "Improvements in Fuel Cells and Related Devices". *PCT Patent Application No. PCT/GB2002/004726*, 1 May **2003**

2 Experimental

2.1 Overview

The procedures and techniques required for the production and evaluation of all the investigated solid oxide fuel cell components are described in the following sections. Details of microstructure, shrinkage and component interfacial reaction analysis are given, together with powder characterisation techniques and control of slip viscosities for repeatable tape batches. In addition, apparatus for fuel cell testing and electrical measurement techniques are discussed.

2.2 Powder preparation

Generally, powders used in this investigation were obtained from commercial sources, due to requirement for large quantities of reproducible materials, and are shown in table 2.1. For prevention of reactions occurring between the YSZ electrolyte and LSM cathode, the commercially obtained stoichiometric LSM was modified by solid state reaction in order to introduce A-site deficiency. 3% A-site deficient LSM: $(\text{La}_{0.8}\text{Sr}_{0.2})_{0.97}\text{MnO}_3$ and 6% A-site deficient LSM: $(\text{La}_{0.8}\text{Sr}_{0.2})_{0.94}\text{MnO}_3$ were produced by reaction of stoichiometric LSM (99.9%, Praxair Specialists Ltd) and MnCO_3 (99.9+%, Aldrich Ltd).

The LSM and MnCO_3 were dried for 2hrs at 800°C and 100°C respectively prior to weighing 21.0000g of LSM and 0.3128g or 0.6256g of $\text{MnCO}_3 \pm 0.0002\text{g}$ for 3% A-site deficient or 6% A-site deficient LSM respectively. The powders were then ground together in a mortar and pestle with acetone and once solvent evaporation was complete calcined in a muffle furnace (Carbolite Ltd) at 1000°C for 5hrs to allow the decomposition of the carbonate prior to solid state reaction.

Chemical	Company
<i>Ceramic Powders</i>	
Yttria stabilised zirconia: YSZ (99.6%)	Daiichi Ltd (supplied by Pi-Kem Ltd)
YSZ (1 μ m, 99.6%)	Unitec Ceramics Ltd
YSZ (2 μ m, 99.6%)	Unitec Ceramics Ltd
NiO mesh 325 (99%)	Aldrich Ltd
(La _{0.8} Sr _{0.2}) _{0.95} MnO ₃ (99.5%)	Nextech Ltd
(La _{0.8} Sr _{0.2}) _{0.98} MnO ₃ (99.5%)	Nextech Ltd
(La _{0.8} Sr _{0.2})MnO ₃ (99.9%)	Praxair Specialists Ltd (supplied by Pi-Kem Ltd)
(La _{0.8} Sr _{0.2}) _{0.97} MnO ₃ – produced at 1000°C	n/a
(La _{0.8} Sr _{0.2}) _{0.97} MnO ₃ – produced at 1050°C	n/a
(La _{0.8} Sr _{0.2}) _{0.97} MnO ₃ – produced at 1100°C	n/a
(La _{0.8} Sr _{0.2}) _{0.97} MnO ₃ – produced at 1150°C	n/a
(La _{0.8} Sr _{0.2}) _{0.97} MnO ₃ – produced at 1200°C	n/a
(La _{0.8} Sr _{0.2}) _{0.94} MnO ₃ – produced at 1050°C	n/a
<i>Pore forming Agents</i>	
Graphite grade 615	Griffin & George Ltd
Graphite powder (>99%)	Fisher Ltd
Graphite powder mesh 100 (99.995%)	Aldrich Ltd
Graphite powder mesh 325 (99.999%)	Aldrich Ltd
Glassy carbon (99.99+%)	Aldrich Ltd
Starch	Fisons Ltd
<i>Solvents</i>	
Methyl ethyl ketone/2-butanone (MEK)	Fisher Scientific
Ethanol	Fisher Scientific
<i>Dispersing Agents</i>	
Triton Q-44	Sigma Ltd
Tri-ethanol amine	Aldrich Chemical Co Ltd
Citric Acid	Acros Organics
Menhaden Fish Oil	Sigma Ltd
Oleic Acid	Hopkin & Williams Ltd
Polyethylene glycol (MW300) (PEG)	Sigma Ltd
<i>Binders</i>	
Poly vinyl butryal (Butvar-98) (PVB)	Sigma Ltd
<i>Plasticisers</i>	
di-butyl phthalate (DBP)	BDH Chemicals Ltd
Polyethylene glycol (MW300) (PEG)	Sigma Ltd

Table 2.1: Materials used throughout for the investigation of tape casting

The solid state reaction was performed at a variety of temperatures for production of the 3% A-site deficient LSM as follows: 1000°C, 1050°C, 1100°C, 1150°C and 1200°C. The heating and cooling rate used was 5°Cmin⁻¹ and the dwell time at high temperature was 15.5hrs. The production of 6% A-site deficient LSM was only performed at 1050°C, with the same heating/cooling rates and dwell times as for the 3% A-site deficient LSM.

Coarsening of YSZ (Pi-Kem Ltd) and 5% A-site deficient LSM: (La_{0.8}Sr_{0.2})_{0.95} MnO₃ (Nextech Ltd) was performed at 1400°C for 5hrs and 1000°C for 16hrs 20mins respectively with heating and cooling rates of 5°Cmin⁻¹.

2.3 Powder characterisation

In order to make reproducible batches of slurry for tape casting, it is important that the powder is well characterised^[1]. Surface area is the most important factor to know when formulating a batch recipe, however for dispersing the powder, the density is also an important factor^[1]. The sintering characteristics of a tape are determined by the surface area, particle size and packing of the powders^[2-4]. In addition, sintering characteristics and electrochemical performance are determined by the material itself. The particle characteristics were analysed as described in the following sections.

2.3.1 BET Surface Area Analysis

The BET analysis was performed on an IGA (Intelligent Gravimetric Analyser), model HAS022120L, Hiden Analytical Ltd. 30-40mg of sample was weighed into the sample boat, which was suspended on the balance. The chamber was then sealed, and heated to 200°C under vacuum, and held at this temperature for

2 hours in order to desorb all substances from the surface of the powder, and once the sample stopped losing weight, the true sample weight could be determined. The sample was then cooled to room temperature before placing a jacket of liquid nitrogen around the chamber, and the sorption run was performed with nitrogen adsorbate at pressures 10-900mbar in 20mbar steps.

2.3.2 SEM Analysis

SEM analysis (see section 2.8 for details) was performed on a JEOL JSM-5600 scanning electron microscope using a voltage between 3kV and 20kV and a small spot size generally between 16 and 20.

For NiO and YSZ powder analysis, the samples were mounted onto the specimen holders using quick drying silver paint (Agar Scientific Ltd), and were sputtered with gold with a home-made machine (see section 2.8.2 for details) due to their low electronic conductivity. For graphite, glassy carbon and LSM powder analysis, the samples were mounted onto the specimen holders with electrically conductive carbon adhesive discs (Agar Scientific Ltd).

Particle counting technique was performed, taking an average particle size from approximately 100 particles. This method gives a number-weighted distribution, generally giving lower average particle size in contrast to laser sizing particle size analysis which is volume-weighted.

2.3.3 X-Ray Diffraction (XRD)

X-ray diffraction (XRD) was used to determine the particle size of the powders, the presence of unwanted pyrochlore species $\text{La}_2\text{Zr}_2\text{O}_7$, from the reaction

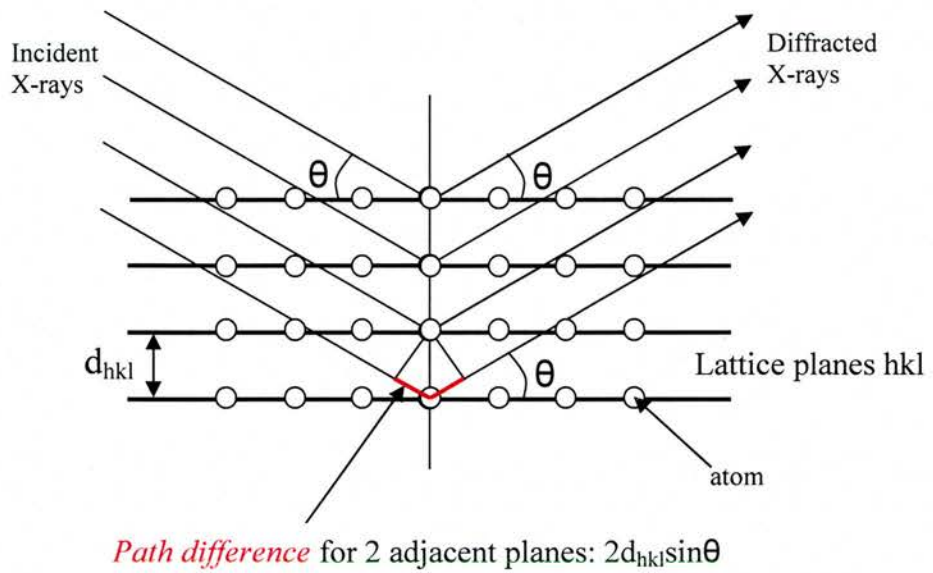


Figure 2.1: Schematic diagram showing the interaction of X-rays of a diffractometer with the atoms in a unit cell

between YSZ (electrolyte material) and LSM (cathode material) and to investigate whether manganese incorporation into the LSM unit cell had been successful to produce A-site deficiency.

The X-rays in a diffractometer are produced by heating a tungsten filament, which bombards electrons on a copper metal target resulting in X-ray emission of energies particular to the metal (see section 2.9). The X-rays are then directed to the powder sample (randomly orientated crystallites) and are scattered by atoms in the unit cell of the sample as shown in figure 2.1. For constructive interference of the X-rays, the path difference between the lattice planes must differ by an integral number of wavelengths, shown in figure 2.1. This is expressed mathematically by the Bragg equation (equation 2.1) giving a relation between the measured θ values controlled by the diffractometer and the unit cell parameters of the sample.

$$\text{path difference} = 2d_{hkl} \sin\theta = n\lambda \quad \text{Bragg Equation} \quad 2.1$$

2.3.3.1 Particle Size

When crystallite sizes are small, the number of planes in the crystallite is small and hence total destructive interference at angles near to the Bragg angle does not occur, resulting in broadening of the peaks^[5-6]. Appreciable broadening occurs for crystallite sizes $<0.1\mu\text{m}$ ^[7]. The broadening is described by the Scherrer equation

$$D \approx \frac{0.9\lambda}{\beta \cos\theta} \quad \text{Scherrer Equation} \quad 2.2$$

$$\beta = \sqrt{B_M^2 - B_S^2} \quad 2.3$$

(equation 2.2), where D is the crystallite thickness, λ the wavelength of the X-rays, θ the Bragg angle and β the peak half width (radians).

The value of β must be corrected for the instrumentation contribution as shown by equation 2.3, where B_M is the peak half width of the sample and B_S is the peak half width of a standard with a crystallite size sufficiently large to not contribute to peak broadening. It should be noted that the peaks can also be broadened by micro-strains in the crystallites, resulting in different measured particle sizes depending on the Bragg angle of the peak used for the calculation as shown in equation 2.4, where ε is the strain^[5, 7].

$$B_M^2 = \left\{ \frac{0.9\lambda}{D \cos \theta} \right\}^2 + \{4\varepsilon \tan \theta\}^2 + B_S^2 \quad 2.4$$

In this investigation, the XRD was performed on a Stoe STADI P between 2θ values of 10 and 80, with a step size of 0.02° . Crystallite sizes were calculated from the combination of equations 2.2 and 2.3. The half widths were obtained from peaks at a low Bragg angle and a silicon standard used to determine the instrumentation broadening.

2.3.3.2 Evaluation of A-site deficiency

Introduction of A-site deficiency to the perovskite structure distorts the unit cell resulting in higher unit cell dimensions. As shown by equation 2.1, higher unit cell dimensions result in lower 2θ values. The degree of A-site deficiency can therefore be determined by the shift in 2θ values. In this case, the XRD was performed on a Stoe STADI P with a slow run between 2θ values of $5-100^\circ$, with a step size of 0.01, 1728seconds/step. The unit cell parameters were indexed using the

Stoe WinX^{POW} software with the space group R-3C, hexagonal setting, and cell parameters of 5.529Å and 13.373Å for a and c respectively^[8]. The method for introducing excess manganese into the unit cell (described in section 2.2) would result in the presence of MnO_x in the sample if the incorporation of the manganese had been unsuccessful. Slow XRD runs were also performed between the 2θ values of 32.0-34.0 and 35.0-37.0 to encompass the highest intensity peaks of Mn₃O₄ (2θ = 32.316, Intensity 85; 2θ = 36.086, Intensity 100^[9]) and Mn₂O₃ (2θ = 32.952, Intensity = 100^[10]). Due to the small quantities of manganese used to produce the A-site deficiency in the unit cell a slow run was performed to reduce the background to peak ratio as follows: 2θ values 32-34 and 35-37 with a step size of 0.01°, 1200sec/step.

2.3.3.3 Examination of presence of pyrochlore

As detailed already in section 1.4.3, at high production temperatures >1200°C the YSZ electrolyte and LSM cathode can react together to form an undesired pyrochlore phase: La₂Zr₂O₇. In order to evaluate whether this phase was forming, powder reactions between the two different materials were performed and analysed by XRD.

1.000g ±0.0005g of YSZ and LSM were ground together with acetone in a mortar and pestle. Once the acetone had evaporated, the mixture was packed into an alumina boat and a variety of heat treatments investigated. The reaction of all the different LSM compositions produced in-house and commercially (detailed in table 2.1) between the YSZ (Pi-Kem Ltd) and additionally of the 5% A-site deficient LSM (Nextech Ltd) and 2µm YSZ (Unitec Ltd) was evaluated. Heat treatments investigated are as follows:

- dwell of 5hrs at 1300°C, heating/cooling rates of 5°Cmin⁻¹
- dwell of 5hrs at 1300°C, with heating rate 2°Cmin⁻¹, cooling rate 5°Cmin⁻¹
- dwell of 5hrs at 1350°C, heating/cooling rates of 5°Cmin⁻¹
- dwell of 5hrs at 1350°C, with heating rate 2°Cmin⁻¹, cooling rate 5°Cmin⁻¹

The reacted powders were then ground in a mortar and pestle prior to XRD analysis. The XRD was performed on a Philips PW 1730/10, between 2θ values of 10 and 80, at 1.5°min⁻¹ with a step size of 0.02°. If no obvious peaks were seen corresponding to the La₂Zr₂O₇ pyrochlore phase, a slower run was performed at 0.2°min⁻¹ in order to obtain a higher signal to noise ratio.

2.4 Tape casting

Tape casting is a widely used process for the production of thin dense sheets of ceramic or metallic material^[1]. It has also been used for production of porous sheets: the pores can be formed by the addition of organic additives which will burn out during firing^[12-14] or by addition of a material which can be subsequently acid leached away^[15]. In this process the desired material is mixed together with a dispersing agent, solvent, binding agent and one or more plasticizing agents to form a slip/slurry. This is then tape cast according to figure 2.2. The slurry is drawn out from under the doctor blade as the casting surface moves. The thickness of the tape is controlled by a combination of the height of the doctor blade, the viscosity of the slurry and the speed of the carrier material and the quantity of slurry in the reservoir^[1,11,17-18].

In this investigation the slurry was made in a two-fold mixing process. Firstly the dispersing agent and solvent were added to a 125cm³ Nalgene bottle (Sigma Ltd) together with 15 zirconia cylindrical pellets, each weighing approximately 7.8g, which acted as the grinding media. Once the dispersing agent had dissolved, the powder was added and the bottles were then placed onto a home-made ball mill and milled overnight – typically for 18hrs at a speed of 160rpm. The purpose of this step is to break down the soft agglomerates and keep the individual particles homogeneously distributed throughout the solvent^[1, 19]. The materials used throughout this investigation are shown in table 2.1. The second stage of the slurry preparation is the mixing of the binder, plasticisers and dispersed powder. Generally the binder is more soluble in the plasticiser than the solvent^[1], and so the plasticiser is added first, to ensure that the binder is coated with the plasticiser before coming into contact with the solvent. The mixture was then placed on a vibratory mixer for 20min

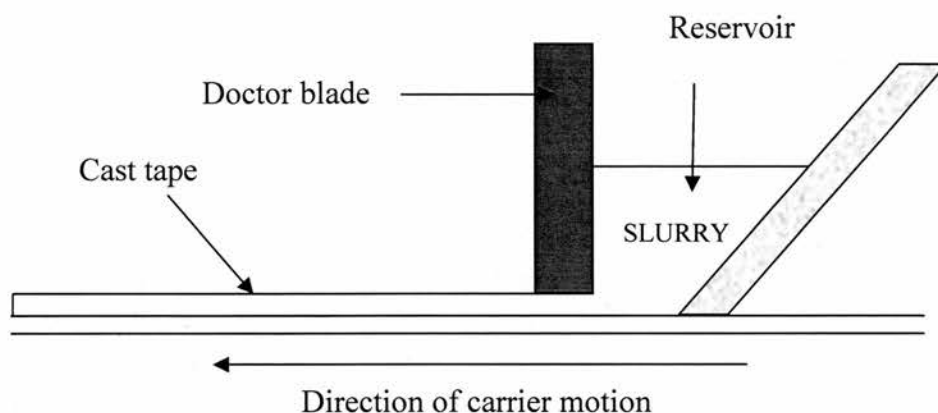


Figure 2.2: Schematic of a tape casting machine

	Electrolyte	Anode (high tpb) Ni:YSZ 40:60 by vol	Anode (current collector) Ni:YSZ 80:20 by vol	Cathode (high tpb) (La,Sr) _{0.95} Mn O ₃ :YSZ 50:50 by wt	Cathode (current collector) stoichiometric LSM only
Ceramic	YSZ 30.000g	YSZ: 7.036g NiO: 8.709g	YSZ: 1.604g NiO: 11.914g	YSZ: 5.000g LSM: 5.000g	LSM: 10.000g
Dispersant: Triton Q-44	0.195g				
Solvent	14.5g	10.1g	10.1g	11.0g	10.0g
Pore former: Graphite -325 mesh		3.279g	4.098g	4.400g	4.400g
Binder: PVB	3.360g	2.520g	2.468g	2.210g	2.210g
Plasticizers: PEG MW 300	2.430g	1.762g	1.785g	1.600g	1.460g
DBP	2.190g	1.588g	1.609g	1.440g	1.440g

Table 2.2: Example formulations of slips for tape casting

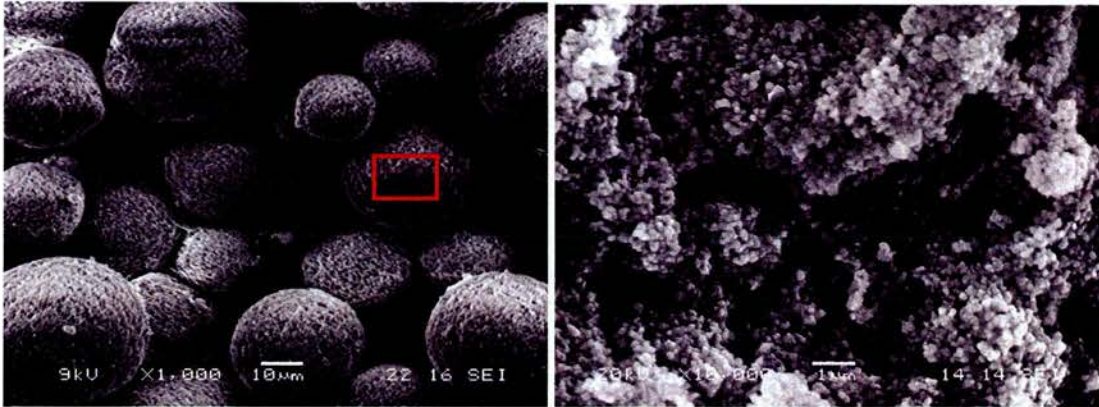
to ensure that the binder had all dissolved before it was returned to the ball mill and mixed for a further 4hrs at a speed of 100rpm. Table 2.2 shows the quantities used in typical batches of electrolyte, cathode and anode.

The slurry is then de-aired before casting to ensure the absence of any air bubbles in the cast tape. The slurry was de-aired either by gentle agitation: the slurry was transferred to another bottle without any grinding media and rotated on the ball mill at approximately 6rpm for 24hrs, or by vacuum: agitated in an ultrasonic bath for 30mins before being placed under slight vacuum with a reduced pressure of 94634Pa for 5mins.

Tape casting was performed on a TTC-1000 (Richard E Mistler Inc) tape caster. Typical settings used were a carrier speed of 50% (approximately 42cms⁻¹), and a 4" (approximately 10cm) width doctor blade with a blade gap of 0.012" (305µm). The tapes were left to dry in air at room temperature - the heating/drying facility was not used.

2.4.1 Particle Dispersion

As described above, the dispersion of the particles is a very important stage of tape casting^[1] breaking down agglomerates/flocs and keeping all particles homogeneously distributed in the slip/slurry. The quantity of dispersing agent is critical to how well the particles are dispersed in the solution, and a series of tests can be performed to judge the dispersion of the particles. Figure 2.3 shows the agglomeration of primary YSZ particles, which are formed due to weak attractive Van der Waal forces. Whilst these agglomerates are broken down during the ball milling process, the use of a dispersing agent is paramount to stop these agglomerates from



a) Agglomerated YSZ particles

b) Higher magnification shows the primary particle size

Figure 2.3: SEM micrographs of agglomerated YSZ particles

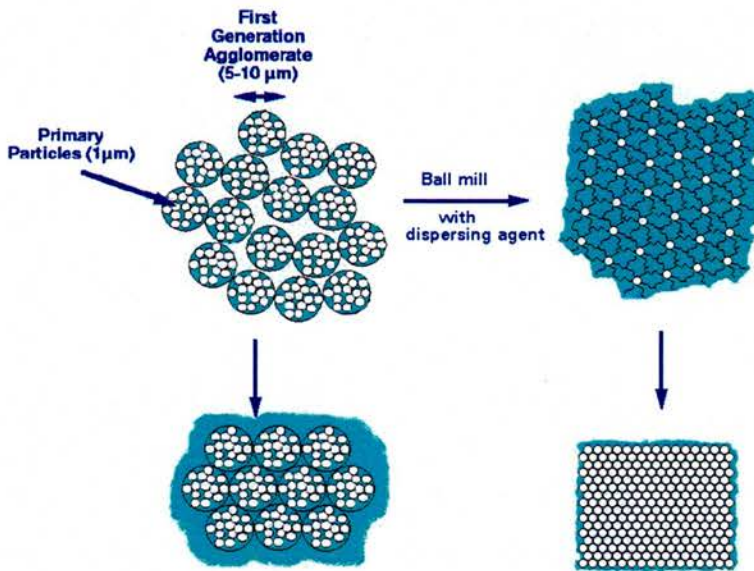


Figure 2.4: Schematic diagram showing the packing of agglomerated particles (flocs) and packing of primary particles

re-forming^[1, 19]. The dispersing agent prevents the primary particles from coming near enough to each other to re-agglomerate, either by charge repulsion or steric hindrance^[1, 19].

Settling tests^[1, 19] were performed to evaluate a good dispersing agent concentration. The powder, solvent and varying amounts of dispersing agent were ball milled at the same ball milling speed as that used in slurry production (160rpm). The powder is in a low solids loading of 1:2 by weight of solids:solvent (20g of solvent, 10g of powder). A control is also performed with no dispersing agent for comparison. Primarily a ball milling time of 4hrs was used, which is a suitable time when using YSZ and LSM ceramics, however, the particle size of the softer NiO and graphite powders were altered during the longer milling times used for tape production (this was most notably seen for the graphite) and in this case dispersion times of that used for slurry production (18hrs) were required.

12cm³ of the resultant suspension was pipetted into a screw-top vial, sealed with Nesco film and left to settle over a period of 2 weeks. The settled height of the powder was noted after 24hours and 2 weeks. Irrespective on how well a powder is dispersed, the particles will always eventually settle due to gravitational forces^[1, 19], the heavier particles settling faster than the lighter ones. The settling rates of particles depend on the size, shape and density of the particles together with the viscosity and density of the solvent^[16]. It is also affected by the solids loading in the suspension^[19], turbulence from other particles and Brownian motion^[16]. A well dispersed powder will show a high 'settled' height after 24 hours, that is the particles will still be well separated and suspended in solution^[19]. After 2 weeks, the powder will have settled to the bottom, and a well dispersed powder will have a low settled height^[1, 19]. This is because the particles will not have re-agglomerated, and will pack densely with a

small pore size unlike agglomerated particles which will pack together giving a large open pore structure as shown schematically in figure 2.4.

2.4.2 Slip Viscosity

The viscosity together with the force exerted by the weight of slurry in the reservoir (see figure 2.2) determines the extent of flow under the doctor blade and hence affects the thickness of the resulting tape^[1, 11, 17-18]. A low viscosity slurry results in a thicker wet tape due to the greater flow under the doctor blade^[1, 17]. Determination of the slurry viscosity prior to casting is therefore an important stage of tape casting for good reproducibility between slurry batches.

Measurement of slurry viscosities is also important for determination of powder dispersion, with better dispersed slips possessing lower viscosities^[1, 11, 20-21]. Whilst the settling test described in section 2.4.1 gives a good indication for optimum dispersion quantities, it relates to low solids loading, which not necessarily the same for high solids loadings^[19].

2.4.2.1 Theory

Figure 2.5 shows the principle behind measuring viscosities of fluids. A shear force (shear stress) is applied to the fluid at a known distance apart. The fluid then moves under these forces, producing a velocity gradient (shear rate) specific to that type of fluid. The viscosity of the fluid is then defined as shown in equation 2.5.

$$\text{Viscosity}(\mu) = \frac{\text{ShearStress}}{\text{ShearRate}} = \frac{\tau_s}{\dot{\gamma}} (\text{Pa} \cdot \text{s}) \quad 2.5$$

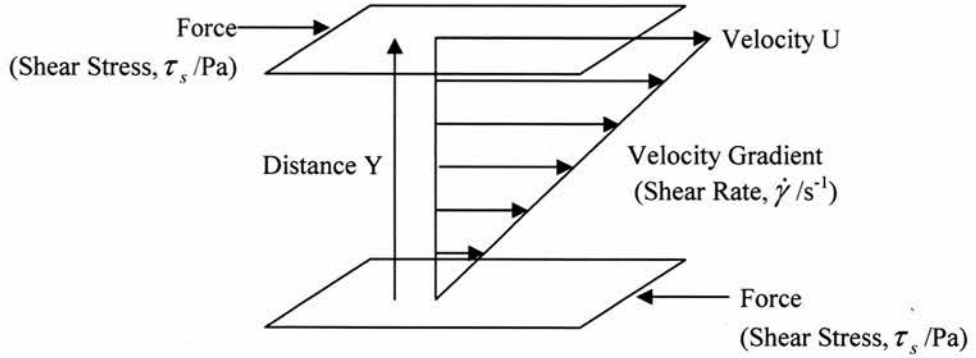


Figure 2.5: Showing the fundamental definition of viscosity

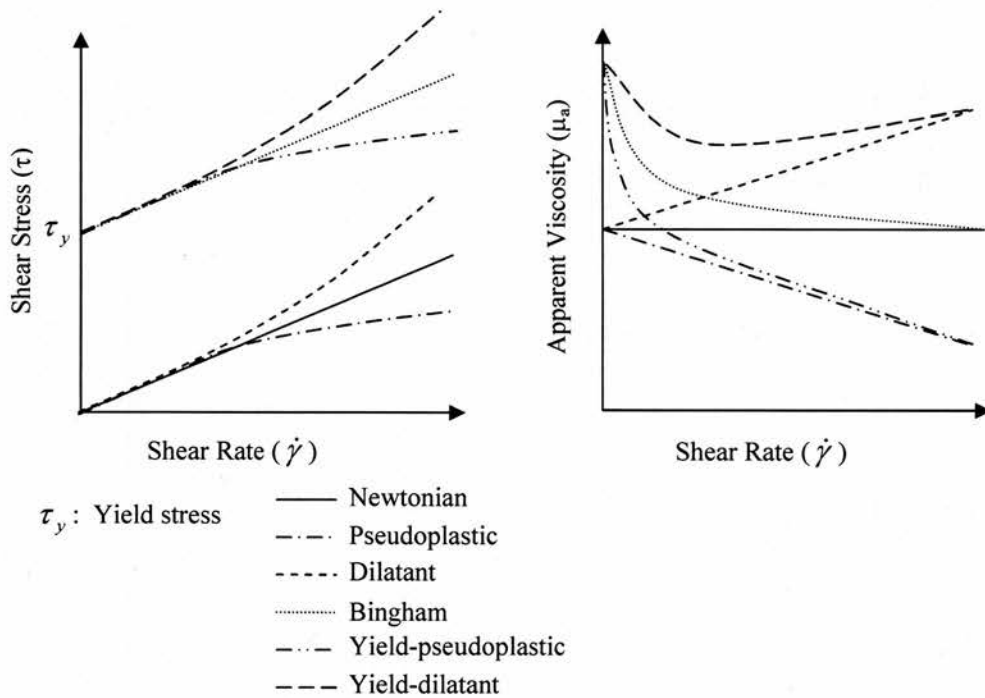


Figure: 2.6: Changes in shear stress and apparent viscosities with applied shear rate for different time-independent rheologies

Viscometers apply shear force to the suspension between a rotating spindle and a stationary surface. The shear force required to move the fluid at a certain shear rate is measured. In the case of tape casting, the shear force is applied between the moving carrier and the stationary doctor blade. For simple Newtonian liquids such as water, the viscosity is independent of the shear rate applied, whilst for non-Newtonian fluids, the viscosity is dependent on the applied shear rate and therefore the viscosity (so called apparent viscosity) of these fluids must be quoted at specific shear rates^[16].

Viscosity is related to particle-particle collisions^[16], the higher the apparent viscosity the higher the number of collisions. Many factors affect the likelihood of particles colliding with each other: one example would be if the liquid content in a suspension is increased (ie reduced solids loading), the particles are less likely to collide and so the apparent viscosity is reduced.

The six different rheology types are shown in figure 2.6. Ceramic bodies, unlike simple fluids, have rheologies which require a certain yield stress before they begin to move, which allow them to hold their shape after forming. Bingham rheology depicts the behaviour of a plastic material and ceramic suspensions fall into the yield-pseudoplastic or yield-dilatant categories^[16].

Suspensions which are pseudoplastic in nature have a tendency to form flocs (clusters of small particles attracted together by Van der Waals forces), which in turn join together to form increasingly larger flocs and so on until highly porous 3-D gel structures are formed^[16]. These gel structures are easily broken down with applied shear. At low shear, the viscosity is at its highest, as the flocs are large and are forced to collide with each other as they move. As the shear rate is increased, the flocs are broken down to smaller and smaller flocs, with the viscosity decreasing as the

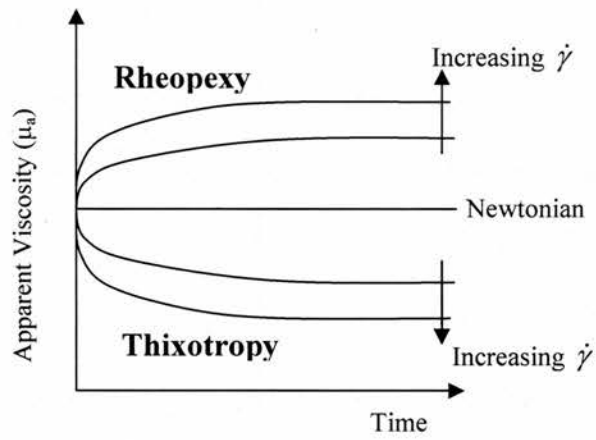


Figure 2.7: Trends of apparent viscosities with time at certain shear rates for time dependent rheologies

particles are less likely to collide, until eventually (at very high shear rates) they exist as primary particles. Pseudoplastic suspensions are also thixotropic in nature, as depicted in figure 2.7. When shear is applied to a pseudoplastic suspension flocs begin to break up (as described above) until equilibrium is achieved between the breakdown of flocs from the applied shear and the formation of flocs. With a higher shear, more flocs are broken down, shifting the equilibrium to give a lower apparent viscosity.

Dilatant suspensions do not form flocs so readily, due to repulsive electrostatic charges on the particle surfaces. Whilst the smaller the particle, the greater the ability to avoid collision with other particles, at high solids loading, the collisions are common and the suspension is dilatant. With increasing applied shear, the number of collisions increases leading to a high apparent viscosity. Dilatant suspensions also tend to be rheopectic. Due to the unstable nature of these suspensions, not many measurements have been performed, as the particles tend to settle very quickly^[16].

2.4.2.2 Procedure used in this investigation

Slips for tape casting tend to be yield-pseudoplastic and thixotropic in nature^[1]. In this investigation, viscometer measurements were performed on a DV-E Low Cost Digital Viscometer with a 2.0ml small sample adapter SSA 14/6R and SC-4 spindle (Brookfield Viscometers Ltd). The measurements were made to investigate both the time independent and time dependent properties of the slips. 10x2cm³ samples were taken and a different shear rate was used for each sample. The shear rates applied to the sample were 30rpm, 20rpm, 12rpm, 10rpm, 6rpm and 5rpm. Care was taken to measure each sample immediately after de-airing stage (for tape casting slips) to eliminate any time dependent errors. The apparent viscosities were measured

for each sample with increasing time until no further change in viscosity was seen, typically approximately 3mins. Throughout testing a plastic lid was placed on top of the sample holder in order to keep the solvent evaporation of the sample to a minimum.

2.5 Thermal Gravimetric Analysis

TG-DTA analysis was performed on a SDT 2960, TA Instruments Ltd. TG-DTA analysis was performed on both the individual organic additives: binders, pore formers and so on as listed in table 2.1, and the green tapes. Two alumina crucibles held the sample (green tape or organic additive) and reference (alumina powder). Sample masses used were 7-10mg for organic compounds and 20-30mg for the green tapes, depending on the organic and pore former content. A lower mass was used for tapes with a higher organic and pore former content. The reference weight used was the same as the sample weight $\pm 0.01\text{mg}$.

The atmosphere used was air at a flow rate of $110\text{cm}^3\text{min}^{-1}$. The heating rate was 1°Cmin^{-1} from room temperature to 900°C before air cooling for the organic additives and $0.5^\circ\text{Cmin}^{-1}$ from room temperature to 1000°C before air cooling for the green tapes.

2.6 Shrinkage Analysis

There is a certain degree of difficulty related to measuring the shrinkage of tape-cast tapes, which is mainly due to sample curling and the small sample thickness^[2, 22]. These difficulties will be discussed further in section 2.6.2. In this investigation, the tape shrinkages were measured in two different ways described below. It should be noted that the first method described measures the shrinkage at room temperature and so measures shrinkage only, whereas the second method measures the change in thickness in situ and so gives a combination of shrinkage and thermal expansion. The second method is therefore more useful when comparing shrinkage profiles for films of different chemicals giving important information regarding co-firing of multi-layers.

2.6.1 Measuring rectangle samples

This is a time-consuming method for one sample and uses a large quantity of material, but many samples can be run at the same time, it is reasonably accurate, and good reproducibility can be achieved^[2]. A 4-layer laminate from the same tape was produced and cut into 18 rectangles measuring 2cm x 1.5cm \pm 0.025cm. A 4-layer laminate was used in order to reduce the curling experienced in the tape, to allow more accurate measuring of the sample after heat treatment. Each rectangle was then put into a furnace (one for each shrinkage measurement at the specific point in the temperature profile) and subjected to the heat programme of that used for the fuel cell up to a certain temperature, and removed at that temperature.

The heating programme investigated was a 5hr dwell at 1000°C with heating and cooling rates of 0.5°Cmin⁻¹ and 5°Cmin⁻¹ respectively, followed by a 5hr dwell at 1300°C with heating and cooling rates of 5°Cmin⁻¹. Shrinkages of the calcining stage were measured after heating to 150°C, 300°C, 450°C, 600°C, 750°C, 900°C, 1000°C, after the 5hr dwell at 1000°C and after then cooling in the furnace to room temperature. Shrinkages of the high temperature sintering stage were measured after heating to 1100°C, 1200°C, 1300°C, after a dwell time of 1hr, each subsequent hour and after cooling in the furnace to room temperature. The sample was cooled after the initial ramp to 1000°C in order to mimic the procedure used for firing the fuel cells (see section 2.10).

Once the samples were cooled after removing from the furnace their shrinkage could be measured. This was repeated a further two times to produce an average shrinkage for each point in the temperature programme and in this way a shrinkage profile of that tape was produced.

2.6.2 Dilatometer Measurements

Figure 2.8 shows a schematic representation of the dilatometer DIL 402 C Dilatometer (Netzsch Instruments), used for these measurements. The principle of a dilatometer is to apply a constant force on the sample throughout a specific temperature programme and measure the displacement of the pushrod due to the resulting contraction or expansion of the sample. Since the dilatometer components (specifically back-stop, push rod and alumina spacers) expand under thermal treatment, a control run is required to eliminate this contribution to data obtained on samples. Control runs were performed using the same temperature profile as required for the sample, using an alumina standard with a thickness of ~ 0.6 cm. This thickness is much larger than that of the tapes produced, and so in order to get reproducible data tapes were laminated together to give a similar thickness $\pm 10\%$ to that of the alumina standard.

A low push rod force of 20cN was applied to both sample and control, as recommended by the manufacturer due to the high compressibility of the tapes, particularly when the binder and plasticizers soften^[22]. The measurements were performed under a constant gas flow of air at $50\text{cm}^3\text{min}^{-1}$. For measuring the shrinkage of each component, the following temperature program was used: dwell 30mins at 30°C , heat to 1000°C at $0.5^\circ\text{Cmin}^{-1}$, dwell 5hrs, cool to 100°C at 5°Cmin^{-1} , dwell 1hr, heat to 1300°C or 1350°C at 5°Cmin^{-1} , dwell 5hrs, cool to 30°C at 5°Cmin^{-1} . The sample was cooled after the initial ramp to 1000°C in order to mimic the procedure used for firing the fuel cells (see section 2.10). Due to the reaction of NiO and LSM in the samples with alumina, the alumina spacers were changed periodically.

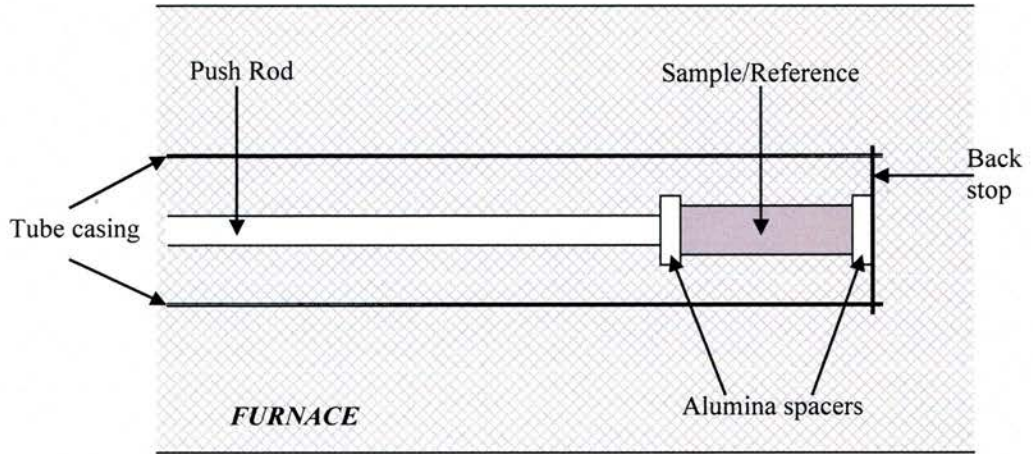


Figure 2.8: Schematic diagram of dilatometer

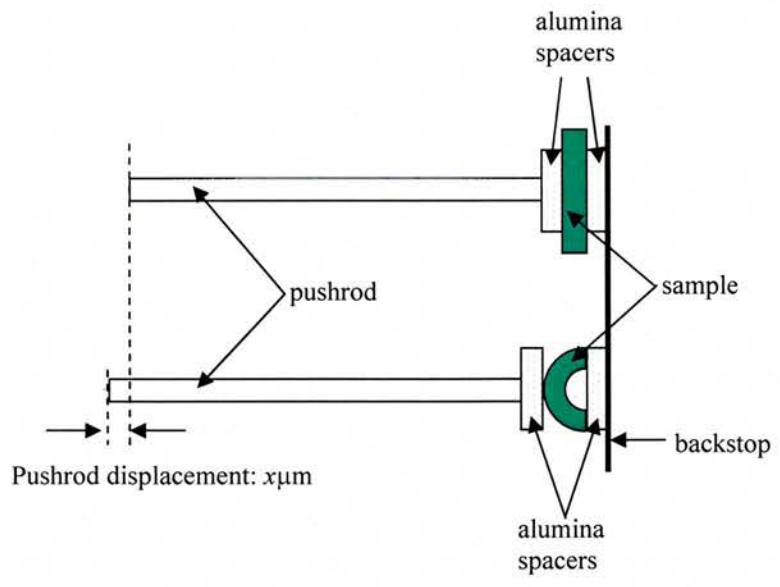


Figure 2.9: Schematic diagram showing how curling of sample gives an error in shrinkage of $x \mu\text{m}$.

Sources of error which can occur when measuring shrinkage of tapes in this manner include the sticking of tapes to the alumina spacers during softening of organic additives, curling of tapes during organic burnout^[2] and sintering of tapes to the alumina spacers. If the ceramic sinters, or if the tapes stick to the alumina spacers during high temperature treatment or softening of the organic additives respectively, the films will be impeded from shrinking in two dimensions and so the resulting shrinkage observed in the film thickness will be higher than the true shrinkage. Conversely, if the tapes curl during organic additive burnout, the measured shrinkage will be smaller than the true shrinkage. In fact the data may even show an expansion as shown in figure 2.9.

2.6.3 Rate Controlled Sintering

Rate controlled sintering of the components used in fuel cell production was performed with the DIL 402 C Dilatometer (Netzsch Instruments) for sintering temperatures of both 1300°C and 1350°C. The sample size, gas flow rate and push rod force used was as described in section 2.6.2. The heating profile used was dwell 30mins at 30°C, heat to 125°C at 0.5°Cmin⁻¹, heat to 1000°C at 5°Cmin⁻¹, dwell 5hrs, cool to 100°C at 5°Cmin⁻¹, dwell 1hr, heat to 1300°C/1350°C at 5°Cmin⁻¹, dwell 5hrs, cool to 30°C at 5°Cmin⁻¹. Rate controlled sintering was performed during the ramp between 125°C and 980°C, and 110°C and 1290°C/1340°C. The sample was cooled after the initial ramp to 1000°C in order to mimic the procedure used for firing the fuel cells (see section 2.10).

The rate controlled sintering was performed using the stop/start mode. The stop/start mode works by stopping the heating of the sample when the rate of

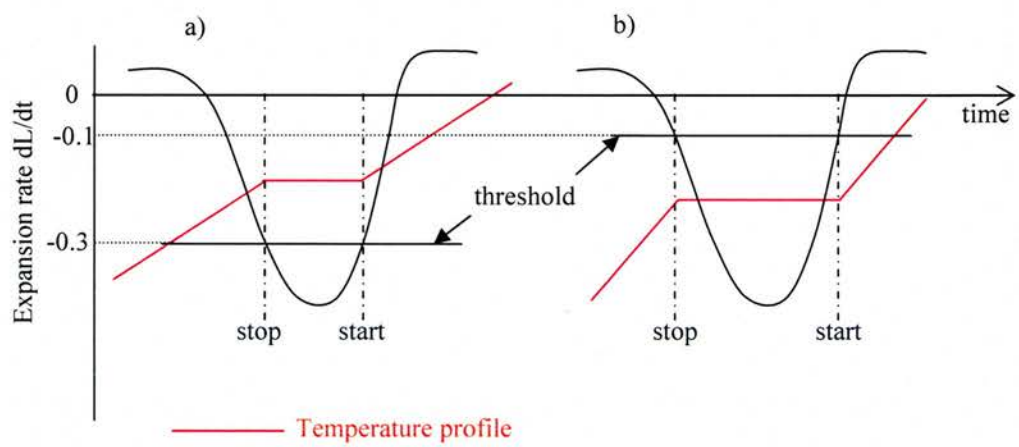


Figure 2.10: Schematic diagram of threshold values used for rate controlled sintering

shrinkage/expansion exceeds the threshold value and re-starting the heating rate when the shrinkage rate falls below this threshold value again, shown schematically in figure 2.10. The threshold value used in this investigation was $0.2\mu\text{m}\cdot\text{min}^{-1}$, with a signal range of $500\mu\text{m}$, derivative range of $5\mu\text{m}\cdot\text{min}^{-1}$ and a filter factor of 75 (smoothing of deviated measurement signal with a time constant of 1s).

2.7 Density Measurements

The density measurements were performed by geometry. A fired, rectangular, 4-layer laminate (produced as described in section 2.6.1) was measured $\pm 0.005\text{cm}$ in x and y directions by micrometer and $\pm 0.20\mu\text{m}$ by SEM analysis (described in section 2.8) and weighed $\pm 0.00005\text{g}$. Anode samples were pre-reduced in a tube furnace (Multi-lab Ltd) in a flowing atmosphere of 5% H_2/Ar (1bubble per second) in the following heat programme: $50^\circ\text{C}-800^\circ\text{C}$ 5°Cmin^{-1} , dwell at 800°C for 5hrs, cool to 50°C at 5°Cmin^{-1} .

The density was calculated from the volume of the rectangular sample and the mass as shown in equation 2.6. The actual density/porosity was then calculated from the density of material (obtained from the manufacturer) by equation 2.7.

$$\text{Density of sample} = \frac{\text{Sample mass}}{\text{Sample volume}} \quad 2.6$$

$$\% \text{ density} = \frac{\text{Density (equation 2.5)}}{\text{Theoretical density}} \cdot 100$$

$$\Rightarrow \% \text{ porosity} = 100 - \% \text{ density} \quad 2.7$$

2.8 Microstructure – SEM Analysis

The microstructure of the components was analysed by SEM analysis (see section 2.3.3), of both fractured/cut edges and polished cross-sections. Microstructural analysis was performed both on tested fuel cells and single component, 4-laminate rectangular tapes after firing (as described in section 2.6.1). The fuel cells comprised of reduced anodes, and the fired rectangles of anode materials (described in section 2.6.1) were pre-reduced as described in section 2.7.

2.8.1 Instrument Lay-out

The scanning electron microscopy (SEM) analysis performed throughout this investigation was with a Jeol JSM-5600 scanning electron microscope. The specifications of this model are as follows: voltage up to 30kV; resolution of 3.5nm, secondary electron image mode (SEI); probe current of 10^{-12} - 10^{-6} A; magnification of up to 300,000 and is coupled to an EDX (Oxford Inca) analysis system (see section 2.9). The voltage used ranged between 3kV and 20kV with a small spot size generally between 16 and 20.

2.8.1.1 Generation of Electron Beam

Figure 2.11 shows a schematic diagram of an electron microscope. The electron source is typically a tungsten filament, which is the lowest brightness cathode for electron microscopes and requires the lowest vacuum of 1.333×10^{-3} Pa^[23]. (For transmission electron microscopy (TEM) a higher brightness cathode electron source is used, which in turn requires a higher vacuum). The filament is heated until the electrons have sufficient energy to overcome E_w (work function) and are emitted from the filament. The current density of these electrons is given by Richardson's Law shown in equation 2.8.

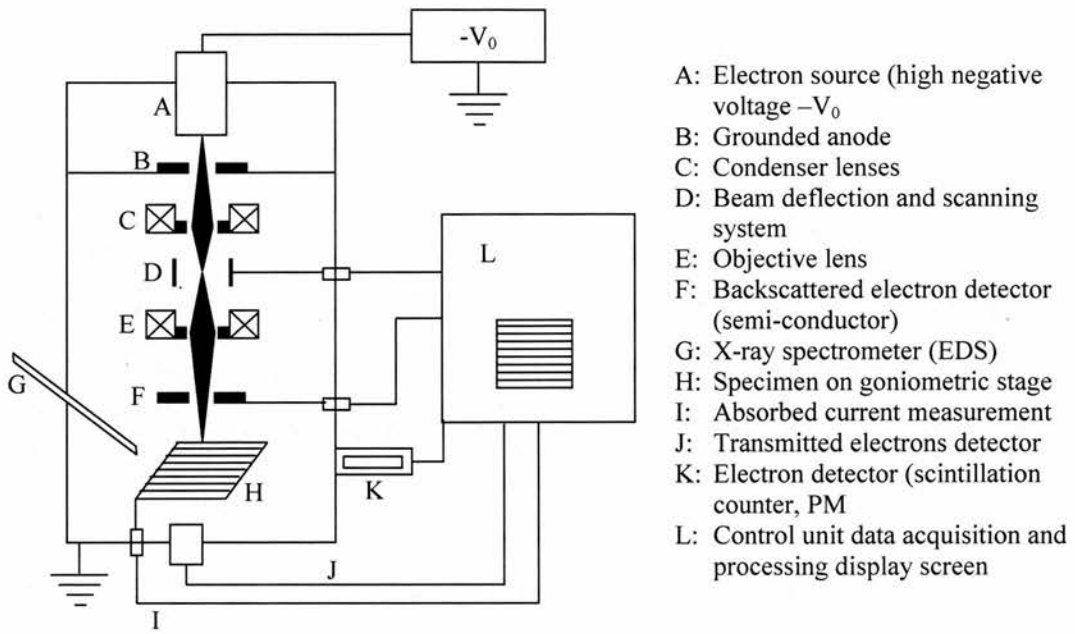


Figure 2.11: Schematic diagram of an electron microscope^[23]. Parts I and J are not present on a scanning electron microscope (SEM).

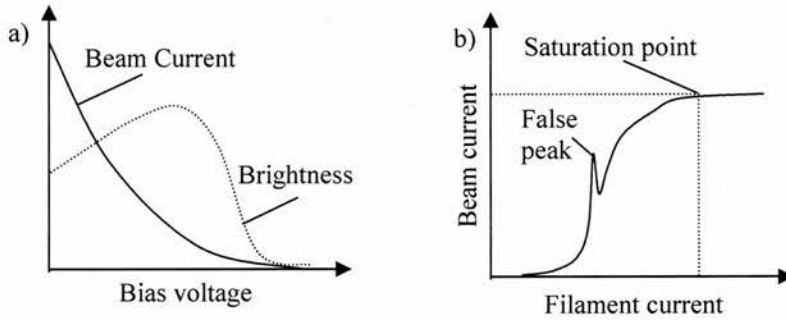


Figure 2.12: a) Affect of bias on beam current and brightness b) effect of filament current on beam current with a self-biased gun

$$\text{Beam current density: } J_c = A_c T^2 \exp\left(\frac{-E_w}{kT}\right) \quad 2.8$$

$$\text{Langmuir equation Brightness: } B = \frac{J_c e V_0}{\pi k T} \quad 2.9$$

The beam of electrons firstly travels through a negative field (bias), which serves to focus the beam (decrease the beam width). The bias pushes the electrons slightly back towards the filament. If the bias is too strong, then the beam current reaching the sample is very low and a low brightness is seen. If the bias is too weak, a large beam current reaches the sample, however it is not well focused (high beam width) and the brightness is still too low^[23]. Figure 2.12a shows how the beam current and brightness are affected by the bias voltage, and equation 2.9 shows the relationship between bias (V_0), beam current (J_c) and brightness (B).

The JSM-5600 scanning electron microscope uses a self biased gun, whereby the filament current is increased until the maximum beam current is achieved, shown in figure 2.12b. Increasing the filament current past this point will not further improve the images obtained, but will merely reduce the lifetime of the filament.

The electron beam then passes through a high voltage of up to 30kV between the anode plates and the cathode^[23], which accelerates the electrons down the microscope ensuring all electrons have equal energy, prior to being focused by a series of electromagnetic lenses before reaching the sample. Equation 2.10 shows the relationship between the focal length (f), magnetic field (in the z-axis) (H) and the incident energy (E_0). The magnetic field and therefore focal length vary with the excitation current and therefore it is very easy to focus.

$$\text{Convergence (reciprocal focal length)} \quad \frac{1}{f} = \frac{k}{E_o} \int_{gap} H_z^2 dz \quad 2.10$$

$$\text{Electron flow intensity:} \quad I_0 = B\phi_0^2 \propto BE_0 d_s^{8/3} \quad 2.11$$

The initial lenses the electron beam travel through are the condenser lenses (shown in figure 2.11), of which there are at least two. These serve to vary the illumination mode as shown in figure 2.13 and equation 2.10. The objective lens focuses the sample and determines the resolution.

The minimum beam width (d_s) is limited by various aberrations of the objective lens: spherical aberrations and astigmatism (all caused by imperfections of lenses) and chromatic aberrations shown in figure 2.14, diffraction aberration (present in a perfect lens) shown in figure 2.15 and the minimum electron intensity required for a significant signal to noise ratio described in equation 2.11^[23]. A typical beam size for an SEM is approximately 30Å.

Astigmatism (figure 2.14a) is caused by the fact that no lens has perfect revolution symmetry, and so the focal lengths differ between perpendicular axial planes. This defect is easily corrected for, by adding an extra electric or magnetic fields, which can be adjusted in direction and intensity. The other aberrations however are not so easily corrected for. Spherical aberration occurs due to differing focusing between axial and non-axial rays. The deviation from the ideal focusing plane increases with increasing angle resulting in a 'spherical aberration smearing disc' (radius r_s) rather than point image as shown in figure 2.14b^[23]. The size of this disk is described by equation 2.12 where C_s is the spherical aberration coefficient' and the defocus value described by equation 2.13, where λ is the electron wavelength.

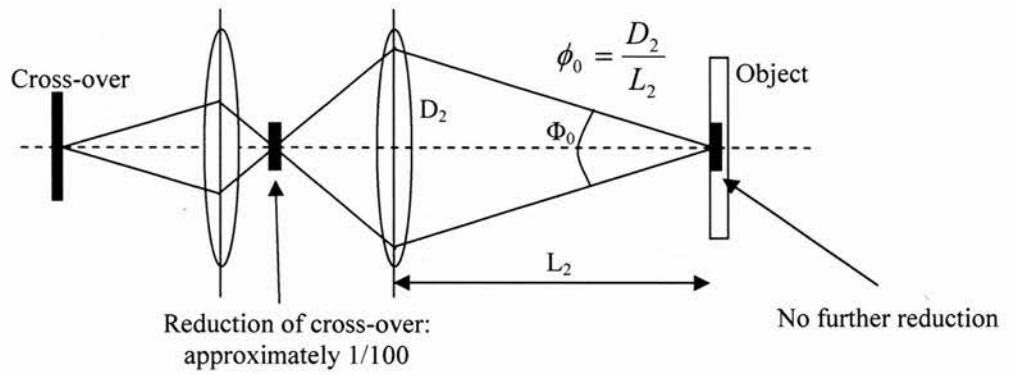


Figure 2.13: Electromagnetic condenser lenses

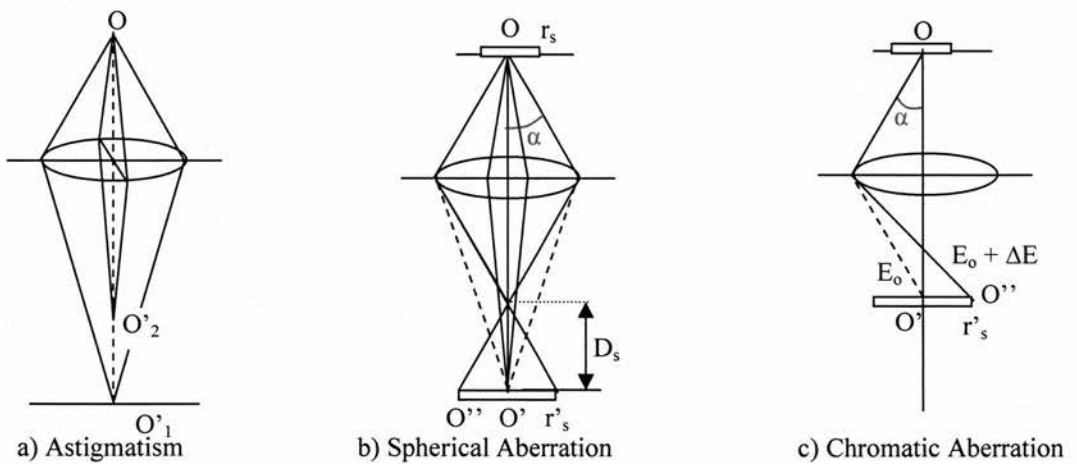


Figure 2.14: Geometrical lens aberrations

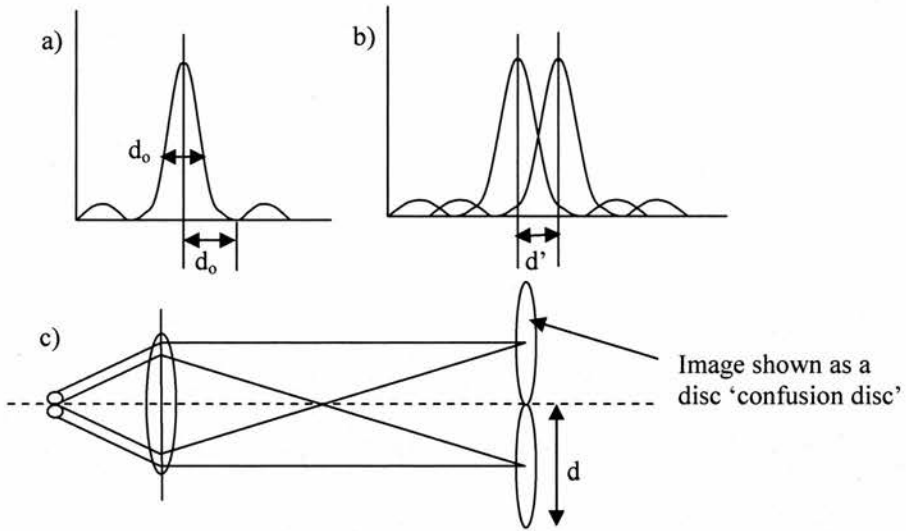


Figure 2.15: Diffraction aberration a) Airy function showing aperture diffraction effect from one point, b) overlapping of two Airy function's representing image from two points and c) Confusion discs of two mathematical points.

Chromatic aberration is caused by an energy loss in the electron beam, which as shown in equation 2.10 causes a change in the focal length, resulting in a 'chromic aberration smearing disc' (radius r_c) shown in figure 2.14c. The size of this disc is defined by equation 2.14, where C_c is the chromic aberration coefficient^[23].

$$\text{Spherical aberration smearing disc radius: } r_s = C_s \alpha^3 \quad 2.12$$

$$\text{Defocus: } D_s = -1.2(C_s \lambda)^{1/2} \quad 2.13$$

$$\text{Chromic aberration smearing disc radius: } r_c = C_c \alpha \frac{\Delta E}{E_o} \quad 2.14$$

The image of a point is a diffraction pattern, described as the Airy function in figure 2.15a. The half-width of the highest intensity peak is described by equation 2.15, where λ is the wavelength of the electron beam, and α is the aperture^[23]. Rayleigh's Rule states that as long as d' is at least as large as d_o , the two maxima of the Airy functions can be resolved^[23]. Similarly, as long as the diameter of the confusion disc is smaller or equal to the half-width of the central maxima of the Airy pattern, then the image of the two points can be resolved.

$$d_o = \frac{0.61\lambda}{\alpha} \quad 2.15$$

Figure 2.16 shows how the size of the confusion discs change with aperture, whilst only the spherical and diffraction confusion discs are shown, addition of the chromic confusion disc does not significantly alter the total instrument confusion disc

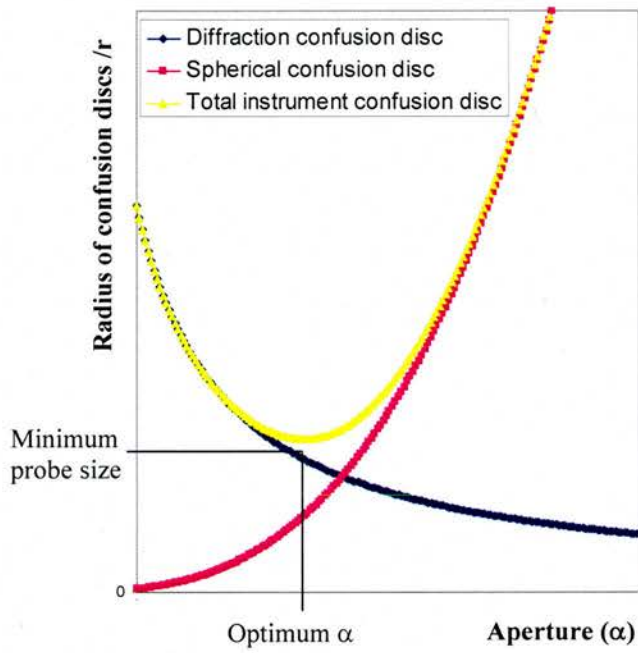


Figure 2.16: Variation of diffraction, spherical and total (calculated by root mean square) confusion disc size with aperture

size^[23]. The minimum probe size shown in figure 2.16 is slightly larger than that observed by Rayleigh aperture and resolution (equation 2.16) where $r_s=r_d$ ^[23].

$$\text{Rayleigh aperture and resolution: } d_{\min} = 0.8C_s^{1/4} \lambda^{3/4} \quad 2.16$$

2.8.1.2 Interaction with Sample and Data Collection

As seen in figure 2.17, many different interactions occur between a high energy electron beam and a solid; it is the secondary electrons which are of interest with scanning electron microscopy (SEM). Secondary electrons are the electrons which leave a sample atom after excitation by the incident electron beam. The secondary electrons are subject to random energy losses after being emitted from the sample atoms prior to reaching the detector and additionally may be absorbed by other atoms which, in turn causes other secondary electron emission. The secondary electrons which reach the detector therefore have a wide range of energies, the maximum intensity being at approximately 50eV^[23]. Their low energy means the secondary electrons which reach the detector come from the immediate surface up to a depth of approximately 10Å of the sample and since the emission cross-section is high, a good signal to noise ratio is obtained^[23].

In the secondary electron imaging mode, both secondary electrons and back-scattered electrons are counted, although the number of secondary electrons counted far out-weigh the number of back-scattered electrons counted^[23]. The low energy of the secondary electrons (<200eV) means that they are easily deflected by the collector field shown by V(grid) in figure 2.18 and the majority of the secondary electrons emitted from the sample in all directions travel through the grid giving a high signal to

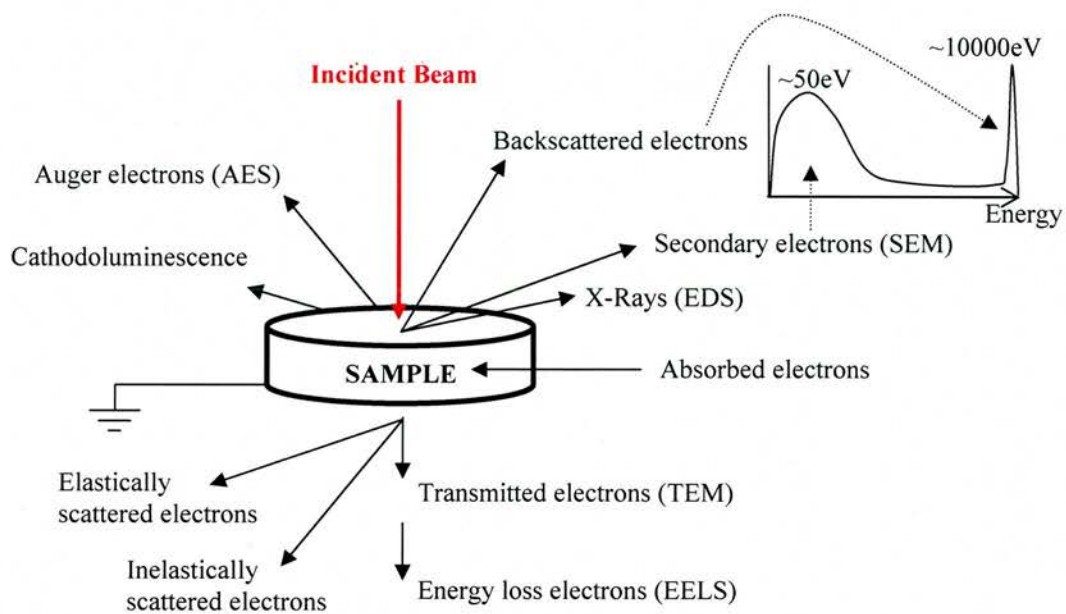


Figure 2.17: Interactions of the electron beam with the sample

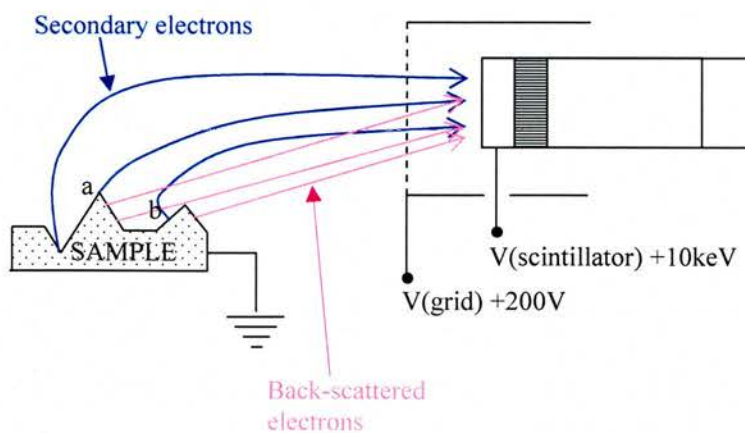


Figure 2.18: Schematic diagram showing the detection of electrons in secondary imaging mode

noise ratio. They are then accelerated by $V(\text{scintillator})$ shown in figure 2.18 which gives the electrons enough energy to generate a scintillation pulse. The back-scattered electrons have much higher energies than the $V(\text{grid})$, so are not deviated by the collector field and only pass through the grid if they are travelling in the correct direction. For this reason not many back-scattered electrons are counted and so the signal to noise ratio is low.

The electron probe scans over the sample by a deflection system of magnetic coils. The detector controls the intensity of an electron beam in a cathode ray tube, which has a scan synchronised to the electron probe. This results in direct correlation between the secondary electrons emitted from a particular point in the sample with the point on the screen. After just one scan on the sample an image of the samples surface can be obtained; the slower the scan the higher the signal to noise ratio, taking approximately 1min for a good signal to noise ratio^[23].

The resolution of the SEM depends on the volume from which the detected secondary electrons are emitted. Due to the low energy of the secondary electrons, this cross-sectional area emitting secondary electrons is not much greater than the area of the beam size as shown in figure 2.21 (section 2.9), resulting in a low emission volume and good resolution^[23]. The resolution is also dependent on the atomic mass of the sample, the heavier elements absorbing more electrons improving the resolution by a factor of 10^[23]. Sputtering samples with heavy elements such as gold therefore increase the resolution, whilst aiding the surface conduction of non-conducting samples minimising the build-up of local charge which changes the electron emission causing increased brightness and hiding surface detail in the images. As detailed in section 2.8.1.1, the image is displayed as a confusion disc and in order to resolve two points, the diameter of the confusion disc (d_s') should equal the eye separation

distance, approximately 0.1mm^[23]. The confusion disc is simply the product of the magnification and probe size, giving a maximum magnification (M) for given probe size (d_s) described in equation 2.17.

$$d'_s = Md_s \quad \Rightarrow \quad M = \frac{0.1}{d_s} \quad 2.17$$

The number of secondary electrons counted by the detector and hence the brightness seen on the screen depends on the surface topography, giving a 3D effect on the screen. A higher number of secondary electrons are emitted from spikes or points in the sample surface (point a in figure 2.18) resulting in a brighter image of this point. Although secondary electrons are counted from 'shadowed' areas of the surface (point b in figure 2.18), the number of secondary electrons counted are lower, resulting in darker image of this point^[23]. In addition, the microscope has a high depth of field which contributes to the 3D effect. A 'blurring' of the probe diameter with respect to the focusing plane occurs as shown in figure 2.19. At a shift of $D/2$ from the focusing plane, the blurring of the probe diameter is given as αD , resulting in a confusion disc (see figure 2.15). In order to resolve the image, the total blurring must be less than the eye separation distance of $\sim 0.1\text{mm}$ (minimum distance required by the eye to resolve two points)^[23]. The depth of field at magnification M, is therefore described by equation 2.18.

$$(d_s + \alpha D)M \leq 0.2 \quad \Rightarrow \quad D \leq \frac{0.2/M - d_s}{\alpha} \quad 2.18$$

The yield of both secondary electrons and back-scattered electrons increases with increased atomic number. Since the energy of secondary electrons is very low,

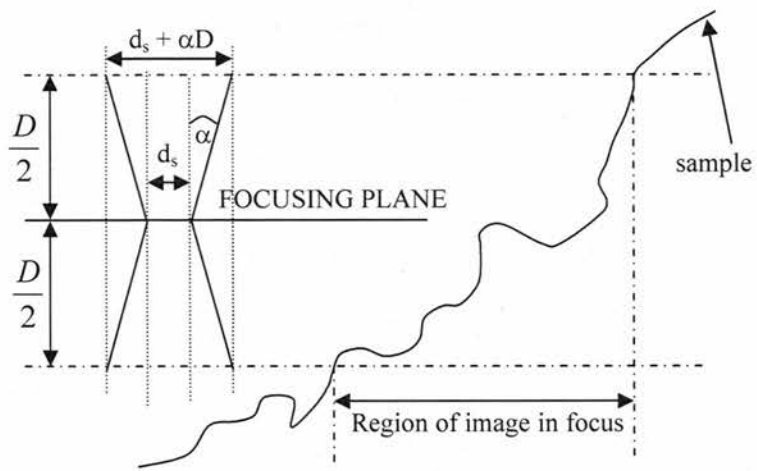


Figure 2.19: Depth of field

they come from a distance of approximately 10\AA from the sample surface; therefore their energies are not related to the bulk composition, but of the metal coating on the surface, contamination or adsorption^[23]. The higher energy of the back-scattered electrons, allow them to easily pass through the surface area, giving compositional information. It is the additional secondary electron emission induced by the back-scattered electrons which gives the contrast in secondary electron images compositional information, with brighter sections corresponding to areas of high atomic number^[23].

2.8.2 Sample Preparation

For impregnation with epoxy, the samples were held up-right with a metal clip or blu-tac for fired sheet or fuel cell respectively in the sample holder, and impregnated by vacuum with epoxy (Kemet Ltd). The epoxy was left overnight to set, before the sample was cut into relevant sections using a Minitom Saw (Struers Ltd), with General use diamond saw (Struers Ltd) at a speed of 200 rpm. Whilst the polishing grits and times were varied as the technique was perfected, the end regime used was as follows: grinding with 600 and 1200 silicon carbide grit (Kemet Ltd) 3 mins each under a 1.5kg weight, before polishing with, $6\mu\text{m}$, $3\mu\text{m}$, $1\mu\text{m}$ and $0.25\mu\text{m}$ diamond paste for 10, 6, 3 and 2 mins respectively (Kemet Ltd) under a 2.5kg weight. After each polishing/grinding step, the samples were cleaned by ultra-sonic agitation for 3 mins to prevent cross-contamination between polishing cloths. The polishing was performed on a Metaserv 2000 grinder/polisher (Buehler UK Ltd) at rotation speed of approximately 70rpm, with the autopole attachment at a rotation speed of approximately 2rpm.

Fuel cells which were not impregnated with epoxy were wrapped with blue roll to prevent breakage when clamped into place in the Minitom Saw (Struers Ltd) and were cut with a High precision cutting of brittle materials diamond saw (Struers Ltd). Again a blade speed of 200rpm was used and great care was taken to use a light weight on the sample whilst cutting. The fuel cells were cut in three places: at the graphite strip (~0.5cm from the end of the fuel cell), half way along the cell, and ~0.5cm from the seal at the gas inlet end of the fuel cell (see sections 2.10 and 2.11).

All samples were sputtered with gold (Advent Materials Ltd) using a home-made machine prior to analysis. Either gold wire or gold foil (compressed to form a thin rod-like shape) was inserted into the tungsten filament (Advent Materials Ltd) and the sample placed directly below. The sample and filament were then covered with a bell jar and shatter guard and a vacuum of 10^{-5} mbar produced by a combination of rotary and diffusion pumps. The sputtering was performed at a filament power of 300-600W for 1-5mins (until an adequate coating of gold was seen on the sample surface).

Sputtering gold to the surfaces was required due to the low electronic conductivity of the epoxy, as well as YSZ and NiO (due to the surface oxidation of the Ni in the anode). A thin line of quick drying silver paste (Agar Scientific Ltd) was painted from the sputtered sample surface to the metal sample holder in order to make electric connection between the epoxy and the sample holder for SEM analysis.

2.9 Homogeneity – EDS Analysis

Energy dispersive spectroscopy (EDS) was performed on cross-sections of the fuel cell electrodes to determine the whether the different materials were distributed homogeneously throughout each material. It was also used as a tool to identify any

foreign substances seen on the sample surface and distinguish between YSZ and silver added to the fuel cells prior to testing for sealing the gas inlet tubes and providing electrical contact respectively (see section 2.11).

2.9.1 Theory

As described in section 2.8, (see figure 2.17) many different interactions occur between a high energy electron beam and a solid. EDS is concerned with the detection of the emitted X-rays from the sample. Figure 2.20 shows how when an electron from an inner electron band is emitted by the electron beam, higher energy electrons from the outer electron bands take its place to stabilise the atom releasing the excess energy in the form of an X-ray. The energy of the X-ray is characteristic of the atom due to the energy gap of the electron bands, increasing in energy from the L, K_{α} to K_{β} transitions, with the K_{α} and K_{β} transitions being closest in energy. Unlike the secondary electrons detected for imaging (section 2.8), the high energy of the X-rays means that it carries information about the bulk sample see figure 2.21, giving information about chemical composition.

In a similar manner to the SEM detection, the electron beam moves over the sample in synchronisation with the imaging system. Higher X-ray counts of a particular energy corresponding to a particular atom results in higher intensity spot on the image which in turn corresponds to that point on the sample. In this manner, element maps are produced showing areas of high and low concentration of each element in the sample^[23]. Additionally, the electron beam can be moved over a line (rather than area), or held in one place for compositional information of set regions.

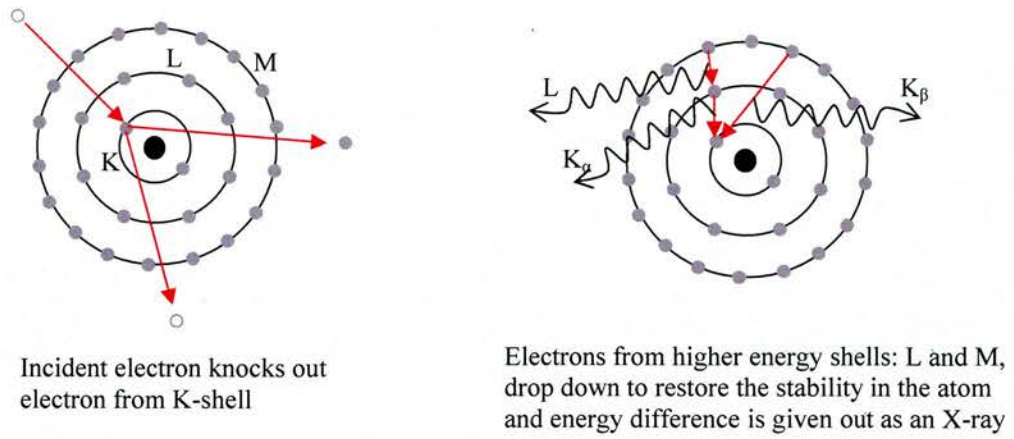


Figure 2.20: showing the relaxation of electrons with the release of X-ray radiation

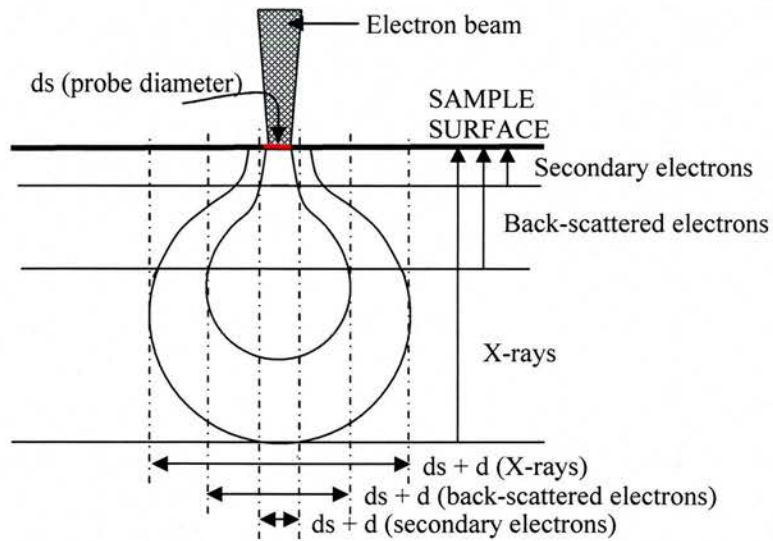


Figure 2.21: Interaction volume of secondary electrons, back-scattered electrons and X-rays

The X-rays are detected by a silicon detector, which when bombarded with an X-ray produces a numerous charge pairs of 3.8eV (the band gap of silicon) causing a pulse. Increasing the beam current increases the rate the X-rays are produced and so reduces the time required to obtain a distribution map. If the two photons arrive too close together, overlapping of peaks from the pulse can occur and can cause the detector to mistake the pulse as resulting from a different number of charge pairs and so identifying the pulse to come from a different element^[23]. In order to improve accuracy, the shape of the peak is analysed to determine whether it is a single peak or two peaks overlapping to a certain degree. If the peak is discarded as two overlapping peaks, this results in deadtime which slows down data acquisition. Additionally, the time taken for the detector to analyse each peak (process time) can be increased to increase the signal to noise ratio, which increases the resolution of peaks close together in energy. Increasing the processing times therefore increases the likelihood that two pulses will arrive too close together as described above resulting in increased deadtimes for the same beam current. A good input rate of X-rays to the detector is 5kcps for a deadtime less than 64% (limit at which increasing beam current does not increase data collection) whilst detecting trace levels of elements.

A high background is seen in the spectrum of intensity vs energy, which decreases with increasing energy. This is caused by a fluorescence effect which is a result of a high energy X-rays obtained from one atom being absorbed by a neighbouring atom resulting in a high yield of low energy X-rays^[23].

For heavy atoms, an electron accelerating voltage at least 20kV is required in order to excite all three X-ray lines from the elements. Increasing the accelerating voltage increases the interaction volume (see figure 2.21), whereas the higher the

element atomic number, the lower the interaction volume (as heavy elements absorb more electrons) and so for lighter atoms a lower accelerating voltage can be used.

2.9.2 Procedure used in this investigation

Energy dispersive spectroscopy (EDS) was performed on gold coated, polished cross-sections of the fuel cell electrodes (prepared as described in section 2.8.2) to determine the whether the different materials were distributed homogeneously throughout each material. Machine settings were as follows: accelerating voltage of 20kV, working distance of 20 mm, with a spot size between 37 and 45. An acquisition rate of 4-5kcps was aimed for and process time of 5 (from a scale of 1-6 where 1 is the shortest) was used.

2.10 Fuel cell Production

The green tape dimensions used to produce the SOFCRoll geometry fuel cell (see section 1.6, figure 1.12) are as shown in figure 2.22. Initially the electrolyte was placed on a clean sheet of glass and air bubbles removed by rolling with an art roller. When two layers of electrolyte were used, the second (still on the Mylar carrier) was placed over the first (on the glass sheet) and laminated slowly rolling with an art roller from one side to the other to ensure no air bubbles were present.

Electrode sheets were laminated to the electrolyte so that it was in the centre of the electrolyte (shown in figure 2.22) and the electrode face which was in contact with the Mylar carrier was the side laminated to the electrolyte. Similarly when laminating the second electrode layer, the face which was in contact with the Mylar carrier of the second electrode layer was laminated to the first electrode sheet. Close to the electrolyte the electrode has a higher concentration of YSZ (electrolyte material in it) for maximisation of the triple-phase boundary and on the outer layer there is a high concentration of the electrically active component for reduced resistances for current collection.

Two further electrolyte strips measuring 0.5cm x 10cm were laminated to the extruding parts of the electrolyte (figure 2.22) to add strength to the central web (shown in figure 2.23). Figure 2.23 shows how the laminated tapes are manipulated to give the SOFCRoll geometry. A graphite strip (produced by tape casting) of 3mm width, was placed approximately 5mm from one end of the electrode material as shown in figure 2.23. The purpose of this was to ensure that after firing a definite channel for the gas to flow around the spirals was in place. After rolling was completed a further strip of electrolyte material was wrapped around the extruding

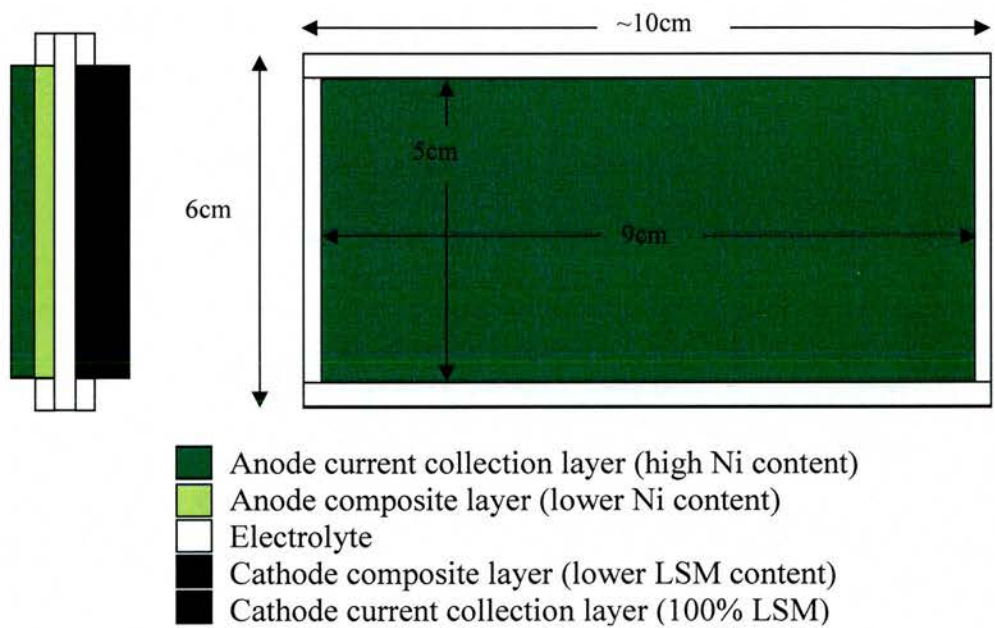


Figure 2.22: Lamination of electrolyte and electrode tapes

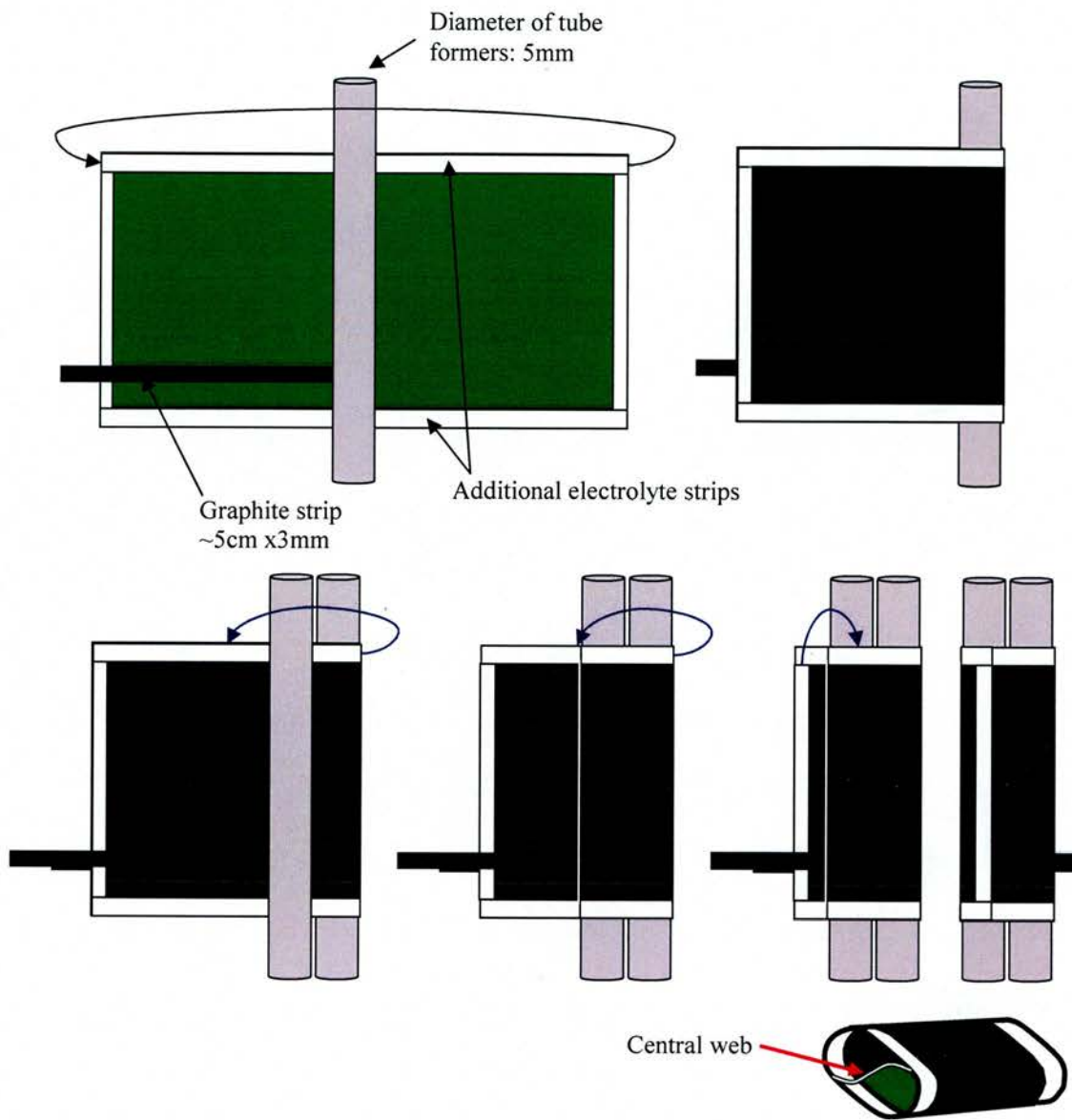


Figure 2.23: Schematic diagram showing the rolling of tapes to produce the SOFCroll geometry

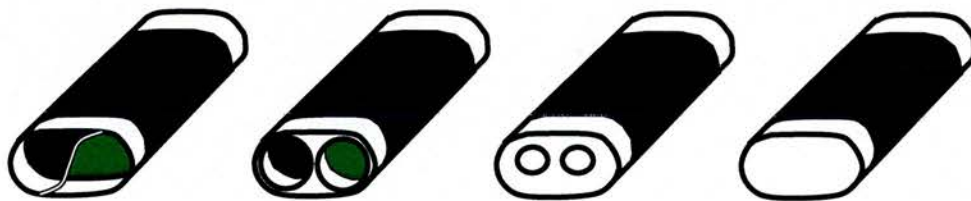


Figure 2.24: Schematic diagram showing the progression of the end sealing

ends of electrolyte to secure the geometry, preventing unravelling of the laminated tapes.

Sealing of the end of the SOFCRoll geometry was achieved by slowly building up layer upon layer of YSZ slurry (same recipe as used for the electrolyte) allowing at least 20mins between each application of slurry allowing the slurry to dry before another layer was added. The principle is shown schematically in figure 2.24. Once the holes at the end were closed (and the slurry dried), the fuel cell was stood up-right and additional slurry added to remove the concave nature of the seal. The end sealed was the end which was closest to the graphite strip. Assuming the graphite strips were the only path the fuel and oxidant gases were able to take along the spirals of the fuel cell, sealing this end would force the gas to travel the length of the fuel cell prior to exiting, thereby utilising the highest quantity of the fuel cell.

Unless otherwise stated, the heating rates used for the fuel cells were as follows: calcined upright with 2mm alumina rods in the furnace brick to prevent the cells falling over, 50-1000°C at 0.5°Cmin⁻¹, dwell for 300mins, cool to 50°C at 5°Cmin⁻¹; fired horizontally on a pre-sintered flat, dense YSZ sheet, 50-1300°C at 5°Cmin⁻¹, dwell for 300mins, cool to 50°C at 5°Cmin⁻¹.

2.11 Performance Testing

A schematic diagram of the cell testing set-up is shown below in figure 2.25. The gas inlet tubes used were commercially produced stainless steel tubes grade 316 with an outer diameter of 3mm and an inner diameter of 2mm (Hydrasun Ltd). The steel was firstly coated (painted by hand) with some silver paint (Advent Ltd) and dried in the furnace at 200°C for 30mins. The purpose of this was firstly to form a protective layer, to try to reduce the corrosion; and secondly form a means for current collection should the conductivity of steel be compromised by corrosion. The steel tubes were removed from the furnace and once cooled a small amount of fresh silver paint applied to the end: approximately 2cm length, before the tubes were slid into the fuel cell. The tubes are secured at the opposite end to the fuel cell on a wood block. For insertion of the tubes into the fuel cell, the tubes were squeezed together slightly and when approximately 1cm length of the gas inlet tube was inside the fuel cell, the tubes were released, causing them to move apart and make good contact with the fuel cell electrodes. The fuel cell together with gas inlet tubes was then placed in the furnace at 200°C for at least 30mins to allow the silver paint to dry, before the seal was made.

At this stage, the system was checked to ensure that no silver paint had crossed over the central web to create a short circuit. If a short circuit had formed, part of the protruding electrolyte from the central web, or from the tubular part was broken to remove the short circuit. With care, only a small quantity of the electrolyte material would be removed. If too much of the central web was broken (ie if some of the electrode was removed), the cell was not tested. However, if only the protruding electrolyte section was removed a seal could still be made and so the cell was tested as usual.

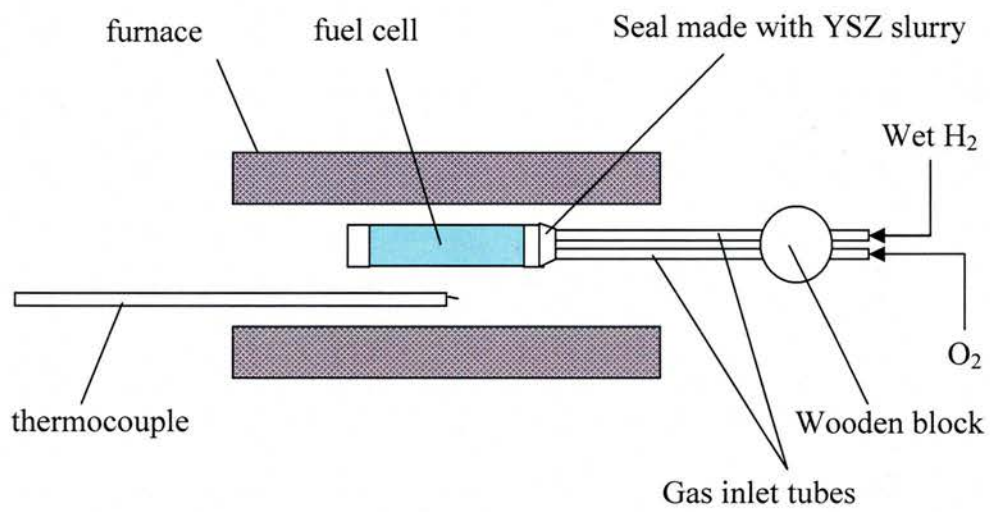


Figure 2.25 Schematic diagram of test set-up

The seal was made with YSZ slurry of the same recipe as that used for the electrolyte prior to tape casting. Care was taken to ensure that the slurry went into the holes not filled by the steel inlet tubes, thereby filling in the holes rather than just covering them up. However, care was taken to ensure that not too much slurry was pushed into the holes so that it did not cover any of the electrode surface. If the protruding electrolyte part of the central web was removed to eliminate a short circuit as described above, the YSZ slurry would of course have to cover up some of the electrode in order to make seal. The YSZ slurry was then left to dry and additionally YSZ slurry then applied as required to ensure a good seal.

Once the solvent had evaporated and the furnace temperature cooled to room temperature, the fuel cell was pushed into the furnace to ensure that the 'hot spot' of the furnace was in between the centre of the fuel cell and the end of the steel gas inlet tubes. The end of the furnace was plugged with glass wool to protect the wood support from the high temperatures and heated slowly from room temperature to $\sim 550^{\circ}\text{C}$ at $0.5^{\circ}\text{Cmin}^{-1}$, before increasing the ramp rate to $5^{\circ}\text{Cmin}^{-1}$ to 800°C . The temperature of 550°C was used as a convenient temperature point for overnight heating at the slow ramp rate. The reasoning behind this heating regime was to use a slow heating rate until all the organics in the slurry were removed. If too fast a heating rate was used, there would be a risk of 'bubbling' of the binder and plasticizers increasing the porosity of the seal.

Once the fuel cell had reached the desired temperature, the gases were introduced. Typical gas flow rates used were $55\text{cm}^3\text{min}^{-1}$ of H_2 and $25\text{cm}^3\text{min}^{-1}$. However, when open circuit voltages (OCV) were very low, the oxygen flow rate was increased. If this caused the open circuit voltages to increase, then the low OCV was thought to be a result of bad sealing and the tests were performed at the increased gas

flow. If increasing the oxygen flow rate caused the OCV to decrease, then the low OCV was thought to be due to cracking in the electrolyte and the fuel cells were not tested.

Tests were performed between 800°C and 925°C. The heating and cooling ramp rate used throughout testing was 5°Cmin⁻¹. After testing, once the furnace had cooled to at least 400°C, the fuel cells were removed from the furnace, and once cooled to a temperature where the fuel cells could be comfortably touched, the gases were turned off. The fuel cells were allowed to cool prior to turning off the gases to ensure that the anode did not re-oxidise prior to microstructural analysis (see section 2.8).

2.11.1 I-V Curves

Figure 2.26 shows how the current changes with voltage due to the losses associated with polarisation resistances at both the cathode (η_c) and the anode (η_a) and ohmic resistance (IR) described in equation 2.19.

$$V = E^0 - IR - \eta_c - \eta_a \quad 2.19$$

The ohmic loss (IR, equation 2.19) is attributed to the internal resistance (transport of electrons in the interconnect, transport of electrons and oxygen ions in the electrodes and transport of oxygen ions in the electrolyte) and the contact resistance (contact between electrode and electrolyte, and electrode and interconnect). The polarisation resistance of the cathode and anode (η_c and η_a , equation 2.19) is attributed to the activation polarisation resistance (charge transfer process, to do with the catalytic activity of the electrode and the area of the triple-phase-boundary) and the concentration polarisation resistance (transport of gaseous substances to and from the triple-phase-boundaries).

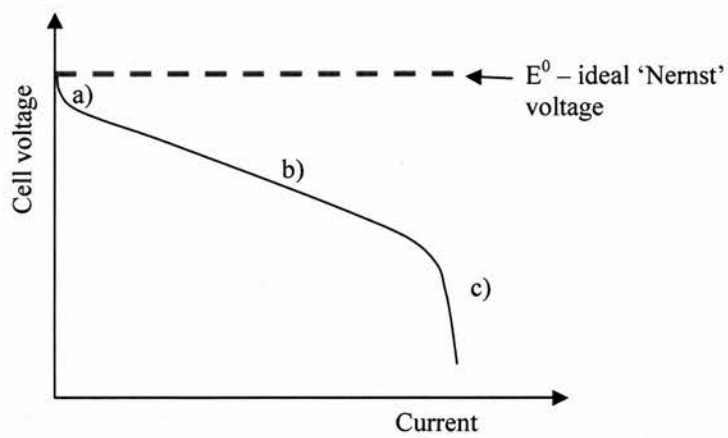


Figure 2.26: Typical trend of voltage vs current of fuel cell a) small initial fall in voltage (activation polarisation losses), b) mostly linear response (IR drop: ohmic losses) and c) rapid decrease in voltage (concentration polarisation/mass transfer losses)

I-V curves were obtained using a ZAHNER messsysteme (Zahner-electrik GmbH & Co KG). Voltages were swept from open circuit voltage (OCV) to OV in steps of 25mV in steady state mode. The power of each cell was calculated from these results according to equation 2.20. Both the measured current and corresponding power output were corrected for lead resistance according to equations 2.21 and 2.22 respectively.

$$P = I \cdot V \quad 2.20$$

$$I_{\text{corrected}} = \frac{I_{\text{measured}} \cdot R_{\text{measured}}}{(R_{\text{measured}} - R_{\text{leads}})} \quad 2.21$$

$$P_{\text{corrected}} = I_{\text{corrected}} \cdot V \quad 2.22$$

2.11.2 A. C. Impedance

a.c. impedance allows (to a certain degree) the different contributions to the cell resistance for example activation polarisation of the anode and cathode and concentration polarisation (detailed in the previous section 2.11.1) to be separated. A.c. impedance is obtained by applying a sinusoidal potential to the resistor and measuring the current. The potential (E_t) is described by equation 2.23 where E_m is the maximum amplitude and f is the frequency in Hertz^[25, 26]. The resulting current is described by equation 2.24, where i_m is the maximum current amplitude and θ is the phase difference^[25, 26].

$$E(t) = E_m \sin(2\pi ft) \quad 2.23$$

$$i(t) = i_m \sin(2\pi ft + \theta) \quad 2.24$$

For an ideal resistor, the resistance follows Ohms law at all current and voltage values and is independent of frequency. The a.c. current and voltage are therefore in phase with each other (so the phase difference θ is zero)^[25], as shown in figure 2.27a. In this case the impedance, $Z(f)$ is simply equal to the resistance (described by Ohms law: $E=IR$).

For a simple capacitor, the current is dependent on the frequency and can be described according to equation 2.25, where the current is out of phase with the voltage by an angle of $\pi/2$ ^[25]. In this case, the impedance is given by the combination of equations 2.23 and 2.25, as shown in equation 2.26.

$$\begin{aligned} i &= \frac{dQ}{dt} = C \frac{dE}{dt} = C[2\pi f E_m \cos(2\pi f t)] \\ &= C[2\pi f E_m \sin(2\pi f t + \pi/2)] \end{aligned} \quad 2.25$$

$$Z(f) = \frac{E(t)}{i(t)} = \frac{1}{C \cdot 2\pi f} \tan(2\pi f t) \quad 2.26$$

In any real complex circuits, the phase difference θ can take any value between 0 and $\pi/2$, and at any given frequency the impedance is as described in terms of real (Z) and imaginary (Z') impedance as shown in equation 2.27^[25]. The impedance is therefore a vector and plotting Z' against Z (at the same frequencies) shows the impedance response of the circuit in a Cole plot^[26], where the magnitude is the distance between any given point (Z, Z') and the origin and the angle of this

$$Z(f) = \frac{E(t)}{i(t)} = Z \sin(2\pi f t) - Z' \cos(2\pi f t) \quad 2.27$$

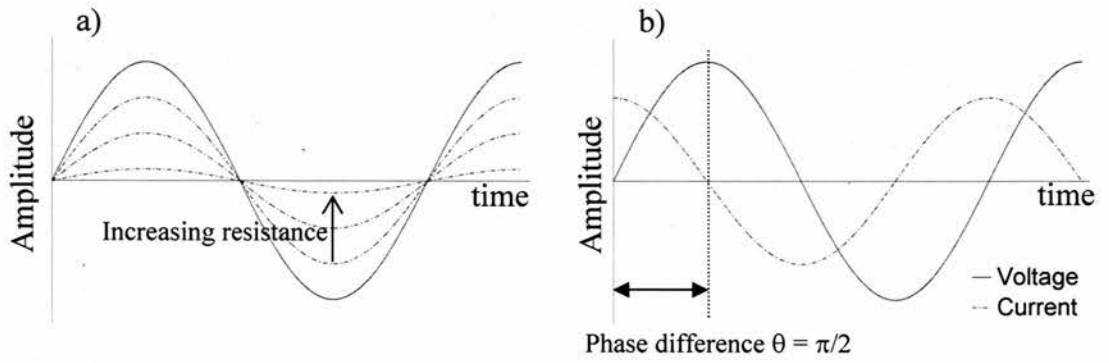


Figure 2.27: Sinusoidal voltage and current responses for a) an ideal resistor and b) a simple capacitor

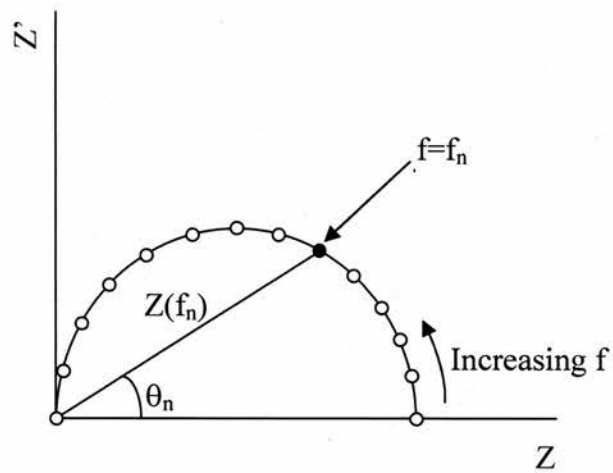


Figure 2.28: Cole plot showing impedance of a resistor and capacitor in parallel. θ_n is the phase difference at frequency of f_n

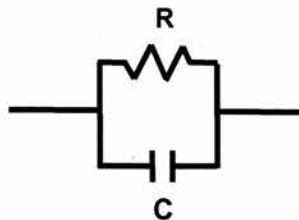


Figure 2.29: Equivalent circuit of a resistor and capacitor in parallel

vector is the phase angle, as shown in figure 2.28. An electrical system can be described by equivalent circuits, where the current flows through a resistor and capacitor in either parallel or series^[25, 26]. Figure 2.29 shows an equivalent circuit for a simple resistance and capacitor in parallel^[25, 26]; the corresponding impedance response for this equivalent circuit is shown in figure 2.28^[25]. As seen by equation 2.26, as the frequency tends to 0, the capacitor contribution to the impedance tends towards infinity, and so the current will travel through the resistor only and so the circuit impedance will be equal to the resistance R , obtained by Ohms law. Conversely, as the frequency tends towards infinity, the impedance of the capacitor tends to zero, becoming very conductive and hence the circuit impedance will be equal to that shown in equation 2.26.

In this investigation, a.c. impedance analysis was performed at open circuit voltage (OCV) with an amplitude of 100mV between frequencies of 100kHz and 50mHz and corrected for lead resistance by a ZAHNER messsysteme (Zahner-electrik GmbH & Co KG). The data was fitted with ZView software, version 2.80 (Scribner Associates, Inc) using the equivalent circuits shown in figure 2.30a and 2.30b depending on how many arcs were seen in the data to correct for the strong inductance effect seen. $L1$ represents the inductance, $R1$ the material resistances (contact resistances, material resistivity) and $R2$, $R3$ and $R4$ the polarisation resistances of the electrodes.

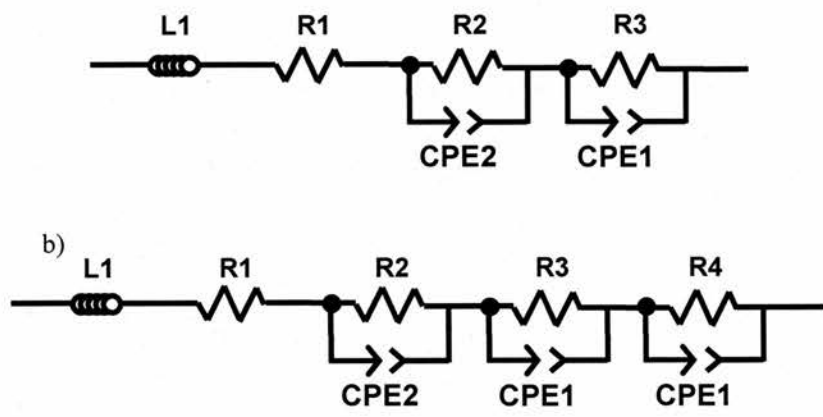


Figure 2.30: Equivalent circuits used to fit a.c. impedance data when a) 2 arcs were observed and b) 3 arcs were observed

2.11 References

- 1 R. E. Mistler, E. R. Twiname, "Tape Casting Theory and Practice", Westerville: The American Ceramic Society, **2000**
- 2 Eric R. Twiname, Mistler Inc; private communication, July **2003**
- 3 M. Barsoum, "Fundamentals of Ceramics", The McGraw-Hill Companies Inc, **2000**
- 4 R. M. German, "Sintering Theory and Practice", Chichester: John Wiley & Sons Inc, **1996**
- 5 M. T. Weller, "Inorganic Materials Chemistry", Oxford Chemistry Primers, Oxford: Oxford University Press, **1994**
- 6 B. M. Clemens, "Diffraction: Real Samples", lecture course, Geballe Lab for Advanced Materials, Stanford University at:
http://www-lam.stanford.edu/xlab/MatSci162_172/LectureNotes/04_Real%20Samples.pdf
- 7 "Particle Size and Strain Analysis by X-Ray Diffraction" – Application Note, H&M Analytical Services, Inc. NJ **2002**, at:
http://www.h-and-m-analytical.com/pdfs/size_strain.pdf
- 8 A. G. Belous, O. I. V'yunov, E. V. Pashkova, O. Z. Yanchevksii, A. I. Tovstolytkin and A. M. Pogorelyi, "Effects of Chemical Composition and Sintering Temperature on the Structure of $\text{La}_{1-x}\text{Sr}_x\text{MnO}_{3\pm y}$ Solid Solutions", *Inorg. Mater.*, *39* (2), **2003**, 161-170
- 9 PDF (Powder Diffraction File) number 24-734, Mn_3O_4 , produced by ICCD (International Centre for Diffraction Data)
- 10 PDF (Powder Diffraction File) number 41-1442, Mn_2O_3 , produced by ICCD (International Centre for Diffraction Data)
- 11 L. A. Salam, R. D. Matthews, H. Robertson, "Optimisation of thermoelectric green tape characteristics made by the tape casting method", *Mater. Chem. Phys.*, *62*, **2000**, 263-272
- 12 S. F. Corbin, P. S. Apté, "Engineered porosity via tape casting, lamination and the percolation of pyrolyzable particulates", *J. Am. Ceram. Soc.*, *82* (7), **1999**, 1693-1701
- 13 N. Das, H. S. Maiti, "Formation of pore structure in tape-cast alumina membranes – effects of binder content and firing temperature", *J. Membr. Sci.*, *140*, **1998**, 205-212
- 14 S. F. Corbin, J. Lee, X. Qiao, "Influence of green formulation and pyrolyzable particulates on the porous microstructure and sintering characteristics of tape cast ceramics", *J. Am. Ceram. Soc.*, *84* (1), **2001**, 41-47
- 15 M. Boaro, J. M. Vohs, R. J. Gorte, "Synthesis of highly porous yttria-stabilised zirconia by tape-casting methods", *J. Am. Ceram. Soc.*, *86*(3), **2003**, 395-400

- 16 D. R. Dinger, "Rheology for Ceramists", Clemson: Dinger Ceramic Consulting Services, **2002**
- 17 Y. T. Chou, Y. T. Ko, M. F. Yan, "Fluid flow model for ceramic tape casting", *J. Am. Ceram. Soc.*, *70 (10)*, **1987**, 280-282
- 18 M. Schmidt, H. Münstedt, M. Svec, A. Roosen, T. Betz, F. Koppe, "Local flow behaviour of ceramic slurries in tape casting, as investigated by laser-doppler velocimetry", *J. Am. Ceram. Soc.*, *85 (2)*, **2002**, 314-320
- 19 M. A. Janney, "Attaining high solids in ceramic slurries", Oak Ridge National Laboratory, Oak Ridge, TN 37831, at:
<http://www.ms.ornl.gov/researchgroups/process/cpg/gelpubs/Mixing.pdf>
- 20 A. Mukherjee, B. Maiti, A. Das Sharma, R. N. Basu, H. S. Maiti, "Correlation between slurry rheology, green density and sintered density of tape cast yttria stabilised zirconia", *Ceram. Int.*, *27*, **2001**, 731-739
- 21 V. L. Richards, "Adsorption of dispersants on zirconia powder in tape-casting slip compositions", *J. Am. Ceram. Soc.*, *72 (2)*, **1989**, 325-327
- 22 Jürgen Blumm, NETZSCH-Gerätebau GmbH; private communication, September **2003**
- 23 J. P. Eberhart, "Structural and Chemical Analysis of Materials", Chichester: John Wiley & Sons Ltd, **1991**
- 24 J. Larminie, A. Dicks, "Fuel Cell Systems Explained", Chichester: John Wiley & Sons Ltd, **2001**
- 25 A. C. Fisher, "Electrode Dynamics", Oxford Chemistry Primers, Oxford: Oxford University Press, **1996**
- 26 J. O'M. Bockris, A. K. N. Reddy, M. Gamboa-Aldeco, "Modern Electrochemistry Volume 2A: Fundamentals of Electrodics", 2nd ed, NY: Kluwer Academic/Plenum Publishers, **2000**

3 Processing

3.1 Introduction

The SOFCRoll fuel cell geometry is such that the simplest production technique dictates the formation of a flexible planar 3-layer laminate of the anode-electrolyte-cathode, which is then manipulated as described in section 2.10 to form the desired geometry prior to firing. In order to produce a mechanically sound fuel cell after the sintering process, the stresses in the system must be minimised.

One unavoidable stress is the thermal mismatch of the different materials. These stresses can be reduced by grading the cathode and anode from high electrolyte material to high electrode material concentrations, but in the absence of any material development (not the scope of this project), these stresses are unavoidable. One of the main challenges of this project however, is the development of near identical shrinkage profiles of each component during the firing procedure. Mismatches in the component shrinkages can lead to cracking and/or de-lamination of components, harming the cell performance. Whilst a certain degree of compromise is necessary, the matching of shrinkage profiles, should not however be achieved at the expense of each components microstructure or composition.

The following chapter describes the tape casting and firing of each component. Particular focus is centred on factors affecting the microstructure and shrinkage profiles of the components when fired singularly, that is with no constraints by other components. The reaction between the LSM cathode and YSZ electrolyte materials is also investigated with regard to the A-site deficiency of the LSM. The effect of the A-site deficiency on the resulting microstructure and shrinkage is noted. Furthermore, rate controlled sintering and particle dispersion are detailed.

3.2 Tape Casting

3.2.1 Particle Characterisation of Ceramic Powders

The ceramic powders used in this investigation were characterised as described in section 2.3, and the particle size, surface area obtained and the corresponding manufacturer information (where appropriate) are detailed in table 3.1. In addition, the images obtained from SEM analysis are shown in figures 3.1 and 3.2.

As described in section 2.3, the Debye Scherrer particle size can only be obtained for crystallite sizes of less than $1\mu\text{m}$ and so where no value is given in table 3.1 the crystallite size is taken to be greater than $1\mu\text{m}$. For these large crystallite sizes, the two methods of particle size analysis (SEM and Debye-Scherrer) are in agreement with the exception of the $(\text{La}_{0.8}\text{Sr}_{0.2})_{0.97}\text{MnO}_3$ produced at 1100°C . This discrepancy can be attributed to the fact that the Debye-Scherrer analysis gives a volume weighted average size (that is a small number of large particles would have a greater contribution to the measured size), whilst the SEM analysis gives a number weighted average size. However, for the majority of powders where values for the crystallite sizes could be obtained by the Debye-Scherrer analysis, larger average particle sizes were obtained when analysed by SEM. This suggests the presence of micro-domains in each particle, which can not visually seen in figures 3.1-3.2 or that the powder is not completely crystalline.

A combination of the particle size and morphology obtained from the SEM analysis and the surface area was used as a starting point when formulating slips/slurries for tape casting. For example, figure 3.1e shows the coarsening of the YSZ resulted in a highly porous particle – essentially a sintered agglomerate of the YSZ primary particles (shown in figure 3.1a and 3.1b). This would result in large

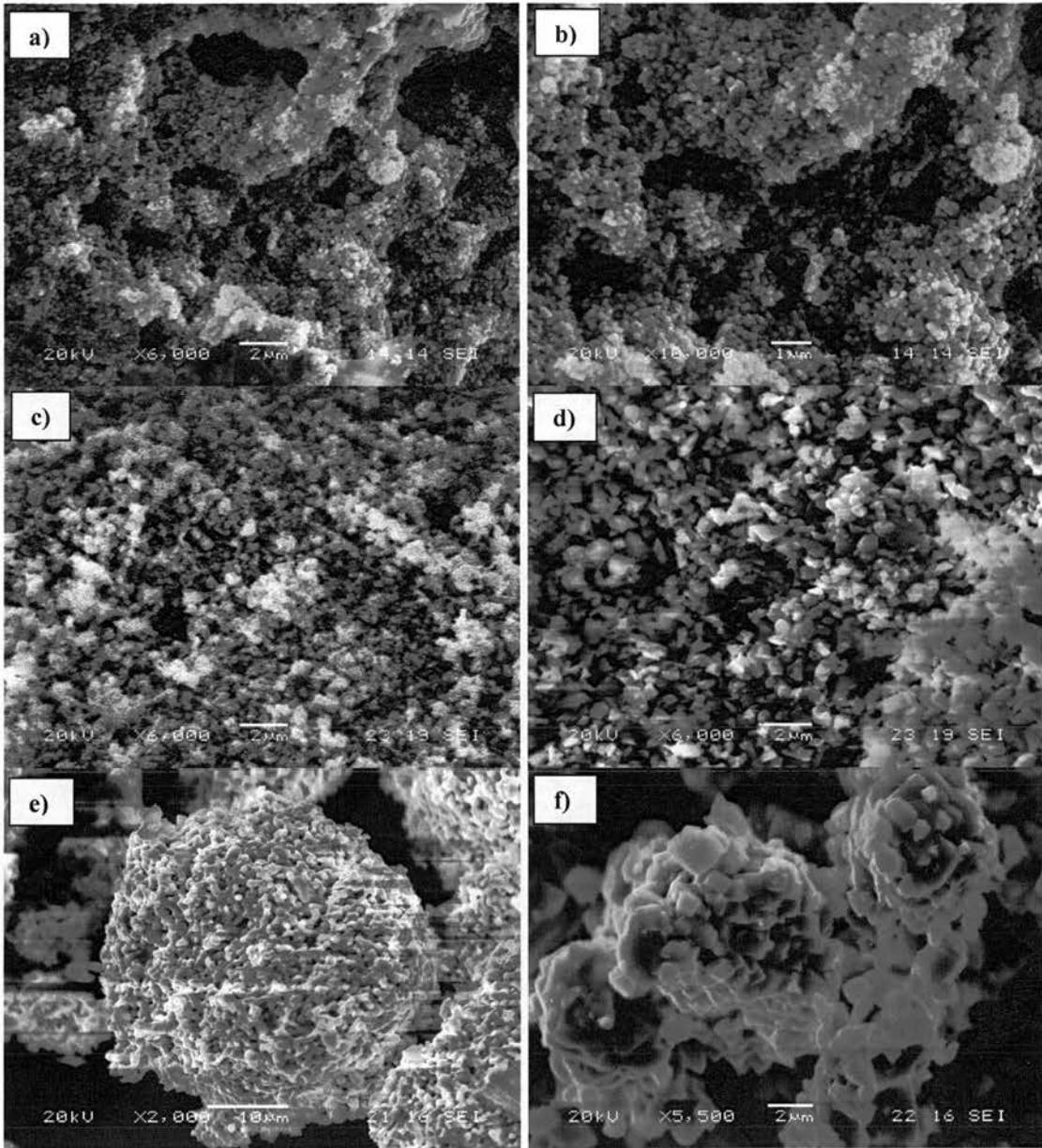
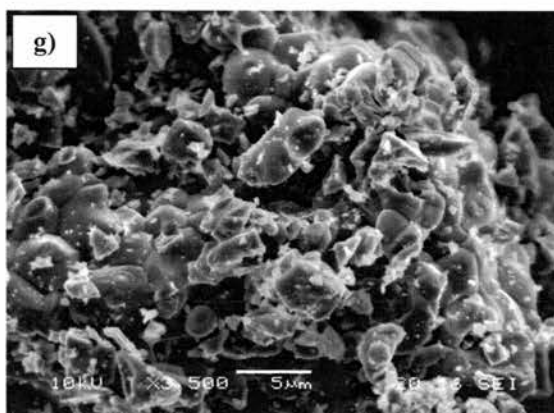
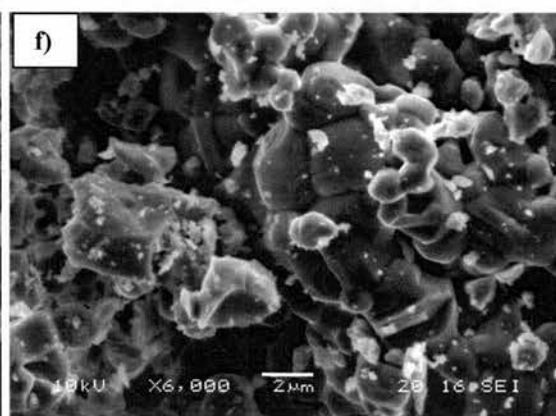
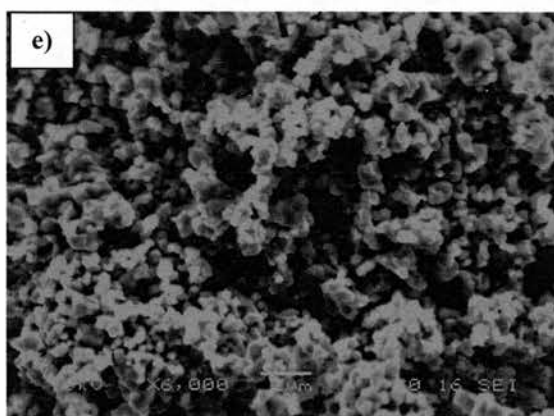
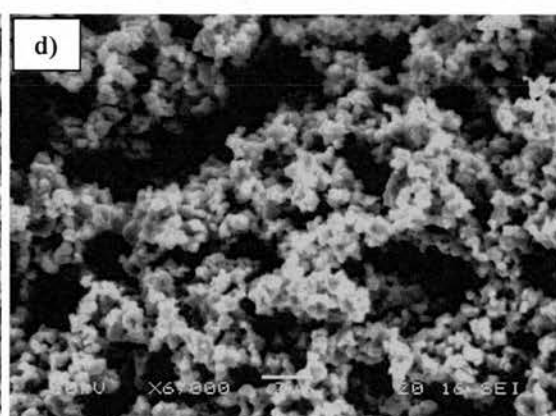
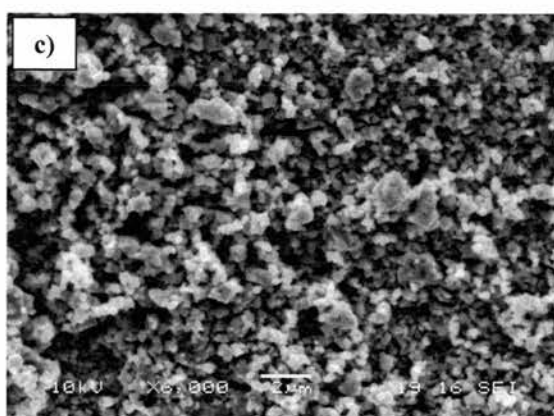
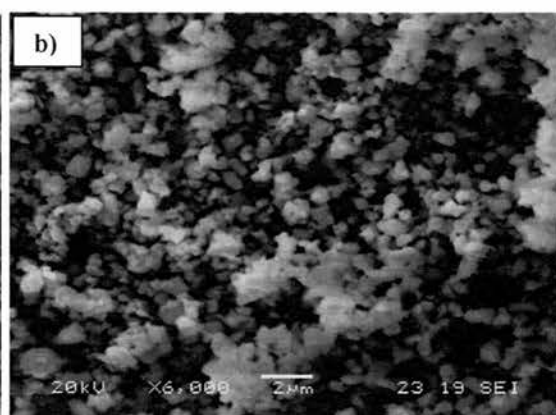
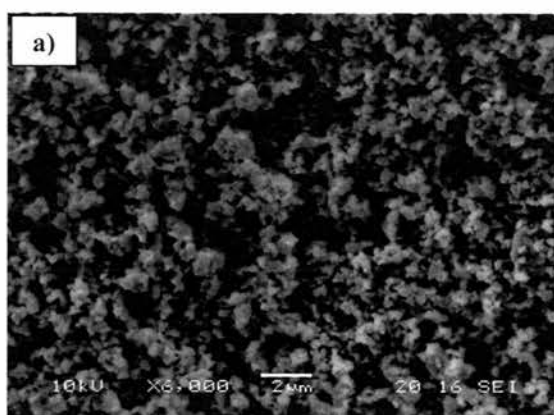


Figure 3.1: SEM images of the YSZ and NiO powders investigated:

a) and b) YSZ (Pi-Kem Ltd), c) YSZ (1 μ m, Unitec Ceramics Ltd), d) YSZ (2 μ m, Unitec Ceramics Ltd), e) YSZ (Pi-Kem Ltd) coarsened at 1400°C for 5hrs, & sieved through 60 μ m mesh and f) NiO (Aldrich Ltd).

Note the scale of b) and e) differ significantly from the others



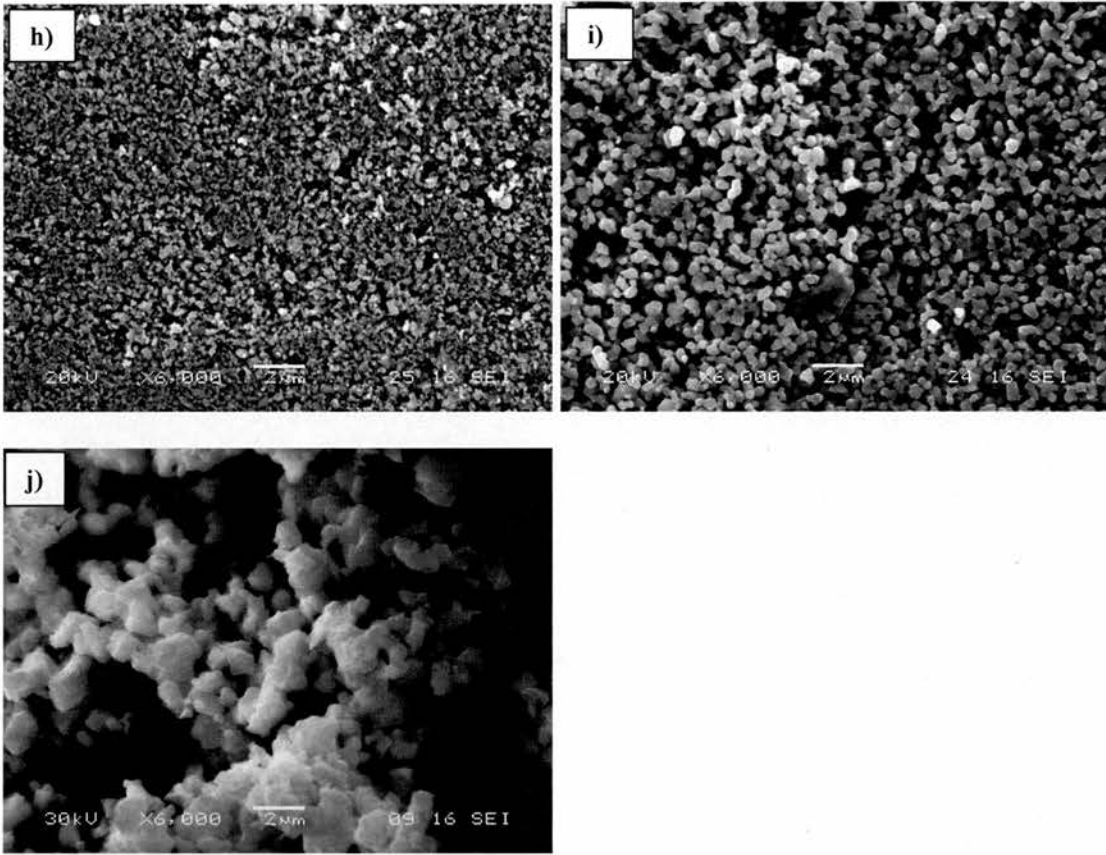


Figure 3.2: SEM images of the different LSM investigated: a) $\text{La}_{0.8}\text{Sr}_{0.2}\text{MnO}_3$ (Pi-Kem Ltd) b) $(\text{La}_{0.8}\text{Sr}_{0.2})_{0.98}\text{MnO}_3$ (Nextech Ltd), c) $(\text{La}_{0.8}\text{Sr}_{0.2})_{0.97}\text{MnO}_3$ reacted at 1000°C , 15.5hrs, d) $(\text{La}_{0.8}\text{Sr}_{0.2})_{0.97}\text{MnO}_3$ reacted at 1050°C , 15.5hrs, e) $(\text{La}_{0.8}\text{Sr}_{0.2})_{0.97}\text{MnO}_3$ reacted at 1100°C , 15.5hrs, f) $(\text{La}_{0.8}\text{Sr}_{0.2})_{0.97}\text{MnO}_3$ reacted at 1150°C , 15.5hrs, g) $(\text{La}_{0.8}\text{Sr}_{0.2})_{0.97}\text{MnO}_3$ reacted at 1200°C , 15.5hrs, h) $(\text{La}_{0.8}\text{Sr}_{0.2})_{0.95}\text{MnO}_3$ (Nextech Ltd), i) $(\text{La}_{0.8}\text{Sr}_{0.2})_{0.95}\text{MnO}_3$ coarsened at 1000°C , 16hr 20min and j) $(\text{La}_{0.8}\text{Sr}_{0.2})_{0.94}\text{MnO}_3$ reacted at 1050°C , 15.5hrs

Ceramic	Manufacturer values				Measured Particle Size				Measured Surface Area /m ² g ⁻¹
	Particle Size / μ m	Surface Area /m ² g ⁻¹	Density /gcm ⁻³	SEM analysis		Debye Scherrer analysis			
				(mean) / μ m	% error	/ μ m	% error		
YSZ (Pi-Kem Ltd)	0.21	7	6.1	0.2	14	0.14	41 ^a	7.4	
YSZ coarsened at 1400°C, 5hrs, sieved 60 μ m		n/a		38	2	/	/	3.3	
YSZ 1 μ m (Unitec Ltd)	1	/	/	0.3	16	0.04	17	7.6	
YSZ 2 μ m (Unitec Ltd)	2	/	n/a	0.7	7	0.06	34	7.6	
NiO (Aldrich Ltd)	-325mesh	/	6.67	1.6	5	/	/	3.7	
L _{a0.8} Sr _{0.2} MnO ₃ (Pi-Kem Ltd)	0.6	5.12	6.65	0.2	19	0.08	30 ^a	7.8	
(L _{a0.8} Sr _{0.2}) _{0.98} MnO ₃ (Nextech Ltd)	/	5.44	/	0.4	11	0.1	37 ^a	6.6	
(L _{a0.8} Sr _{0.2}) _{0.97} MnO ₃ reacted at 1000°C, 15.5hrs		n/a		0.4	13	0.2	57 ^a	4.6	
(L _{a0.8} Sr _{0.2}) _{0.97} MnO ₃ reacted at 1050°C, 15.5hrs		n/a		0.4	11	0.2	68 ^a	4.7	
(L _{a0.8} Sr _{0.2}) _{0.97} MnO ₃ reacted at 1100°C, 15.5hrs		n/a		0.5	10	/	/	3.3	
(L _{a0.8} Sr _{0.2}) _{0.97} MnO ₃ reacted at 1150°C, 15.5hrs		n/a		4.0	3	/	/	2.9	
(L _{a0.8} Sr _{0.2}) _{0.97} MnO ₃ reacted at 1200°C, 15.5hrs		n/a		7.5	1	/	/	3.5	
(L _{a0.8} Sr _{0.2}) _{0.95} MnO ₃ (Nextech Ltd)	0.44	11.29	/	0.3	16	0.04	29	14.7	
(L _{a0.8} Sr _{0.2}) _{0.95} MnO ₃ coarsened at 1000°C, 16hr 20min		n/a		0.4	11	0.7	88 ^a	12.3	
(L _{a0.8} Sr _{0.2}) _{0.94} MnO ₃ reacted at 1050°C, 15.5hrs		n/a		1.0	6	/	/	6.8	

Table 3.1: Comparison of particle sizes of ceramic powders

^a Measured sizes are very close to the particle size limit for the analysis technique

porosities in fired ceramic tapes both due to the porous nature of the particle and due to packing inefficiencies. Similarly, consideration of the $(\text{La}_{0.8}\text{Sr}_{0.2})_{0.97}\text{MnO}_3$ powders shown in figure 3.2 and the corresponding surface areas shown in table 3.1, show a relatively small change in the surface area allowing similar binder and plasticizer contents. The sudden increase in particle size when producing these powders at 1150°C or above however, would lead to a decrease in packing efficiency and increase in inter-particle spacing in the slurry, requiring a decreased organic content in the slurry and decreased shrinkage when firing.

3.2.1a Production of A-site deficient LSM

Temperatures between 1000°C and 1200°C were investigated for incorporation of excess manganese into the unit cell of $\text{La}_{0.8}\text{Sr}_{0.2}\text{MnO}_3$ to produce a 3% A-site deficiency: $(\text{La}_{0.8}\text{Sr}_{0.2})_{0.97}\text{MnO}_3$. Whilst a higher temperature could easily be utilised for the reaction, the end use for these powders is to be tape cast, which ideally requires surface areas of $5\text{-}15\text{m}^2\text{g}^{-1}$ [1]. Additionally the resulting cathode tape is to be co-fired together with the YSZ electrolyte at as low a temperature as possible and as short a time for densification of the YSZ to eliminate reactions between the YSZ and LSM, described in section 1.4.3).

Analysis of the resulting powder produced at each temperature was performed by XRD as detailed in section 2.3.3. Slow runs between 2θ values of 32.0-34.0 and 35.0-37.0 were performed to encompass the highest intensity peaks of Mn_3O_4 ($2\theta = 32.316$, Intensity 85; $2\theta = 36.086$, Intensity 100)^[2] and Mn_2O_3 ($2\theta = 32.952$, Intensity = 100)^[3] - the product of high temperature treatment of MnCO_3 in air. The peak of Mn_3O_4 at $2\theta = 32.316$, is also shared with that of LSM^[4], but the presence of the other peaks would show the excess manganese had not been incorporated into the unit cell.

Figure 3.3 shows just two peaks in the XRD spectrum, corresponding to the 2θ values of 32.3 and 32.6 of LSM^[4]. There are no obvious peaks at $2\theta = 36.0$ and 32.9 indicating no presence of MnO_x or too low a concentration of MnO_x resulting in an insufficient signal to noise ratio. From figure 3.3, it seems that at incorporation temperatures of 1050°C and above, the peaks of LSM are at lower 2θ value, suggesting that these powders have higher unit cell dimensions, as expected with non-stoichiometry. This data would therefore suggest that temperatures of at least 1050°C are required for successful production of A-site deficiency. For this reason the incorporation of excess manganese to produce $(\text{La}_{0.8}\text{Sr}_{0.2})_{0.94}\text{MnO}_3$ (6% A-site deficiency) was performed at 1050°C only and as with production of 3% A-site deficiency, only peaks corresponding to the LSM were seen, shown in figure 3.4, suggesting incorporation of the manganese into the unit cell was successful. Again, this could merely be that the concentration of MnO_x was too low resulting in an insufficient signal to noise ratio.

X-ray diffraction patterns between 2θ values of 10-80 were obtained for all LSM powders investigated and their unit cell parameters obtained, as shown in table 3.2. Plotting the unit cell parameters of all the A-site deficient LSM produced by high temperature treatment of the stoichiometric LSM gives no clear relationship between temperature of manganese incorporation to the LSM and unit cell parameters, shown in figure 3.5. The increase in unit cell parameter dimensions for all A-site deficient powders with respect to the starting LSM material, shows A-site deficient LSM has been produced. Considering the 3% A-site deficient LSM, the sudden increase in unit cell parameters when the temperature was increased to 1100°C suggests that the A-site deficiency was increased at this temperature and whilst temperatures as low as 1000°C added A-site deficiency, it was not high enough, or held for long enough at

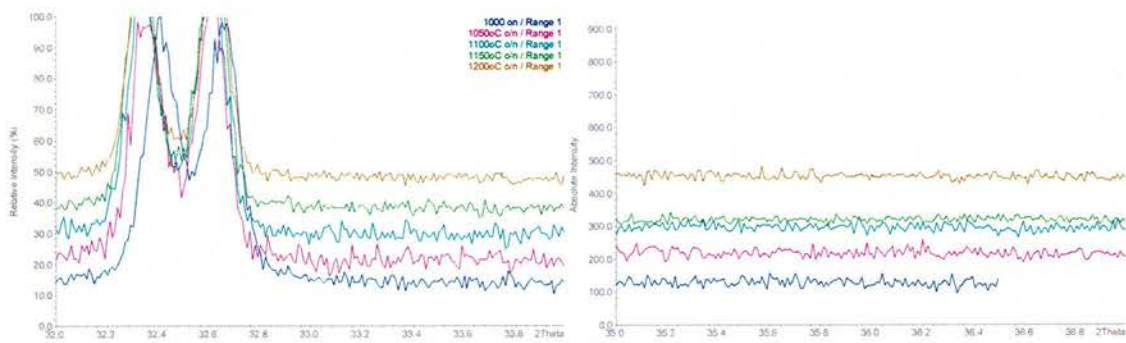


Figure 3.3: XRD data between $2\theta = 32.0$ and 34.0 ; $2\theta = 35.0$ and 37.0 of $\text{La}_{0.8}\text{Sr}_{0.2}\text{MnO}_3$ reacted with MnCO_3 to form 3% A-site deficiency at 1000°C , 1050°C , 1100°C , 1150°C and 1200°C

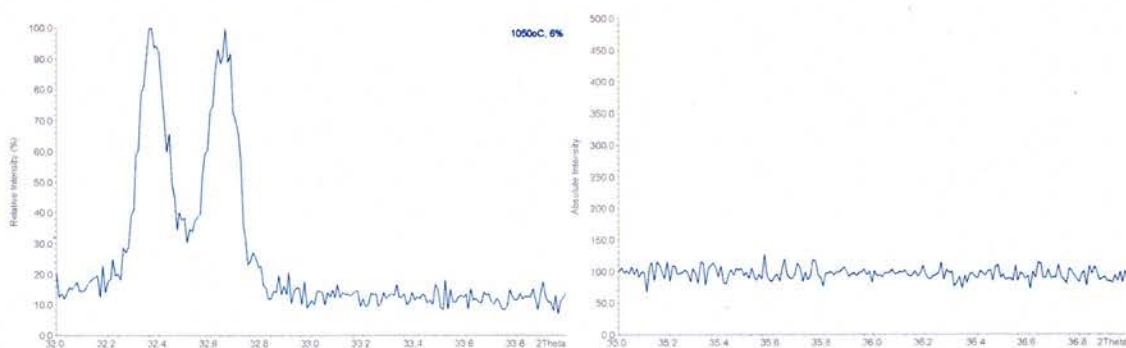


Figure 3.4: XRD data between $2\theta = 32.0$ and 34.0 ; $2\theta = 35.0$ and 37.0 of $\text{La}_{0.8}\text{Sr}_{0.2}\text{MnO}_3$ reacted with MnCO_3 to form 6% A-site deficiency at 1050°C

A-site deficiency	Production temperature /°C	a /Å	c /Å	Unit cell volume /Å ³
0	n/a	5.5169 (20)	13.360 (3)	352.15 (24)
2	n/a	5.525 (3)	13.375 (4)	353.6 (4)
3	1000	5.527 (5)	13.383 (7)	354.0 (6)
	1050	5.525 (3)	13.377 (4)	353.6 (3)
	1100	5.536 (3)	13.394 (5)	355.5 (4)
	1150	5.534 (6)	13.388 (9)	355.1 (7)
	1200	5.5308 (9)	13.3738 (12)	354.29 (9)
	1200 – post annealed at 1000°C for 15hrs	5.5240 (10)	13.3685 (15)	353.29 (10)
5	n/a	5.520 (6)	13.383 (9)	353.2 (7)
6	1050	5.5328 (17)	13.382 (3)	354.75 (21)

Table 3.2: Unit cell parameters of LSM of various A-site deficiency obtained by XRD refinement

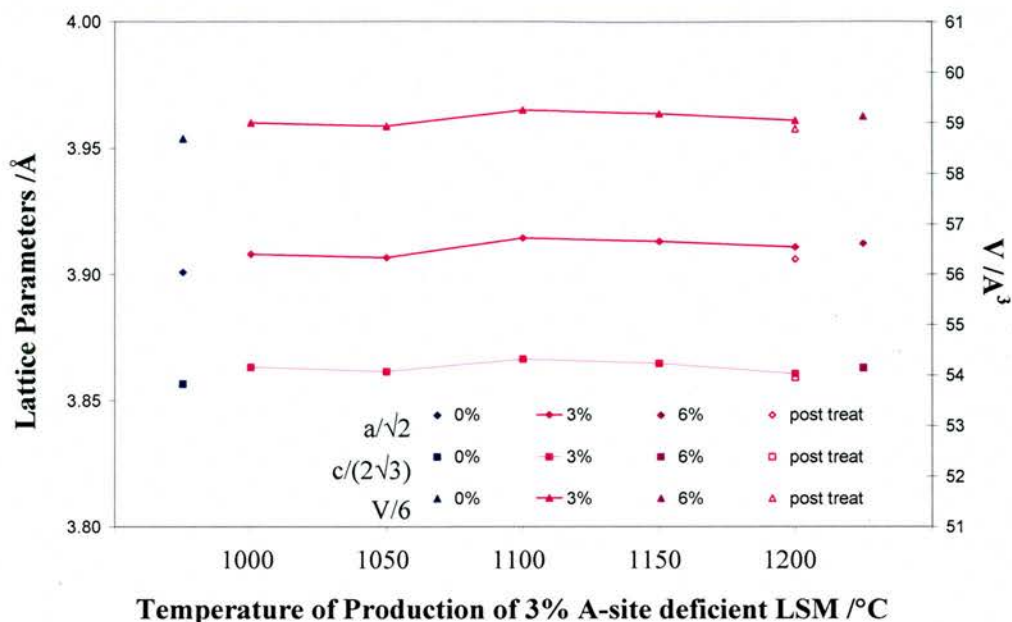


Figure 3.5: Graph showing the unit cell parameters of the LSM produced by high temperature treatment of MnCO_3 and stoichiometric LSM (shown as a reference). Also shown is the unit cell parameters of the A-site deficient LSM produced at 1200°C after post-annealing at 1000°C for 15hrs.

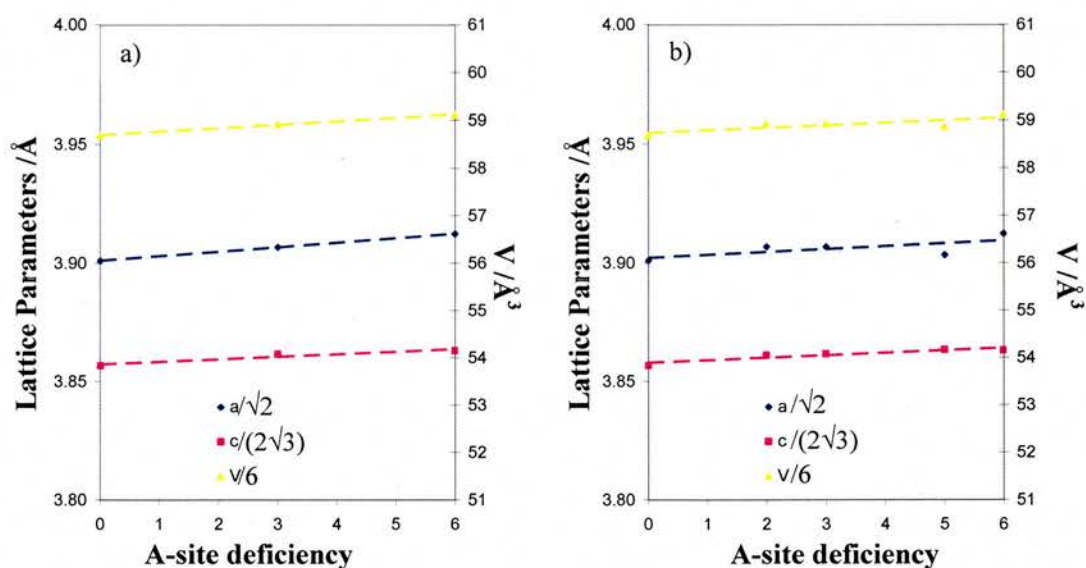


Figure 3.6: Graphs showing the variation in unit cell parameters with A-site deficiency of a) LSM produced in-house together with the stoichiometric LSM starting material and b) re-plot of a) with commercial powders with a 2% and 5% A-site deficiency. Production temperature of 1050°C only shown for LSM produced in-house.

this temperature for all the excess manganese to be introduced to the unit cell. The decrease in unit cell parameters between 1000°C and 1050°C, and 1100°C and above could be due to the mobility of the manganese at these temperatures diffusing into the alumina crucible resulting in an actual decrease in the A-site deficiency, or due changes in the oxygen stoichiometry. Post annealing a sample of the 3% A-site deficient LSM powder at 1000°C for 15hrs in a platinum crucible (to eliminate the possibility of further manganese migration) had the affect of decreasing the unit cell dimensions (see table 3.2 and figure 3.5). This decrease in dimensions suggests that the oxygen content is reduced^[5] at increased production temperatures, which, after post-annealing at 1000°C is regained. The end lattice parameters of this sample were slightly smaller than the 3% A-site deficient powder produced at 1000°C, which could show a slight decrease in A-site deficiency as a result of manganese mobility at the increased production temperatures.

A linear relationship between the unit cell parameters and the A-site deficiency is expected^[6]. Plotting the unit cell dimensions against the target A-site deficiency for the LSM produced at 1050°C (together with the starting material of the stoichiometric LSM), figure 3.6a, shows that the a parameters do indeed show a linear trend. Adding the unit cell parameters obtained from the commercial powders as shown in figure 3.6b shows a degree of discrepancy in proportionality between unit cell parameters and A-site deficiency, presumably due to the different production techniques and resulting oxygen stoichiometries. In order to clarify the exact degree of A-site deficiency of these powders, further analysis is required. The scope of this investigation however, is how these powders react with the electrolyte material and how they behave during sintering in tape cast films, detailed in section 3.6.

It can be seen from figure 3.2 and table 3.1, that the amount of manganese added to the unit cell and the temperature at which the reaction was performed affects the particle size and hence surface area. When producing 3% A-site deficient LSM, increasing the temperature from 1000°C to 1200°C increased the degree of particle coarsening occurring, with definite grains being visible from particle sintering in powders reacted at 1150°C and 1200°C (figure 3.2). Comparison between 3% A-site deficient LSM and 6% A-site deficient LSM produced at 1050°C, shows that when increasing the A-site deficiency increases the degree of particle coarsening. This suggests that either the manganese oxide acts as a sintering aid to the LSM or that increased A-site deficiency increases the degree of particle sintering (a known phenomenon^[7]), or a combination of both.

3.2.2 Particle Characterisation of Pore Formers

Figure 3.7 shows the SEM analysis of the pore formers powders used for this investigation in their pre-milled, as received state. It is clear from these images that the particle size and distribution of the graphite differs greatly with all sources. The graphite -325 (Aldrich Ltd) seems to have the largest particles, whilst the original un-sourced graphite together with graphite -100 (Aldrich Ltd) having the greater number of smaller particles. The average particle size and distribution will be changed during slurry preparation for tape casting, as the graphite particles are reduced in size, as shown in figure 3.8 and discussed further in section 3.2.3.2. For this reason together with the difficulty in determining the difference between particles and particle topography SEM analysis was only used to obtain the particle size of the spherical shaped glassy carbon pore former, shown in table 3.3 together with values received from the manufacturer.

Pore former	Manufacturer values		Measured Particle Size (mean)
	Particle Size / μm	Density / gcm^{-3}	SEM analysis / μm
Graphite grade 615 (Griffin & George Ltd)	<i>unknown</i>		/
Graphite (Fisher Ltd)	<i>not given</i>	2.0	/
Graphite -325 mesh (Aldrich Ltd)	10.23	1.9	/
Graphite -100 mesh (Aldrich Ltd)	6.80	1.9	/
Glassy Carbon (Aldrich Ltd)	10-40	1.5	19.5 (4% error)
Soluble starch (Fisons Ltd)	n/a	1.5	n/a

Table 3.3: Physical data of pore formers powders

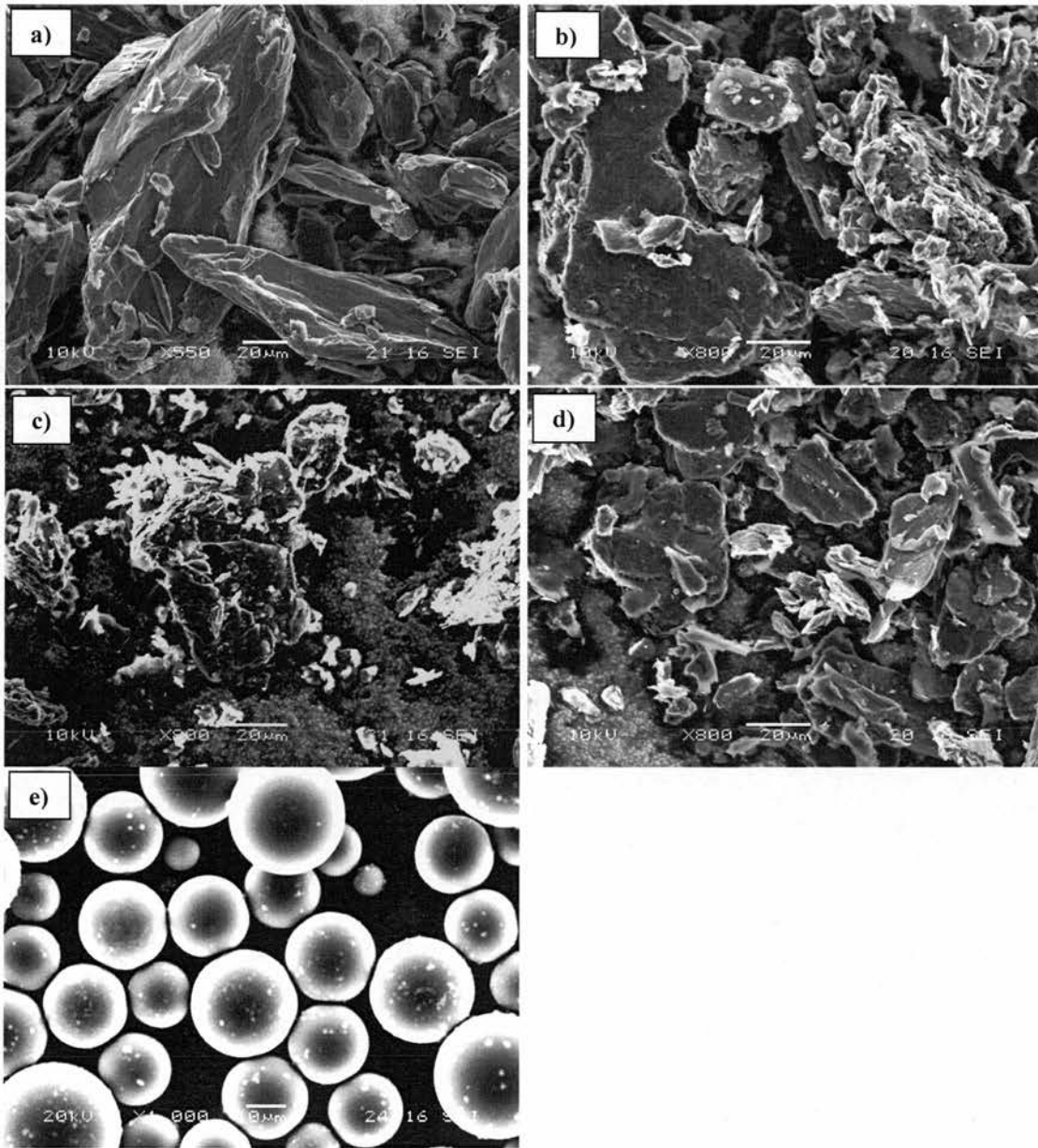


Figure 3.7: SEM images of the pore formers investigated: a) Graphite -325 mesh (Aldrich Ltd), b) Graphite grade 615 (Griffin & George Ltd), c) Graphite -100 mesh (Aldrich Ltd), d) Graphite (Fisher Ltd) and e) Glassy carbon (Aldrich Ltd). Note the difference in magnifications.

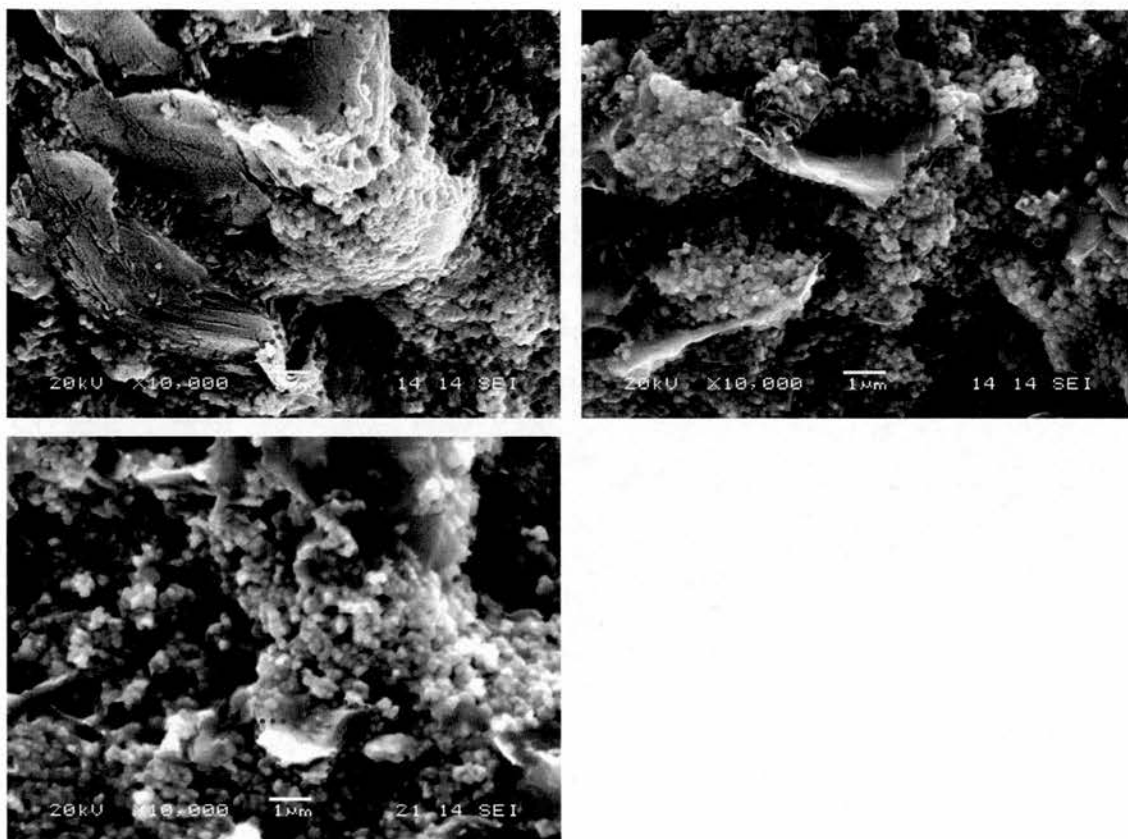


Figure 3.8: SEM images of green tape produced with YSZ (Pi-Kem Ltd) and graphite grade 615 (Griffin & George Ltd) after a) 4hrs ball milling, b) 18hrs ball milling and c) 24hrs ball milling (graphite particle identified by blue outline)

3.2.3 Dispersion Settling Tests

The following sections detail the dispersion of particles with various dispersion agents and milling times. The solvent used was the same as that used in tape production: butan-2-one:ethanol 3:2 by mass and the solids loading (mass of powder/[mass of solvent + mass of powder]) was 0.33 unless otherwise stated. Both a single component system for the YSZ electrolyte and multi-component systems for the anode and cathode are detailed. Particular attention was paid to the homogeneity of the powders in multi-component systems and how the particle packing efficiency changes with milling times, ie particle size.

3.2.3.1 YSZ (Pi-Kem Ltd) only

Figure 3.9 shows that whilst all the dispersion agents investigated decreased the settled volume, only triton Q-44 showed good dispersion properties for YSZ. A good quantity of dispersing agent for 10g of YSZ is between 0.10g and 0.12g, as these quantities of triton Q-44 gave the lowest settled height after 2wks and the highest height of fine particles after 24hrs. It was noted that too high a concentration of Triton Q-44, in excess of 1.5g, whilst maintaining a low settled volume after long time periods of 2wks, had detrimental effects to its dispersing ability shown by the reduced volume after only 24hrs.

In the case of the Menhaden fish oil, one settling test was performed with a large quantity of the dispersing agent (0.53g Menhaden fish oil for 10.00g YSZ) to clarify whether this was a good dispersion agent for YSZ, but weaker in contrast to the Triton Q-44, thereby requiring higher concentrations. The general trend of the settled heights with this dispersing agent was as expected^[1] ie the settled volume

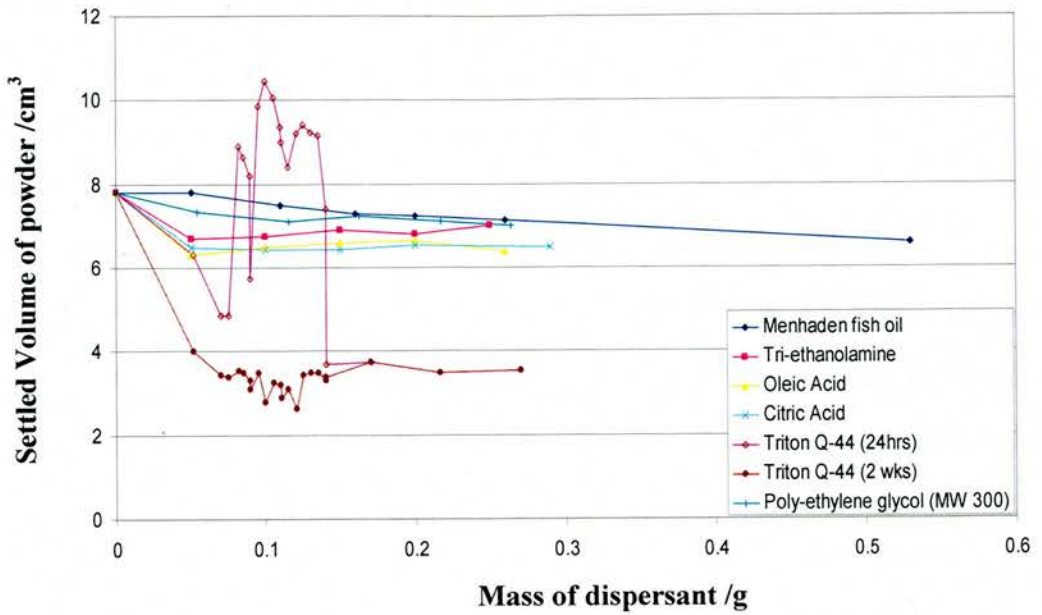


Figure 3.9: Graph showing settling behaviour of YSZ (Pi-Kem Ltd) with varying quantities of various dispersing agents. Difference in settled volumes after 24hrs and 2wks was negligible unless shown otherwise.

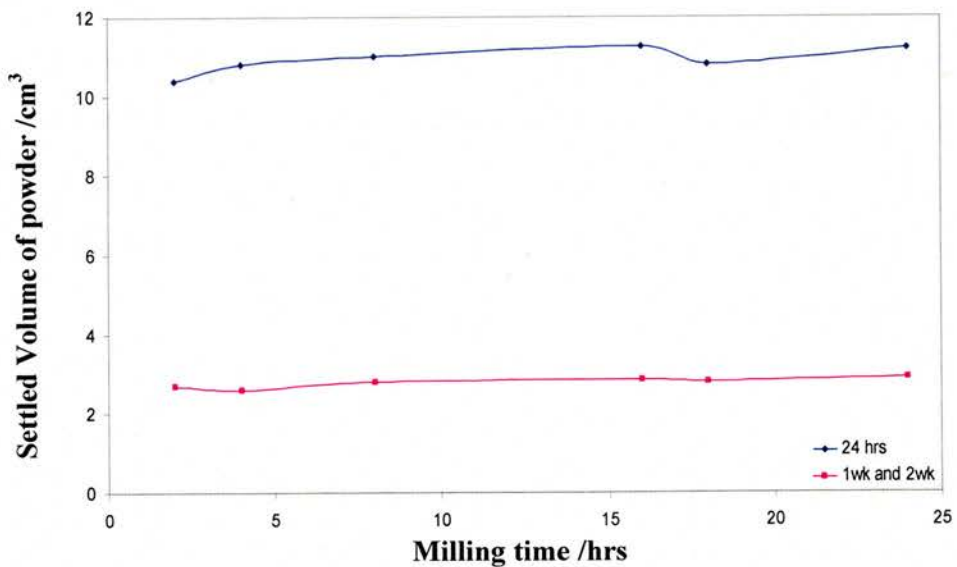


Figure 3.10: Graph showing settling behaviour of YSZ (Pi-Kem Ltd) with 0.1g triton Q-44 per 10g YSZ, at varying milling times.

decreased with increased dispersing agent concentrations, however, clearly the dispersing ability was inferior to that of the triton Q-44 for use with this YSZ.

Whilst the dispersion tests were performed by milling for 4hrs, the dispersion milling stage for tape casting is performed for 18hrs during slurry production, and so in order to check whether the dispersion is affected by milling times, settling tests were performed on 0.1g Triton Q-44 per 10g YSZ (Pi-Kem Ltd) for varying milling times. Figure 3.10 shows that the settled heights for YSZ (Pi-Kem Ltd) are unaffected by the milling times.

3.2.3.2 YSZ (Pi-Kem Ltd) and graphite grade 615 (Griffin & George Ltd)

Dispersion tests were undertaken for a mixture of graphite and YSZ in a ratio of 1:1 by volume (5g YSZ and 1.6393g graphite) at a solids loading of 0.25. Only triton Q-44 was investigated as a dispersion agent as previous analysis has shown this to be the only satisfactory dispersing agent for YSZ (Pi-Kem Ltd). Figure 3.11 shows the initial settling tests performed with a milling time of 4hrs gave an inhomogeneous mixture at low dispersant concentrations, with the fine YSZ particles being held in suspension after 24hrs, and the majority of the graphite particles all settling. The bottom layer clearly has more YSZ content than the next layer up, due to its lighter colour. This could either be due to the turbulence of the large graphite particles falling immediately to the bottom of the vial dragging some of the YSZ particles and smaller graphite particles with it^[8], or that due to the higher density of YSZ relative to the graphite. However, the powders were dispersed to a certain extent as shown by the decrease in settled height of the powder with the addition of the dispersing agent.

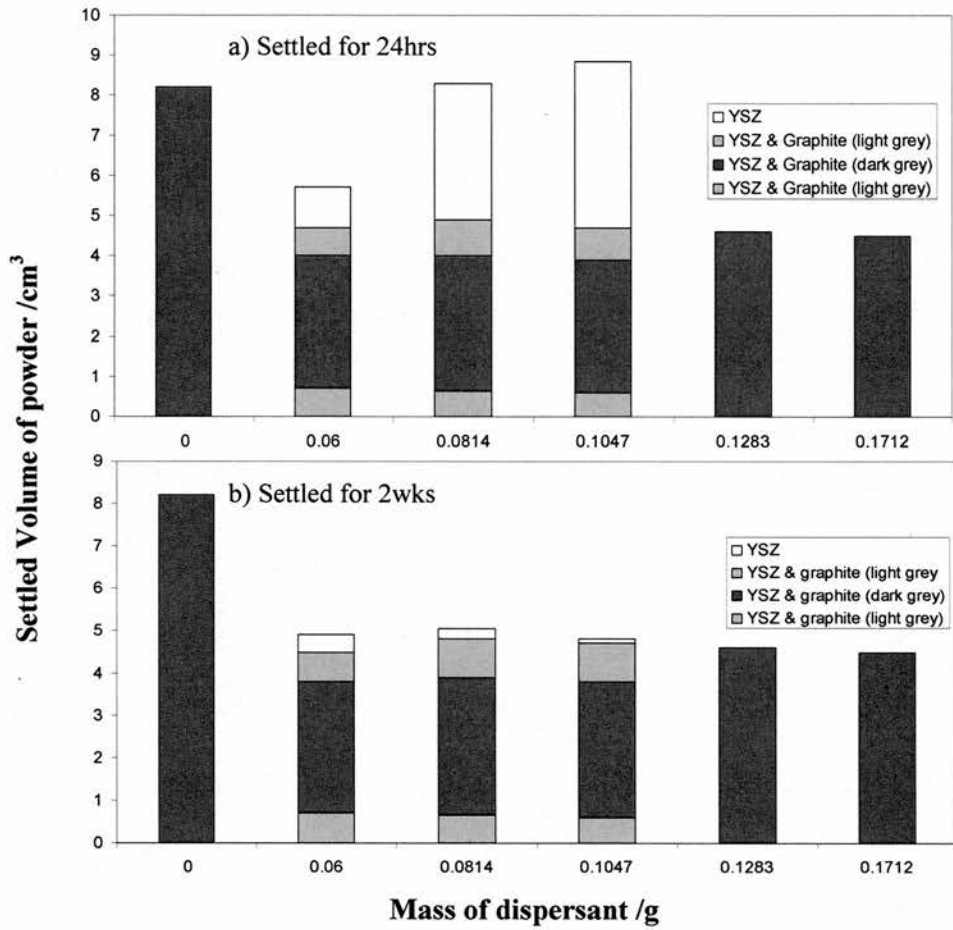


Figure 3.11: Graph showing settling behaviour of YSZ and graphite in 1:1 volume ratio with varying quantities of triton Q-44 (4hr milling)

The purpose of the graphite is to act as a pore-former in the subsequent tapes produced and so a densely packed system is not as critical as for that of the electrolyte, which must be gas-tight after sintering. Therefore, the high settled height of these powders in comparison to when only YSZ is used (see section 3.2.3.1) could be beneficial. A higher concentration of YSZ on the bottom layer could actually be advantageous in electrodes: leading to graded tapes with a higher YSZ concentration on the bottom (part in contact with electrolyte) and a higher porosity on the top (aiding in gas flow – of particular importance in the SOFCRoll design, detailed in section 1.6). However, a higher concentration of YSZ on the top side is undesirable as this would hinder gas flow and be detrimental to forming electrical contacts in the fuel cell. The results obtained in figure 3.11 suggest that any grading of the settled powder results in higher YSZ concentrations at both the top and bottom of the settled powder, and so a quantity of at least 0.13g triton (for 5g YSZ and 1.6393g graphite) would be required in order to achieve good homogeneity of powders.

In a similar manner to that used in the YSZ only system, the dispersion tests were repeated for different milling times to ensure that the information obtained from figure 3.11 could be directly related to tape production when longer milling times were used, the results obtained are shown in figures 3.12 – 3.13. As shown in section 3.2.2, figure 3.8, the graphite particle size is reduced when ball milled together with YSZ, hardly surprising as the small hard YSZ particles will be grinding the large, soft graphite particles during ball milling (much more efficiently in fact, than the zirconia milling media, due to their smaller size). This also affects the packing ability of the YSZ/graphite mixture as seen by the settled height of the powder when no dispersing agent is used (figure 3.12). Increased milling times increases the settled height of the powders by 4cm^3 from 4hrs to 24hrs and by a further 1.7cm^3 from 24hrs to 72hrs,

showing that a plateau would be reached as the graphite particle size is reduced to a minimum under these ball milling conditions.

Figure 3.13 shows that whilst 0.06g triton dispersing agent was an unsuitable concentration for dispersing the YSZ/graphite mixture at milling times of 4hrs (figure 3.11), when milled at 18hrs and longer, this quantity of dispersing agent gives the desirable settling behaviour of achieving a layer of higher YSZ concentration at the bottom when settling. In addition, the higher settled height when milling for 18hrs should give a more porous tape (due to the poorly packed powders). One point to note from figure 3.13 would be that the settled height of the high YSZ concentration layer at the bottom increases with settling time, whilst the total height of the powders remains the same. This would suggest that the dispersing agent is keeping some YSZ particles in suspension after 24hrs, which are able to settle to the bottom with time, presumably through a porous network of graphite particles whilst the graphite particles are not in suspension, but merely loosely packed quickly falling out of suspension.

Repeating the dispersion tests with milling times of 18hrs, eliminated any high concentration YSZ layers on the top of the settled powder mixture regardless of dispersant concentration, as shown in figure 3.14. Dispersion quantities between 0.03g and 0.09g resulted in a layer with a high concentration of YSZ at the bottom of the settled powders, whilst quantities of 0.12g and higher eliminated it.

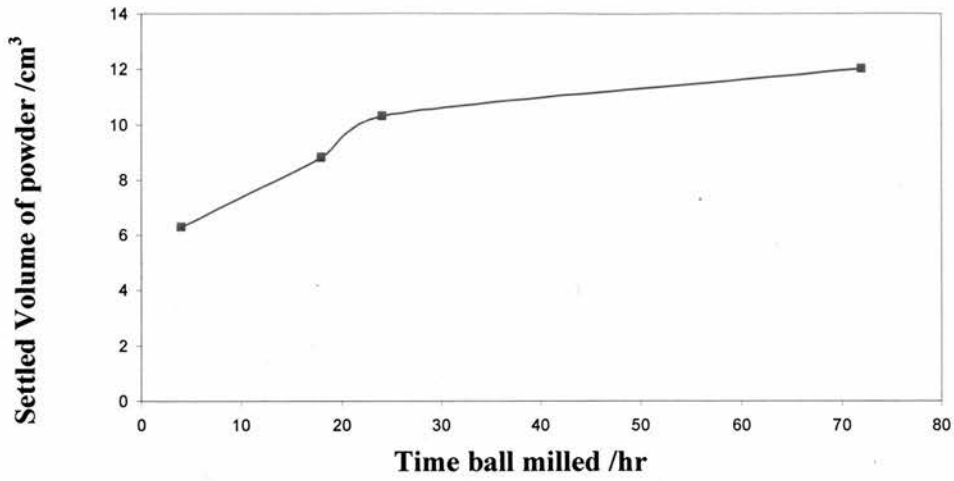


Figure 3.12: Graph showing settling behaviour of YSZ and graphite in 1:1 volume ratio after ball milling for varying times (no dispersing agent used)

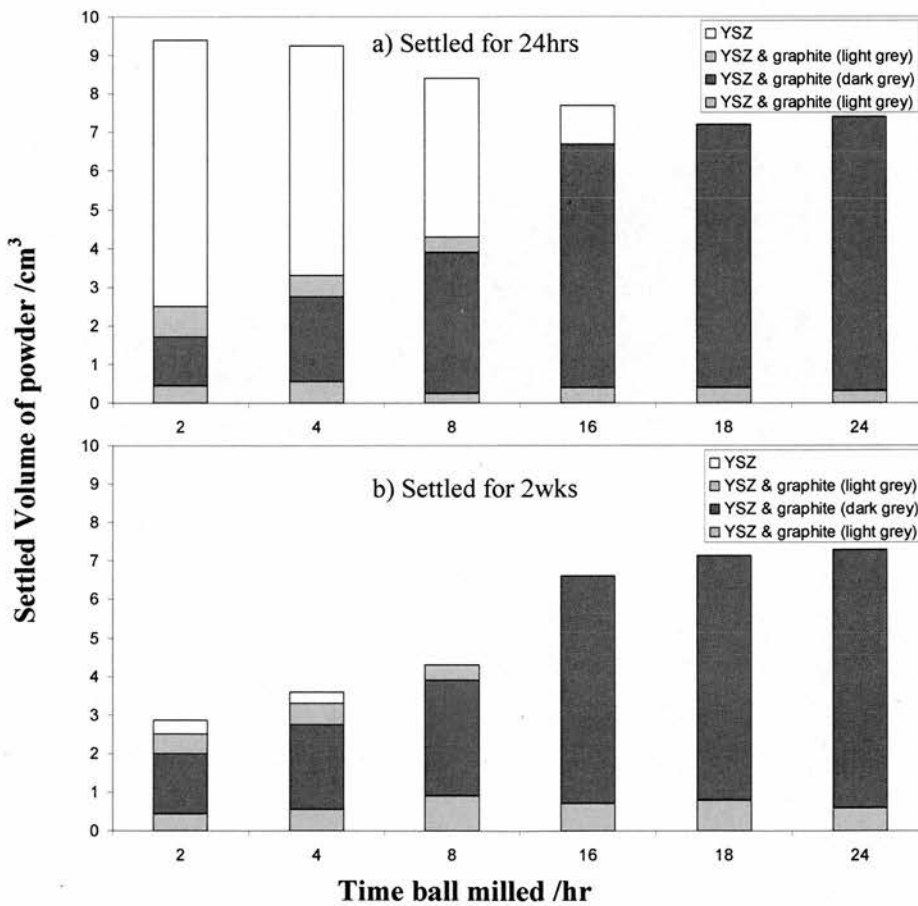


Figure 3.13: Graph showing settling behaviour of YSZ and graphite in 1:1 volume ratio after ball milling for varying times (0.06g triton Q-44)

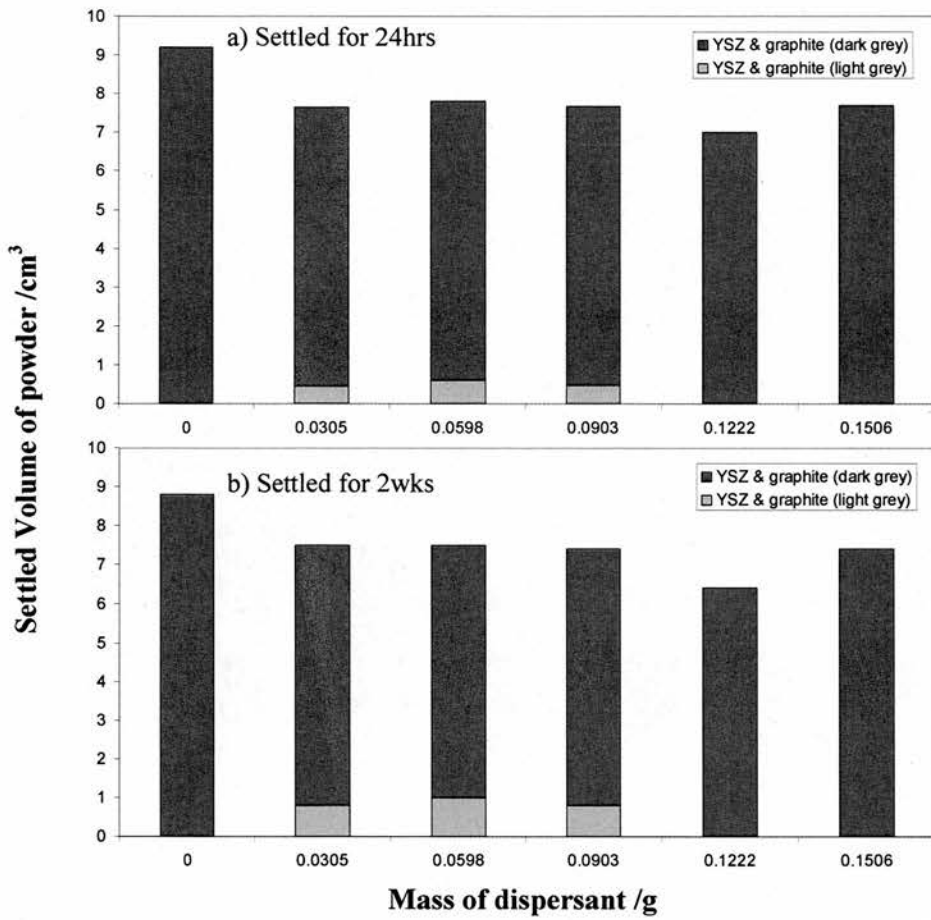


Figure 3.14: Graph showing settling behaviour of YSZ and graphite in 1:1 volume ratio with varying quantities of triton Q-44 (18hr milling)

3.2.3.3 NiO, YSZ (Pi-Kem Ltd) and graphite -325mesh

Initial dispersion tests for the anode were performed on a mixture of NiO and YSZ in the ratio of 55:45 (by mass), which equates to a Ni:YSZ ratio of 40:60 (by volume) when the NiO is fully reduced to Ni in the fuel cell. The solids loading used in the dispersion tests was 0.29, with NiO and YSZ masses of 4.53g and 3.66g respectively. Dispersion tests of NiO, YSZ and the graphite pore former were performed with a solids loading of 0.30 with NiO, YSZ and graphite masses of 3.629g, 2.932g and 2.049g respectively. Dispersion tests concerning the graphite pore former, 18hr milling times were used.

Figure 3.15 shows results similar to that obtained with the YSZ and graphite mixture: the use of triton Q-44 dispersing agent leads to improved packing of powders, shown by the lower settled height of powder and a low dispersing agent concentration, results in layering of settled powders, with the higher density NiO at the bottom. A desirable quantity of dispersing agent would be 0.1g (for 3.66g YSZ, 4.53g NiO), as this gives a homogeneous mixture of the two powders.

Figure 3.16 shows that the settled height of the powders increases slightly with increasing milling times – suggesting that the particle size of the NiO is reduced with milling (as the graphite, see section 3.2.3.2). The increase in settled height was much smaller than that observed with graphite, mainly due to the fact that the graphite particle size was much larger than the NiO prior to milling. A colour change was noticed – the green of NiO looking murkier after long milling times. This is most likely due to a small degree of oxidation of NiO and could be another reason for the increased settling height of the powders with increased milling times.

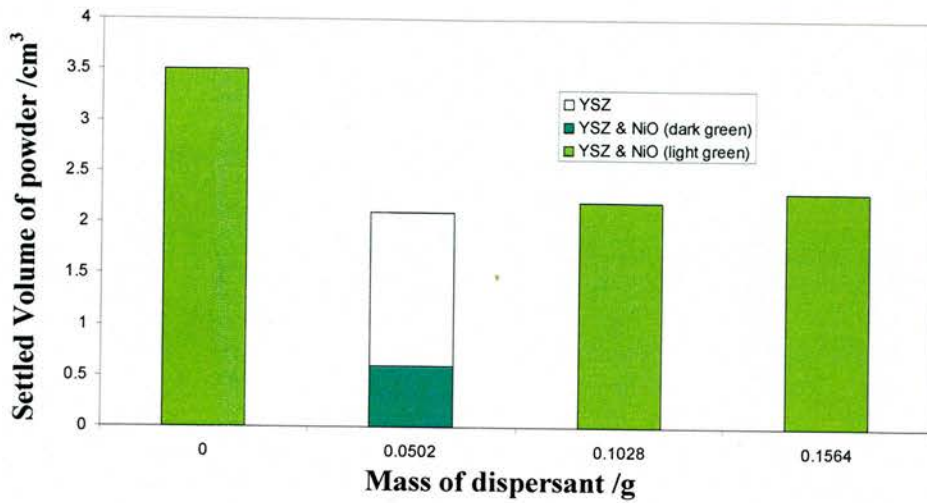


Figure 3.15: Graph showing settling behaviour of NiO and YSZ in 55:45 weight ratio with varying quantities of triton Q-44 (4hr milling)

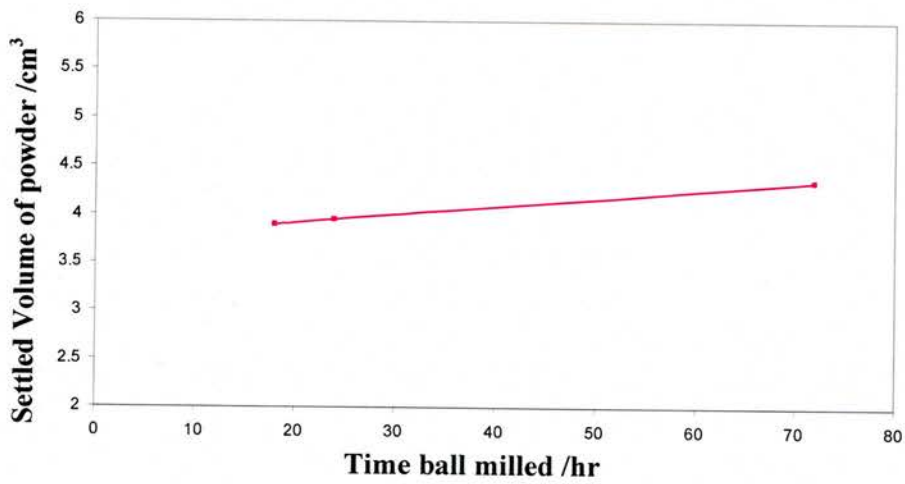


Figure 3.16: Graph showing settling behaviour of NiO and YSZ in 55:45 weight ratio after ball milling for varying times (no dispersing agent used)

Addition of the graphite pore former to the mixture resulted in an increase in settled volume as expected due to packing efficiency and lower density of the graphite particles, (see section 3.2.3.2), but also because the solids loading was increased from 29% to 30%. The solids loading of the YSZ and graphite mixture described in section 3.2.3.2 was 33.3% and the settled volume was much smaller than that seen with the mixture of NiO, YSZ and graphite. Since the settled volume of the NiO and YSZ (in the absence of graphite) was lower than that of the YSZ only (section 3.2.3.1), the higher settled height was attributed mainly due to the use of the different graphite powder used in the two tests.

The triton Q-44 dispersing agent did not have the effect of reducing the settled volume; in fact if anything, a slight increase was noted with increased dispersing agent quantities. There was no visible layering of different powders regardless of quantity of dispersing agent used. The slight increase in settled height with increased dispersing agent could possibly increase the porosity of any tape produced, however it seems likely that the use of triton Q-44 as a dispersing agent will have little if any effect on the microstructure of resulting tapes.

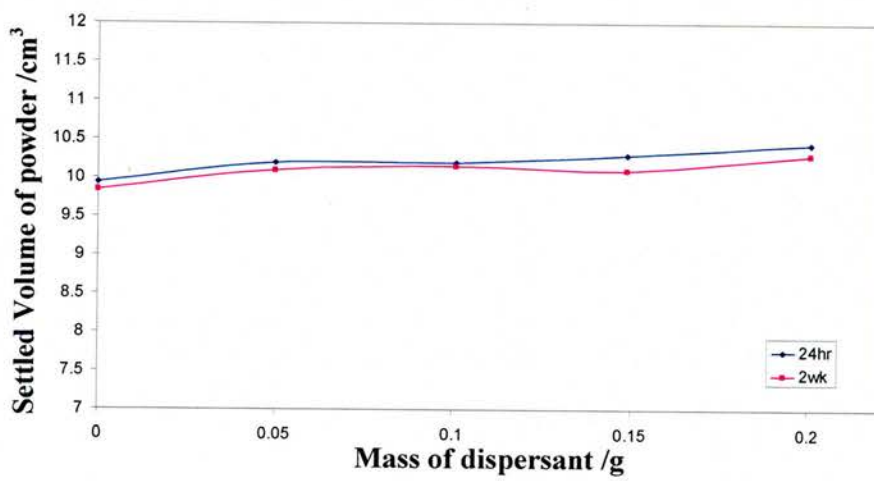


Figure 3.17: Graph showing settling behaviour of NiO, YSZ and graphite -325 with varying quantities of triton Q-44 (18hr milling)

3.2.3.4 LSM (Pi-Kem Ltd, 5% A-site deficient Nextech Ltd), YSZ (2 μ m Unitec Ltd) and graphite -325mesh

Dispersion tests were initially performed on stoichiometric LSM with graphite as used for the cathode current collector layer (see section 3.6). The solids loading was 0.26 with LSM and graphite masses of 5.0g and 2.2g respectively and the milling time used was 18hrs. In all cases in the presence of the triton Q-44 dispersing agent, the LSM particles were held well in suspension after short periods of time (figure 3.18a) whereas the graphite settled almost immediately, as seen when milling for 18hrs with YSZ and graphite in figure 3.13. After 2wks the majority of these LSM particles settled without giving a separate layer on top (as far as could be seen by the naked eye) in contrast to the YSZ/graphite system with short milling times (section 3.2.3.2, figure 3.13). At dispersion contents of 0.1g and 0.15g, a reasonable quantity of the fine LSM particles had settled, but the solvent layer remained a murky almost brown colour, suggesting that some fine particles were still suspended as observed in well dispersed systems^[9].

In contrast with the YSZ/graphite system, after 24hrs there was no evidence of LSM particles settling to the bottom (figure 3.18a), whereas after prolonged periods of time (2wks), clear layers of high LSM content were seen at the bottom of the vials (figure 3.18b). This can be explained as with the YSZ/graphite system, where the graphite particles pack together loosely to form a porous network due to the graphite particle size and shape and some of the ceramic particles (which are much smaller in size) then fall through the pores leading to layering of the settled powders. The height of this layer peaks at 0.15g dispersing agent, suggesting that increasing the quantity of dispersing agent, or in combination with the PVB binder (a known dispersing agent^[11]) would eliminate this layer.

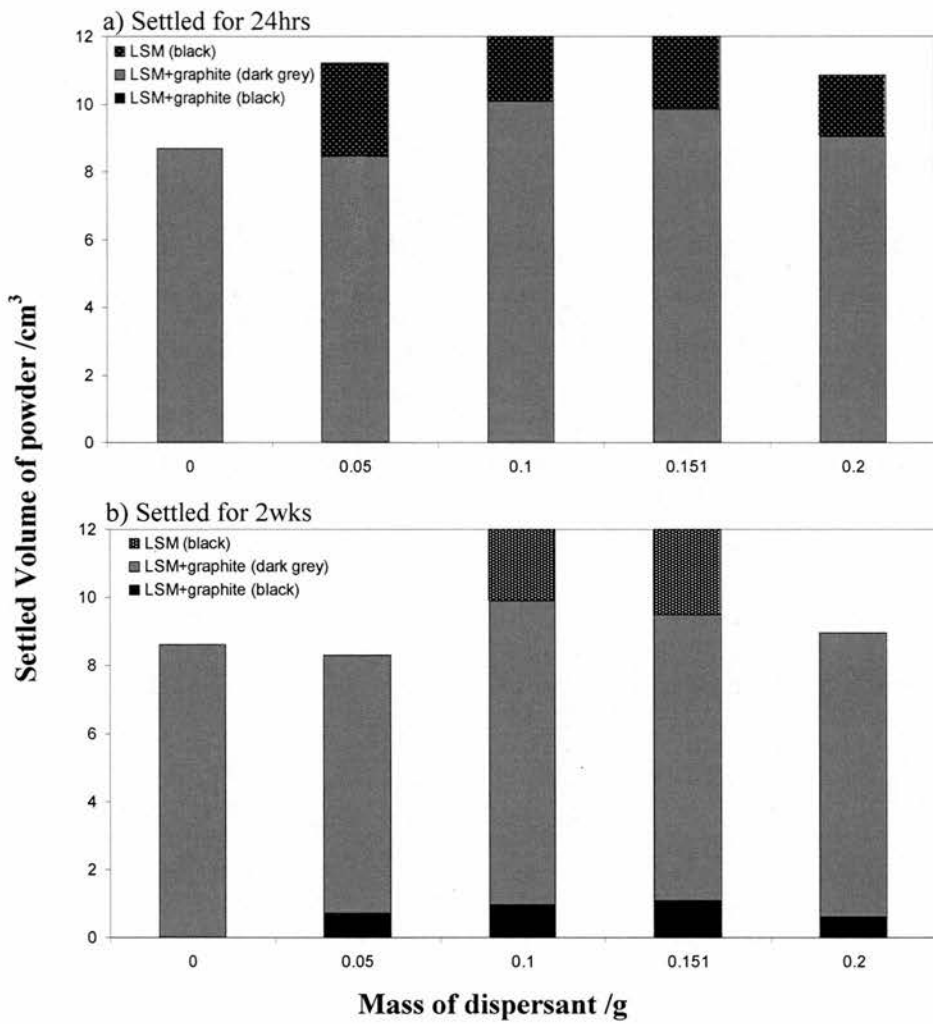


Figure 3.18: Graph showing settling behaviour of stoichiometric LSM20 and graphite -325 with varying quantities of triton Q-44 (18hr milling)

Dispersion tests were performed on a LSM/YSZ/graphite system, using the $(\text{La}_{0.8}\text{Sr}_{0.2})_{0.95}\text{MnO}_3$ (Nextech Materials Ltd, 5% A-site deficiency) and $2\mu\text{m}$ YSZ (Unitec Ceramics Ltd) in a 1:1 ratio (by mass), as this combination gave a cathode with a reasonable shrinkage profile match with the electrolyte whilst forming no pyrochlore (see section 3.6). In this case the solids loading was 0.26 with LSM, YSZ and graphite masses of 2.5g, 2.5g and 2.2g respectively and only 18hr milling times were used. The trends seen in the LSM/graphite and YSZ/graphite system are also seen in the LSM/YSZ/graphite system. Figure 3.19 shows a suspension of fine LSM particles with triton contents of 0.1g and higher, which although fewer in number (assumed by the increased transparency) remain after long settling times of 2wks. Again some YSZ particles fall to the bottom of the suspension causing layers in the settled powders. The maximum height of the YSZ rich layer in the settled powder was obtained at a dispersion content of 0.15g (as with the YSZ/graphite system and the LSM in the LSM/graphite system). Again the settled volume of this layer increased with time, which was again attributed to loosely packed graphite particles, resulting in a porous network, which the smaller ceramic particles pass through, settling to the bottom.

Figure 3.19 shows the settled YSZ layer at the bottom of the vials as effectively two layers, the bottom being white and the top being a light grey. The interface between these two layers was not horizontal, however in some instances the white part of the layer was clearly seen on one side of the vial, whereas on the opposite side, only the grey part was visible. This meant that separation of this layer allowing quantification of the two layer system was not feasible.

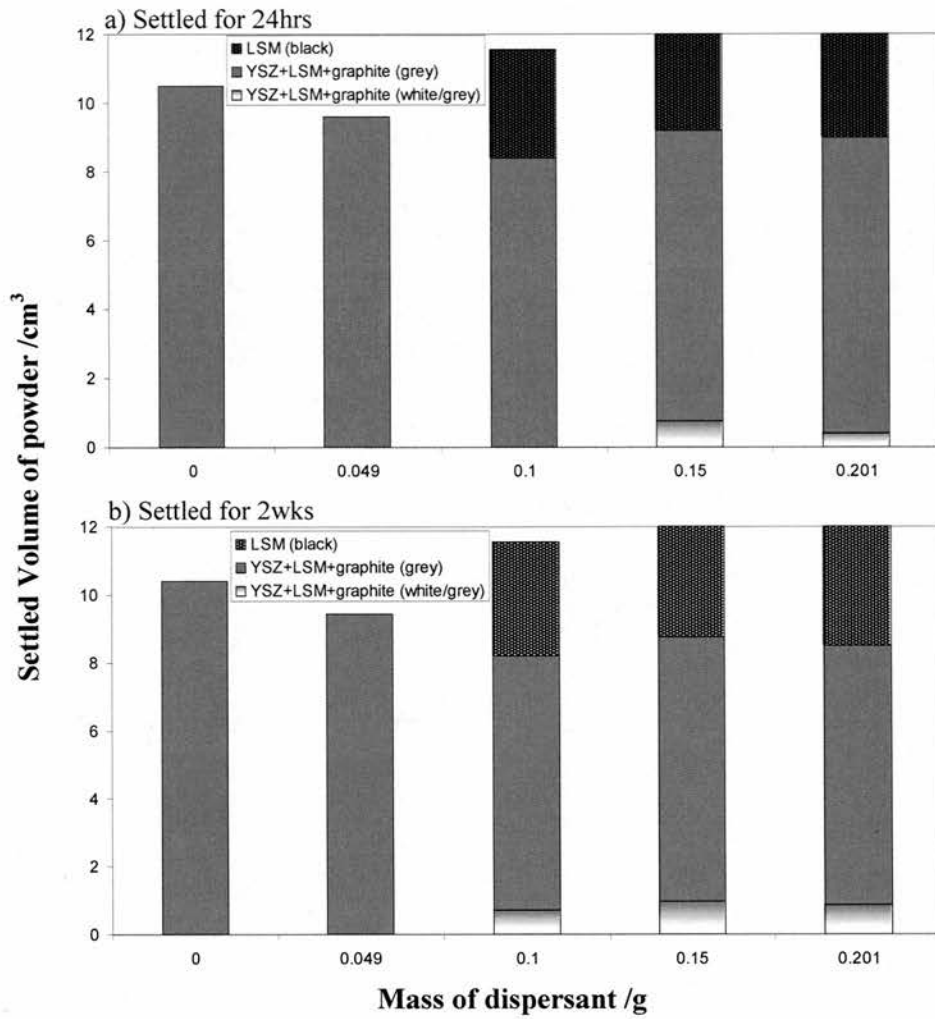


Figure 3.19: Graph showing settling behaviour of LSM, YSZ and graphite -325 with varying quantities of triton Q-44 (18hr milling)

These results suggest that in order to obtain a homogeneous mixture of the powders, the dispersing agent should not be used for the LSM/graphite mixture and at the most 0.05g/5g ceramic weight for the LSM/YSZ/graphite mixture. This however does not take into consideration the dispersion properties of the binder, which could change the settled nature of the powders to that seen with higher dispersion concentration, and so dispersion quantities of in excess of 0.2g would be required.

For the LSM/YSZ/graphite system, having a YSZ rich layer at one end is not necessarily a bad thing for this cathode. It would aid adhesion between the cathode and electrolyte layer when sintering^[10] and the light grey layer would add to the functionally graded nature of the cathode which has been shown to reduce the polarisation resistance^[11]. However, having a LSM only layer at the top would only be beneficial if it retained adequate porosity to allow good gas transport to the bulk of this cathode.

The high content LSM layer in the LSM/graphite system gives no real advantage to the fuel cell system. It would presumably have a lower porosity and hence higher conductivity, but would impede gas transport to the remainder of the cathode and as a result increase gas transport resistance through the spirals of the SOFCRoll geometry.

3.2.4 Dispersion Properties of the Binder

It is important to note that the dispersion of particles can be affected by the solids loading^[9] (as described in section 2.4.2). The solids loading (mass of powder/[mass of powder + mass of solvent]) increases from ~0.3 to ~0.6 in settling tests to tape production respectively. Additionally, of particular importance for this investigation, is the fact that the binder PVB used in the slips/slurries has known dispersing properties and has been used by other researchers as the dispersing agent in the initial dispersion milling step^[1, 12]. This will affect the final dispersion of the particles in the slurry, the viscosity, and the sintered microstructure. The following sections investigate the effect of the binder on microstructure and slurry viscosity.

3.2.4.1 Microstructure

A good example of how the binder has dispersion properties would be the final microstructure of one of the Ni/YSZ anodes (no graphite in the green tape). Referring back to section 3.2.3.3, when no dispersing agent was used, a homogeneous mixture would be expected from the settling tests shown in figure 3.15. Micrographs of the cross-section of two sintered and reduced 4-layer laminate anodes (approximately 2.5 layers are shown) with no triton Q-44 and differing binder content in the green tape are shown in figure 3.20. The micrograph of the anode produced from a lower binder concentration has one cast tape thickness marked in figure 3.20a, showing the anode is clearly graded from high YSZ content (left hand side of marked layer) to high Ni content (right hand side of the marked layer). This type of layering was seen with 0.05g dispersing agent for the settling tests (see section 3.2.3.3, figure 3.15). The layering was also evident from the green tape, which was visibly whiter in colour on

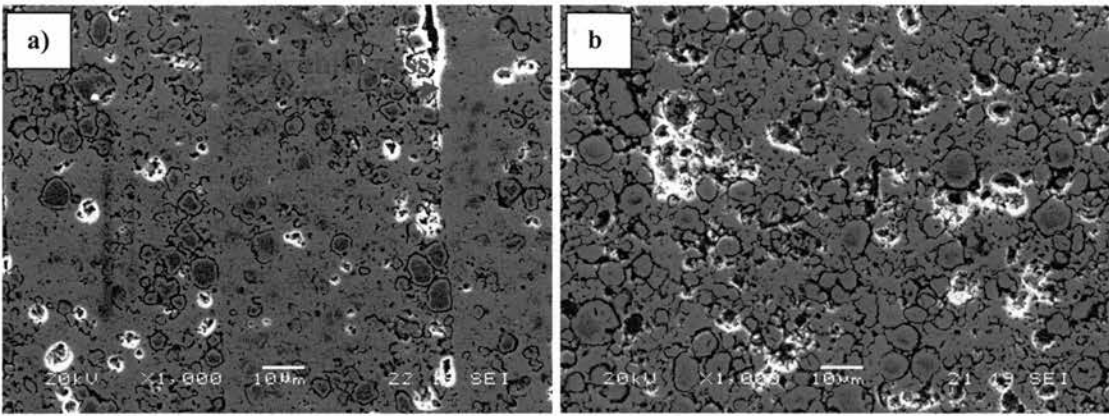


Figure 3.20: SEM images of reduced anodes produced from NiO and YSZ, in the absence of Triton Q-44, with a) 3.54wt% binder in slip, b) 5.09wt% binder in slip.

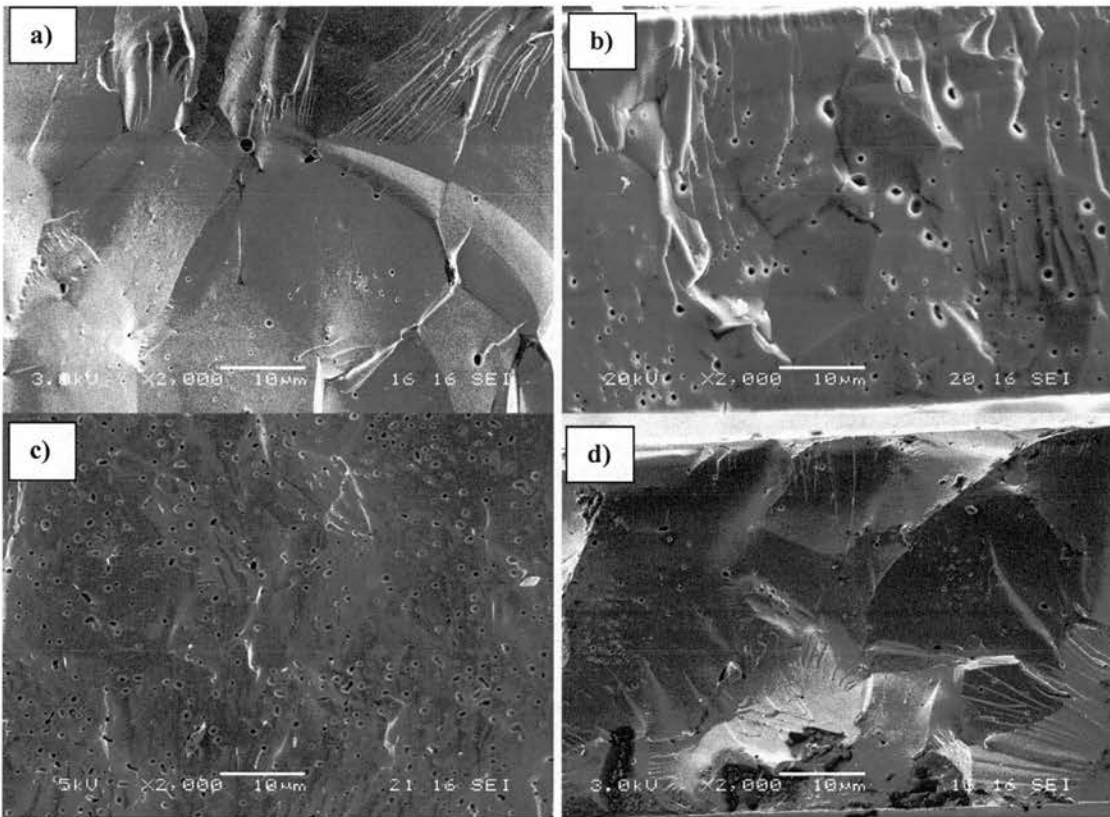


Figure 3.21: SEM images of films produced with a) 0g, b) 0.065g c) 0.10g and d) 0.15g triton Q-44 dispersing agent per 10g YSZ. Sintering temperature 1500°C.

the top surface and greener in colour on the surface in contact with the Mylar® carrier. Increasing the binder content and hence increasing the dispersion of the binder whilst keeping the solids loading constant resulted in a homogeneous mixture, where the area of lamination of the tapes was not visible, as shown in figure 3.20b.

With the above result in mind, different batches of YSZ slurry were produced with varying quantities of triton Q-44 dispersing agent. The batch size used for this investigation was 30g YSZ, but the triton Q-44 content is quoted per 10g YSZ for comparison to the settling tests performed at low solids loading (section 3.2.3.1). The triton Q-44 dispersing agent quantities used were: 0.15g (showed low settled volume after 24hrs), 0.1g (resulted in good dispersion characteristics), 0.065g (also gave good dispersion characteristics, but resulted in a smaller settled volume after 24hrs, and larger settled volume after 2wks), and 0g (resulted in very high settled volumes irrespective of the time left to settle).

Figure 3.21 shows that the quantity of dispersing agent in the green tape visibly affects the microstructure of the fired tapes. Interestingly, the ‘optimum’ dispersing agent quantity (obtained from dispersion tests in section 3.2.3.1) did not give the densest tapes, which could be attributed either to the dispersion of the YSZ differing at the high solids loading used in tape production, or alternatively to the dispersing ability of the binder. Generally speaking, at dispersion quantities of 0.1g and above, the tape had more pores, of a smaller size, whereas at dispersion quantities of 0.065g and below, the tape was slightly denser, with an increased pore size. Whilst the microstructure was affected by the quantity of dispersing agent, the variation in measured density was small: $\pm 3\%$ and the final shrinkage was unaffected.

3.2.4.2 Slurry viscosities

The four different YSZ slurries produced in section 3.2.4.1 were tested for their change in viscosities. Whilst the batch sizes used for this investigation was 30g YSZ, the triton Q-44 content is quoted per 10g YSZ for comparison to the settling tests performed at low solids loading (section 3.2.3.1). If the binder does act as a dispersing agent, it would be expected that the viscosities of the slurries with no dispersion would be much lower than the settling tests would suggest. From the microstructures obtained (figure 3.21), it would be expected that the viscosities would increase with increasing triton Q-44 dispersing agent.

Time independent rheology tests performed on the YSZ slurry (see section 2.4.2 for details) at different dispersing agent concentrations showed that as the shear rate increased, the shear stress increased and apparent viscosities decreased, as expected for all non-Newtonian suspensions. Due to the small batch sizes used in this investigation, the small sample holder adapter was used in the viscometer (see section 2.4.2), which limited the maximum shear rate to 30rpm for no dispersion and 0.065g triton Q-44, to 20rpm for 0.1g triton Q-44 and to 10rpm for 0.15g triton Q-44 (per 10g YSZ). It is therefore difficult to ascertain the shape of the curves shown in figure 3.22 to determine whether they are yield-pseudoplastic or yield-dilatant.

What is evident from figure 3.22 however is that as the concentration of triton Q-44 increases, the viscosity also increases as predicted from the resulting microstructures (section 3.4.2.1, figure 3.21). The apparent viscosity of the slurry with 0.15g triton Q-44 was much higher as expected from the settling tests due to low settled volume after just 24hrs (section 3.2.3.1). The apparent viscosities of slurries produced with 0g and 0.065g triton Q-44 were within the 500cP error deemed

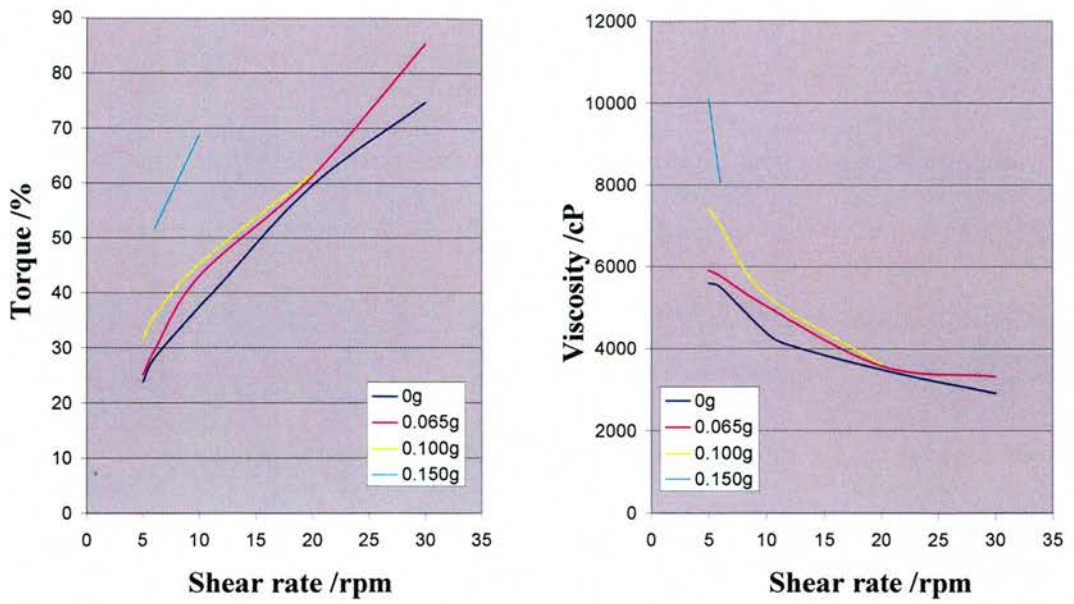


Figure 3.22: Graphs show changes in shear stress (torque) and apparent viscosities with applied shear rate for YSZ slurries with differing dispersing agent concentrations. Each data point taken after shear was applied for 20seconds.

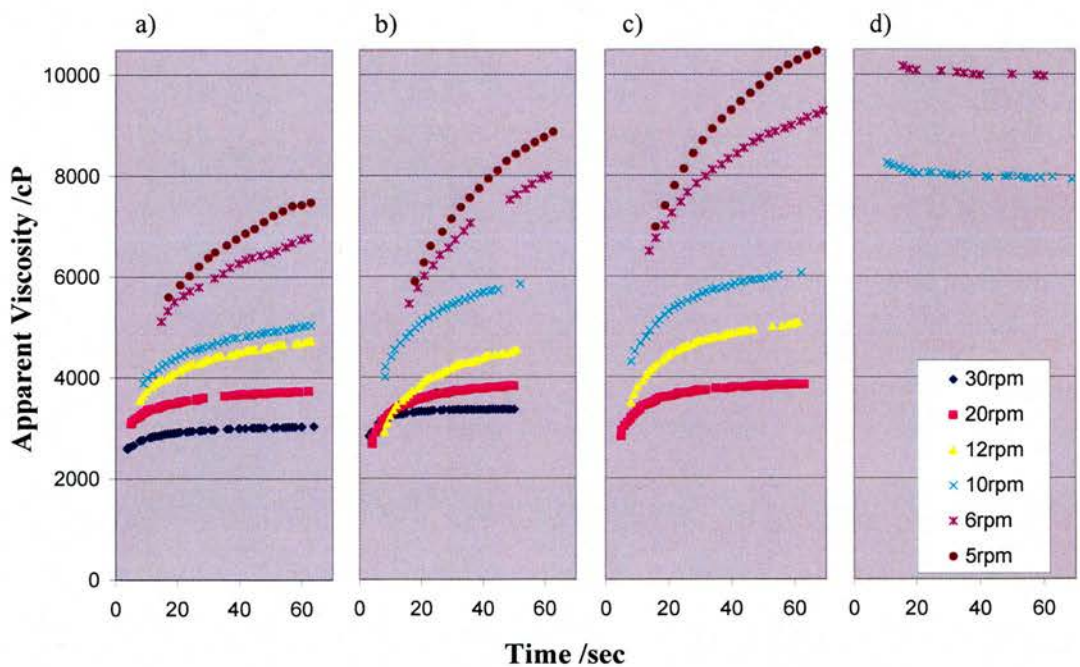


Figure 3.23: Graph showing change in viscosity with time at varying shear rates with a) 0g, b) 0.065g, c) 0.1g and d) 0.15g Triton Q-44 per 10g YSZ.

acceptable from batch to batch for tape casting^[12], and so the YSZ is clearly being dispersed by the PVB binder. The slurry produced with 0.1g triton Q-44 reached 1000cP higher at low shear rates showing the YSZ was more poorly dispersed than with lower triton Q-44 concentrations. This shows that the dispersion of the PVB binder has resulted in an effective increase in dispersion concentration, resulting in this case in a more poorly dispersed system.

The general shape of the time dependent rheology curves shown in figure 3.23 show rheopexy behaviour (suggesting dilatant suspensions) for dispersion contents of 0.1g and below, and thixotropy behaviour (suggesting pseudoplastic suspensions) for a dispersion content of 0.15g. However, the apparent viscosities for all slurries increase with decreasing shear rate, as expected with floc formation (slower shear rate results in fewer flocs being broken down, increasing the viscosities) suggesting all slurries are pseudoplastic in nature.

Initially it was thought that the increase in apparent viscosity with time was a result of solvent evaporation resulting in a skin forming at the top of the sample, increasing torque and hence apparent viscosities, however, this can't be the case as high dispersing agent concentration resulted in a decrease in apparent viscosities. It was thought therefore to be a combination of viscosity, floc formation, the nature of slurry mixing in the ball mill and the slow shear rates used. The slurry was mixed in the absence of the milling media on the ball mill at 6rpm for de-airing prior to each 2cm³ sample being taken for the viscosity measurement. The diameter of the ball mill (5cm) is much larger than that of the small sample adapter of the viscometer (1.3cm). When the slurry is mixed in the ball mill, it sticks to the inner walls, and dependent on its viscosity is either in motion due to gravity constantly coating the inner walls, or is not moving at all, stuck to inner walls. If the apparent viscosity is low, and the slurry

is in constant motion, the flocs will constantly be being broken up until the equilibrium is set for that speed, ie the slurry is under shear. If the apparent viscosity is high enough for the slurry not to move in the ball mill at the slow de-airing speed, in the absence of any milling media, the flocs will not be broken up.

Using the above hypothesis and applying it to the time dependent data (figure 3.23) suggests that for dispersing agent contents of 0.1g and less, the shear rate applied to the slurry in the ball mill was greater than that of the viscometer, and for a dispersing agent content of 0.15g the opposite is true. So due to the lower apparent viscosities of the slurries with 0.1g of dispersing agent and below, the slurry was constantly moving in the de-airing stage of ball milling; after being transferred to the viscometer, the effective shear rate decreased, which resulted in formation of flocs and so increased apparent viscosity with time until the equilibrium of floc formation/destruction is established. This also explains why at lower shears, the apparent viscosity takes a longer time to reach a constant value. For the slurry with 0.15g of dispersing agent, the apparent viscosity is higher and so during the de-airing step, the force of gravity is not sufficient to cause the slurry to constantly coat the ball mill. This is reflected in the much higher shear force required when the shear rate of 10rpm was applied in the viscometer, shown in figure 3.24. When the slurry was transferred to the viscometer, the shear force on the slurry was higher, resulting in the slurry having a greater applied shear rate than when in the ball mill and so resulted in floc break up and decrease in apparent viscosities with time.

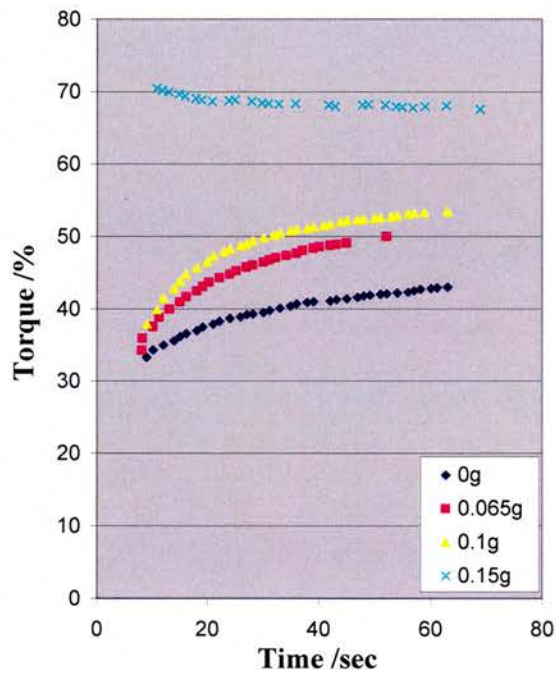


Figure 3.24: Graph showing time dependent behaviour of slurries with varying dispersion agent concentrations at shear rate of 10rpm

3.2.5 Summary

3.2.5.1 Single component slurry

The triton Q-44 dispersing agent was found to be the most effective of all investigated for the YSZ (Pi-Kem Ltd) powder. It was the only dispersing agent able to keep the fine particles in suspension after 24hrs, and gave greatly reduced settled volumes after 2wks. Triton Q-44 concentrations in excess of 0.15g/10g YSZ prevented the suspension of particles after 24hrs, although still resulted in low settled volumes after 2wks. The detrimental effect on the dispersion of YSZ with high concentrations of triton Q-44 was also noted with the resulting slurry viscosities: the apparent viscosities of slurries containing 0.15g triton Q-44 per 10g YSZ being much higher than slurries of lower triton Q-44 content at the same solids loading.

The PVB binder was demonstrated to possess dispersion properties, with slurries produced with this binder but containing no separate dispersing agent giving similar apparent viscosities to slurries with low (0.065g per 10g YSZ) triton Q-44 concentrations. The lowest apparent viscosities were shown to be for slurries containing no triton Q-44 or 0.065g triton Q-44 per 10g YSZ. The quantity of triton Q-44 shown to be optimum from the settling tests at low solids loading (0.1g per 10g YSZ), had higher apparent viscosities at low shear rates attributed to additional dispersion from the binder.

Time dependent apparent viscosities increased with time for slurries of triton Q-44 contents of 0.1g (per 10g YSZ) and below, whereas with a triton Q-44 content of 0.15g (per 10g YSZ) decreased with time. This was thought to reflect the movement of the slurry in the de-airing stage of ball milling: high apparent viscosities resulted from low slurry agitation during de-airing, reducing the effectiveness of this

stage in removing air bubbles present in the slurry. More vigorous techniques such as ultrasonic agitation would therefore be required for effective de-airing.

3.2.5.2 Multi-component slips

Milling times had little if any effect on the settling volumes of the ceramic materials, but greatly changed the settled volume when a graphite pore former was used, due to the change in particle size. The decrease in graphite particle size was thought to approach a plateau at long milling times (greater than 24hrs), however the increase in settled height between 18hr milling (as used for slip/slurry production) and 24hr milling means that care is needed to ensure consistent milling times are used for reproducible slips.

Settling tests with more than one type of powder showed poor homogeneity of powder mixtures at low dispersion concentrations irrespective of milling times. This effect was not removed at high solids loading. The use of a dispersion agent, either in the form of the triton Q-44 or with increased PVB binder concentrations is therefore essential for formation of homogeneous tapes with the exception of the NiO/YSZ/graphite system.

From information obtained for YSZ only systems, it is likely that the increased content of dispersing agent required for homogeneous distribution of the suspended particles in a slip would result in higher apparent viscosities. The de-airing stage would therefore require a higher energy technique than the slow mixing step such as ultrasonic agitation.

3.3 Electrolyte Sintering

The microstructural criteria of the electrolyte (as detailed in section 1.4.1) is that it be gas tight: >94% with no open pores. Additional requirements for the electrolyte in the SOFCRoll are that it be sintered to achieve this density at as low a temperature as possible to prevent reactions between the YSZ electrolyte and LSM cathode during co-firing (section 1.4.3). This section focuses on the production of dense films – the reaction between YSZ electrolyte and LSM cathode is detailed later in section 3.6.1.

3.3.1 Sintering temperatures on microstructure

Once a good formulation for the YSZ slurry was achieved, the effect of sintering temperature on density was investigated. Figure 3.25 shows that sintering YSZ at 1200°C for 5hrs (the maximum sintering temperature when considering prevention of reaction between YSZ and LSM^[14]) does not produce dense films. The YSZ particles have begun to sinter together, but the result is a highly porous network. Sintering temperatures of 1300°C, 1400°C and 1500°C for 5hrs do however produce films of >94% as shown in figure 3.26a-c. It is worth noting that when fired as a laminate with anode and cathode in the SOFCRoll geometry, this density was improved as seen in figure 3.26d. As described in section 1.4, the manganese ions originating from the LSM cathode^[14-15] and NiO originating from the anode^[16] dissolve into the YSZ electrolyte at processing temperatures, stabilising the cubic structure^[16-17]. The presence of these composition gradients at the electrolyte-electrode interfaces have the effect of increasing the diffusional fluxes resulting in the improved electrolyte densities seen when co-firing the electrolyte and electrode laminates^[18].

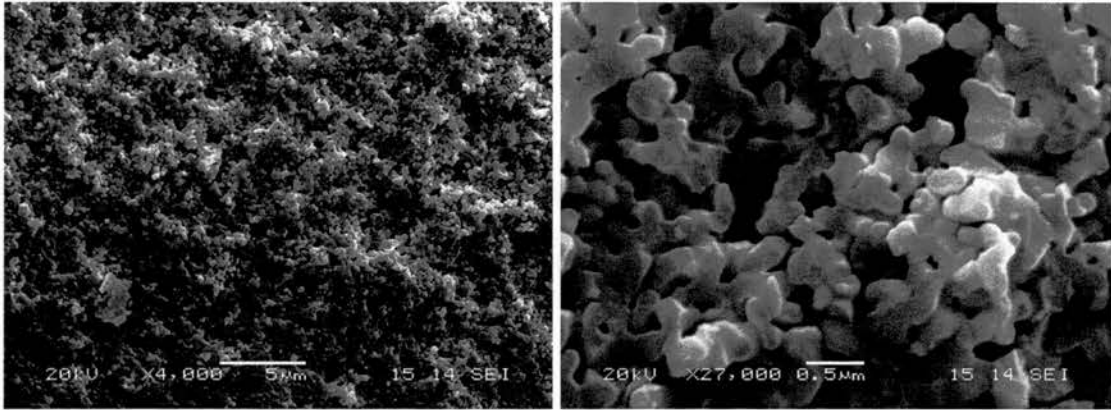


Figure 3.25: SEM images of YSZ film when sintered at 1200°C for 5hrs

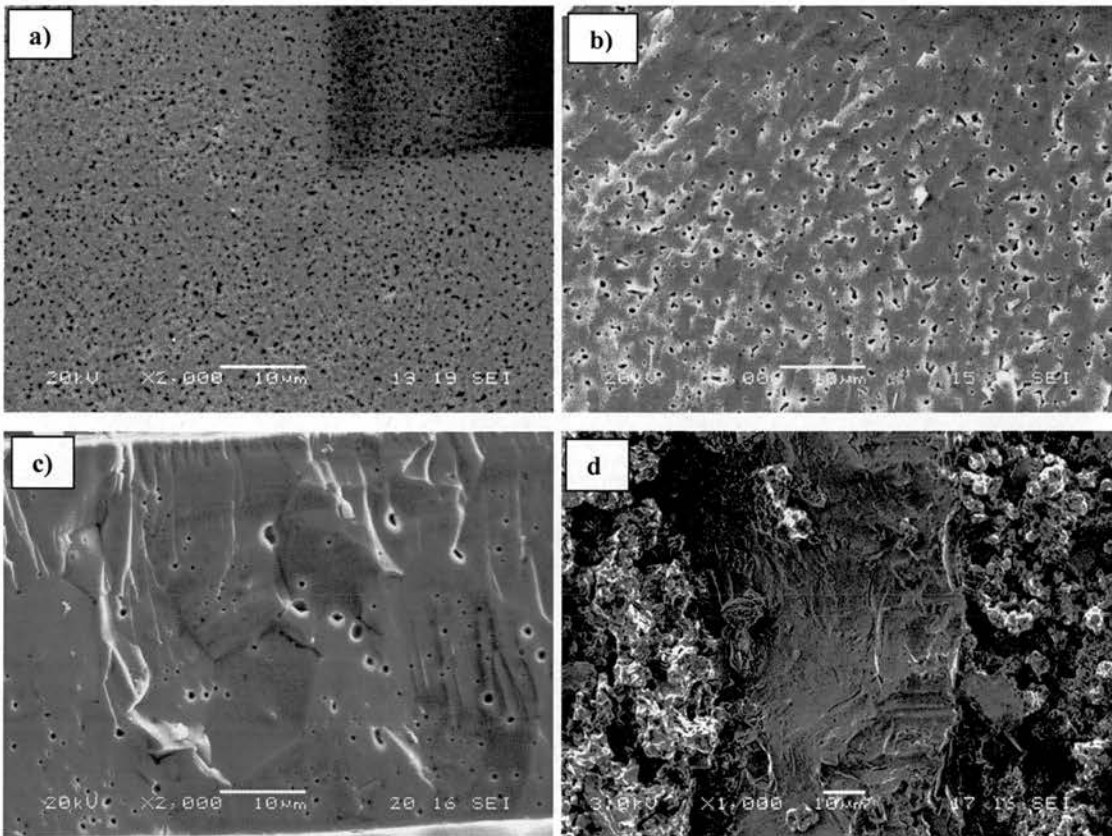


Figure 3.26: SEM images of YSZ films when sintered for 5hrs at a) 1300°C, b) 1400°C c) 1500°C and d) 1300°C in a laminate of LSM-YSZ-Ni/YSZ

3.3.2 Sintering times on microstructure

Whilst section 3.3.1 showed 1200°C was not sufficient for production of a dense electrolyte film, when sintering for 5hrs, further tests were performed to see whether prolonged sintering times at lower temperatures, or shorter sintering times at 1300°C followed by longer sintering times at lower temperatures would produce films of adequate density. Figure 3.27 shows that even after 24hrs at 1250°C, the density of the films was not sufficient at a measured value of 87%. Sintering for this length of time at this temperature would however result in pyrochlore between electrolyte and cathode^[19-21]. When an initial sintering temperature of 1300°C for just 2hrs, was used prior to a dwell of only 12hrs at 1200°C, shown in figure 3.28 a poor density of ~83% was obtained. Keeping this initial short time at 1300°C and further increasing the dwell time at 1200°C to 24hrs gives a much denser film, whilst a dwell of 72hrs at 1200°C gives a similar microstructure to that of a 5hr dwell at 1300°C (figures 3.28 and 3.26). The measured densities of these films were 83%, 88% and 95% with a dwell at 1200°C of 12hrs, 24hrs and 72hrs respectively.

It is therefore possible to produce an adequate density electrolyte with only 2hrs sintering above 1200°C (temperature above which the pyrochlore is reported to form^[14]). However, using such a long sintering time for SOFCRoll production, whilst it is just as cheap to produce A-site deficient LSM material as to produce stoichiometric LSM would lead to unnecessary increases in fuel cell production costs. Additionally, whilst the quantity of pyrochlore may be reduced, it is unlikely to be eliminated as it still relies on sintering at 1300°C albeit for only 2hrs. Therefore modification of the cathode material (detailed in section 3.6.1) to prevent reaction with the electrolyte was investigated and no further experiments were performed on densification of the electrolyte at lower temperatures than 1300°C for 5hrs.

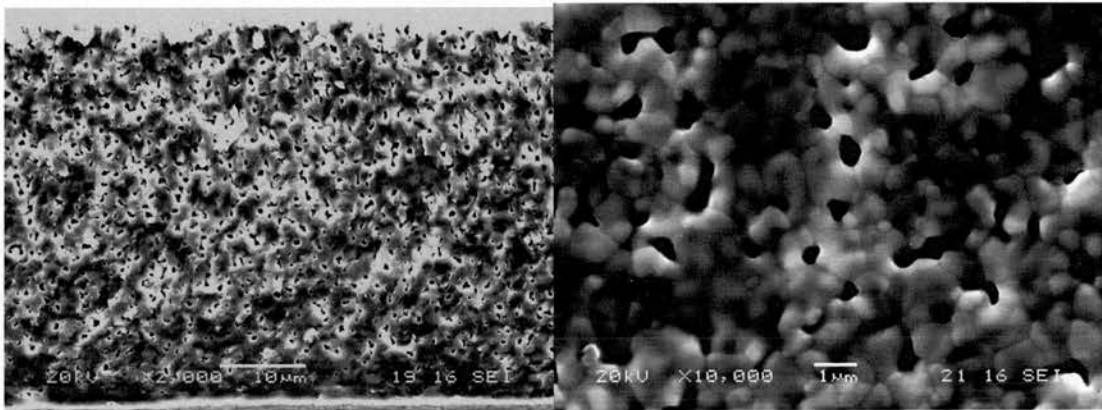


Figure 3.27: SEM images of the cross-section and surface of YSZ films sintered at 1250°C for 24hrs

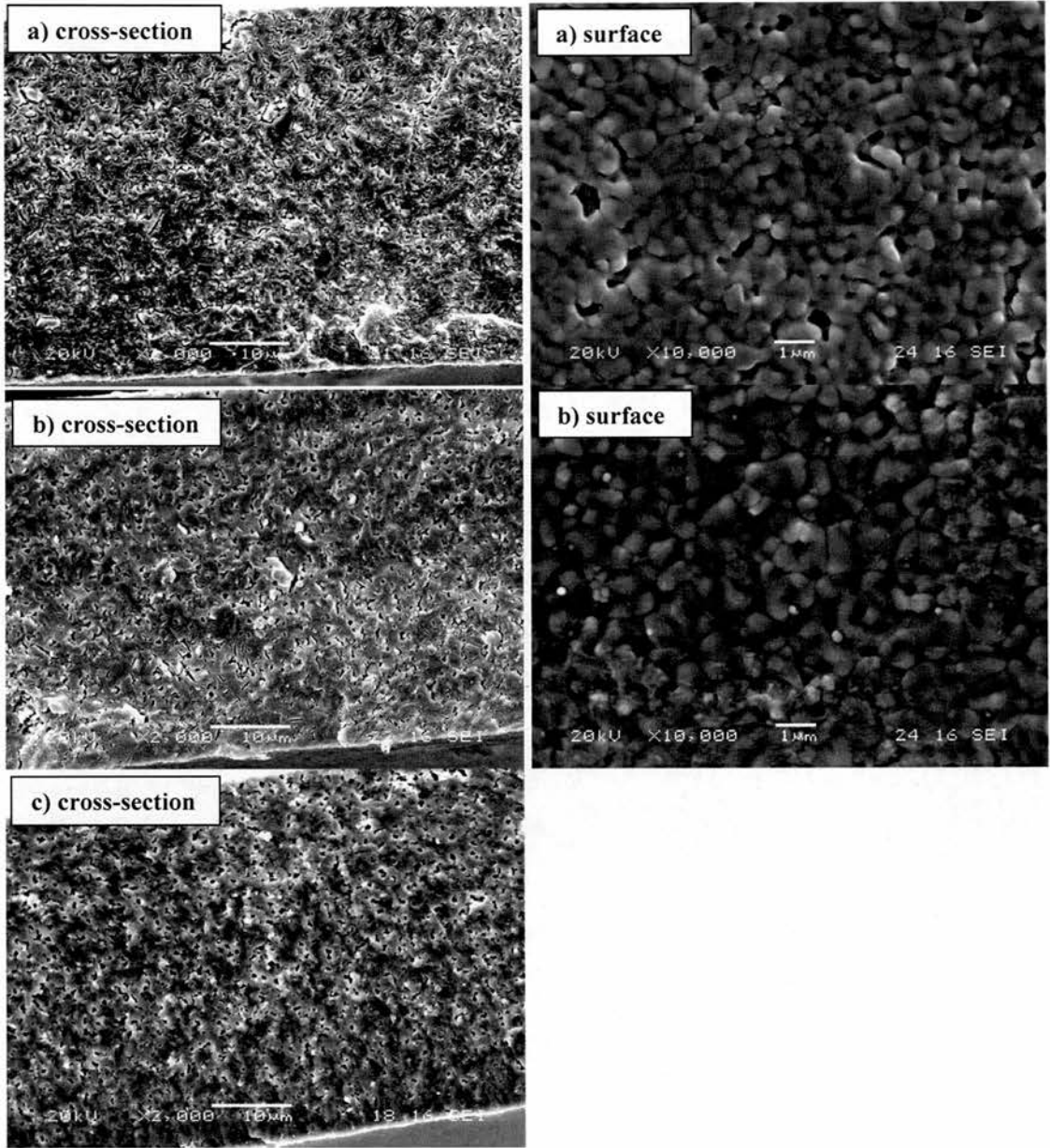


Figure 3.28: SEM images of the cross-section and surface of films fired at 1300°C for 2hrs followed by 1200°C at a) 12hrs, b) 24hrs and c) 72hrs

3.3.3 Shrinkage Profile

The electrolyte shrinkage profile measured by the two different methods described in section 2.6 is shown in figure 3.29. When comparing the two profiles, it is important to note that the tape thickness was measured at different temperatures when measured with the dilatometer and so is a combination of shrinkage and thermal expansion as opposed to the rectangle method where each data point is measured at room temperature. This is clearly visible when comparing the two traces between temperature ranges of 300°C-1000°C, where the dilatometer data shows the material is expanding and data from the measured rectangle samples shows no change. Direct comparison of the two techniques can therefore only be performed at the final shrinkage and after the sample has been cooled from 1000°C to 100°C in the dilatometer (where the effect of thermal expansion will be at a minimum). The differences between the two methods in final shrinkage and after cooling from 1000°C are approximately 5% and 2% respectively.

Measuring the rectangles was difficult during heating to 900°C due to the extremely fragile nature of the ceramic films and the curling experienced in the tapes – as can be seen by the uneven nature of the shrinkage profile in this temperature range. The rectangles were much more robust after heating to 1000°C for 5hrs however, so the shrinkage at this stage of the heating profile, measured by this technique was thought to be more accurate. The difference between the two measured shrinkages could be due to the difference in real temperature in the furnaces, the curling of the sample in the dilatometer resulting in lower recorded shrinkages, or the fact that the shrinkage of the tape is different when sandwiched between two plates of alumina.

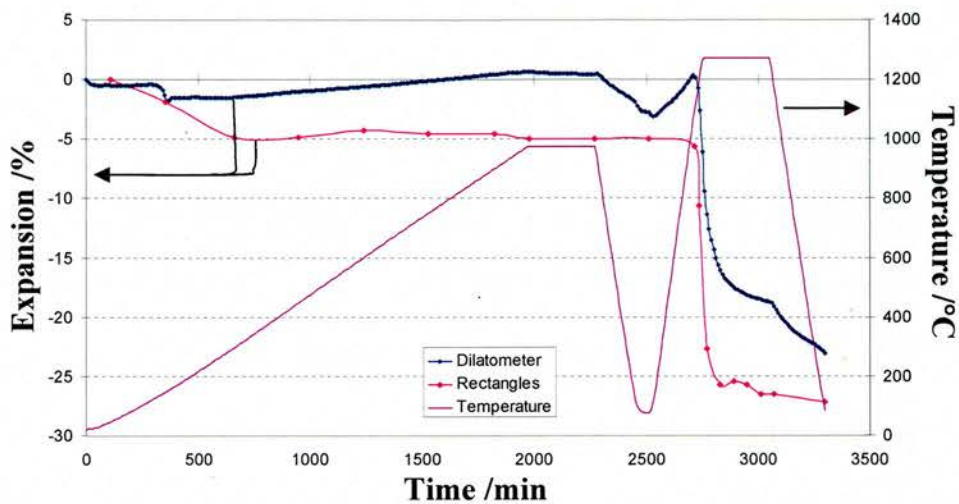


Figure 3.29: Shrinkage profiles of the YSZ electrolyte when sintered at 1300°C obtained by measurement of rectangles and the dilatometer (see section 2.6). The temperature profile shown is that measured by the dilatometer.

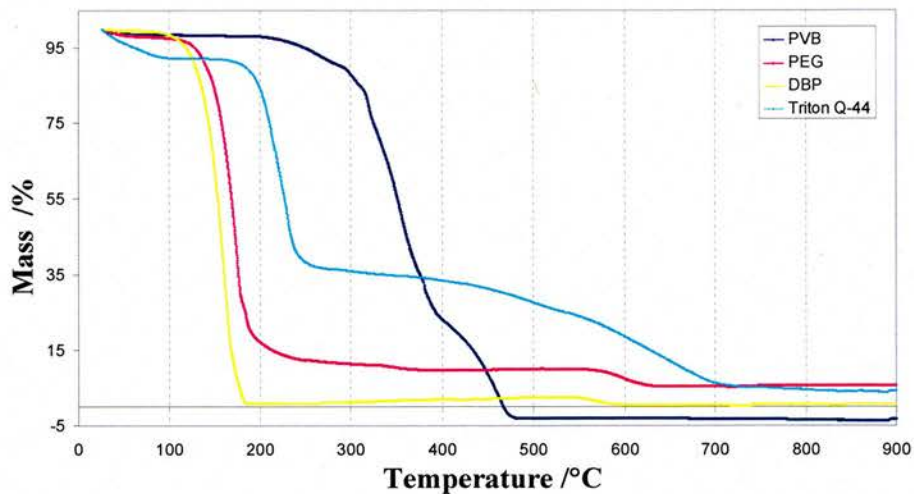


Figure 3.30: Graph showing the mass loss of the organic additives of the electrolyte with temperature.

The difference in temperature is certainly a possibility for the difference in shrinkage – figure 3.29 clearly shows that whilst the dilatometer was programmed to heat to 1000°C and 1300°C, only heated to ~970°C and 1272°C respectively; similarly the true temperature used for rectangle heating is strongly dependent on where the sample is placed in the furnace. The sample is known to curl during heating to 750°C, and flattens between 900°C and 1000°C, as seen with the rectangles. If the sample curled, a lower shrinkage would be measured in the dilatometer (see figure 2.9, section 2.6.2) during heating, followed by larger shrinkage when the sample flattens. There is a small shrinkage seen with the dilatometer during the dwell stage at 1000°C, however this is very small and could also have occurred in the rectangles, but was too small a shrinkage to be measured. It is also possible that the force of the push-rod reduces the curling of the tapes which would therefore alter the way the tape shrinks. Finally with all electrolyte samples analysed with the dilatometer, the final sintered film was cracked in the centre. When sheets of electrolyte were fired in a furnace on an alumina plate, after heating to 1000°C, catastrophic cracking had occurred, resulting in a crazed ceramic sheet. This was believed to be due to the green tape sticking to the alumina plate and not freely contracting in the x-y dimensions (where z is the thickness of the film). It is highly probable this was happening with the electrolyte green tape in the dilatometer and so affecting the measured shrinkage.

Both shrinkage profiles show that the low temperature shrinkage is complete by 300°C, by which temperature (with the exception of the binder), all organic additives have been removed as shown in figure 3.30. This suggests that the binder burn-out has little effect on the shrinkage up to 1000°C. Additionally, both methods

showed similar high temperature shrinkage profiles, the greatest rate of shrinkage seen between 1150°C and 1300°C.

Figure 3.31 shows the difference in final shrinkage when sintering at 1300°C and 1350°C is 1.5%. The majority of this increased shrinkage occurs during the ramp from 1300°C to 1350°C and during the first hour dwelling at sintering temperature. It is clear from this figure that the higher sintering temperature for the electrolyte tape results in denser films, demonstrated by the decreased peak width seen in the first derivative plot.

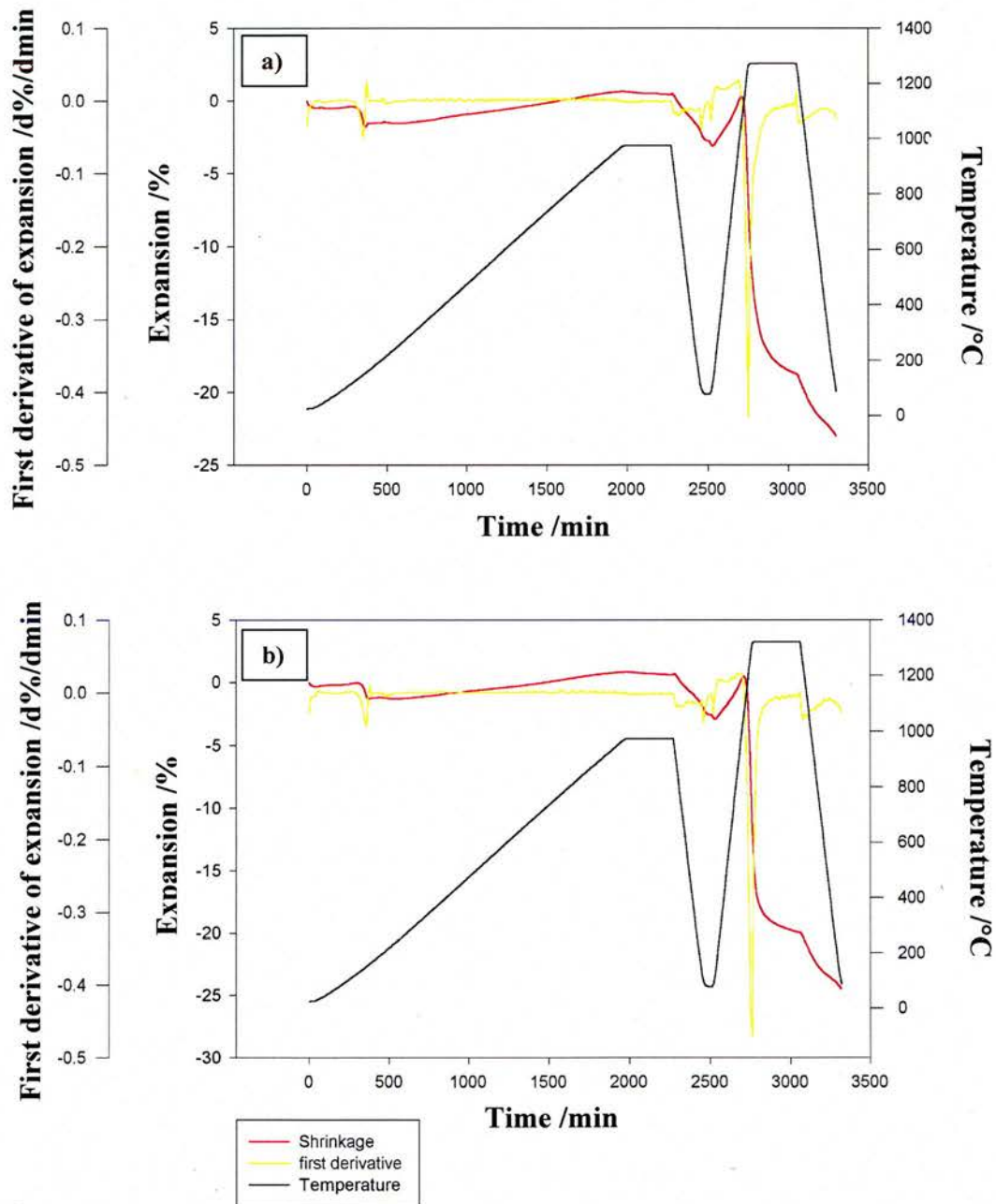


Figure 3.31: Graphs showing the first derivative of the electrolyte expansion measured by the dilatometer during heat treatment to a) 1300°C and b) 1350°C

3.4 Production of Porous films (YSZ)

Methods of introducing porosity to tape cast films were initially investigated using YSZ (Pi-Kem Ltd) only. Where graphite is mentioned, graphite grade 615 (Griffin & George Ltd) was used. The films were heated as the electrolyte, but with a final sintering temperature of 1500°C.

3.4.1 Addition of a pore former

Addition of a pore former was the most effective method for introducing porosity into the fired films. The effect of the graphite concentration on porosity and final shrinkage is shown in figure 3.32. A porosity of 47% (as preferred for SOFCRoll geometry electrodes) was achieved with a ratio of 30:70 YSZ to graphite (by volume). However, in this instance, when a porous-dense-porous system was produced in the SOFCRoll geometry, the sintered structure was under so much strain, it fell apart when touched, due to the 10% difference in final shrinkage of the dense and porous films. The 5% difference in shrinkages occurring with lower graphite contents investigated however seemed to be tolerated, resulting in a strong SOFCRoll geometry system.

3.4.2 Particle size/shape of pore former

The graphite particle shape is that of a flat plate (figure 3.7), their size being reduced by the ball milling process (figure 3.8), whereas the glassy carbon particle is spherical (figure 3.7) and soluble starch is a long chain polymer. Figure 3.33 shows that both the glassy carbon and soluble starch pore formers produce large occluded pores in the fired tapes (undesirable for the electrode of a fuel cell). It is evident from

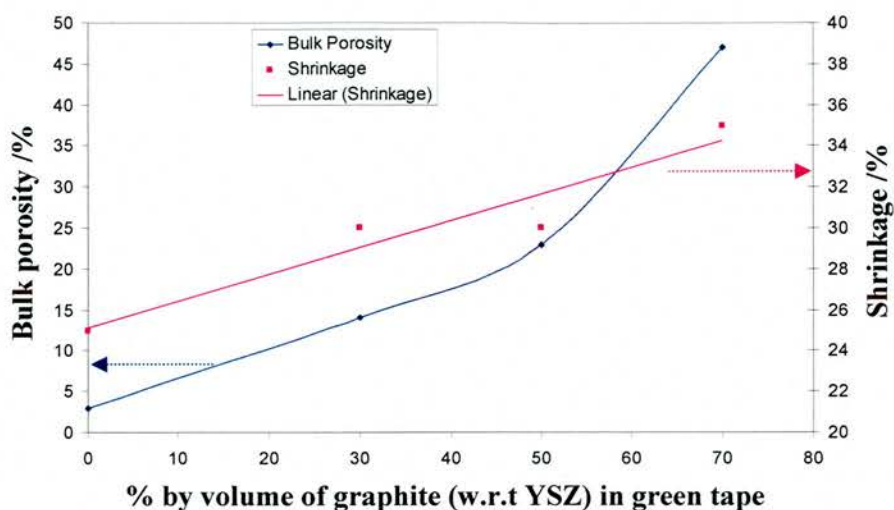


Figure 3.32: Graph showing the effect of graphite concentration on porosity and final shrinkage of fired YSZ sheets. Linear (shrinkage) shows the line of best fit for the shrinkage.

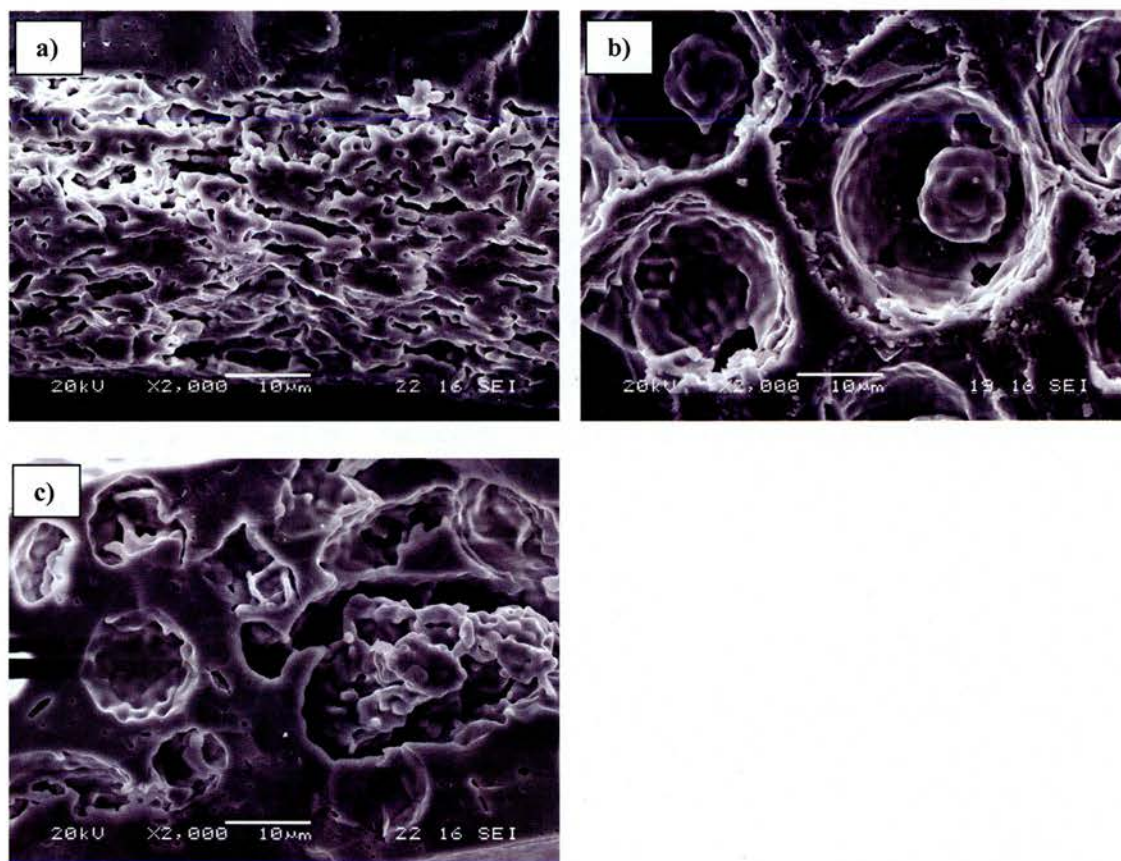


Figure 3.33: SEM images of fired YSZ tapes containing 50vol% a) graphite pore former, b) glassy carbon pore former and c) soluble starch pore former

the images that the starch molecules either 'ball up' causing large pores similar in geometry, but smaller in size, to that of the glassy carbon, or the polymer wraps itself around some YSZ particles, causing the 'loop' pore. The porous network produced from the graphite pore former seen in figure 3.33 is suitable for fuel cell electrodes and further work therefore concentrated on this pore former.

Different ball milling times for the dispersion of the graphite and YSZ particles were investigated, the resulting microstructures shown in figure 3.34. Clearly the porosity of the network was improved with increased milling times. After 4hrs ball milling, the graphite particle size was large and resulted in large pores. It is clear from the SEM image (figure 3.34, 4hr milling) that the graphite particles lay down parallel to the carrier surface during casting of the green tape, which doesn't aid the diffusion of gas from the surface of the fired film. From these images it seems that the best microstructure was obtained when milling for 24hrs.

Measured porosity and final shrinkage respectively of these films were as follows: 18%, 28% (4hrs milling), 23%, 30% (18hrs milling) and 50%, 35% (24hrs milling). This shows that decreasing the graphite particle size increases the shrinkage^[22] and the porosity. Since a 10% difference in final shrinkage between dense and porous layers was shown to put too much strain on the SOFCRoll geometry (section 3.4.1), in this case a sacrifice would have to be made on the porosity in order to preserve strength in multi-layer systems.

3.4.3 Ceramic particle size

A known method of introducing porosity is to increase the particle size of the ceramic thereby reducing the packing efficiency of the particles in the green state^[23].

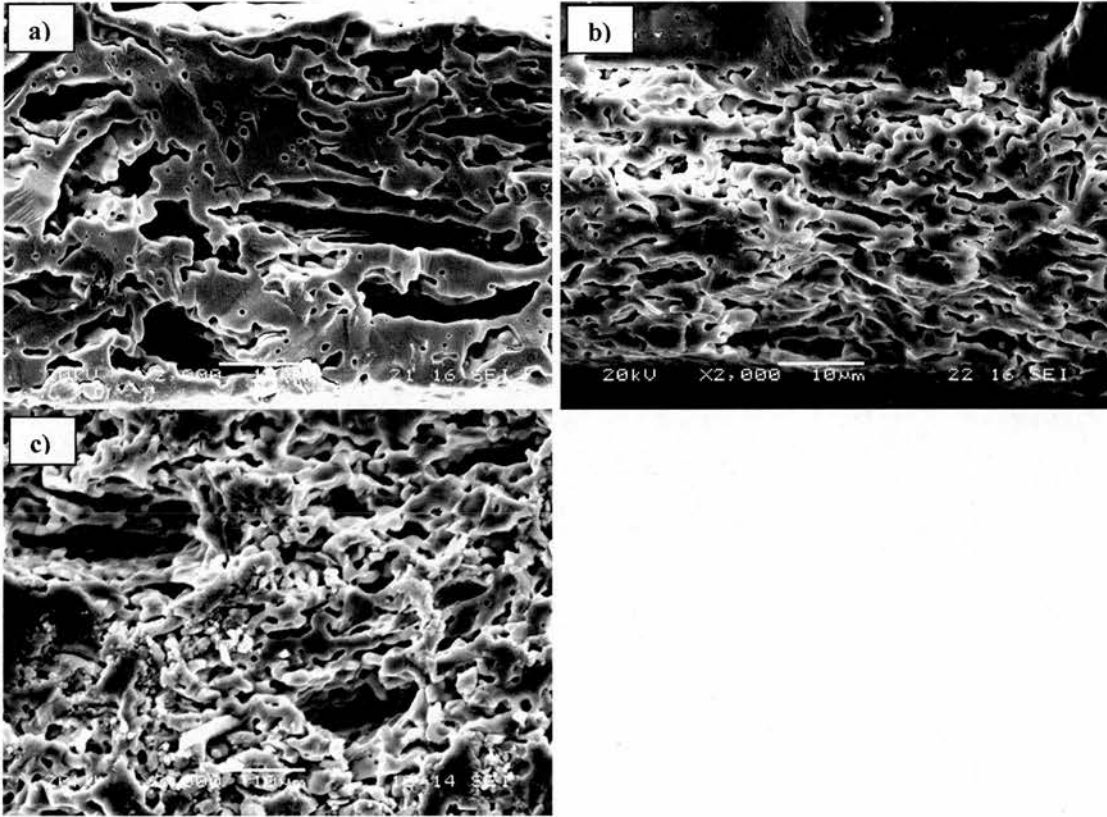


Figure 3.34: SEM images of fired YSZ tapes containing 50vol% graphite pore former with dispersion milling times of a) 4hrs, b) 18hrs and c) 24hrs

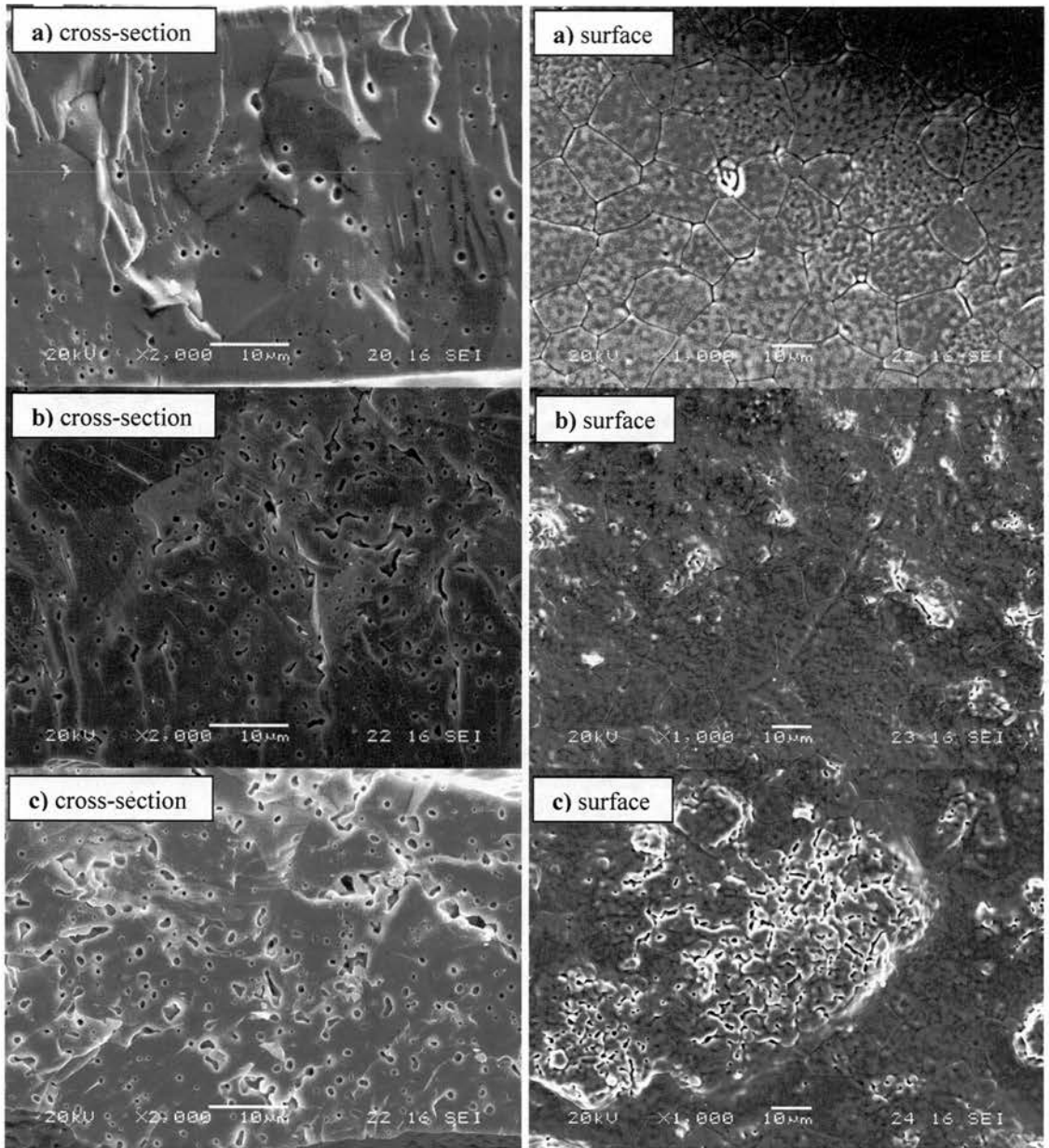


Figure 3.35: SEM images of films produced from a) fine YSZ particles; and 1/3 coarse, 2/3 fine YSZ after b) 18hrs milling before binder addition and c) 0hrs milling before binder addition

A mixture of 2/3 fine and 1/3 coarsened YSZ particles is recommended for use in the anode^[24-26]. YSZ particles were coarsened (as described in section 2.2) which led to a porous agglomerated YSZ particle shown in figure 3.1. Whilst the ball milling of YSZ powder in the as received, pre-coarsened state was thought not to affect the particle size (section 3.2.3.1), it is conceivable that it would affect the sintered agglomerates and therefore tapes were produced both with and without the 18hr dispersion step. Figure 3.35 shows that the use of coarsened YSZ particles clearly increases the porosity: from a measured 3% (all fine YSZ particles), 6% (18hr milling) to 11% (no milling). The 18hr milling decreased the coarsened particle size to a certain extent, leading to larger areas of high density on the surface, seen in figure 3.35. This decrease in particle size would have the affect of decreasing the inter-particle separation (related to surface area of particles and binder/plasticizer concentration detailed in section 3.4.5), therefore reducing porosity. The final shrinkages were as follows: 25% (all fine YSZ particles), 25% (18hr milling), 20% (no milling). This is as expected as the coarsened YSZ had been pre-sintered therefore reducing the further sinterability and therefore the associated shrinkage.

3.4.4 Binder/plasticizer concentration

An increase in the binder and plasticizer concentration increased the porosity of the sintered tapes. A 50% increase in binder content gave a 5% increase in linear shrinkage, regardless of the presence of a pore former or not. However, whilst an increase in porosity was noted with increased binder concentration, the effect was larger in the tapes containing the graphite pore former, 10% compared with only ~2% in the absence of a pore former.

This can be explained by the distribution of the particles in the green tape^[22, 27]. In the absence of any pore former, an increase in binder content will increase the organic material in the green tape, thereby increasing the separation distance of each YSZ particle. During heating of the green tapes, by 600°C the organic additives are completely removed (figure 3.30, section 3.3.3), leaving a porous, fragile ceramic tape. It is at higher temperatures, particularly at sintering temperatures, where the tapes are densified. The similarity in densities obtained therefore can only be achieved by an increase in shrinkage.

In the presence of the pore former, the effects can be explained by difference in total surface area of the particles. The surface area of the YSZ was measured at $7\text{m}^2\text{g}^{-1}$. In a green tape containing 20g of YSZ, the particle surface area is therefore 140m^2 . In a 1:1 (by volume) graphite:YSZ tape, the composition used was 10g YSZ ($\rho=6.1\text{gcm}^{-3}$) and 3.28g graphite ($\rho=2.0\text{gcm}^{-3}$). Assuming the surface area of graphite to be $5\text{m}^2\text{g}^{-1}$ (measured for the pre-milled graphite), the particle surface area in the tape would be only $\sim 86\text{m}^2$. This huge decrease in surface area would further increase the particle separation and hence increase porosity.

3.4.5 Summary

All the methods investigated of introducing porosity have been effective. The high porosity required for the SOFCRoll electrodes has been achieved with 70vol% graphite, 30vol% ceramic or by 50vol% graphite, 50vol% ceramic with a longer ball milling step reducing the graphite particle size.

The final shrinkage of sufficiently porous films differed to too great an extent when compared with the dense film. However, since the various methods of introducing porosity investigated affect the microstructure and shrinkage in different

ways, a combination of different methods could produce the desired microstructure without the shrinkage of porous layers deviating too much from the dense layer. For example, addition of both graphite pore former and coarser ceramics (both of which add porosity), one increasing shrinkage and one decreasing shrinkage.

Finally it should be noted that for co-firing of a fuel cell consisting of NiO/YSZ, YSZ and LSM components, sintering temperatures would need to be lower to prevent reactions between cathode and electrolyte^[14, 19-20]. This lower sintering temperature would reduce the sintering of YSZ, therefore increasing the electrode porosity and so lower pore former concentrations may suffice.

3.5 Anode Production

The anode was produced from NiO and YSZ ceramic materials, the NiO being reduced in situ to form the Ni electro-catalyst. Literature showed the minimum Ni concentration for adequate conductivity to be 40vol% (equating to 55:45 NiO to YSZ by mass) with a porosity of approximately 35%^[14]. This formed the basis of initial research for the anode and this ratio of Ni to YSZ was used unless otherwise stated.

Literature refers to possible associated problems with the use of phosphate ester as a dispersing agent for electronic applications, as it does not burn out cleanly, leaving residual phosphorus: a contributor to dielectric conductivity^[1]. Since the settling tests (section 3.2.3.3) showed a homogeneous distribution of powder regardless of dispersion concentration in the presence of a pore former and section 3.2.4 demonstrated the dispersing ability of the binder, no dispersing agent was used in the production of the tapes. The absence of any dispersing agent during the more vigorous “dispersion milling” stage would also allow some particle agglomerates to remain in the slip, thereby decreasing the green and hence final density.

3.5.1 No pore former

The complete reduction of NiO to Ni results in a decrease in volume by 59% (calculated from their respective densities). This volume reduction introduces porosity into the films and so initial work on the anode concentrated on tape production with no pore former. The dispersion properties of the binder were relied upon to produce homogeneous tapes. Two methods of tape production therefore were investigated: dissolving all organics and then mixing in the powders as the standard binder/plasticizer addition stage or ball milling the powders with only the solvent as

the standard dispersion stage (as it was shown the packing ability changed with increased ball milling times section 3.2.3.3) and milling with the organics as usual.

3.5.1.1 Microstructure

The dispersion tests (section 3.2.3.3) showed that not enough dispersion agent caused layering of the YSZ and NiO. From the lower magnification SEM micrograph shown in figure 3.36a (shows 2.5 layers laminated together), it is clear that for this anode, there was not enough binder to keep the YSZ and NiO homogeneously distributed, with a higher concentration of YSZ to the left of the layers. It can be seen however, from the other anode produced with higher binder/plasticizer content shown in figure 3.36b, that a homogeneous mixture of NiO and YSZ can be produced without the use of a dispersing agent.

The dispersion tests performed in section 3.2.3.3 showed that with increased ball milling times the settled height of the powder increased, proposing decreased NiO particle sizes. Comparison of the microstructures obtained from anodes produced with no ball milling and 18hr ball milling prior to binder/plasticizer addition shown in 3.36b and 3.37b respectively show that 18hr ball milling does decrease the nickel particle size from 4-10 μm to 2-6 μm . The decrease in particle size had little effect on the porosity at approximately 18% (obtained by image contrast analysis) and so a further anode was produced with increased binder/plasticizer content with the 18hr ball milling step which gave a porosity of 26% (by image contrast analysis). The microstructure of which is shown in figure 3.37a.

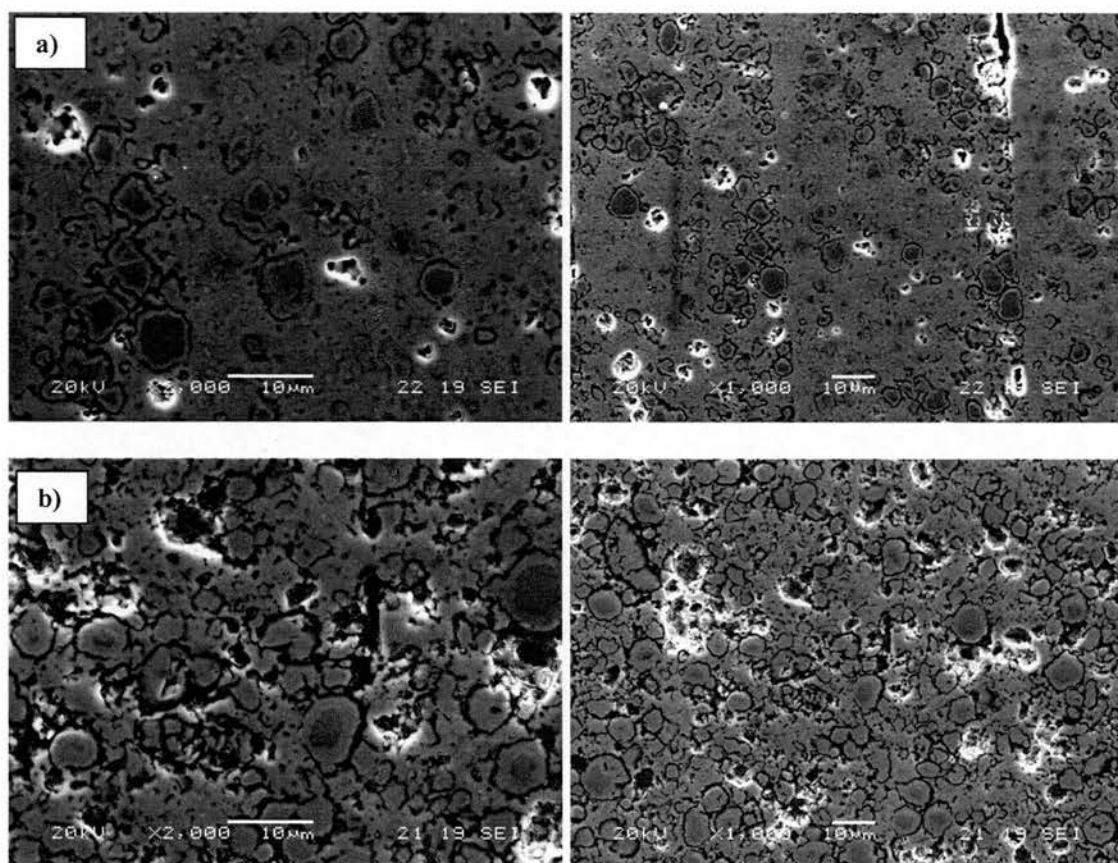


Figure 3.36: SEM images of polished cross-sections of reduced anode microstructures produced at different magnifications (with no ball milling prior to binder/plasticizer addition) with a) 3.54wt% binder and b) 5.09wt% binder in slip.

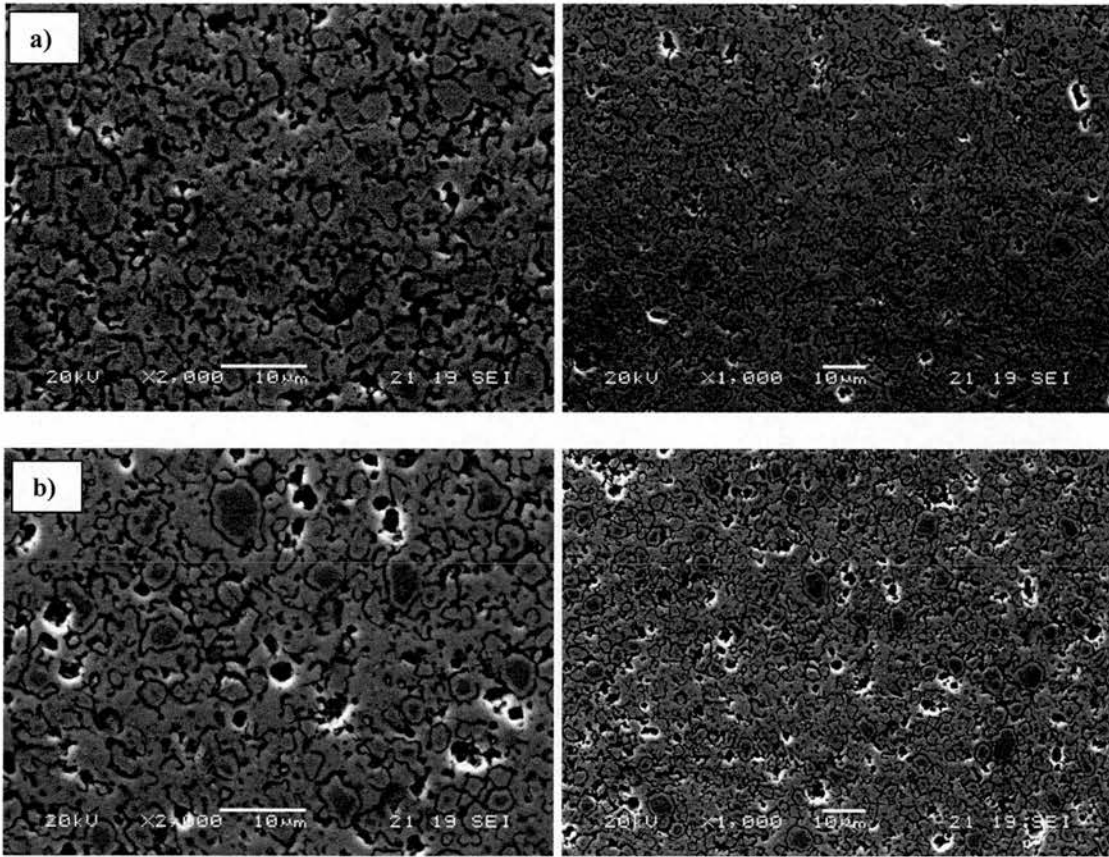


Figure 3.37: SEM images of polished cross-sections of reduced anode microstructures produced at different magnifications (with 18hr ball milling prior to binder/plasticizer addition) with a) 6.53wt% binder and b) 5.09wt% binder in slip.

3.5.1.2 Shrinkage

The shrinkages of all four anodes produced with no pore former were analysed as described in section 2.6.1 and are shown together with the measured shrinkage of the electrolyte in figure 3.38. All anodes, (with the exception of the low binder/plasticizer concentration anode) show a large initial shrinkage when heating to 300°C, which according to thermogravimetric analysis shown in section 3.3.3, figure 3.30 corresponds to the burn-out of the plasticizers. After this temperature, the tapes were rigid and didn't then undergo any notable shrinkage until temperatures in excess of 1000°C. The difference in shrinkages up to 1000°C seems primarily dependent on the plasticizer content.

The shrinkages of the two anodes with the same plasticizer content showed very similar shrinkages, the anode with the smaller NiO particles having a slightly larger shrinkage. At high temperatures, where the particles begin to sinter together, this is as expected as the smaller particles have a higher surface area and so sinter to a greater extent. The difference between the shrinkage of these two anodes however is also present at low temperatures, and doesn't notably increase at high temperatures, suggesting the difference is instead due to the particle packing in the green state. On consideration of inter-particle spacing, this is the opposite of what would be expected: the larger particles have a smaller surface area, so have a greater particle separation and therefore a larger associated shrinkage. However, referring back to the settling tests (section 3.2.3.3), increased milling (smaller particles) led to a decrease in packing efficiency, which would give a greater particle separation, which in this case seems to have the greatest effect on the shrinkage.

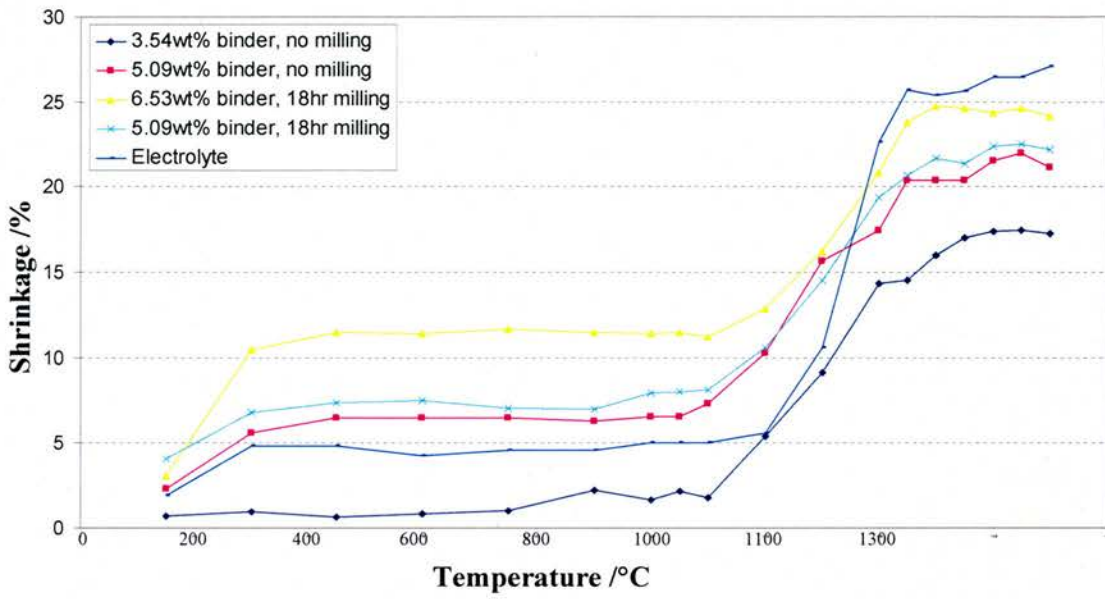


Figure 3.38: Shrinkage profile of anodes produced with no pore former with the profile of the electrolyte for comparison. Binder to plasticizer ratios were the same for all anodes, and so binder concentration relates to plasticizer concentration

An important thing to note from these shrinkages, is that no anode shrinkage profile matched that of the electrolyte. At temperatures up to 1000°C, a binder content in the slurry between 3.54wt% and 5.09wt% (note the binder to plasticizer ratio was kept constant) would be required to match the shrinkage profile of the electrolyte. At high temperatures however, a much reduced NiO particle size or a reduction in NiO content would be required to obtain shrinkages closer to that of the electrolyte.

3.5.2 Use of pore former

Anodes produced with no pore forming agent described in section 3.5.1 were not suitable for the SOFCRoll as the porosity was not high enough and the shrinkage too low in comparison to that of the electrolyte. The use of a pore former would go towards solving these problems: it would increase the porosity and final shrinkage very easily as described in section 3.4. Indeed, it could be expected that the increase in shrinkage would only be experienced at higher temperatures, as the graphite pore formers stay in the tape until temperatures between 600°C and 800°C shown in figure 3.39. The following examines the differences in anode microstructure and shrinkage with different graphite pore formers in different quantities.

3.5.2.1 Microstructure

Comparison of figures 3.37 and 3.40 shows the porosity of the anodes was greatly increased with the use of a pore former. The type of graphite used also affected the porosity, with the graphite obtained from Fisher Ltd producing the most porous anode and the -100mesh graphite obtained from Aldrich Ltd producing the

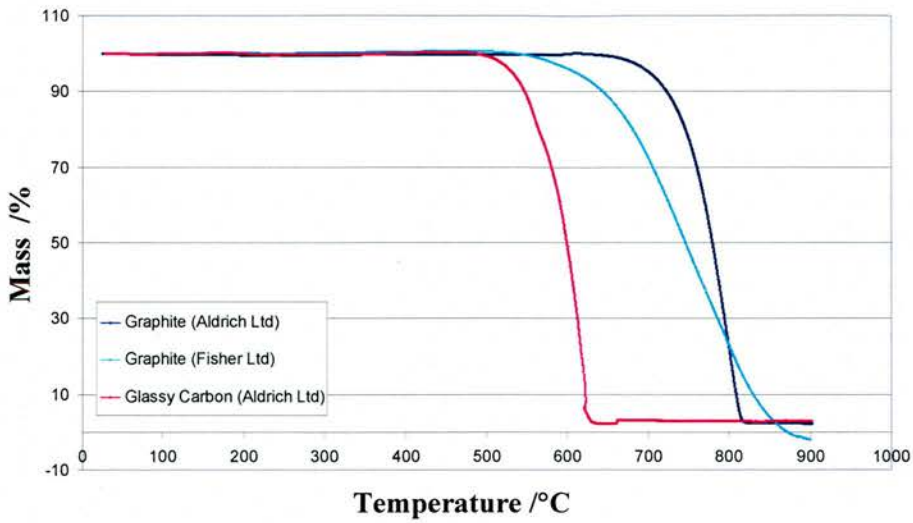


Figure 3.39: TG analysis of the pore formers used in air

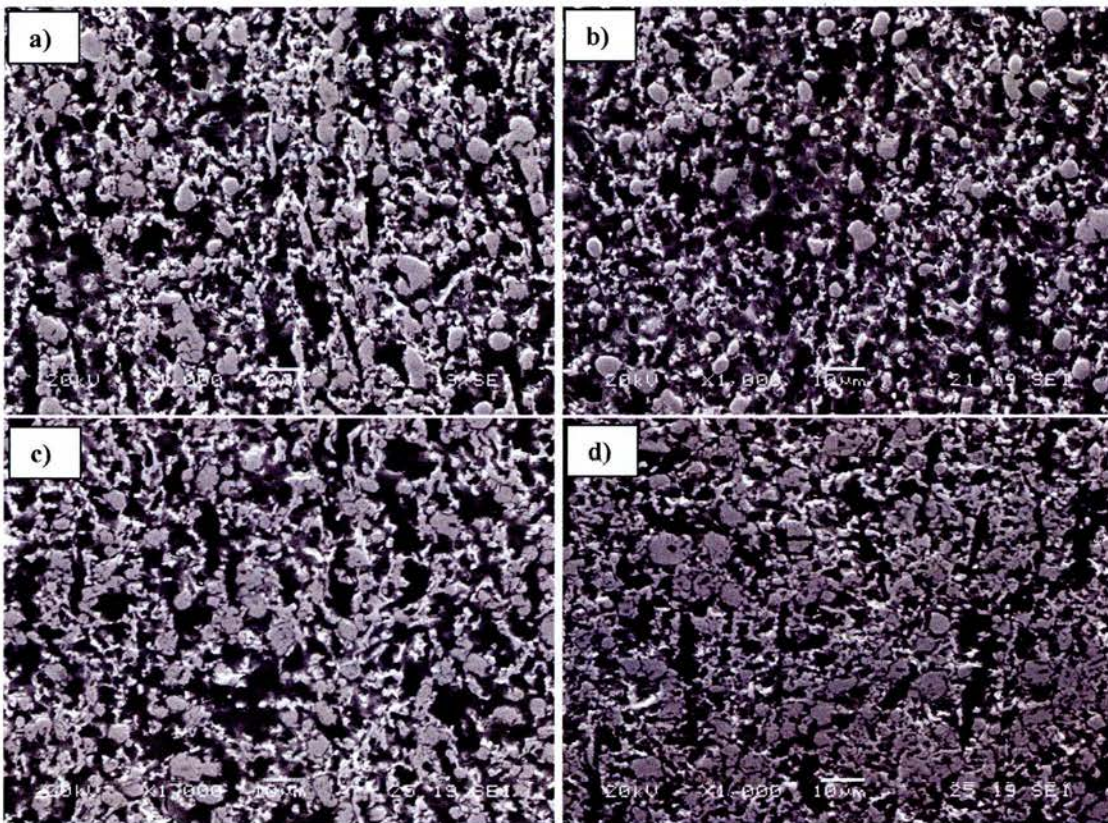


Figure 3.40: SEM images of reduced anode microstructures produced from a) Griffin & George Ltd grade 615, b) Fisher Ltd, c) Aldrich Ltd -325mesh and d) Aldrich Ltd -100 mesh with a (NiO+YSZ): graphite ratio of 1:1 by volume.

least porous. These porosities were measured as described in section 2.7 and are listed in table 3.4. Irrespective of the method used to measure the porosity, all anodes had adequate porosity for the SOFCRoll (~50%, see section 1.6).

The two methods used to measure the porosity gave good agreement for some samples, but varied significantly (over 12%) with others. There are various areas for error with both methods. Obtaining porosities using image analysis required good images and no polish damage for accurate results. Where polishing had lifted part of the sample away from the epoxy, or scratched the surface, the image analysis mistook that to be porosity due to its darker colour. Similarly, if the image was grainy the measured porosity would be higher than the true value. The porosity measurements taken by image analysis relied on homogeneous porosity throughout the entire sample, as measurements were only taken through one cross-section, whereas measurements taken by geometry took bulk values from the entire sample. Errors in measurements performed by geometry could be large due to inaccurate measurements in the x-y dimensions (where z is the thickness of the film); the measurement of the thickness relied upon the sample being completely vertical in the epoxy allowing the cross-section to be perfectly perpendicular to the x-y dimensions, otherwise the thickness measurements would be larger than the true values. Additionally porosity measurements relied upon complete reduction of the NiO to Ni for correct densities to be used.

Despite the various areas for error in porosity measurements between the two methods used, they both showed the anode produced from graphite obtained from Fisher Ltd to have the highest porosity, and the anode produced from -100 mesh graphite obtained from Aldrich to have the lowest porosity, as was visible from the microstructures. Section 3.4.2 showed increased milling times (ie reduced graphite

particle size) resulted in increased porosity. This was not the case with the anode when the initial graphite particle size was considered. The largest initial particle size belonged to the -325 mesh (see table 3.3) which resulted in the second densest sample, and the smallest initial particle size belonged to the -100 mesh, which resulted in the densest sample. The particle size of the graphite changes during milling (see section 3.2.2, figure 3.8) and it is conceivable that the reduction in particle size of the -325 mesh would be greater than that of the -100 mesh due to its larger initial particle size.

Whilst the porosity of these anodes is adequate for the gas flow through the SOFCRoll spirals, when the porosity of these samples is taken into consideration, the effective volume of nickel in the anode is much reduced; the highest obtained being just 20.4% as tabulated in table 3.4. Literature states that the percolation threshold for conductivity is at a nickel to YSZ ratios in excess of 30:70^[28]. This value of nickel however fails to take into consideration the porosity of the anode, the conductivity at a nickel to YSZ ratio of 30:70 increases by 2 orders of magnitude when the sintering temperature is increased from 1200°C to 1350°C^[29], ie the density of the anode is increased. Assuming that prior to reduction of NiO to Ni, the film was 100% dense, no change in volume of the film occurs upon reduction, and taking the densities of Ni and NiO to be 8.9gcm⁻³ and 6.72gcm⁻³ respectively^[30], if the ratio of Ni to YSZ was 30:70 (by volume), then after complete reduction of NiO to Ni, the porosity of the sample would be 17.1%, giving an effective nickel volume of 24.9%. By the same theory, if the ratio of Ni to YSZ was 40:60 (by volume), the ratio to minimise overpotential of the anode^[31], the porosity of the sample would be 21.5%, giving an effective nickel volume of 31.4%. The anodes produced from a ceramic to graphite

Graphite source	(NiO+YSZ) to graphite ratio by volume in green tape	Measured porosity after reduction /%		Effective volume of nickel in reduced anode /%	
		By geometry	By image analysis	By geometry	By image analysis
Griffin & George Ltd Grade 615	1:1	65.0	56.4	14	17.4
Fisher Ltd	1:1	69.7	57.3	12.1	17.1
Aldrich -100 mesh	1:1	49.0	48.9	20.4	20.4
Aldrich -325 mesh	1:1	63.8	51.3	14.5	19.5
	3:2	62.3	49.5	15.1	20.2
	7:3	49.6	48	20.2	20.8

Table 3.4: Comparison of porosities and volume of nickel in the reduced anodes, produced from different quantities and particle sizes of graphite.

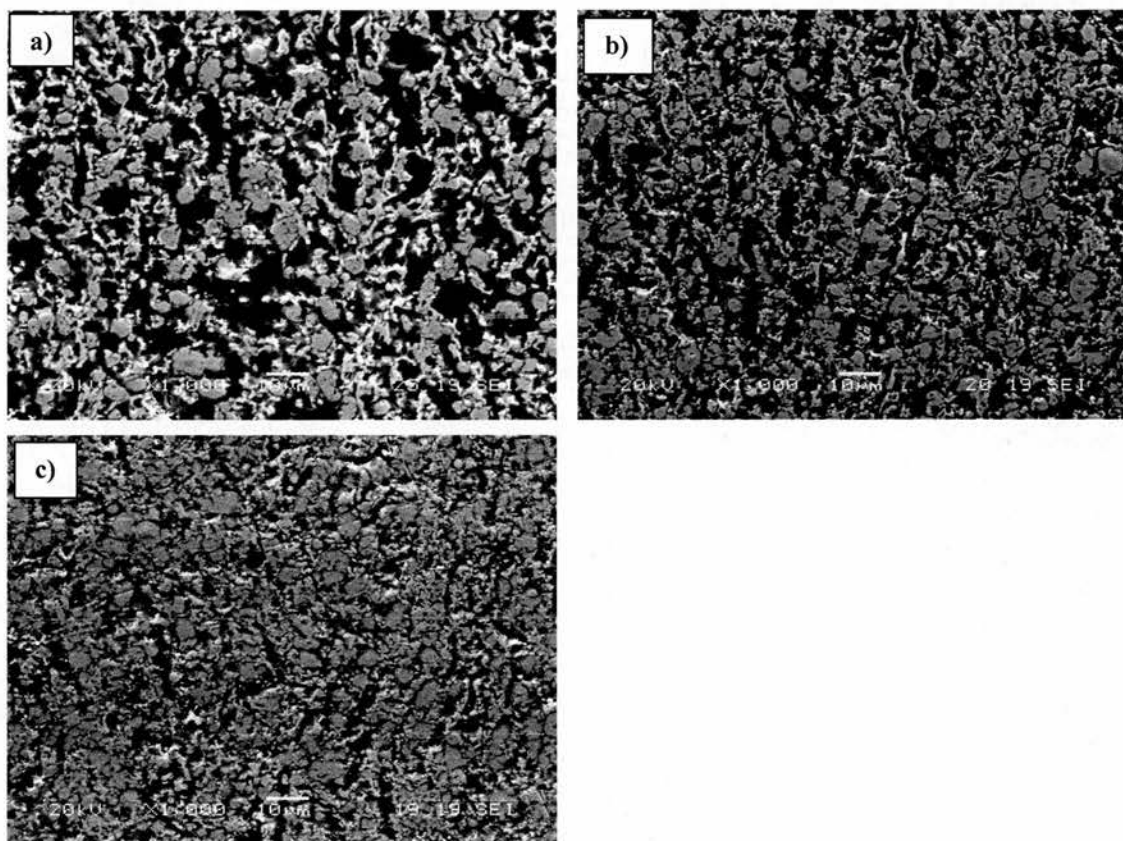


Figure 3.41: SEM images of the reduced anode microstructures produced from a) 50vol%, b) 40vol% and c) 30vol% graphite (Aldrich -325 mesh) relative to the NiO and YSZ content in the green tape

ratio of 1:1 (by volume) all have effective nickel volumes below these values, suggesting percolation of the nickel has not been achieved. Whilst these calculations give a rough guide of the nickel percolation, it is important to remember that pore size and distribution and relative ratios of YSZ to Ni particle size also affect the percolation threshold of the nickel^[23, 25-26].

Further anodes were produced with reduced quantities of the -325 mesh (Aldrich Ltd) graphite. The microstructures shown in figure 3.41 show as expected a reduction in the volume of graphite in the green tape results in a reduced porosity in the final reduced anode. The decrease in porosities measured by image analysis show only a small decrease, whereas when measured by geometry show a small decrease from 50vol% to 40vol%, followed by a larger decrease from 40vol% to 30vol% graphite content relative to NiO and YSZ volumes. Both methods show all anodes still have a porosity of ~50% or above: adequate for the SOFCroll geometry, however, the maximum measured effective nickel volume is only 20.8%.

3.5.2.2 Shrinkage

Initial shrinkage tests, shown in figure 3.42 performed by measuring rectangles (see section 2.6.1) on the anodes with different pore former particle sizes (cross-sectional images as shown in figure 3.40) showed similar high temperature shrinkage rates to 1300°C. The shrinkages were however much increased when compared to the shrinkages of anodes with no graphite content in the green tape, giving shrinkage profiles much closer to that of the electrolyte. The least porous anodes (produced from -100 mesh graphite) gave the highest shrinkage during the dwell at 1300°C, and the highest porosity anodes (produced from graphite obtained

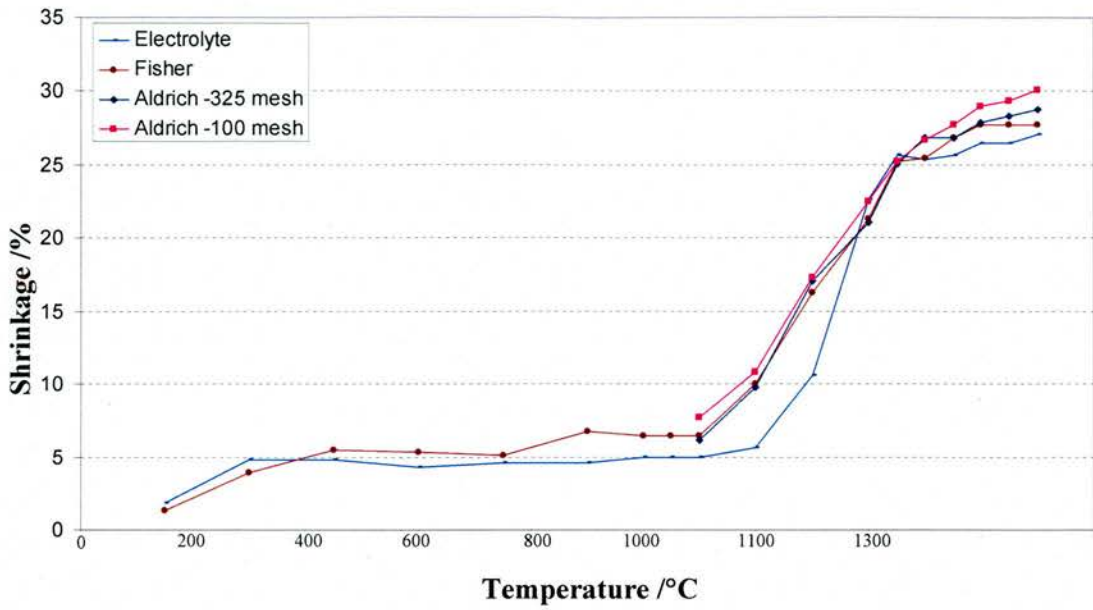


Figure 3.42: Shrinkage profiles of the anodes produced with various graphite powders in a YSZ to NiO ratio of 45:55 (by wt) and graphite to ceramic ratio of 1:1 by volume

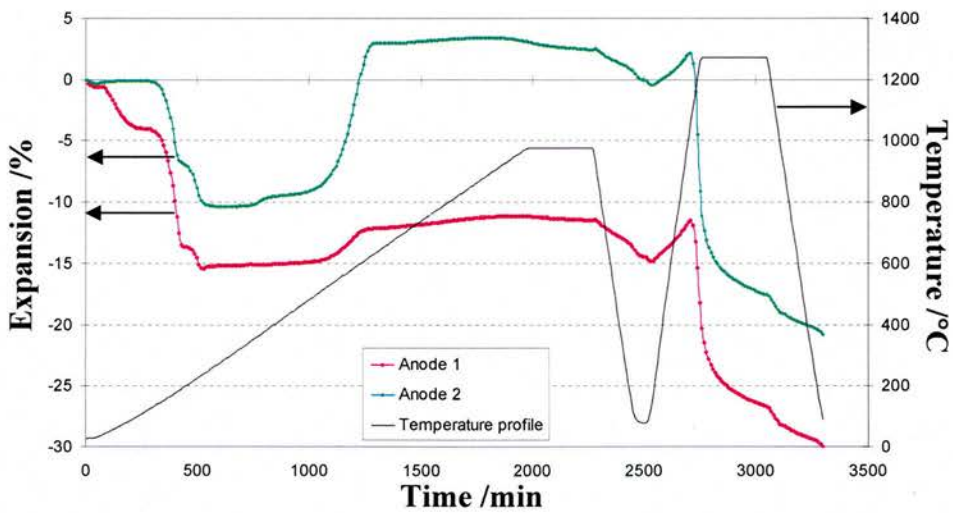


Figure 3.43: Shrinkage profiles of two separate anodes produced with a YSZ to NiO ratio of 45:55 and graphite to (NiO and YSZ) ratio of 2:3 by volume. Graphite used was -325mesh (Aldrich Ltd), shrinkage analysis performed on the dilatometer.

from Fisher Ltd) gave the smallest shrinkage during the dwell at 1300°C. Since the ratios of organic additives and graphite to ceramic powder were kept constant in the green tape, these shrinkages reflect the resulting porosities seen in the anodes.

The shrinkages of anodes with varying quantities of graphite -325 mesh (microstructures shown in figure 3.41) were performed on both the dilatometer and by measurement of rectangles (see section 2.6). Figure 3.43 shows the shrinkage profile of two separate anodes produced with a graphite (-325 mesh) to ceramic ratio of 2:3 by volume, performed by the dilatometer measured approximately 8 months apart, vary to a large extent. The first anode measured (labelled as anode 1 in figure 3.43) gave a 2% shrinkage between 44°C and 107°C, whereas the other anode (labelled as anode 2 in figure 3.42) didn't shrink at all in this temperature range. Referring back to the TG analysis performed on the organic additives used in the tape (see figure 3.30, section 3.3.3), only the triton Q-44 shows any weight loss in this temperature range, which was not used in the anode formulations. By 250°C, the difference in relative shrinkages had increased to ~5%. The shrinkage associated with plasticizer burn-out in the range of 130°C to 195°C was larger for anode 1, and the shrinkage associated with the initial mass loss of the binder (see figure 3.30, section 3.3.3), presumably due to tape deformation by the pushrod as the binder softens between 205°C to 245°C was larger for the second anode.

Anode 2 showed a small expansion of approximately 0.7% between 360°C and 420°C not seen in anode 1. Referring back to the TG analysis, the binder has lost ~50% of its weight by 360°C, and has lost ~80% of its weight by 420°C (see figure 3.30, section 3.3.3). Finally both anodes showed an expansion in the temperature range of 520°C to 635°C, consisting of 2.4% and 12% for anode 1 and anode 2 respectively. When measuring rectangles, this was the temperature range where a

large degree of curling occurred in the tapes. It does not correspond to the graphite burn-out, which begins at approximately 640°C (see figure 3.39).

The shape of the two curves were similar from 635°C to 930°C. Above this temperature and during the dwell at 1000°C both tapes showed a small shrinkage of 0.5% and 0.8% for anode 1 and anode 2 respectively. The difference in shrinkage was attributed to the tapes beginning to flatten; anode 2 having curled to a greater extent between 520°C and 635°C being able to flatten out to a greater extent. Both anodes started to shrink at 1065°C, however the high temperature shrinkage of anode 2 (19.8%) was greater than anode 1 (15.3%), which was again attributed to the fact that anode 2 had more scope for shrinkage due to the higher degree of curling between 520°C and 635°C.

It was hypothesised that the initial difference in shrinkage was due to anode 1 being measured sooner after casting than anode 2, so the initial shrinkage seen for anode 1 corresponded to removal of some trapped solvent and the older tape anode 2 had shrunk with time on the Mylar sheet as the remaining solvent evaporated. Another possibility was that this shrinkage was due to the removal of trapped air in poorly laminated anode sheets for anode 1 (not present in anode 2) due to a combination of the pushrod force and the softening of the tapes with temperature. Furthermore, there is a possibility that the pushrod force had not been correctly altered to 20cN when anode 1 was tested thus altering the shrinkage profiles as detailed below. Additional sources of errors would be that the position of the thermocouple changed between samples, thus altering the temperature heated to.

Figure 3.44 shows there is no clear relation between the expansion of an anode between 520°C and 635°C and different pushrod forces. The sudden shrinkage noted

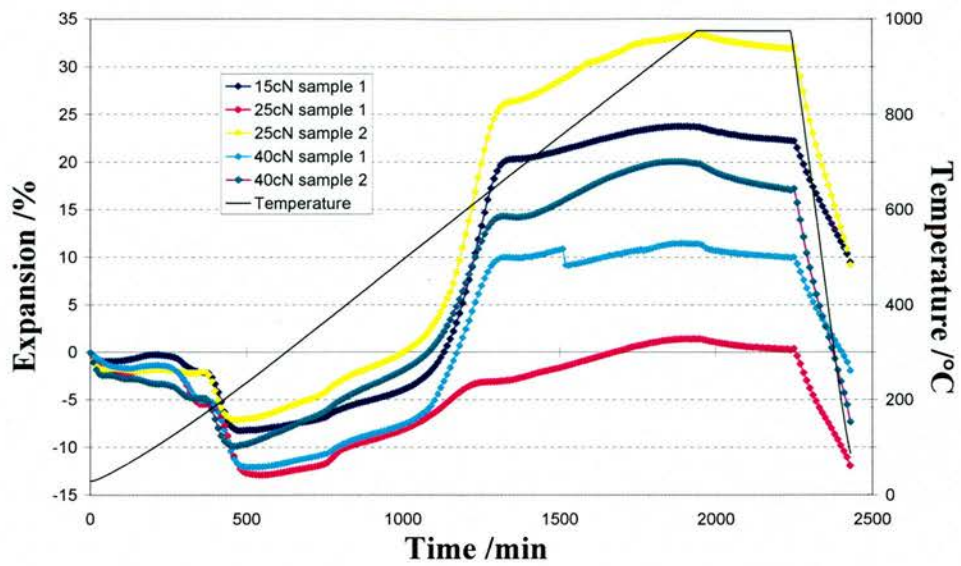


Figure 3.44: Shrinkage profile of anode NiO to YSZ ratio of 55:45 by weight and ceramic to graphite ratios of 1:1 by volume, performed with the dilatometer at different push rod tensions

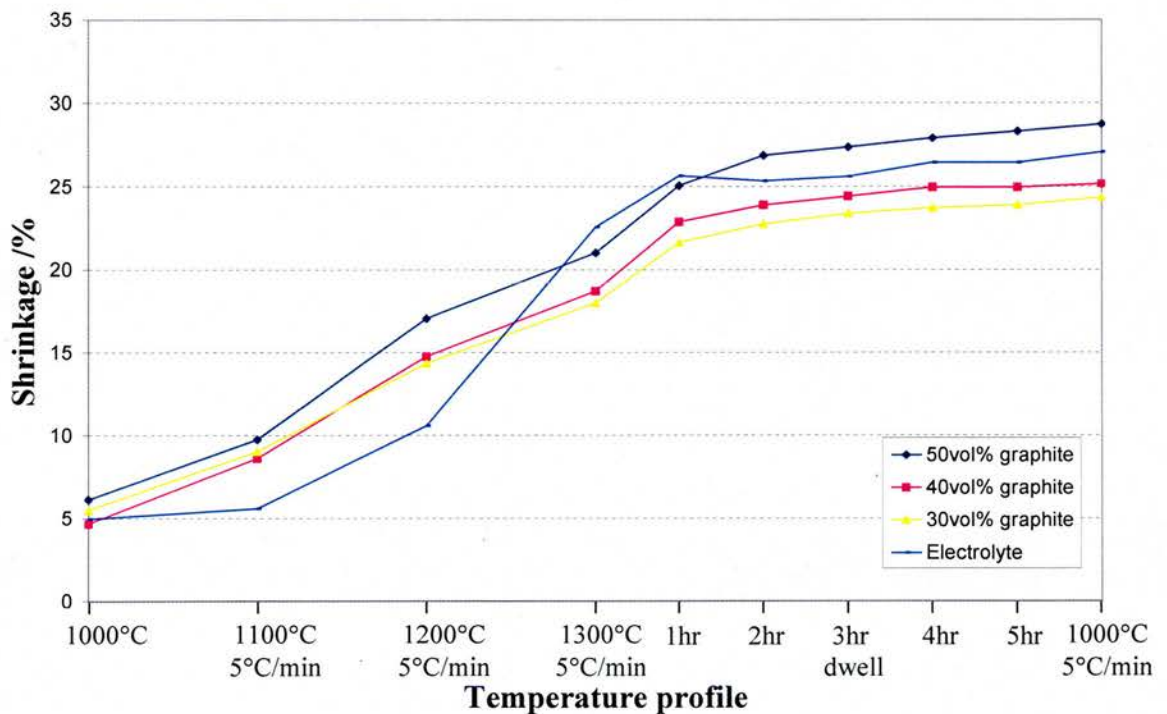


Figure 3.45: Shrinkage profile of anodes with a NiO to YSZ ratio of 55:45 (by mass) with varying graphite contents in the green tape.

in sample 1 with a push rod force of 40cN at approximately 750°C, was believed to be due to cracking of the anode. The factors affecting reproducibility of the shrinkage profiles by the dilatometer are unclear and the curling of the tapes, age of tapes and whether the push rod force had been changed in between runs should be noted when comparing shrinkages of tapes.

The high temperature shrinkage profiles of the anodes produced with varying quantities of graphite -325mesh measured by firing rectangular samples as detailed in section 2.6.1, are shown in figure 3.45. The final shrinkages noted are as expected: the shrinkage is increased with increased graphite content in the green tape. Increased graphite content would result in increased porosity, which in turn increases the shrinkage^[32-33], as seen in section 3.4 and by the difference in shrinkage of anodes with and without graphite (figures 3.38 and 3.42). The unexpected result is that after calcining to 1000°C, the lowest to highest shrinkage was observed for the anode containing 40vol%, 30vol% and 50vol% graphite in the green tape respectively.

3.5.3 Varying NiO content

The previous section showed how whilst introducing the graphite particles to the tapes improved the shrinkage profile match with the electrolyte and increased the porosity for improved gas flow in the spirals of the SOFCRoll, the effective nickel content was thought to be too low for percolation. The following section investigates the effects of increasing the nickel to YSZ ratio on microstructure, shrinkage and effective nickel content in the reduced anodes.

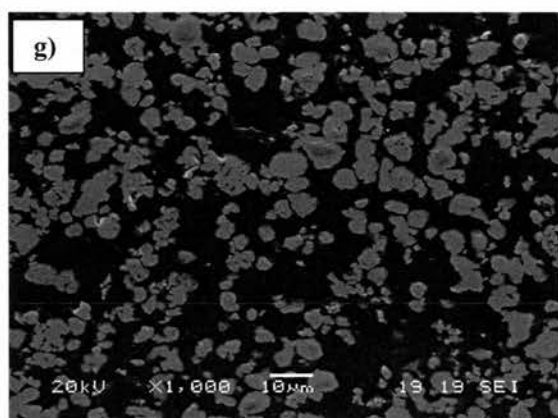
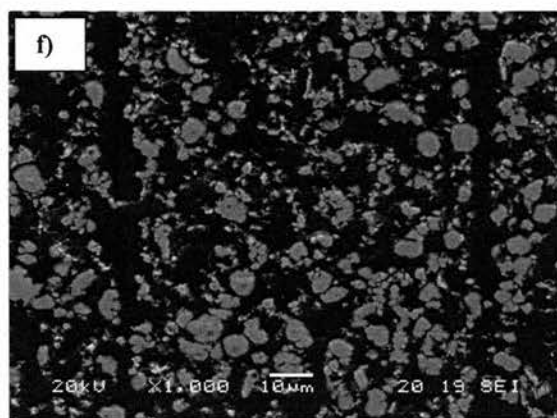
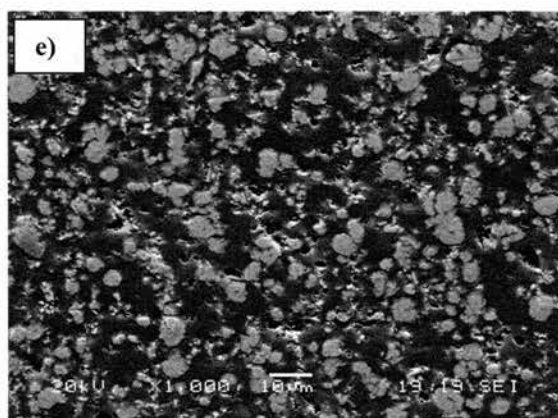
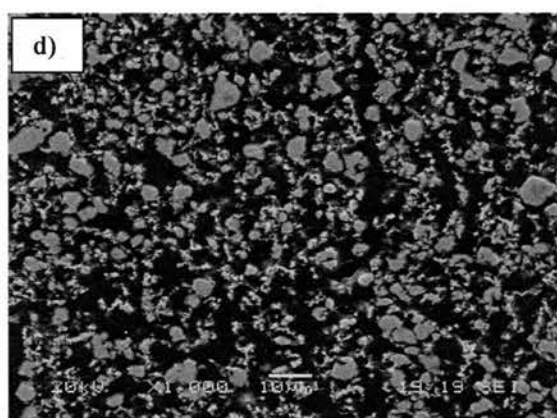
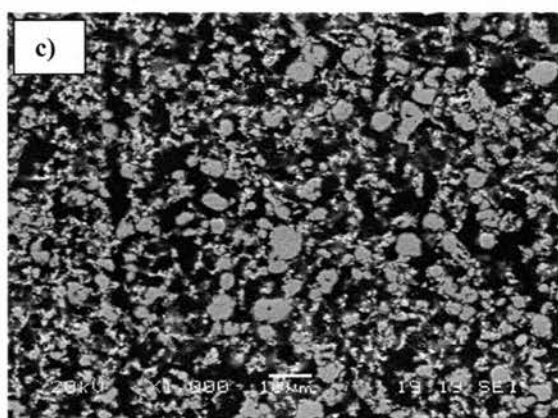
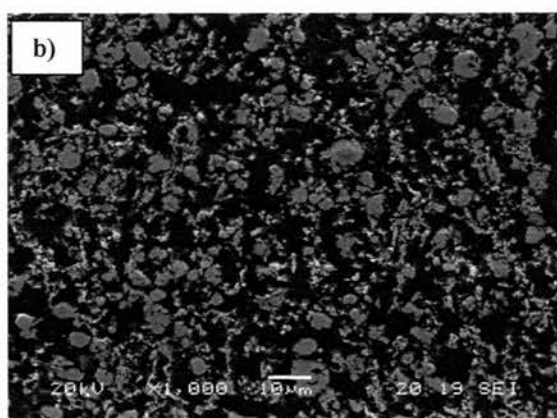
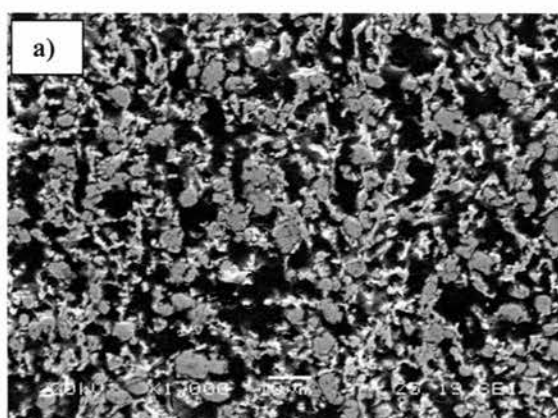


Figure 3.46: SEM images of anodes produced as in section 2.6 with 50vol% graphite (-325 mesh) relative to ceramic content in the green tape, fired at 1300°C and reduced at 800°C, 4hrs with nickel content of (with respect to YSZ)
a) 40vol% Ni, b) 50vol% Ni, c) 55vol% Ni, d) 60vol% Ni, e) 70vol% Ni, f) 80vol% Ni and g) 100% Ni

3.5.3.1 Microstructure

The microstructure and measured porosities of anodes produced with varying Ni to YSZ ratios and graphite contents are shown in figures 3.46-3.48. As expected, the effective volume of nickel in the anodes increased as the NiO to YSZ ratio was increased, and as the ceramic to graphite ratio in the green tape increased due to decreased porosities. As the NiO to YSZ ratio was increased and graphite content kept constant, the final porosity increased (up to Ni to YSZ ratios of 70:30 by volume after reduction), which again is as expected due to increased volume reduction when the NiO is reduced to Ni. The reason for the decrease in final porosity for films at higher Ni to YSZ ratios was attributed to the decrease in anode volume when the NiO was reduced to Ni, caused by Ni-Ni particle coarsening clearly visible in figure 3.46.

As seen in section 3.5.2, generally the two different methods used to obtain the porosities of the anodes varied significantly, the porosities sometimes differing by over 10%. If the desired effective nickel volume in the anode is 31.4% (see section 3.5.2.1), and assuming the porosity obtained by image analysis is correct, this is achieved with a Ni to YSZ ratio of 7:3 or 4:1 by volume (equating to NiO to YSZ ratios prior reduction of 81:19 or 88:12 by mass) with a ceramic to graphite ratio of 2:3 or 1:1 by volume respectively in the green tape. Both of these anodes have porosities in excess of 50%, as required in the SOFCRoll design. Using the porosity values obtained by geometry, the maximum effective nickel volume in the anodes produced is just under 25% for a Ni to YSZ ratio of 1:0 or 4:1 by volume (equating to a NiO to YSZ ratio prior to reduction of 1:0 or 88:12 by mass) with a ceramic to graphite ratio of 1:1 or 2:3 by volume respectively in the green tape, showing that no anodes produced have adequate effective nickel volume for the fuel cell. Both image

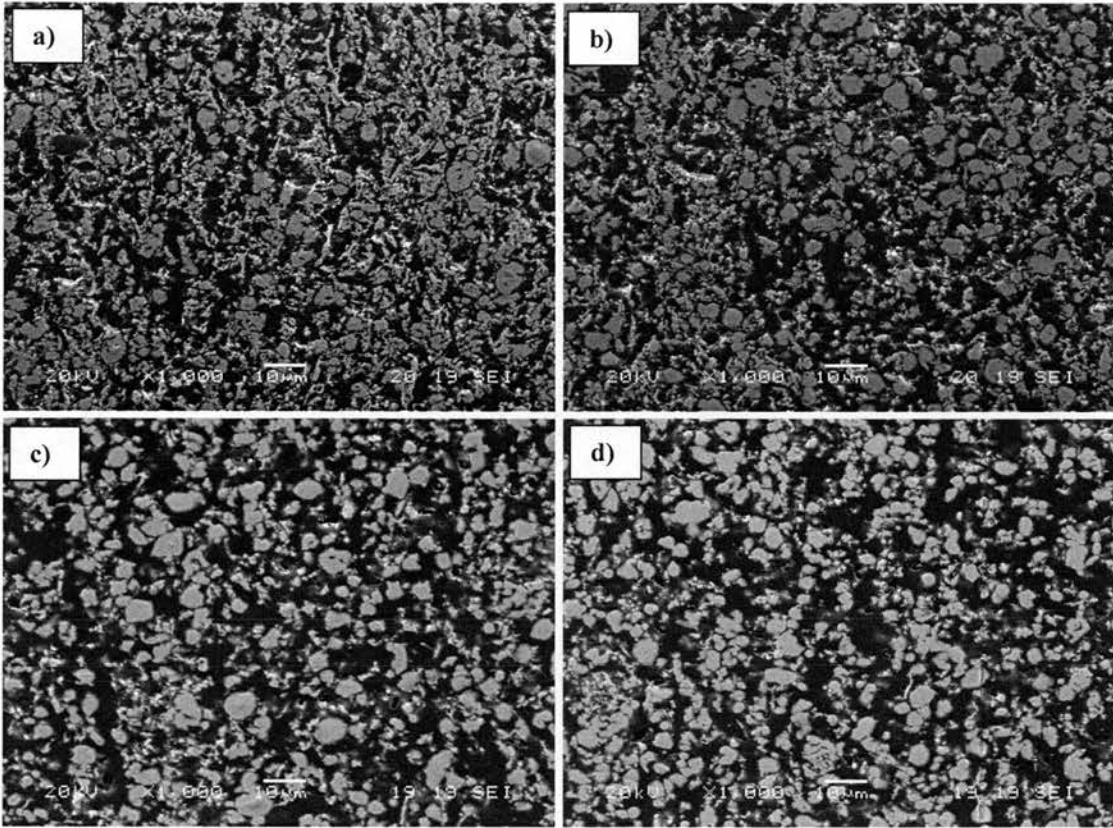


Figure 3.47: SEM images of reduced anodes with SEM images of anodes produced as in section 2.6 with 40vol% graphite (-325 mesh) relative to ceramic content in the green tape, fired at 1300°C and reduced at 800°C, 4hrs with nickel content of (with respect to YSZ)
a) 40vol% Ni, b) 50vol% Ni, c) 70vol% Ni and d) 80vol% Ni

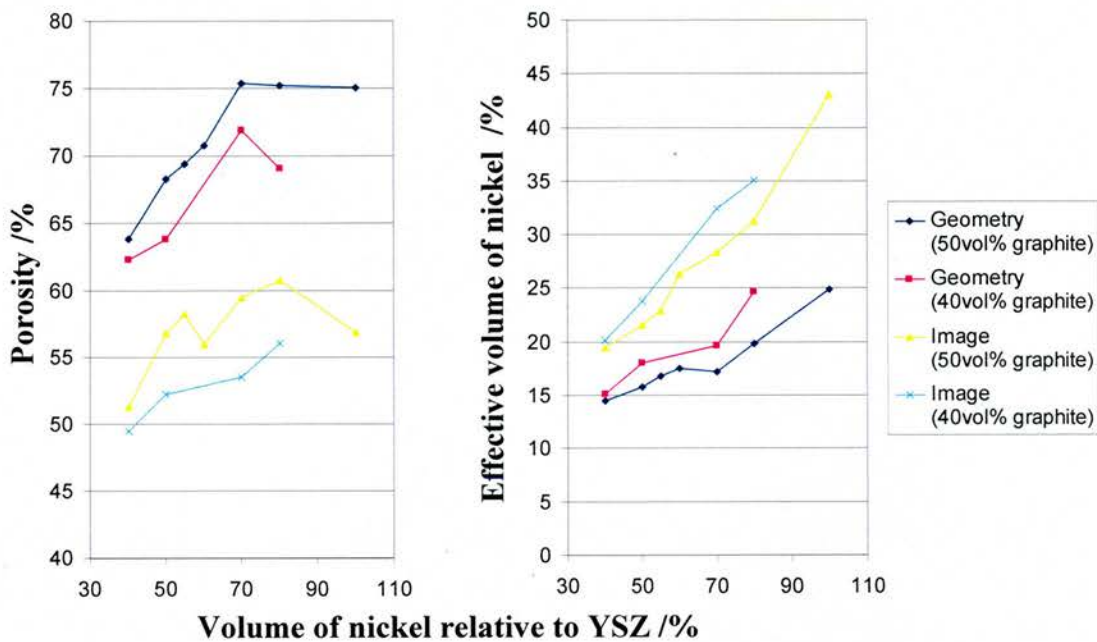


Figure 3.48: Graph showing porosity calculated by image and geometry analysis and corresponding effective nickel volume, calculated by measured porosities with differing Nickel to YSZ ratios (by volume). Graphite contents are shown relative to the ceramic content in the green tape.

and geometry analysis show that the porosities of all anodes produced in excess of 50% and so can be reduced in order to increase the effective nickel content. This is true even for the anode produced with a nickel to YSZ ratio is 2:3 (by volume) if a 2-layer anode is produced: a higher nickel content, high porosity current collector layer would maintain gas transport through the SOFCRoll spirals, allowing a reduction in porosity in the “active” high triple phase boundary layer.

3.5.3.2 Shrinkage

The shrinkage profiles obtained by the dilatometer for the anodes with a ceramic (NiO +YSZ) to graphite ratio of 1:1 in the green tape (by volume) are shown in figure 3.49. The profile of the anode containing NiO to YSZ ratio of 81:19 (by mass) is omitted due to the change of push rod force in between measurements, resulting in an incomparable measured shrinkage profile (see section 3.5.2.2). With the exception of the anode with no YSZ content, the shrinkage curves were very similar in shape.

The first expansion seen between 375°C and 430°C increased with increasing NiO to YSZ ratio. An 11% shrinkage of the 100% NiO anode occurs between 490°C and after the 5hr dwell at 975°C, resulting in a final shrinkage of 35.8% by the time the sample has cooled to 1133°C after the 5hr dwell at 1273°C (at this temperature, the shrinkage of the anode has reached the machine limit, hence no negative thermal expansion is seen between 1133°C and 30°C). The anode with a NiO to YSZ ratio of 88:22 by mass (equating to a Ni to YSZ ratio of 4:1 by volume after reduction) also shows a larger shrinkage than the other anodes between 795°C and after the 5hr dwell at 975°C. Whilst this anode has a much smaller shrinkage than the 100% NiO anode, this shrinkage was believed to be due to the pushrod crushing the weak ceramic

framework, as since the particle size of the NiO is much larger than the YSZ (see table 3.1), the porosity after graphite burnout would be much higher with no or little YSZ content. Indeed these anodes were very weak, when removing from the dilatometer after the run had finished, they broke either during the run, or when removed; in both cases nickel oxide powder remained on the alumina spacers.

As described in sections 3.3.3, the temperature of the samples in the dilatometer was less than that seen in the furnace when heating the rectangle samples and so the final shrinkages would be expected to be larger for the rectangular samples. The final shrinkages measured by the rectangles both before and after reduction are shown in figure 3.50. The general trend seen is that as the NiO to YSZ ratio is increased the shrinkage prior to reduction decreases as seen in the literature^[23, 33]. Also as the graphite to ceramic ratio in the green tape is decreased, the shrinkage prior to reduction decreases. Additionally, as the NiO to YSZ ratio is increased, the shrinkage upon reduction increases. With a NiO to YSZ ratio of 7:3 by mass (corresponding to a Ni to YSZ ratio of 56:44 by volume upon reduction), the shrinkage during reduction of NiO to Ni is very small - only 0.5% with respect to the green tape dimensions. Such a small shrinkage upon reduction is likely to be tolerated in the fuel cell system without the production of micro-cracks.

Referring back to figure 3.48 and taking values obtained by image analysis only, the minimum Ni to YSZ ratio required for the desired 'effective nickel volume' (shown in section 3.5.3.1), is 7:3 by volume upon reduction (NiO to YSZ ratio of 81:19 by mass), with the reduced graphite content. In this case, the shrinkage upon reduction is a further 2.5% (relative to green tape dimensions). Whether or not this shrinkage on reduction can be tolerated, the difference in shrinkage during high

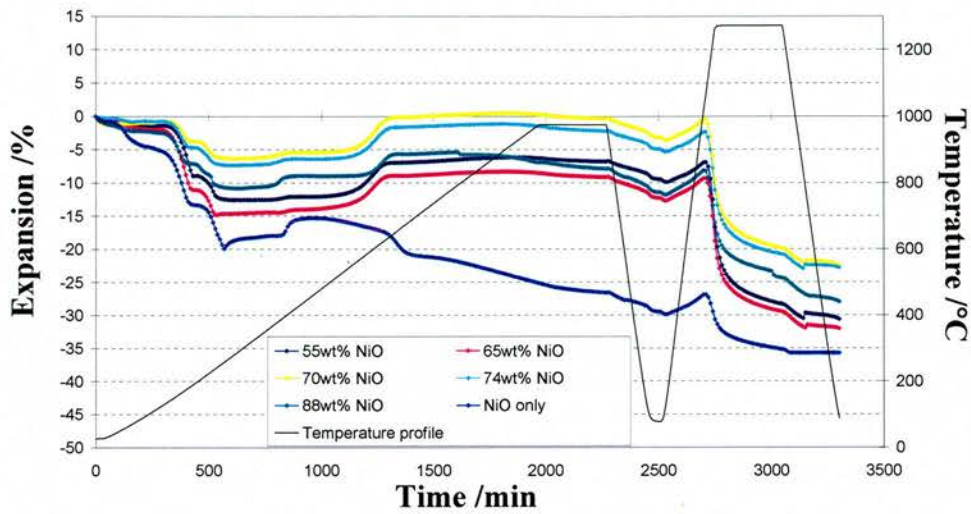


Figure 3.49: Shrinkage profile obtained by dilatometer of anodes with a ceramic to graphite ratio of 1:1 (by volume) in the green tape with varying nickel contents, shown by the NiO to YSZ ratios in the legend.

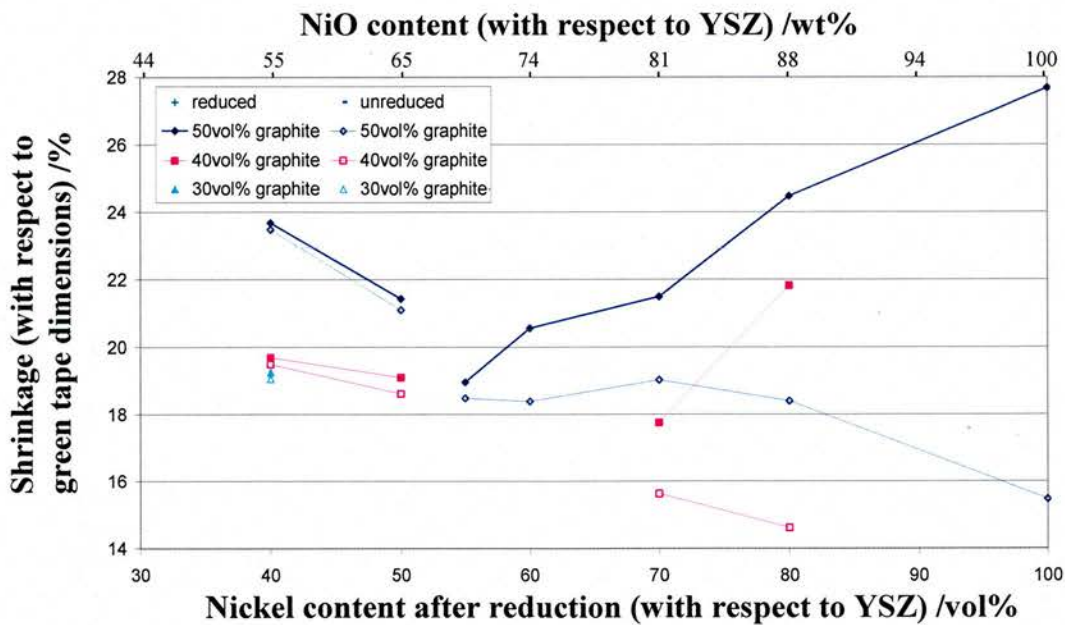


Figure 3.50: Graph showing the final shrinkages of anodes produced with various NiO:YSZ ratios and shrinkages after reduction of NiO to Ni. All shrinkages are calculated relative to the green tape dimensions.

temperature treatment prior to reduction between this anode and the electrolyte is too high at 10%. The other anode giving the desired 'effective nickel volume' (shown in section 3.5.3.1), has a Ni to YSZ ratio of 4:1 by volume upon reduction (NiO to YSZ ratio of 88:22 by mass) with a 1:1 ceramic to graphite ratio in the green tape. This has a shrinkage difference to that of the electrolyte of 7% prior to reduction, which whilst better than the other anode is still a large difference in shrinkage. More to the point, the shrinkage upon reduction is too large leading to crazing of the anode in the multi-layer system (see chapter 4, section 4.3.3, figure 4.12).

3.5.4 Summary

The trends observed in the fabrication of various anodes are as follows: increasing the graphite content and/or YSZ to NiO ratio in the green tapes increased the shrinkage; increasing the NiO to YSZ ratio increased the shrinkage upon reduction; increasing the graphite content and NiO to YSZ ratio had the affect of increasing the porosity of the reduced anodes. The only anodes with a similar shrinkage to that of the electrolyte were those with a low NiO to YSZ ratio and produced with the use of a pore former. Whilst these anodes also had the advantage of small shrinkages upon reduction, the effective Ni content (taking into account the anode porosity) was too low.

Further work is therefore required to optimise the anode by reducing the porosity whilst maintaining the higher shrinkages to avoid cracking during co-firing with the electrolyte. Introducing larger YSZ particle size or smaller NiO particle size would reduce the NiO to YSZ ratio required to achieve high triple phase boundaries and decreasing the NiO particle size would also aid increasing the shrinkage.

3.6 Cathode Production

The cathode was comprised of $(\text{La}_{0.8}\text{Sr}_{0.2})_{1-x}\text{MnO}_3$, either mixed with YSZ or alone. The following sections investigate the effect of the A-site deficiency in the LSM20 on the production of insulating pyrochlore phase $\text{La}_2\text{Zr}_2\text{O}_7$, microstructure and shrinkage profiles.

3.6.1 Pyrochlore analysis

Section 3.3 showed 1300°C to be the minimum temperature required for the densification of YSZ tapes with a 5hr dwell time. This will therefore be the minimum temperature used for the co-firing of all fuel cell components. However, formation of the $\text{La}_2\text{Zr}_2\text{O}_7$ pyrochlore species between LSM and YSZ is a well documented occurrence at temperatures above 1200°C^[14, 19-20]. The insulating nature of $\text{La}_2\text{Zr}_2\text{O}_7$ to oxygen ion conduction leads to reduced performance of the fuel cell (see section 1.4.3). Reactions of different LSM and YSZ powders were performed at 1300°C for 5hrs to ensure that during fuel cell production, no pyrochlore was synthesised.

The 4 main (highest intensity) lanthanum zirconate pyrochlore peaks^[34] at $2\theta = 28.6, 32.2, 47.6$ and 56.5 are clearly seen in figure 3.51 for the reaction between the stoichiometric LSM20 and YSZ (Pi-Kem Ltd). Therefore, as expected an A-site deficient LSM powder is required for production of the cathode^[20-21]. Various A-site deficient LSM powders were obtained either from Nextech Ltd, or by reaction of the stoichiometric LSM with MnCO_3 (see section 3.2). $(\text{La}_{0.8}\text{Sr}_{0.2})_{0.98}\text{MnO}_3$ (2% A-site deficiency) is the standard LSM20 sold by Nextech Ltd for fuel cell production. However, the majority of manufacturing techniques of SOFC designs allow lower

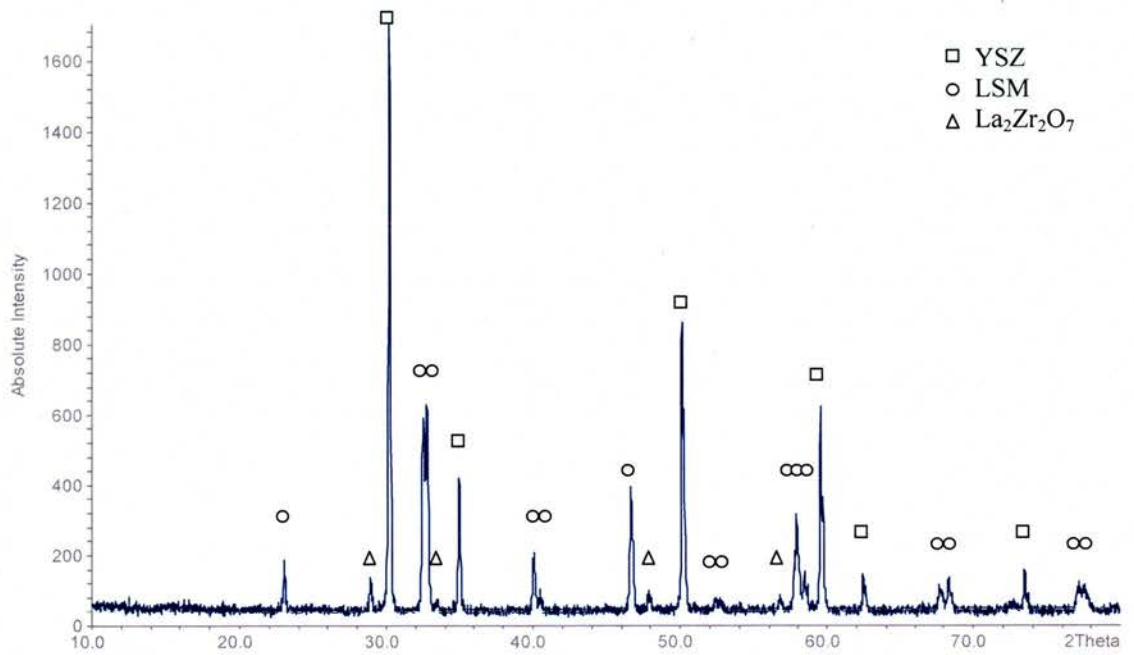


Figure 3.51: XRD trace for reaction of YSZ (Pi-Kem Ltd) and $\text{La}_{0.8}\text{Sr}_{0.2}\text{MnO}_3$ at 1300°C , for 5hrs

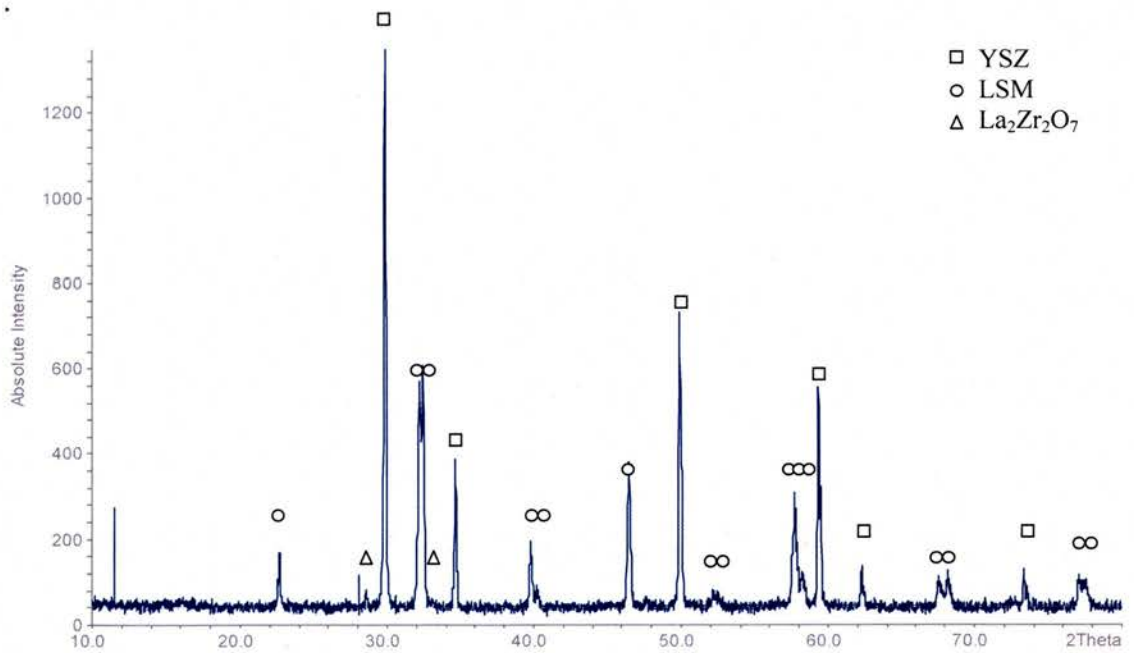


Figure 3.52: XRD trace for the reaction of YSZ (Pi-Kem Ltd) and $(\text{La}_{0.8}\text{Sr}_{0.2})_{0.98}\text{MnO}_3$ (Nextech Ltd) at 1300°C , for 5hrs

temperatures to be utilised for sintering of the cathode (see section 1.5) and it is therefore not surprising that 2 peaks corresponding to the pyrochlore at $2\theta = 28.6$ and $33.2^{[34]}$ are still seen in the XRD trace, figure 3.52. Comparison with the XRD analysis for the reaction between YSZ (Pi-Kem Ltd) and $\text{La}_{0.8}\text{Sr}_{0.2}\text{MnO}_3$ (stoichiometric), the pyrochlore peak height is smaller, showing a reduction in the pyrochlore formation.

Figure 3.53 shows the small peak of the lanthanum zirconate pyrochlore are evident at $2\theta = 28.6$ only, for the reaction of YSZ (Pi-Kem Ltd) and $(\text{La}_{0.8}\text{Sr}_{0.2})_{0.97}\text{MnO}_3$ produced by reaction of the stoichiometric LSM (Pi-Kem Ltd) with MnCO_3 at 1000°C , 1050°C , 1100°C and 1150°C . It is possible that a small peak is present at this 2θ value for reaction between YSZ (Pi-Kem Ltd) and $(\text{La}_{0.8}\text{Sr}_{0.2})_{0.97}\text{MnO}_3$ produced at a temperature of 1200°C , however without longer analysis times, it is difficult to say.

There is no obvious difference in intensity of the $2\theta=28.6$ peaks from the reaction between YSZ (Pi-Kem Ltd) and $(\text{La}_{0.8}\text{Sr}_{0.2})_{0.97}\text{MnO}_3$ produced at temperatures of manganese incorporation between 1000°C and 1100°C , all of which show a decrease in peak height when compared to the reaction with $(\text{La}_{0.8}\text{Sr}_{0.2})_{0.98}\text{MnO}_3$ (2% A-site deficient).

The likely explanation for the reduced zirconate peaks when reacted with $(\text{La}_{0.8}\text{Sr}_{0.2})_{0.97}\text{MnO}_3$ produced at 1150°C and 1200°C is the LSM particle size. Referring back to figure 3.2 in section 3.2.1, a small increase in particle size is seen when increasing manganese incorporation temperature from 1000°C to 1100°C . However, there is a marked increase with temperatures of 1150°C and 1200°C , with

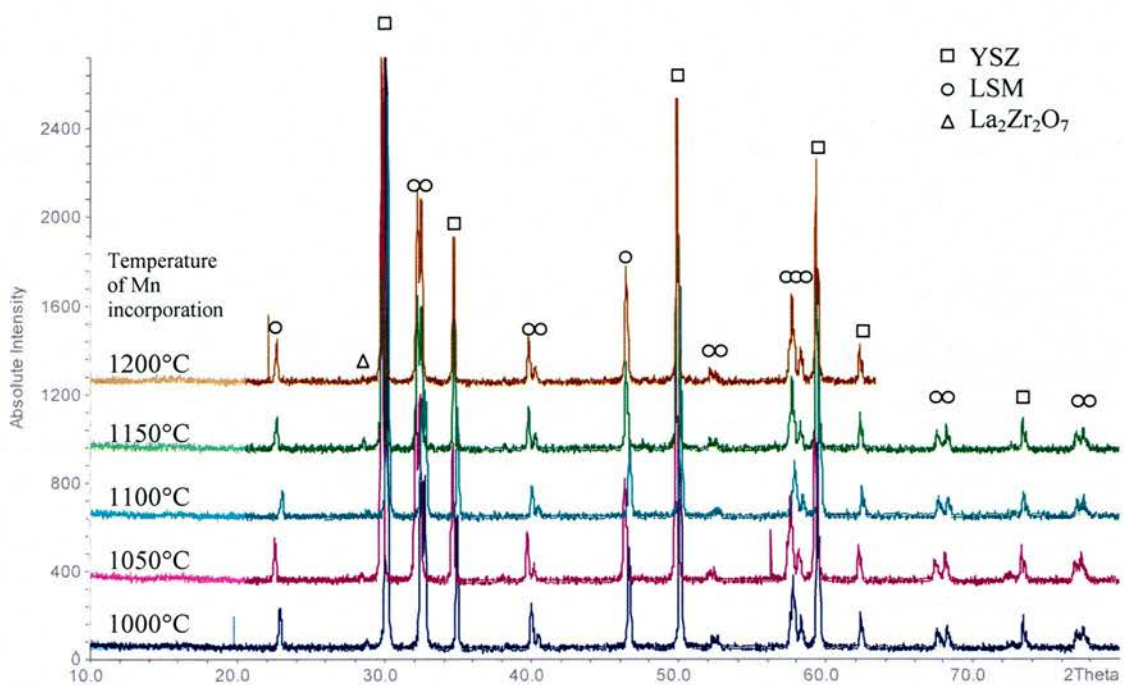


Figure 3.53: XRD trace for the reaction of YSZ (Pi-Kem Ltd) and $(\text{La}_{0.8}\text{Sr}_{0.2})_{0.97}\text{MnO}_3$ (synthesised at various temperatures) at 1300°C , for 5hrs

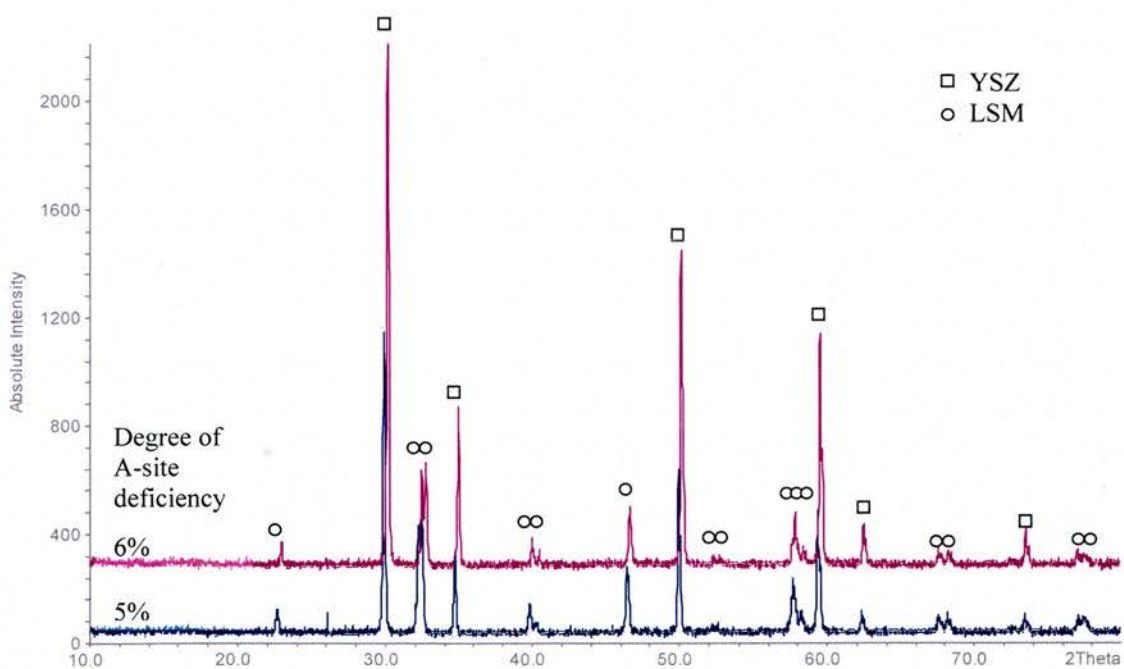


Figure 3.54: XRD trace for the reaction of YSZ (Pi-Kem Ltd) and $(\text{La}_{0.8}\text{Sr}_{0.2})_{0.95}\text{MnO}_3$ (Nextech Ltd) and $(\text{La}_{0.8}\text{Sr}_{0.2})_{0.94}\text{MnO}_3$ (synthesised at 1050°C), at 1300°C , for 5hrs

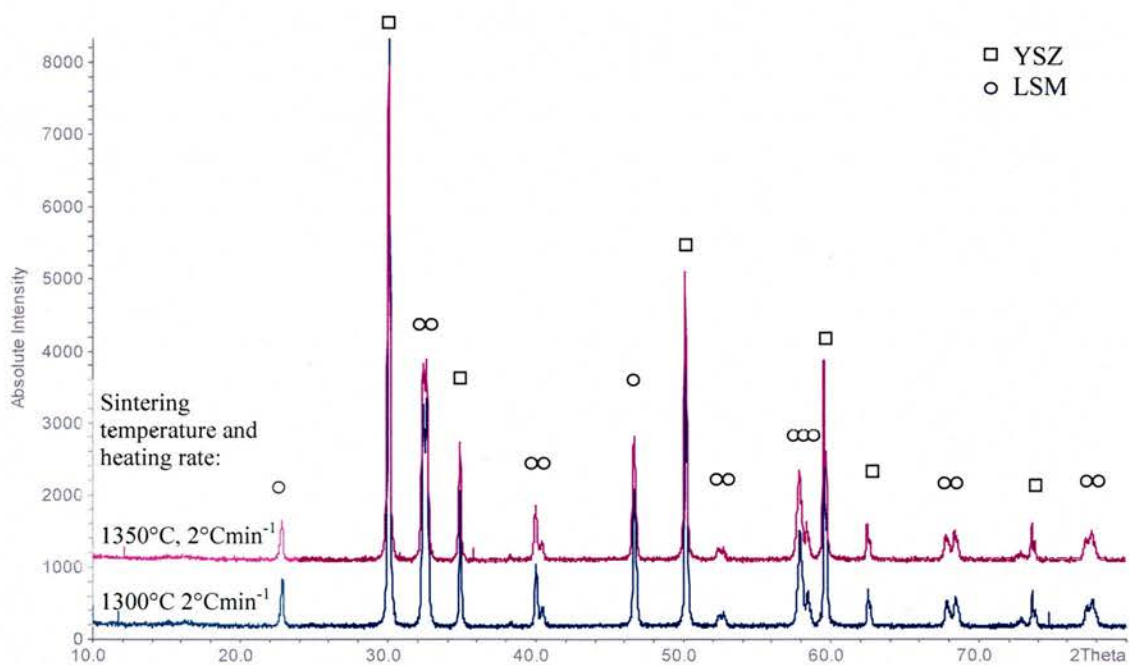
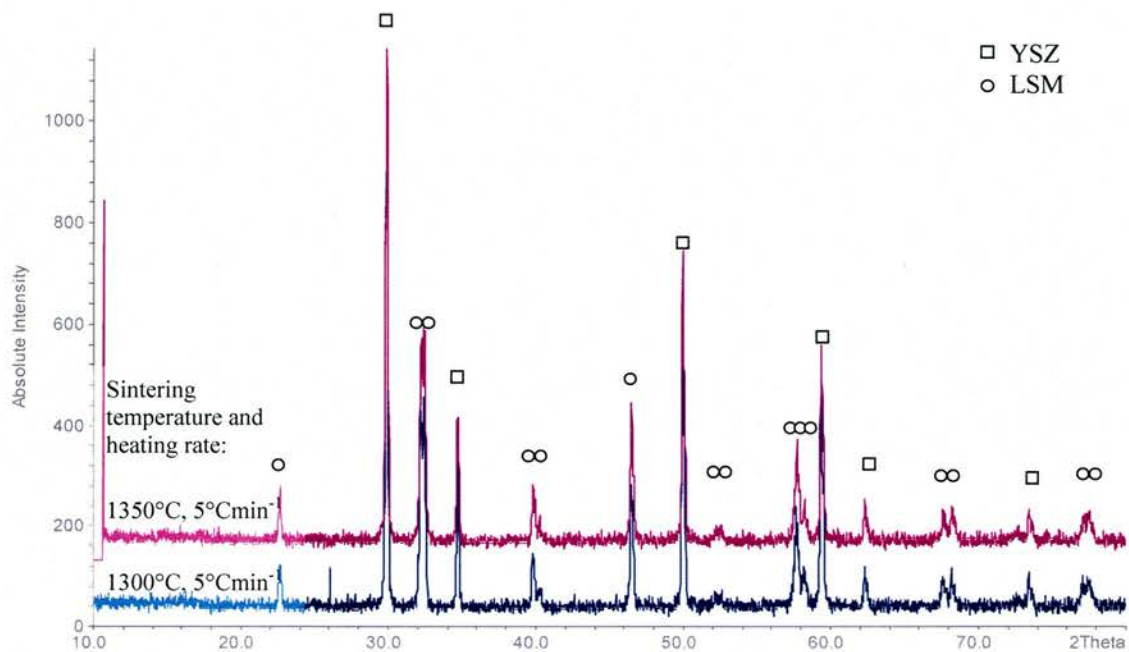


Figure 3.55: XRD trace for the reaction of YSZ (Pi-Kem Ltd) and $(La_{0.8}Sr_{0.2})_{0.95}MnO_3$ (Nextech Ltd) at 1300°C for 5hrs, and 1350°C for 5hrs at a) 5°Cmin⁻¹ and b) 2°Cmin⁻¹

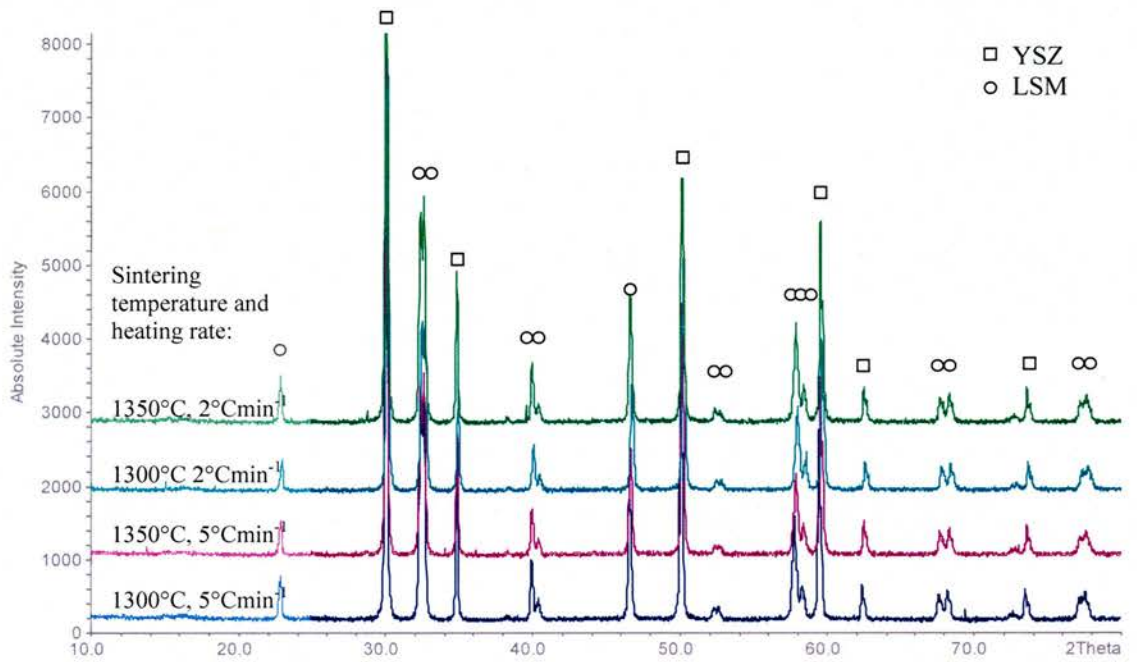


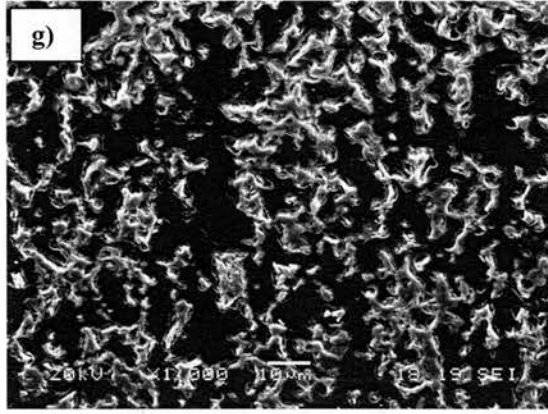
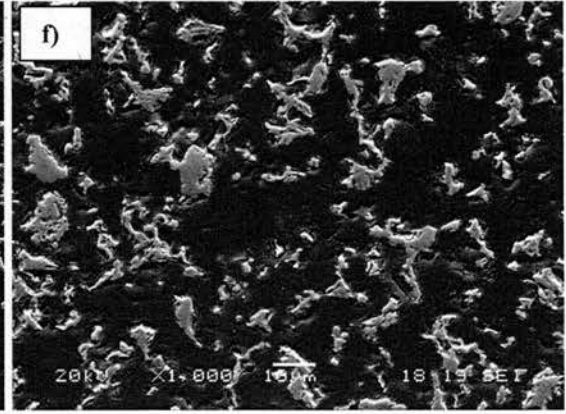
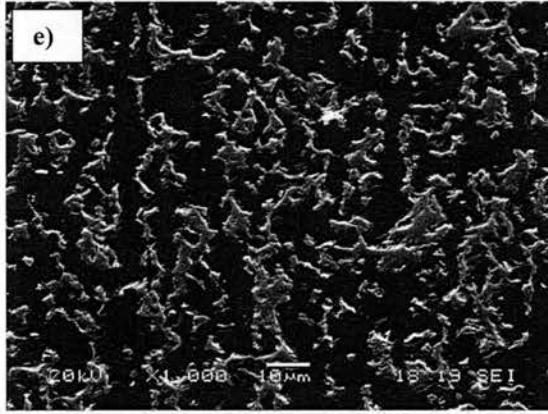
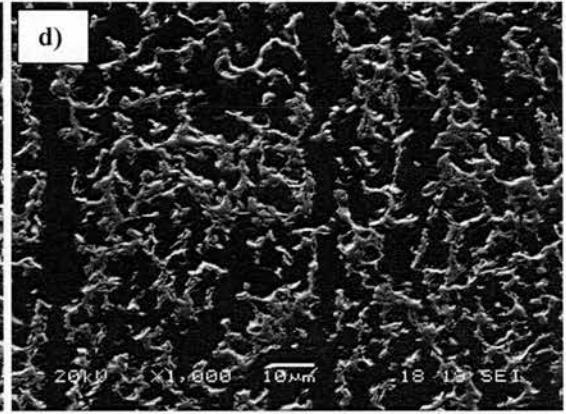
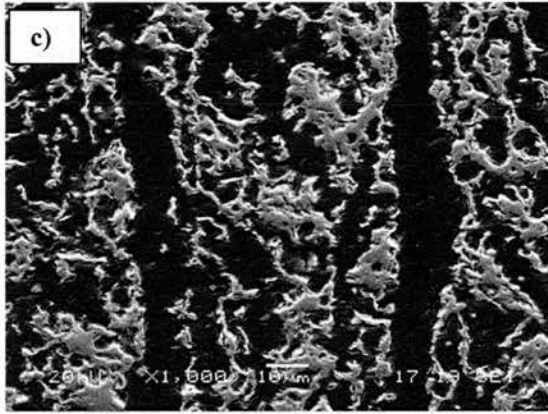
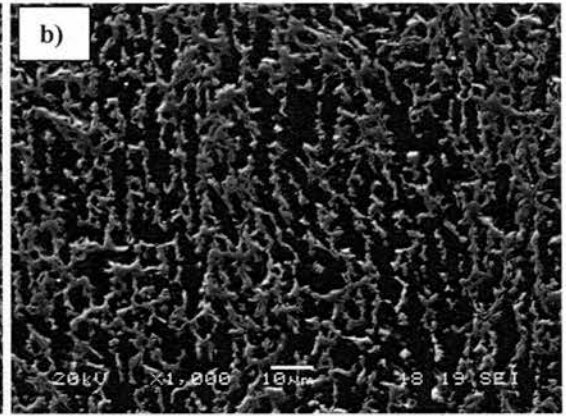
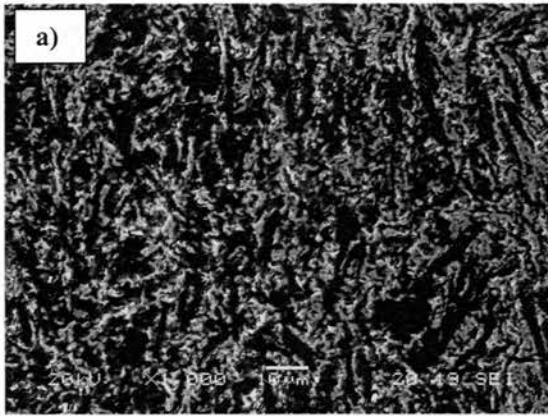
Figure 3.56: XRD trace for the reaction of 2µm YSZ (Unitec Ltd) and $(\text{La}_{0.8}\text{Sr}_{0.2})_{0.95}\text{MnO}_3$ (Nextech Ltd) at 1300°C for 5hrs, and 1350°C for 5hrs at different heating rates

large grains seen from particle sintering. This decreases the surface area (table 3.1) thereby reducing the contact area between the YSZ (Pi-Kem Ltd) and LSM, resulting in a reduced quantity of pyrochlore formation.

Production of $(\text{La}_{0.8}\text{Sr}_{0.2})_{0.94}\text{MnO}_3$ (6% A-site deficiency) was performed at 1050°C only and results from the reaction of both $(\text{La}_{0.8}\text{Sr}_{0.2})_{0.94}\text{MnO}_3$ and 5% A-site deficient $(\text{La}_{0.8}\text{Sr}_{0.2})_{0.95}\text{MnO}_3$ (Nextech Ltd) with YSZ (Pi-Kem Ltd) shown in figure 3.54, show no presence of the lanthanum zirconate pyrochlore. Further tests investigating pyrochlore formation between both YSZ (Pi-Kem Ltd) and 2µm YSZ (Unitec Ltd) and $(\text{La}_{0.8}\text{Sr}_{0.2})_{0.95}\text{MnO}_3$ at a higher sintering temperature of 1350°C and at slower heating rates of 2°Cmin⁻¹ for flexibility in SOFCRoll production. Figures 3.55 and 3.56 show that no reaction occurs between the 5% A-site deficient LSM for the two YSZ sources at a temperature as high as 1350°C and at both temperatures with the slower heating rate.

3.6.2 100% LSM Cathodes (porous)

Tapes were produced from all LSM20 powders listed in table 3.1. In order to produce a porous microstructure upon firing, a graphite pore former was used (-325 mesh, Aldrich Ltd) in a ratio of 30:70 (by mass) of graphite to LSM respectively, which is equivalent to 60:40 (by volume, considering the density of stoichiometric LSM20). The quantities of relevant organic additives and batch sizes are detailed in table 2.2 (section 2.4), and the firing profiles used are as detailed in section 2.10 with a sintering temperature of 1300°C.



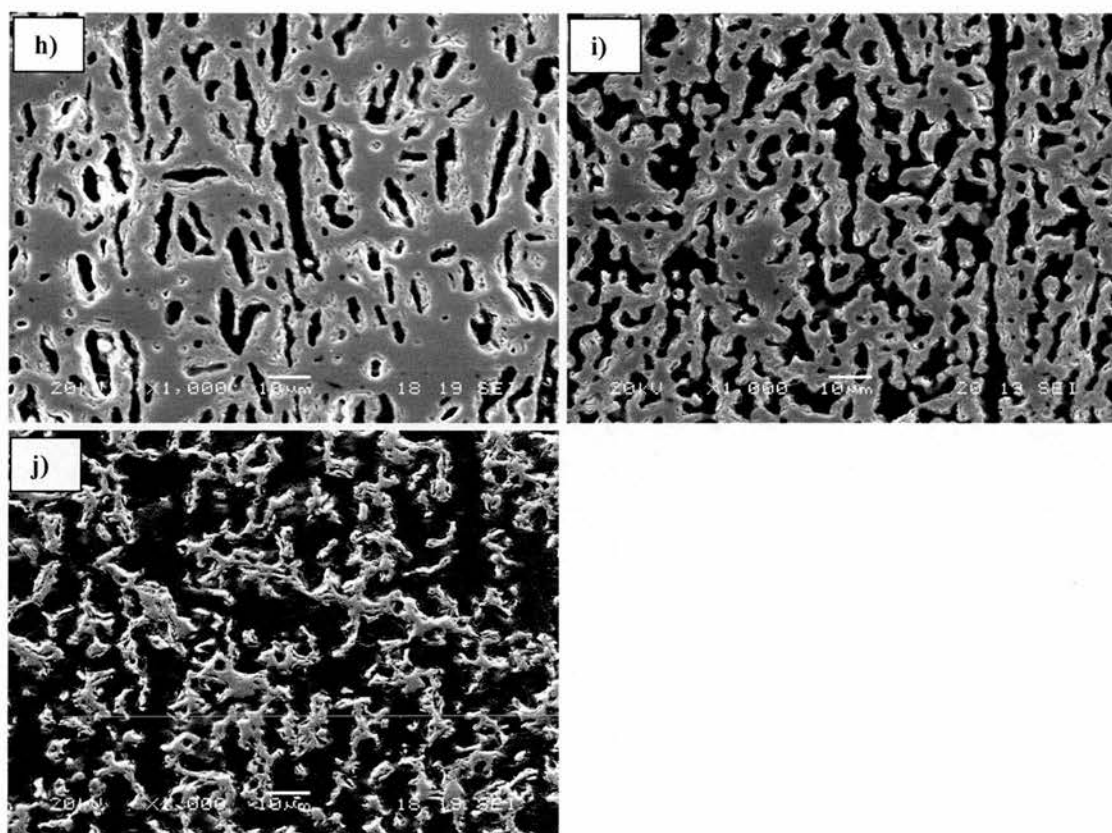


Figure 3.57: SEM images of cathode sheets fired as described in section 2.6.2 with a sintering temperature of 1300°C.

- a) stoichiometric LSM used as received, b) 2% A-site deficient LSM used as received,
- c) 3% A-site deficient LSM produced at 1000°C, d) 3% A-site deficient LSM produced at 1050°C, e) 3% A-site deficient LSM produced at 1100°C, f) 3% A-site deficient LSM produced at 1150°C, g) 3% A-site deficient LSM -2/3 produced at 1050°C and 1/3 produced at 1150°C,
- h) 5% A-site deficient LSM used as received, i) 5% A-site deficient LSM coarsened at 1000°C, j) 6% A-site deficient LSM produced at 1050°C

3.6.2.1 Microstructure

The cathode microstructures shown in figure 3.57 differ greatly depending on their A-site deficiency and initial particle size. The measured porosities of the cathodes are shown in table 3.5. As seen in section 3.5, the two different methods used to measure the porosity gave varied results, the maximum difference seen with the densest cathode at approximately 13%. Overall however, the agreement between the two different methods was much closer than that observed for the anodes. Additionally, whilst measurements performed by geometry always gave larger porosities for the anode, this was not the case for all cathodes produced. Similar to the porosity measurements by geometry for the anodes depending on the NiO being completely reduced to Ni thereby using the true density values, the accuracy of the porosity measurements by geometry for the cathodes depend on the density of the LSM staying constant with A-site deficiency – an additional area for errors.

Comparing the cathodes produced from the 3% A-site deficient LSM, the porosity increased with increasing temperature of manganese incorporation to the unit cell. The microstructure of the cathode comprised of 3% A-site deficient LSM produced at 1200°C was not able to be investigated as films produced from this powder did not compact enough to produce a film, but remained a powder after calcining to 1000°C, preventing the cathode being transferred from the furnace brick to the YSZ sheet used for high temperature sintering. When cathodes of this LSM (produced at 1200°C) were fired as a laminate on YSZ sheets, even after firing to 1300°C for 5hrs, the LSM particles had not sintered well together, as when brushed lightly with some tissue paper some LSM powder was transferred to the paper. Although the cathodes made from 3% A-site deficient LSM produced at 1150°C, did

form films after calcination at 1000°C, these were very weak in nature as reflected by the large porosity in the fired structure.

The large particle size of the deficient LSM produced at high temperatures of 1150°C and 1200°C (see figure 3.2, table 3.1) would mean that the interparticle spacing of the LSM particles in the green tape would be very high due to the large volume of graphite. Additionally, these LSM powders had begun to sinter together (with grain boundaries being visible in the SEM analysis, see figure 3.2) prior to being made into a cathode tape, so weak further sintering at only 1300°C for 5hrs further explains the reason for the high porosity and weakly sintered films. The particles of the LSM powder produced at temperatures between 1000°C and 1100°C showed no visible grain boundaries in the SEM analysis (see figure 3.2) and sintered to a greater extent during heat treatment as a cathode film at 1300°C. It is likely that the LSM produced at the higher temperatures would sinter to a lesser extent at 1300°C, contributing to the increased porosities. The increased production temperature results in larger particle size (see figure 3.2, table 3.1) leading to increased inter particle spacing of the LSM particles in the green tape (as described above regarding LSM produced at 1150°C and 1200°C) a further explanation for the higher resulting porosities.

Comparison between the cathodes made from 3% and 6% A-site deficient LSM produced at 1050°C is not straightforward, as different graphite pore formers were used (Fisher Ltd and Aldrich -325 mesh respectively). Section 3.5.2.1 shows when anodes were produced with these pore formers, the porosity from graphite (Fisher Ltd) pore former was marginally greater than anodes produced with graphite (Aldrich -325 mesh) pore former irrespective of the method used to analyse porosity.

Cathode produced from $(\text{La}_{0.8}\text{Sr}_{0.2})_{1-x}\text{MnO}_3$		Measured porosity /%	
A-site deficiency (x)	Treatment of powders prior to tape casting	Geometry	Image analysis
0	n/a (powder used as received)	69.7	56.6
2	n/a (powder used as received)	58.6	58.0
3	*Produced at 1000°C, 15.5hrs	54.1	55.2
	*Produced at 1050°C, 15.5hrs	55.1	62.7
	*Produced at 1100°C, 15.5hrs	57.7	68.6
	*Produced at 1150°C, 15.5hrs	72.6	73.6
	*Produced at 1200°C, 15.5hrs	<i>unknown</i>	
	1/3 produced at 1150°C, 2/3 produced at 1050°C	61.4	56.7
5	n/a (powder used as received)	31.8	18.6
	Coarsened at 1000°C, 16hr 20mins	47.1	33.1
6	Produced at 1050°C, 15.5hrs	61.3	59.3

Table 3.5: Measured porosities of cathodes produced with varying different A-site deficient LSM powders *denotes graphite (Fisher Ltd) was used as the pore former, otherwise graphite -325mesh (Aldrich Ltd) was used.

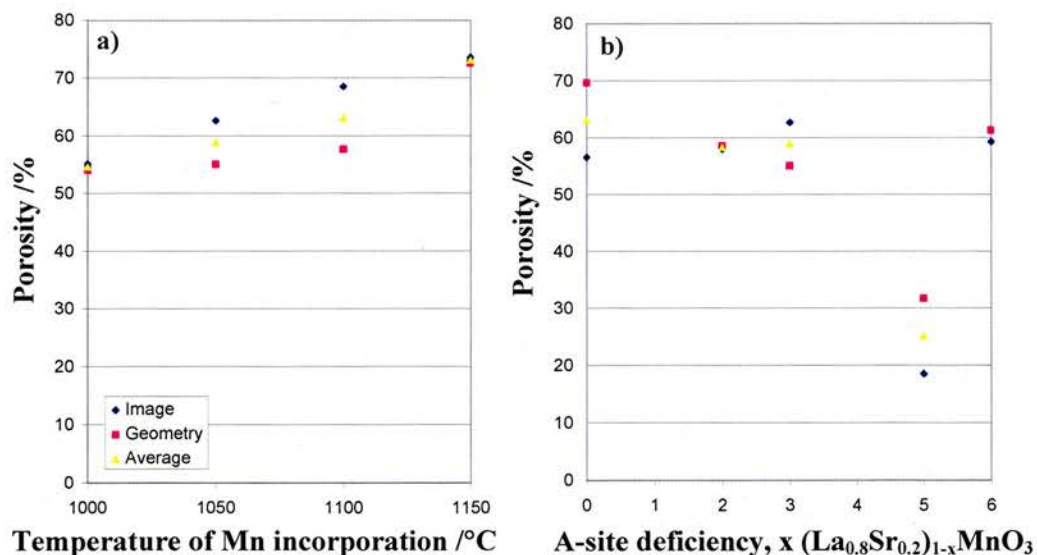


Figure 3.58: Graph showing a) the porosity vs production temperature for 3% A-site deficient cathodes and b) porosity vs LSM A-site deficiency for cathodes produced from commercial powders and powders modified at 1050°C

When the porosity values obtained from image analysis are considered, the 6 A-site deficient LSM cathode has the lower porosity, whilst the measurements by geometry show the opposite result. Consideration of the particle size only would suggest the porosity would increase with increased A-site deficiency (as increasing the A-site deficiency increases the particle size and so the inter-particle spacing in the green tape would be higher). This is also seen by the trend seen for the 3% A-site deficient LSM cathodes: the larger particle size LSM (obtained with higher production temperatures) leads to higher porosities. However, the sintering characteristics with different degrees of A-site deficiency change^[7], as reflected by the larger particle size of the 6% A-site deficient LSM compared to that of the 3% A-site deficient LSM produced at the same temperature, and by the increased shrinkages of the cathodes with higher A-site deficient LSM (see section 3.6.2.2). It is therefore not clear which method of analysis (geometry or image) gives the correct trend for cathode porosity with LSM A-site deficiency.

Plotting the measured porosities against the A-site deficiency of the LSM showed a general decrease in porosity with increasing A-site deficiency, see figure 3.58a. It is difficult to obtain a trend of porosity with LSM A-site deficiency due to the different routes and physical properties of the different LSM powders. The 2% and 5% A-site deficient powders were both produced by the same techniques (obtained by Nextech Ltd) and their resulting porosities would suggest that increasing the A-site deficiency resulted in reduced porosities. However, as shown in table 3.1, the surface area of the 5% A-site deficient powder was much higher, which would lead to increased sintering at high temperatures and could be the sole reason for the lower porosities.

Assuming the 5% A-site deficient LSM case to be an anomaly due to its much higher surface area, re-plotting to give figure 3.58b (production temperature of 1050°C taken for 3% and 6% A-site deficient LSM cathodes) all with similar surface areas $\pm 1\text{m}^2\text{g}^{-1}$ (table 3.1) shows very little change in porosity with A-site deficiency. This increase is probably due to a combination of particle size seen with increased A-site deficiency giving greater inter particle spacing in the green tape (due to the ceramic to organic additive ratio being the same for all cathodes)^[22, 27], leading to higher porosities and increased deficiency promoting particle-particle sintering^[7].

3.6.2.2 Shrinkage

The shrinkages of all the cathodes produced in section 3.6.2.1 were analysed for their shrinkage as described in section 2.6.1 in the high temperature region only to assess their suitability as the cathode material for co-firing with the electrolyte.

Figure 3.59 shows that the higher the degree of A-site deficiency of the LSM in the cathodes, the greater the shrinkage during the high temperature heat treatment. In this figure only one cathode produced from each A-site deficient LSM is shown: no prior heat treatment for 5% A-site deficient and for 3% and 6% A-site deficient powders produced at 1050°C. After calcining the cathodes at 1000°C, the cathodes produced from high A-site deficient LSM (5% and 6%) already have a significantly higher shrinkage than that of the electrolyte. It could be argued that this is related to the packing efficiency or inter-particle spacing of the LSM being lower or higher respectively than the cathodes with lower A-site deficiency LSM, however, since this is related to the initial particle size this cannot be the case as the 6% A-site deficient LSM has the largest particle size and 5% A-site deficient LSM has one of the

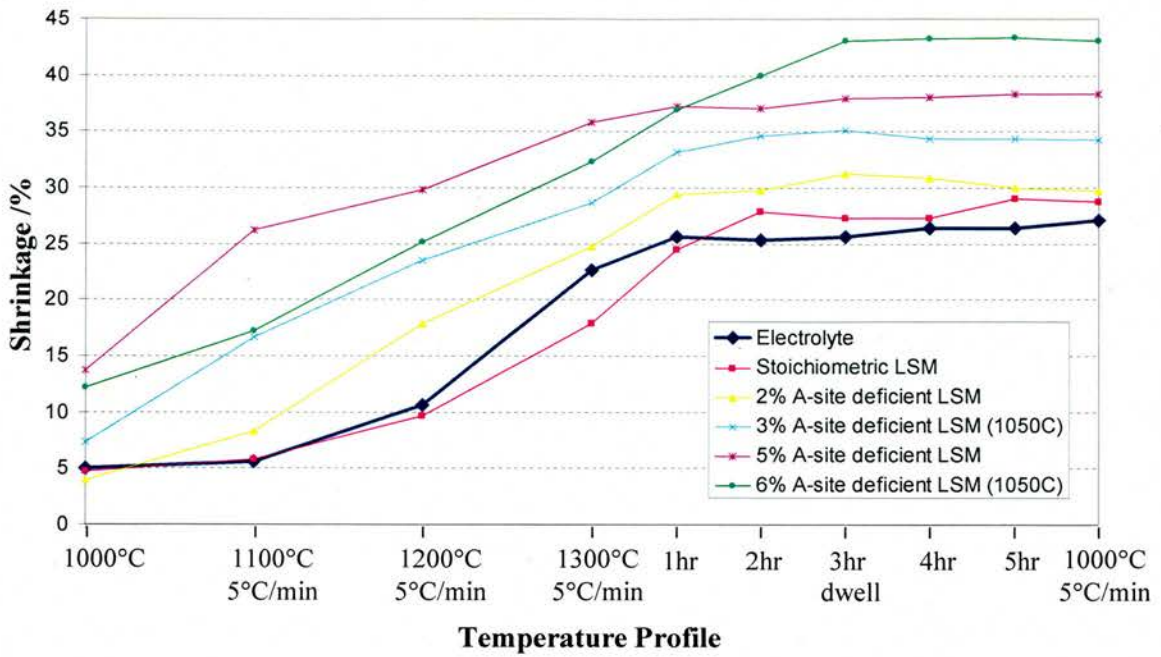


Figure 3.59: Shrinkage profiles of cathodes of LSM with different A-site deficiencies.

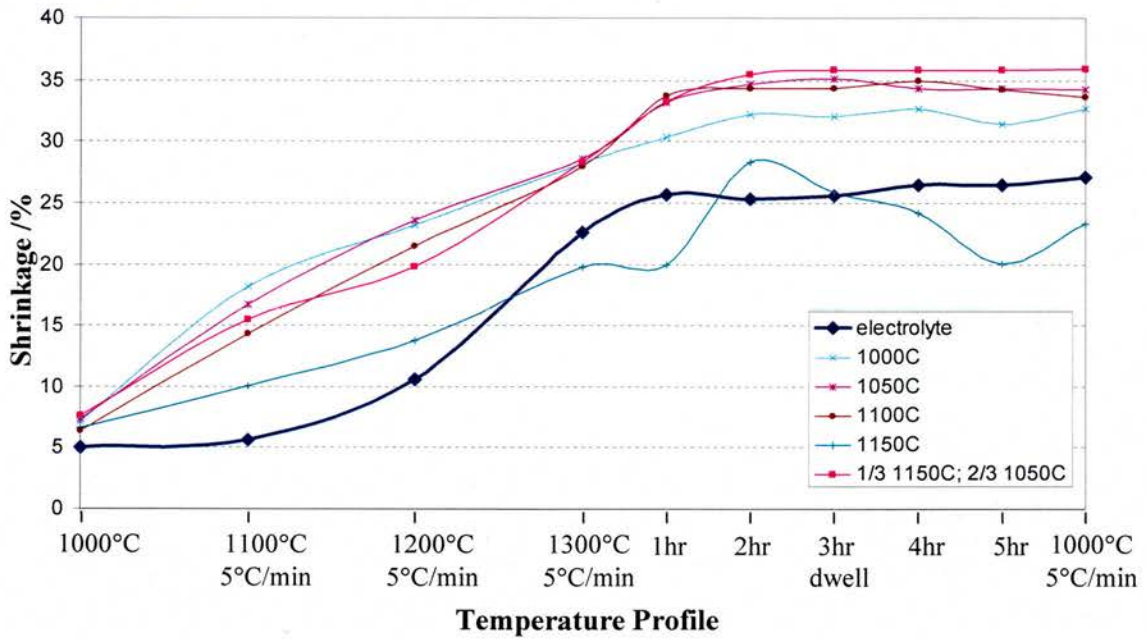


Figure 3.60: Shrinkage profiles of cathodes of $(La_{0.8}Sr_{0.2})_{0.97}MnO_3$ (3% A-site deficiency) powders produced at various temperatures

smallest. Section 3.2.1 showed that during the same temperature treatment, the resulting particle size of the 6% A-site deficient LSM was much larger than that of the 3% A-site deficient LSM, showing that the higher the A-site deficiency of the LSM, the greater the rate of sintering. The most likely explanation for the difference in shrinkage at 1000°C therefore, would be related to the sintering ability of A-site deficient powders^[35]: the higher A-site deficient LSM powders starting to sinter and hence show increased shrinkage by 1000°C.

If the shrinkage profile of the cathode produced from the 5% A-site deficient LSM is removed, there is a clear trend: the higher the A-site deficiency, the increased shrinkage. The cathode produced from the 5% A-site deficient LSM however has a higher shrinkage by 1000°C and during the ramp to 1300°C than the cathode produced from the 6% A-site deficient LSM. The most likely explanation for this is due to the difference in surface area of the particles (see table 3.1). The surface area of 2% A-site deficient and 6% A-site deficient LSM are the same and the stoichiometric and 3% A-site deficient LSM similar at $\pm 1\text{m}^2\text{g}^{-1}$. The surface area of the 5% A-site deficient LSM however, is double this value and it follows that it would sinter to a greater degree at lower temperatures. When the microstructures of the samples produced are compared (section 3.6.2.1), the change in porosity with A-site deficiency (removing the 5% A-site deficient sample) is minimal suggesting that it is related to initial particle size: the larger the particle size, the larger the inter-particle spacing, as the volume of graphite remains constant. After graphite burn-out therefore, the cathodes made from the larger particles have a higher porosity and hence greater ability for volume reduction, resulting in larger shrinkages.

The high temperature shrinkage profile of cathodes made from 3% A-site deficient LSM produced at 1200°C are not shown in figure 3.60, as after calcining to

1000°C, the remaining powder had not stuck together to form a rigid rectangular sheet. It could therefore not be transferred to the YSZ sheet for high temperature firing allowing no data to be collected. It was thought that the reason for the powder not forming a rigid rectangle after calcining was due to the high temperature used for incorporation of excess manganese into the structure rather than too high an organic content in the green tapes.

Particle size analysis of LSM powder produced at 1150°C (see section 3.2.1) shows that whilst the particles are smaller than when produced at 1200°C, there is still clear evidence of grains within particles. It is therefore not surprising that during high temperature shrinkage tests the powder in the rectangular samples had a higher affinity to sinter to the pre-coarsened LSM powder sprinkled on the YSZ sheet rather than to each other. This caused the rectangular samples to stick to the YSZ sheet at various points, preventing the uniform shrinkage of the samples resulting in the erratic nature of the high temperature shrinkage profile seen in figure 3.60.

Examination of the shrinkage profiles of cathodes from 3% A-site deficient LSM produced between 1000°C and 1100°C do show some trends with the temperature of manganese incorporation. During the ramp from 1000°C to 1300°C, the lower the temperature of manganese incorporation into LSM, the higher the shrinkage, whilst during the dwell at 1300°C, the tapes made with LSM produced at higher temperatures shrunk to a greater extent, resulting in greater final shrinkage. Attempts were made to reduce the shrinkage of 3% A-site deficient LSM cathodes by mixing 1/3 coarse (produced at 1150°C) with 2/3 fine (produced at 1050°C) particles. However as seen in figure 3.60 the high temperature shrinkage profile was much closer to that of the cathodes produced from entirely fine particles (manganese

incorporation at 1050°C) during the ramp to 1300°C, with the final shrinkage being slightly higher still.

There is not a clear trend for the shrinkage of these cathodes. Due to the differing initial particle size and hence surface area, it is probably not a 'fair' test to compare tapes produced with the same organic:powder ratios as the interparticle spacing in the green tapes will be different. The differing LSM particle sizes will also have different effects on the graphite particle sizes (the larger LSM particles grinding the graphite particle sizes less efficiently) and different packing efficiencies, all of which will affect the shrinkage of the tapes. The heating profile used for these samples was not sufficient to cause good sintering of 3% A-site deficient LSM particles produced at 1200°C and particles produced at 1150°C compacted poorly during high temperature sintering. It is therefore plausible that the tapes made from LSM made at lower temperatures had a higher shrinkage during the ramp to 1300°C, as they were able to begin sintering at a lower temperature. The powders produced at higher temperatures would have a larger inter particle separation after graphite burnout, greater porosity, and so be able to compact to a larger extent once the temperature was sufficiently high enough. Of the powders investigated, an A-site deficiency of at least 5% was required to prevent pyrochlore formation (section 3.6.1) and so further experiments concentrated on reducing the shrinkage of the cathodes with an A-site deficiency of 5%.

It was thought that the reason for the high shrinkage after the dwell at 1000°C in the cathodes produced with a 5% A-site deficient LSM was due to the high surface area and resulting lower temperature required for sintering of the LSM particles. Figure 3.61 supports this theory, as tapes produced from the coarsened 5% A-site

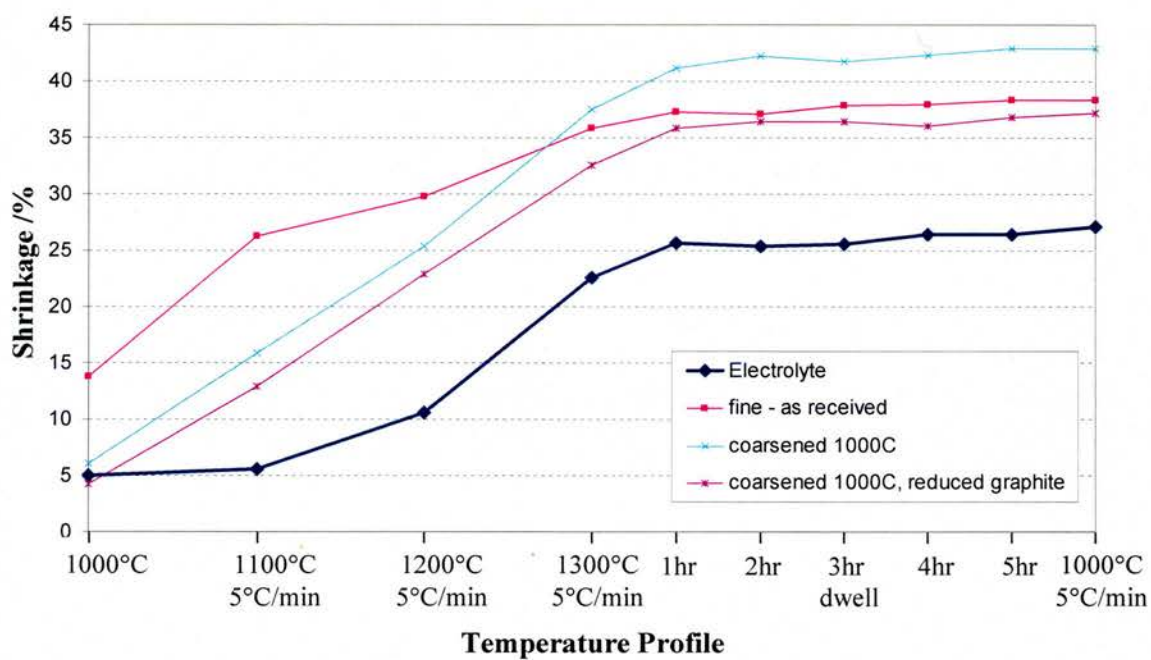


Figure 3.61: High temperature shrinkage profiles of cathodes of 5% A-site deficient LSM

deficient LSM had a shrinkage much closer to that of the electrolyte by 1000°C. Unfortunately however, in a similar manner to the coarser 3% A-site deficient LSM, this resulted in an increased shrinkage during the dwell at 1300°C, which can again be explained by a combination of larger inter particle spacing (due to increased particle size with no change in graphite/organic additive volume) with a higher temperature required to begin significant particle sintering (due to the particles being treated at 1000°C for over 16hrs prior to tape formation). An effective method for reducing shrinkage profiles (sections 3.5.1.2 and 3.5.2.2) is to reduce the graphite content. Whilst a reduction in graphite content from 60vol% in the green tape to 50vol% (regarding ceramic to graphite ratio) of the coarsened 5% A-site deficient LSM, was effective in reducing the shrinkage for the cathode, this reduced the porosity from 47.1% to 37.7% (analysis by geometry) 33.1% to 25.8% (analysis by image): less than ideal for the SOFCRoll, whilst not sufficiently reducing the shrinkage to match that of the electrolyte.

3.6.3 LSM & YSZ composite

Production of 100% $(\text{La}_{0.8}\text{Sr}_{0.2})_{0.95}\text{MnO}_3$ cathodes detailed in section 3.6.2 proved difficult as increasing graphite content or coarsening the particles (methods for introducing porosity section 3.4) further increased the high temperature shrinkages, which were already much higher (approximately 10% difference) than the electrolyte. Work on the anode showed that increasing YSZ content moved the shrinkage profile closer to that of the electrolyte (section 3.5.3), also seen in the literature^[23, 33] and this was investigated as a solution to shrinkage/microstructure problems with the cathode.

Having a composite LSM-YSZ will greatly reduce the electronic conductivity of the cathode, which will have detrimental effects on the performance of the

SOFCRoll due to the long current paths and the reliance on the electrodes for current collection. The composite LSM-YSZ will however have beneficial effects of improving adhesion between the electrolyte^[10] and increased triple-phase boundaries for lowering polarisation losses^[11-12, 36]. Referring back to section 3.6.2, the shrinkage profile and microstructure of cathodes produced from the stoichiometric LSM fit the requirements of SOFCRoll, so it seems sensible to produce a double cathode consisting of a thin 'functional' YSZ-LSM cathode and a thicker 100% LSM for current collection and gas transport through the spirals.

This section describes the production of a composite cathode with an LSM:YSZ ratio of 1:1 by mass. The ceramic to graphite ratio was kept at 2:3 by volume in order to achieve adequate porosities. Only the 5% A-site deficient LSM was investigated as it is imperative that no pyrochlore phase is present in this layer.

3.6.3.1 Microstructure

The microstructures and measured porosities of the cathodes produced are shown in figure 3.62 and table 3.6 respectively. Having a multi-layer cathode, one with a high triple phase boundary and one purely as a current collector allows the porosity of the LSM-YSZ composite layer to be below the desired 50% for the SOFCRoll. Again as seen in section 3.6.2 and 3.5, the two different methods used for obtaining porosities vary greatly by as much as 15%. The porosity obtained for the cathode composed of fine LSM and 1 μ m YSZ by image analysis was thought to be inaccurate, as not all of the pores were filled with epoxy, as seen in figure 3.62, resulting in poor contrast between the epoxy filled holes and the ceramic, giving lower than true porosity.

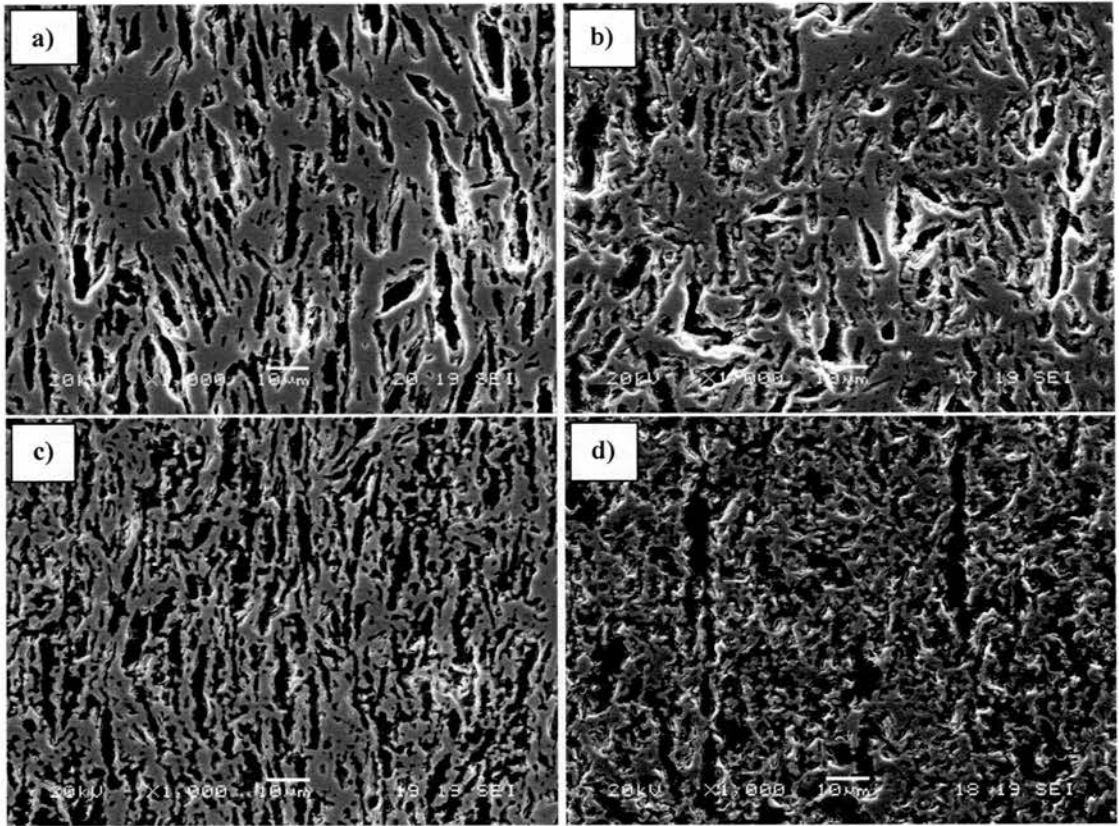


Figure 3.62: SEM images of composite cathodes fired as described in section 2.6.1 of a) YSZ (Pi-Kem Ltd), 5% A-site deficient LSM (Nextech Ltd), b) 1µm YSZ (Unitec Ceramics Ltd), 5% A-site deficient LSM (Nextech Ltd), c) 2µm YSZ (Unitec Ltd), 5% A-site deficient LSM (Nextech Ltd) and d) YSZ (Pi-Kem Ltd), 5% A-site deficient LSM coarsened at 1000°C, 16hr 20mins

Heat treatment of (La _{0.8} Sr _{0.2}) _{0.95} MnO ₃ (Nextech Ltd)	YSZ source	Measured porosity	
		Geometry analysis	Image analysis
As received	Pi-Kem Ltd	45.0	29.5
	1µm Unitec Ceramics Ltd	31.7	22.7
	2µm Unitec Ceramics Ltd	52.9	40.3
Coarsened at 1000°C, 16hr 20min	Pi-Kem Ltd	54.9	42.2

Table 3.6: Measured porosities of composite cathodes produced with 5% A-site deficient LSM powders and various YSZ powders in a 1:1 ratio by weight.

By visual examination of the microstructures (figure 3.62) it seemed that a preferable porous network was obtained when coarsened LSM was used, resulting in smaller pores. Since the porosity of the cathodes composed of 2 μ m YSZ or coarse LSM was still reasonably high, the graphite content could be reduced, to give better shrinkage match with the electrolyte, see section 3.6.3.2.

3.6.3.2 Shrinkage

Comparison of the high temperature shrinkages obtained from composite cathodes (figure 3.63) with the high temperature shrinkages obtained from 5% A-site deficient LSM only cathodes (figure 3.61), shows that addition of the YSZ into the tape reduces the high temperature shrinkages. As seen in figure 3.61, the sintering of the fine (as received) LSM in the absence of any YSZ had begun by 1000°C, the cathode shrinkage being approximately 13% higher than the electrolyte, whilst coarsening at 1000°C prior to tape production reduced this shrinkage to just 1.5% higher than that of the electrolyte. Addition of the YSZ material reduced this shrinkage in all composite cathodes, to approximately 2% below that of the electrolyte when coarse LSM was used, and between 1.5% (with the fine YSZ and LSM investigated) and 2.5% (with the coarser two YSZ and fine LSM particles used) higher than the electrolyte.

After the ramp to 1300°C the shrinkage of all the cathodes was very close to that of the electrolyte, however during the ramp, the cathodes began to shrink at lower temperatures than that of the electrolyte, with no cathode giving an ideal shrinkage profile in this temperature range. The cathode with the closest shrinkage match to the electrolyte during the ramp to 1300°C was produced from the pre-coarsened LSM,

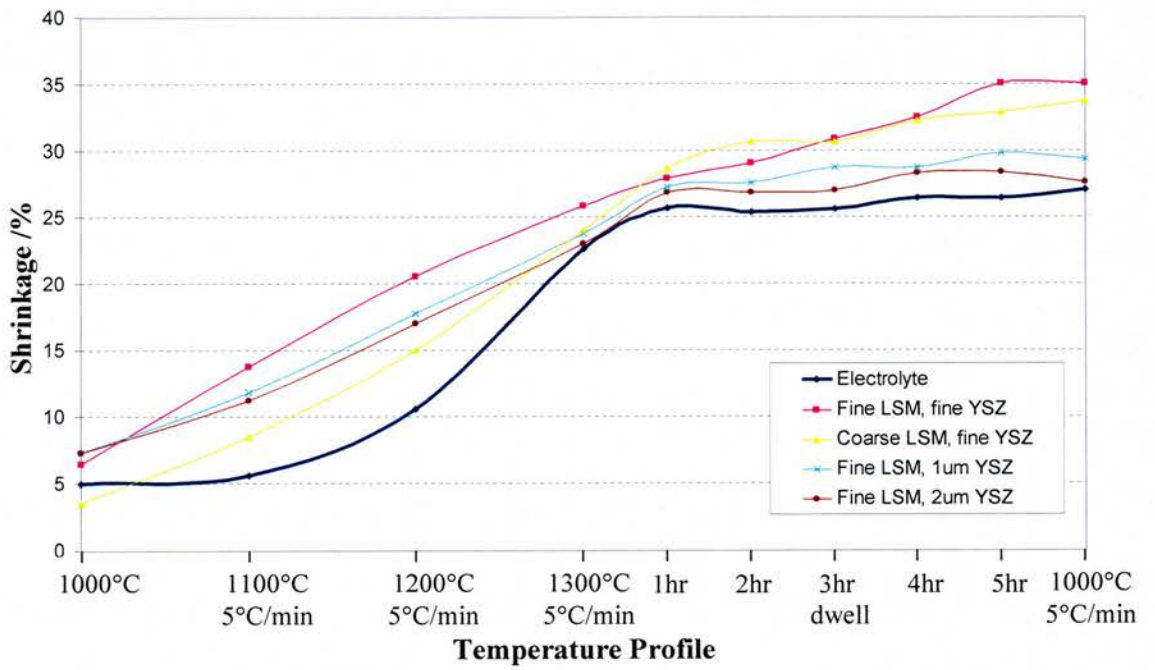


Figure 3.63: Shrinkage profile of $(La_{0.8}Sr_{0.2})_{0.95}MnO_3$ and YSZ (1:1 by weight) composite cathodes

however as seen with the LSM only cathodes, when coarser LSM particles were used, the final shrinkage during the dwell at 1300°C was higher. Unlike the case with the cathodes containing no YSZ, the shrinkage during the dwell at 1300°C, was not great enough to result in a final shrinkage higher than the cathodes produced from fine LSM particles (with fine YSZ particles). This was presumably due to the better packing efficiency of the powders in the composite cathodes, comprised of coarse and fine particles, resulting in a denser structure after graphite burnout and so reducing the shrinkage at high temperatures. The reason that the shrinkage during the ramp to 1300°C remained lower than the corresponding cathode produced from fine YSZ and fine LSM particles was due to the pre-sintering at 1000°C.

The best shrinkage match to the electrolyte during the dwell at 1300°C was seen by the composite cathode produced from the coarsest YSZ investigated: 2µm, and with the fine LSM particles, and the best shrinkage match to the electrolyte during the ramp to 1300°C was seen by the composite cathode produced from the coarsened LSM and fine YSZ particles: 0.2µm. Whilst neither cathode had an ideal shrinkage profile to that of the electrolyte, the cathode composed of fine LSM and coarser YSZ particles was used in fuel cell production.

A lot of literature exists concerning the effects of YSZ content on the polarisation resistance of the cathodes. The polarisation resistance approaches a minimum value as the triple phase boundary length is maximised, whilst the ohmic resistance increases with increasing YSZ to LSM ratios^[37]. With the use of a double layer cathode as proposed at the start of section 3.6.3, allows the composite layer to have a maximum tpb length without sacrificing the fuel cell performance due to an increased ohmic resistance. In this study the high YSZ content of LSM to YSZ ratio 1:1 (by mass) was required to obtain a better shrinkage match to the electrolyte. The

high YSZ to LSM particle size ratio used in this investigation helps to maximise the triple phase boundaries, however the performance is very dependent on the microstructure^[36] and so the high porosity will have the opposite effect since increasing porosity of the cathodes mean higher LSM to YSZ ratios are required for minimum polarisation resistance^[10]. Additionally the particle size ratios of the LSM to YSZ would have a large effect on the relative ratios required for maximising triple phase boundaries and hence minimising polarisation resistance as shown with the anode^[23, 25-26, 29]. Further work would therefore be beneficial to obtain cathodes of higher LSM to YSZ ratios with matching shrinkages to be used in conjunction with this cathode to improve both polarisation resistance and further reduce strain on the system caused by thermal mismatch between the cathode and the electrolyte^[11].

3.6.4 100% LSM (dense)

Section 3.6.2 showed that when tapes were produced with 5% A-site deficient LSM and 60vol% graphite (in terms of ceramic and graphite particles), that the tapes are surprisingly dense. Referring to the shrinkage tests of these samples, the shrinkage was improved by coarsening the LSM particles and reducing the graphite content. It therefore seems feasible that the shrinkage could be matched to the electrolyte by removing the graphite completely to produce a dense film. Dense LSM could be beneficial in the SOFCroll for current collection and possibly gas flow if made in a mesh or strips rather than a solid film^[38].

3.6.4.1 Microstructure

Films produced from both fine and coarsened 5% A-site deficient LSM have a high density after firing to 1300°C as can be seen by their cross-sectional

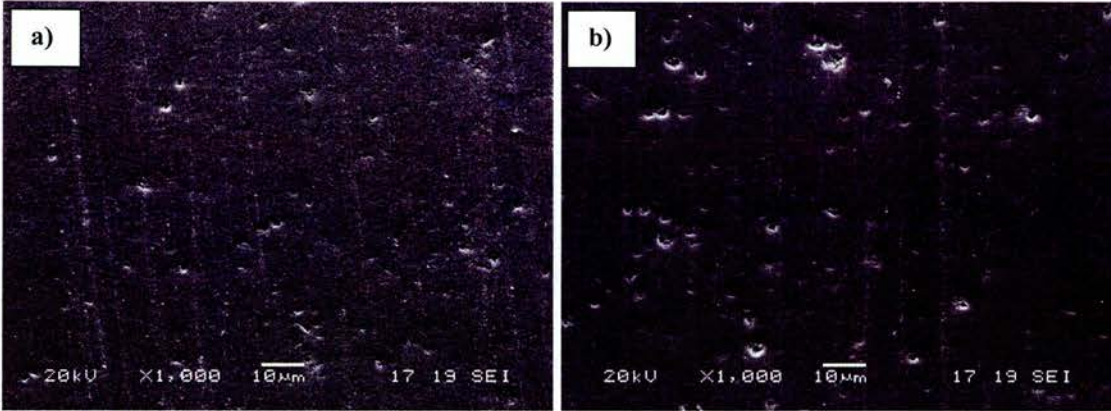


Figure 3.64: SEM images of dense 5% A-site deficient LSM films produced from a) fine (as received particles) and b) coarsened at 1000°C 16hr, 20mins

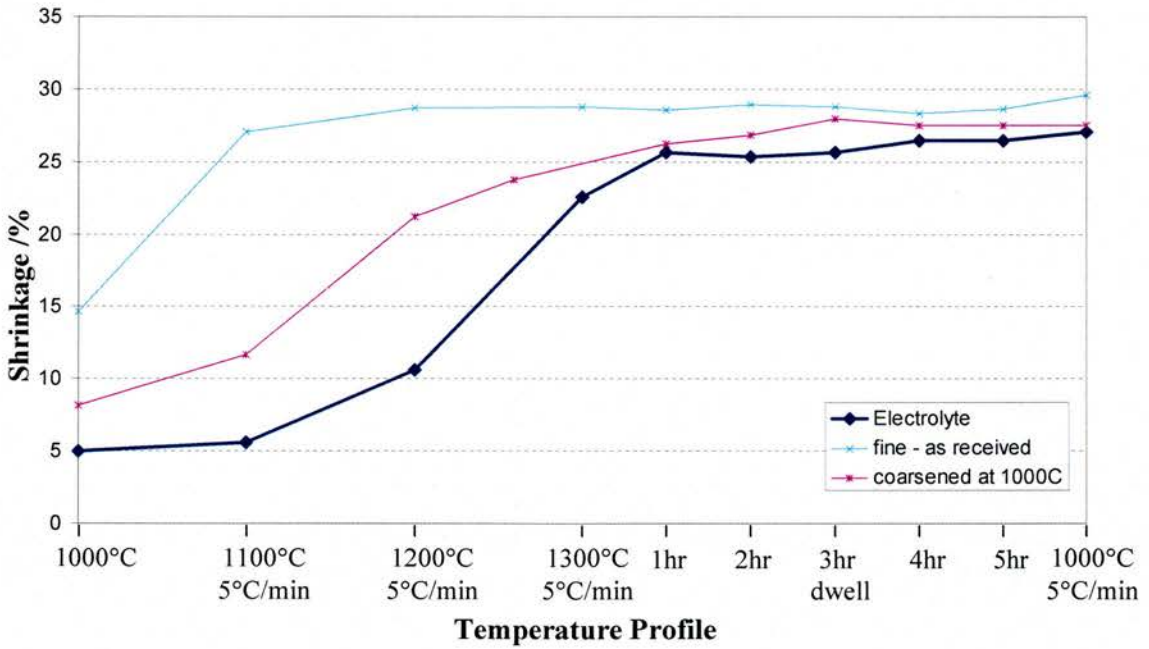


Figure 3.65: High temperature shrinkage profiles of dense films of 5% A-site deficient LSM

microstructure shown in figure 3.64. The density of the sintered films were similar with the film produced from the coarser LSM having fewer, but larger pores. Measured densities were 88.4% and 84.2% (by geometry analysis), 97.9% and 97.2% (by image analysis) when produced from as received or coarsened at 1000°C for 16hr, 20mins powders respectively. The grainy nature of the images obtained for these cathodes, meant that the density values obtained by image analysis had a high level of inaccuracy. Coarsening the particles however, resulted in reduced densities (irrespective of which method was used), however the densities are too high to aid gas flow and as such could only be used as a current collector in the form of strips through the spirals of the SOFCRoll^[38].

3.6.4.2 Shrinkage

Figure 3.65 shows that the high temperature shrinkages of the dense tapes are close to that of the electrolyte during the dwell period of the temperature profile. However, it was necessary to pre-coarsen the LSM particles for matching of the shrinkage during the ramp from 1000°C to 1300°C, otherwise the shrinkage was much too high – similar to the porous cathodes produced from the as received 5% A-site deficient LSM in section 3.6.3.2. Further pre-coarsening, reduction in the amount of organics, or a mixture of both would be beneficial in order to reduce the shrinkage during the ramp further still to give a better match with the electrolyte.

3.6.5 Summary

As expected from the literature^[14, 19-21] (see section 1.4.3) the stoichiometric LSM reacted with the YSZ at 1300°C to form the LZO pyrochlore. With an A-site

deficiency of 5% however, no pyrochlore was visible by XRD analysis at sintering temperatures up to 1350°C.

Increasing the A-site deficiency in the LSM resulted in increasing the high temperature shrinkage giving a difference of 10% to that of the electrolyte after sintering to 1300°C. This is believed to be due to an increased affinity for particle-particle sintering, suggested by the literature on other A-site deficient perovskites^[35] and the increased particle size with increased A-site deficient LSM, when produced at 1050°C. Bearing this information in mind, a 2-layer electrode was proposed: 1:1 by mass of 5% A-site deficient LSM to YSZ and 100% stoichiometric LSM. The composite electrolyte would give high triple phase boundaries and improved adhesion to the electrolyte, whilst the 100% LSM layer aids the cathode conductivity.

Dense 5% A-site deficient LSM can be produced, the shrinkage of which has been improved relative to the electrolyte by particle coarsening prior to tape production. Further work is however required if this material is to be fully matched as a current collector for the SOFCroll.

3.7 Sintering of multi-layers

3.7.1 Introduction

This section deals with the shrinkage of different anodes and cathodes used in the fuel cells whose performance is detailed in chapter 4. Throughout this chapter, anode 1 and cathode 1 refer to the anodes with a high triple phase boundary: nickel to YSZ ratio of 2:3 by volume, (NiO to YSZ ratio of 55:45 by mass, ceramic to graphite ratio of 3:2 by volume in the green tape) and LSM20 (with 5% A-site deficiency) to YSZ ratio of 1:1 by mass (ceramic to graphite ratio of 2:3 by volume in the green tape) respectively. Anode 2 and cathode 2 therefore refer to the electrodes with high electronic conductivity, used as current collectors: nickel to YSZ ratio of 4:1 by volume (NiO to YSZ ratio of 88:12 by mass, ceramic to graphite ratio of 1:1 by volume in the green tape) and LSM20 only (ceramic to graphite ratio of 2:3 by volume in the green tape).

Sections 3.3, 3.5 and 3.6 have detailed the production and firing of the electrolyte, anode and cathode as single components. It has been attempted to match the shrinkage profiles of these components in order to minimise stresses during firing of laminates of all components, however in order to obtain a high performance fuel cell, sacrifices have been made to the shrinkage match, such as increased NiO content to give adequate conductivity upon reduction leading to below ideal shrinkages. This section details results obtained by the dilatometer for rate controlled sintering. Controlling the sintering in this way, by incorporating a series of dwell stages in the heating profile, will lead to reduced rates of shrinkages allowing a greater toleration of shrinkage mismatches between components. Additionally it will highlight temperature ranges where the heating rate can be increased resulting in a quicker overall sintering regime.

3.7.2 Rate Controlled Sintering (RCS) of fuel cell components

Figures 3.66 and 3.67 show the shrinkage profiles of the anodes, electrolyte and cathodes obtained by the dilatometer with sintering temperatures of 1300°C and 1350°C, using the heating rates described in section 2.10. When considering these shrinkage profiles, points to note regarding the measurements performed using the dilatometer for the electrolyte and anodes should be borne in mind. The large shrinkages seen during plasticizer burnout present in the cathodes and anodes was thought to be due to the increased organic content required due to the presence of graphite particles and the softness of the graphite particles, resulting in greater deformation by the pushrod, as shrinkages of this magnitude were not seen when analysed by measurement of rectangle samples (see section 2.6.1). Similarly, the large expansion seen at temperatures between 500°C and 700°C for the anodes was believed to be due to tape curling. The force of the push rod was also thought to affect the shrinkage of the anode current collector, as it was very weak in nature and easily broken. Finally, the electrolyte always had cracks in the centre of the sample after the shrinkage run was performed, suggesting it is constrained in the x-y direction (z being the thickness of the film) which would affect the measured shrinkages.

Rate controlled sintering of the samples was performed after the initial slow ramp to 125°C at 0.5°Cmin⁻¹. If rate controlled sintering was performed from room temperature, catastrophic cracking of the electrolyte occurred. The low temperature rate controlled sintering profiles are shown in figure 3.68, showing that by increasing the ramp rates where little or no shrinkage is seen and incorporating dwell periods during high shrinkage rates reduced the time taken to heat to 1000°C by 19hr, 20min. The observed shrinkages however changed; after heating to 1000°C by rate controlled

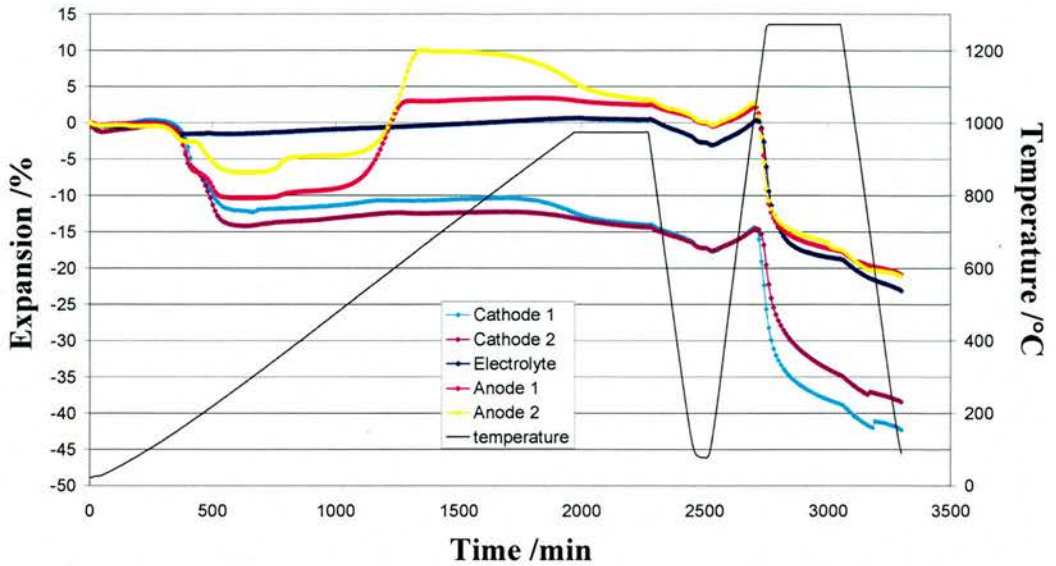


Figure 3.66: Shrinkage profile of anodes, electrolyte and cathodes used in fuel cell production. Heating rate to 1000°C was 0.5°Cmin⁻¹, heating rate to 1300°C and all cooling rates were 5°Cmin⁻¹ and a dwell time of 5hrs at both 1000°C and 1300°C was used.

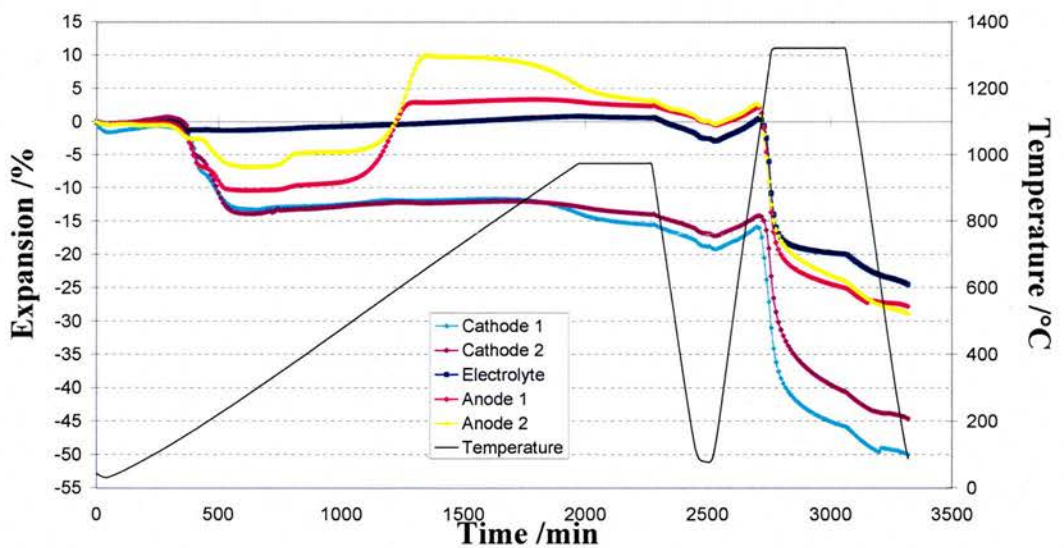


Figure 3.67: Shrinkage profile of anodes, electrolyte and cathodes used in fuel cell production. Heating rate to 1000°C was 0.5°Cmin⁻¹, heating rate to 1350°C and all cooling rates were 5°Cmin⁻¹ and a dwell time of 5hrs at both 1000°C and 1350°C was used.

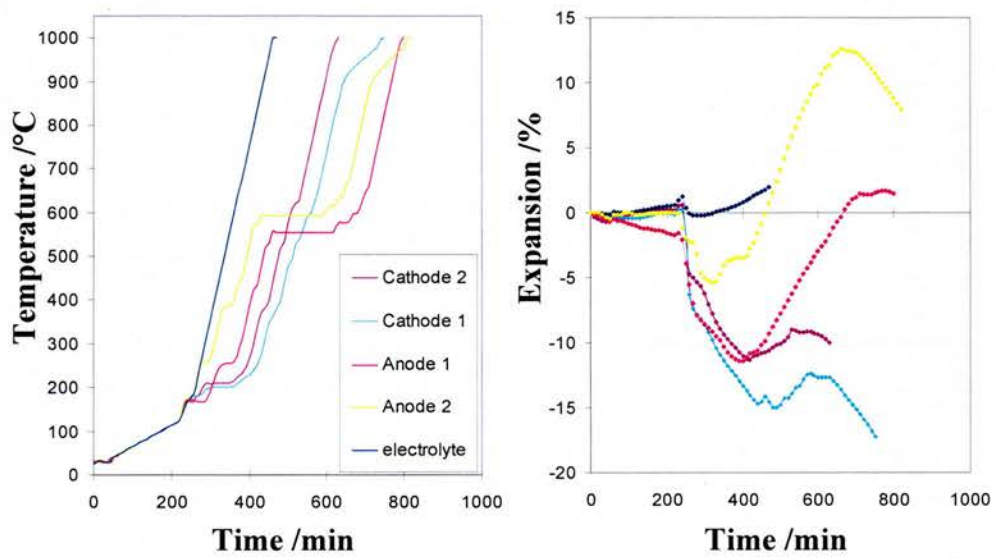


Figure 3.68: Rate controlled sintering of the 5 fuel cell components between 125°C and 1000°C corresponding to removal of all organic material in the tape. Samples were heated to 125°C at 0.5°Cmin⁻¹ prior to rate controlled sintering.

sintering, the electrolyte, anode 1 and anode 2 showed an expansion of 1.95% (previously 0.65%), 1.4% (previously 3.0%), 7.9% (previously 5.2%) and cathode 1 and cathode 2 had a shrinkage of 17.2% (previously 12.6%) and 10.0% (previously 13.2%) respectively. Additionally, the largest expansion seen by anode 2 increased from 10.0% to 12.5% and the largest shrinkage observed from cathode 1 increased from 12.6% to 17.2%. Although it is difficult to compare the shrinkage mismatches between the different materials as each component experienced a different heating profile, the rate controlled sintering seemed to be detrimental to the shrinkage matching of the different components.

The high temperature rate controlled sintering at 1300°C and 1350°C are shown in figures 3.69 and 3.70 respectively. Just as the heating rate of the composite cathode and current collector anode were reduced above 900°C during the low temperature rate controlled sintering (figure 3.68), their high temperature heating profiles were similar, slowing down at 1070°C. The reduction in heating rate at 1070°C, whilst being lower than the onset of rate controlled sintering for the other components was at a faster heating rate than the reduced heating rate required for rate controlled sintering with the other 3 components. The electrolyte, anode 1 and cathode 2 had similar heating rates up to approximately 1290°C, where the shrinkage rate of the electrolyte slowed and resulting in a return to the 5°Cmin⁻¹ heating rate.

When considering the modification of heating rates when firing the fuel cells, the heating rates were slowed between 50°C and 260°C corresponding to the shrinkages observed during plasticizer burn-out, and between 360°C and 650°C corresponding to the large expansions seen in the anode. Since the affect of the push

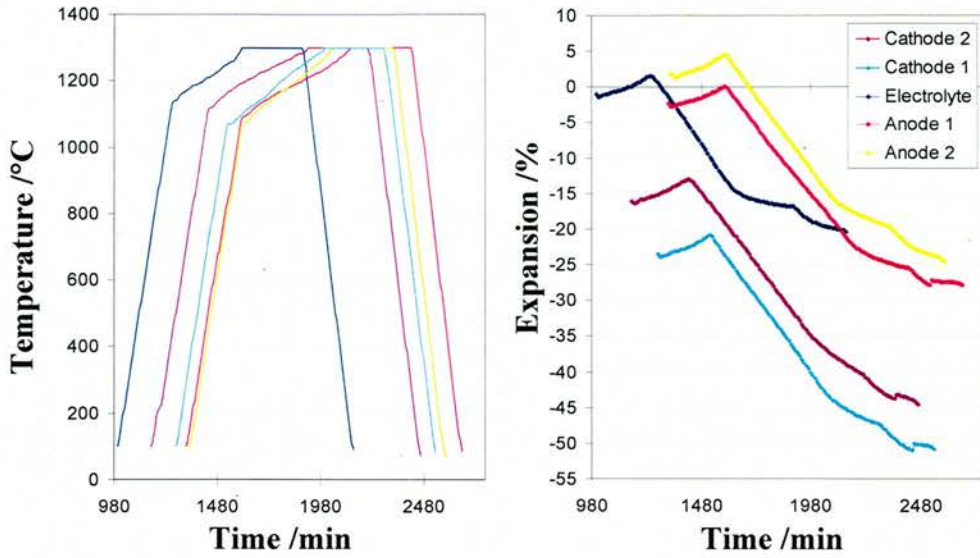


Figure 3.69: Rate controlled sintering of the 5 fuel cell components between room temperature and 1300°C. Samples had been subjected to rate controlled sintering according to figure 3.68 prior to high temperature rate controlled sintering.

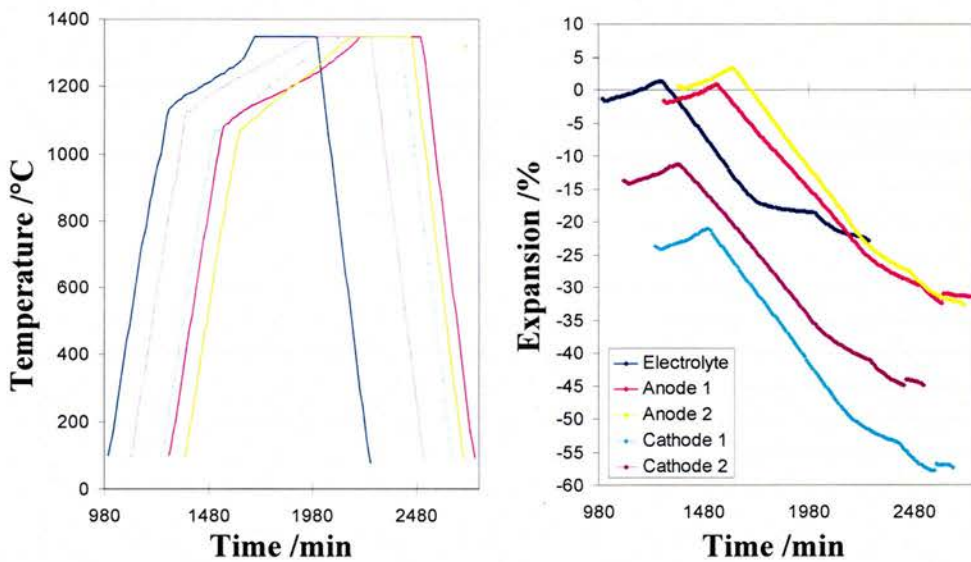


Figure 3.70: Rate controlled sintering of the 5 fuel cell components between room temperature and 1350°C. Samples had been subjected to rate controlled sintering according to figure 3.68 prior to high temperature rate controlled sintering.

rod on the microstructures at low temperatures could affect the high temperature shrinkages, the heating rates were slowed from 1000°C to the sintering temperature.

3.8 Summary

The density of the electrolyte when fired at 1300°C for 5hrs was sufficient for use in a fuel cell. This density was improved when co-fired between the anode and cathode.

Formation of the LZO (lanthanum zirconate) was shown to be eliminated by an A-site deficiency of 5% and 6% in the LSM at temperatures up to 1350°C. The sinterability of the LSM increased with higher A-site deficiencies leading to greater shrinkages and lower porosities. In order to match the shrinkage with the electrolyte whilst maintaining cathodes of adequate porosity, the high A-site deficient LSM was mixed with YSZ in a 1:1 (by mass) ratio.

Shrinkage matching of the anode with the electrolyte was achieved at low Ni to YSZ ratios by the addition of a graphite pore former. This led to high porosities and low effective nickel contents (taking the porosity into account). Increasing the Ni to YSZ ratios increased the effective nickel content of the ceramic, whilst decreasing the shrinkage and increasing the porosities and shrinkages upon reduction.

Initial fuel cells were produced from components with very similar shrinkage profiles at both 1300°C and 1350°C. The cathode was a bi-layer cathode: composite cathode was made from 1:1 (by mass) 5% A-site deficient LSM:YSZ (2 μ m) and a current collector cathode made from stoichiometric LSM. The composite cathode will give a high triple phase boundary length and no pyrochlore phase. The anode had a low Ni to YSZ ratio of 40:60 (by volume). Additionally, the thickness of the electrolyte and the addition of an anode current collector with a Ni to YSZ ratio of 80:20 (by volume) were investigated, varying the heating rates based on the results obtained by the rate controlled sintering.

3.8 References

- 1 R. E. Mistler, Eric R. Twiname, "Tape Casting Theory and Practice", Westerville: The American Ceramic Society, **2000**
- 2 PDF (Powder Diffraction File) number 24-734, Mn_3O_4 , produced by ICCD (International Centre for Diffraction Data)
- 3 PDF (Powder Diffraction File) number 41-1442, Mn_2O_3 , produced by ICCD (International Centre for Diffraction Data)
- 4 PDF (Powder Diffraction File) number 40-1100, $La_{0.8}Sr_{0.2}MnO_3$, produced by ICCD (International Centre for Diffraction Data)
- 5 L. Rørmark, K. Wiik, S. Stølen, T. Grande, "Oxygen stoichiometry and structural properties of $La_{1-x}A_xMnO_{3\pm\delta}$ ($A=Ca$ or Sr and $0 \leq x \leq 1$)", *J. Mat. Chem.*, *12*, **2002**, 1058-1067
- 6 M. T. Weller, "Inorganic Materials Chemistry", New York: Oxford University Press Inc, **1994**
- 7 M. Barsoum, "Fundamentals of Ceramics", The McGraw-Hill Companies Inc, **2000**
- 8 D. R. Dinger, "Rheology for Ceramists", Clemson: Dinger Ceramic Consulting Services, **2002**
- 9 M. A. Janney, "Attaining High Solids in Ceramic Slurries", Oak Ridge National Laboratory, Oak Ridge, TN 37831, at: <http://www.ms.ornl.gov/researchgroups/process/cpg/gelpubs/Mixing.pdf>
- 10 S. Wang, Y. Jiang, Y. Zhang, J. Yan, W. Li, "Promoting effect of YSZ on the electrochemical performance of YSZ + LSM composite electrodes", *Solid State Ionics*, *113-115*, **1998**, 291-303
- 11 P. Holtappels, C. Bagger, "Fabrication and performance of advanced multi-layer SOFC cathodes", *J. Euro. Ceram. Soc.* *22*, **2002**, 41-48
- 12 K. Blackman, R. M. Sliaty, J. A. Lewis, "Competitive Adsorption Phenomena in Nonaqueous Tape Casting Suspensions", *J. Am. Ceram. Soc.*, *84(11)*, **2001**, 2501-2506
- 13 E. R. Twinane of Richard Mistler Inc: Technical Ceramic Consultants, Tape Casting Specialists, private communication, September **2002**
- 14 N. Q. Minh, "Ceramic Fuel Cells", *J. Am. Ceram. Soc.* *76 (3)*, **1993**, 563-88
- 15 S. P. Badwal, "Stability of Solid Oxide Fuel Cell Components", *Solid State Ionics*, *143*, **2001**, 39-46
- 16 A. Kuzjukevics, S. Linderoth, "Interaction of NiO with yttria-stabilised zirconia", *Solid State Ionics*, *93*, **1997**, 255-261

- 17 C. C. Appel, G. A. Botton, A. Horsewell and W. M. Stobbs, "Chemical and Structural Changes in Manganese-Doped Yttria-Stabilized Zirconia Studied by Electron Energy Loss Spectroscopy Combined with Electron Diffraction", *J. Am. Ceram. Soc.*, **82** (2), **1999**, 429-435
- 18 R. M. German, "Sintering Theory and Practice", Chichester: John Wiley & Sons Inc, **1996**
- 19 C. Brugnoni, U. Decati, M. Scagliotti, "SOFC cathode/electrolyte interface. Part I: Reactivity between $\text{La}_{0.85}\text{Sr}_{0.15}\text{MnO}_3$ and $\text{ZrO}_2\text{-Y}_2\text{O}_3$ ", *Solid State Ionics*, **76**, **1995**, 177-182
- 20 A. Mitterdorfer, L. J. Gauckler, " $\text{La}_2\text{Zr}_2\text{O}_7$ formation and oxygen reduction kinetics of the $\text{La}_{0.85}\text{Sr}_{0.15}\text{Mn}_y\text{O}_3$, O_2 (g)|YSZ system", *Solid State Ionics*, **111**, **1998**, 185-218
- 21 A. Weber, R. Männer, B. Jobst, M. Schiele, H. Cerva, R. Waser, E. Ivers-Tiffée, "The influence of A-site deficiency on the performance of Strontium doped Lanthanum-manganate perovskite type SOFC-cathodes" in: Poulsen, Bonanos, Linderoth, Mogensen, Christiansen, (Ed.), Proceedings on the 17th Risoe International Symposium on Materials Science: High Temperature Electrochemistry: Ceramics and Metals Risoe National Laboratory, Roskilde, Denmark, **1996**, 473-478
- 22 S. F. Corbin, "Engineered Porosity via Tape Casting, Lamination and the Percolation of Pyrolyzable Particulates", *J. Am. Ceram. Soc.*, **82** (7), **1999**, 1693-1701
- 23 T. Matsushima, H. Ohrui, T. Hirai, "Effects of sinterability of YSZ powder and NiO content on characteristics of Ni-YSZ cermets", *Solid State Ionics*, **111**, **1998**, 315-321
- 24 P. Charpentier, P. Fragnaud, D. M. Schleich, E. Gehain, "Preparation of thin film SOFCs working at reduced temperature", *Solid State Ionics*, **135**, **2000**, 373-380
- 25 S. P. Jiang, P. J. Callus, S. P. S. Badwal, "Fabrication and performance of Ni/3mol% $\text{Y}_2\text{O}_3\text{-ZrO}_2$ cermet anodes for solid oxide fuel cells", *Solid State Ionics*, **132**, **2000**, 1-14
- 26 S. K. Pratihari, A. Das Sharma, R. N. Basu, H. S. Maiti, "Preparation of nickel coated YSZ powder from application as an anode for solid oxide fuel cells", *J. Power Sources*, **129**, **2004**, 138-142
- 27 S. F. Corbin, J. Lee, X. Qiao, "Influence of Green Formulation and Pyrolyzable Particulates on the Porous Microstructure and Sintering Characteristics of Tape Cast Ceramics", *J. Am. Ceram. Soc.*, **84** (1), **2001**, 41-47
- 28 D. W. Dees, T. D. Claar, T. E. Easler, D. C. Fee, F. C. Mrazek, "Conductivity of Porous Ni/ $\text{ZrO}_2\text{-Y}_2\text{O}_3$ Cermets", *J. Electrochem. Soc.*, **134** (9), **1987**, 2141-2146
- 29 S. K. Pratihari, R. N. Basu, S. Mazumder, H. S. Maiti, "Electrical Conductivity and Microstructure of Ni-YSZ Anode Prepared by Liquid Dispersion Method", in: S. C. Singhal, M. Dokiya (Eds), Proceedings of the Sixth International Symposium on Solid Oxide Fuel Cells (SOFC-VI), Honolulu, Hawaii, 1-22 October **1999**, 513

- 30 "CRC Handbook of Chemistry and Physics", Ed. D. R. Lide, H. P. R. Frederikse, 76th Edition, CRC Press, **1995-1996**
- 31 W. Z. Zhu, S. C. Deevi, "A review on the status of anode materials for solid oxide fuel cells", *Mat. Sci. Eng. A362*, **2003**, 228-239
- 32 E. R. Twinane of Richard Mistler Inc: Technical Ceramic Consultants, Tape Casting Specialists, private communication, July **2003**
- 33 R. M. C. Clemmer, S. F. Corbin, "Influence of porous composite microstructure on processing and properties of solid oxide fuel cell anodes", *Solid State Ionics*, *166*, **2004**, 251-259
- 34 PDF (Powder Diffraction File) number 17-450, $\text{La}_2\text{Zr}_2\text{O}_7$, produced by ICDD (International Centre for Diffraction Data), PA: **1995**
- 35 S. P. Simner, J. F. Bonnett, N. L. Canfield, K. D. Meinhardt, J. P. Shelton, V. L. Sprenkle, J. W. Stevenson, "Development of lanthanum ferrite SOFC cathodes" *J. Power Sources*, *113*, **2003**, pp. 1-10
- 36 M. J. Jørgensen, S. Primdahl, C. Bagger, M. Mogensen, "Effect of sintering temperature on microstructure and performance of LSM-YSZ composite cathodes", *Solid State Ionics*, *139*, **2001**, 1-11
- 37 J.-D. Kim, G.-D. Kim, J.-W. Moon, Y.-i. Park, W.-H. Lee, K. Kobayashi, M. Nagai, C.-E. Kim, "Characterization of LSM-YSZ composite electrode by ac impedance spectroscopy", *Solid State Ionics*, *143*, **2001**, 379-389
- 38 J. T. S. Irvine, F. G. E. Jones and P. A. Connor, University Court of the University of St Andrews. "Improvements in Fuel Cells and Related Devices". *PCT Patent Application No. PCT/GB2002/004726*, 1 May **2003**

4 Fuel Cell Testing

4.1 Introduction

Whilst the geometry of the SOFCRoll utilises cheap production techniques, reduced firing times and allows removal of high temperature interconnect materials promising reduced costs, in order for it to be considered as a feasible fuel cell design it must perform well – at least giving similar costs/kW as the alternatives. Chapter 3 concerns the processing of the individual components tailoring tape casting slip/slurry recipes to obtain the desired microstructure of components whilst shrinking at relatively similar rates and avoiding formation of undesirable phases during co-firing. In this chapter, the electrochemical responses and the general condition of the fuel cells after electrochemical testing are examined.

Cell I-V responses described in section 2.11 not only give information on the power outputs achieved from each fuel cell produced, but they give valuable information on areas requiring improvements. The open circuit voltage (OCV) obtained for each fuel cell is limited thermodynamically, depending on the partial pressures of both oxidant and fuel as described in section 1.2. An OCV below the theoretical suggests either cracks in the electrolyte or an insufficient seal. It is worth noting however, that for the SOFCRoll design, whilst sealing is performed on both the gas inlet holes and opposite end of the fuel cell, the end of the spiral (along the length of the fuel cell) where the gases exit is unsealed and so it is unlikely to achieve perfect OCVs. Additionally, the shape of the I-V curve gives valuable information shown in figure 2.26 (section 2.11) regarding cell polarisations and ohmic resistances.

More detailed information can be obtained from the a.c. impedance data. The material resistances: internal resistance (transport of electrons in the steel tubes and electrodes, and transport of oxygen ions in the electrolyte and electrodes) and the

contact resistance (contact between electrode and electrolyte, and electrode and interconnect) will be obtained from the intercept at high frequencies corresponding to R_1 shown in the equivalent circuit figure 4.1. It should be noted that this material resistance also includes the resistance of the electrical wires: lead resistance. Arcs in the Nyquist plots (Imaginary impedance Z'' vs real impedance Z') will be present for electrode resistances corresponding to gas transport to and from the triple phase boundaries (tpb) and activation polarisation, giving information on porosity, tpb area and catalytic activity. Nyquist plots obtained showed either two or three arcs, depending on operating temperature and cell component variations. Equivalent circuits shown in figure 4.1 were used depending on the number of arcs seen in the impedance spectra.

Literature states that the YSZ-LSM and Ni-YSZ electrode responses result in 3 arcs^[1-3]. The high frequency arc is very sensitive to microstructure and is related to the triple phase boundary area^[1-2, 4]. The mid frequency arc is sensitive to the partial pressures of oxygen in the cathode and hydrogen and water in the anode therefore giving information on the diffusion of oxide ions travelling along the LSM surface to the triple phase boundary in the cathode^[1] and the oxidation of the hydrogen in the anode^[2]. The low frequency arc gives information on the diffusion of gaseous reactants and products to and from the electrodes and varies significantly with partial pressure giving information about the porosity^[1,3-4]. At electrode porosities of 50% and higher, the R_4 arc becomes very small again making it very difficult to separate^[3]. Since the porosities in the SOFCRoll are easily this high, the R_4 arc would not be expected to be separated. At higher temperatures, the R_2 in the cathode becomes very small making it very difficult to separate the resistances^[1], which is one possibility for the difference in number of arcs seen in the fuel cell tests.

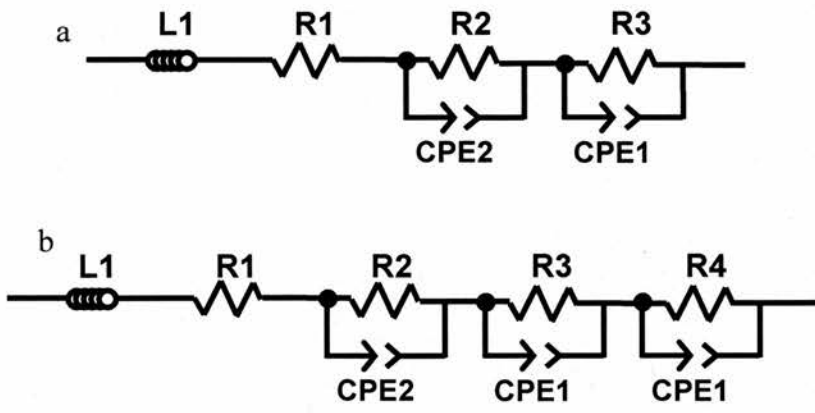


Figure 4.1: Equivalent circuits used to fit a.c. impedance data when a) 2 arcs were observed and b) 3 arcs were observed

For a complete evaluation of the fuel cell, SEM images of the cell cross-sections gave information of the factors contributing towards the material resistance: de-lamination, cracking of electrolyte/electrodes and loss of electrical contact evident from silver migration through electrodes.

The following chapter examines the performance of the fuel cells taking into consideration heating rates, firing temperatures, current collection on the anode side and methods used during testing. All data has been corrected to eliminate the contribution of the lead resistance as described in section 2.11. Unless otherwise stated, the fuel cell is made up of a double layer of electrolyte, and two-layer anode and cathodes as described in section 2.10, with the Ni:YSZ:graphite and LSM:YSZ:graphite ratios as examined in section 3.7.

4.2 Testing methods

The following section discusses the effects the experimental set-up has on the measured material resistances and open circuit voltages (OCVs) of cells. Emphasis is centred on inconsistencies between cells such as geometry and steel-electrode contacts. The factors which could worsen the fuel cells condition between electrochemical testing and SEM analysis are also discussed.

4.2.1 Material resistance

The material resistances were obtained from the high frequency intercept of the Nyquist plot of a.c. impedance and corrected for both inductance according to the equivalent circuit model shown in figure 4.1, and lead resistance. The sections below discuss the factors affecting the measured material resistances of cells.

4.2.1.1 Electrode-steel contact and Steel corrosion

The method used to obtain electrical connection between the electrodes and steel tubes detailed in section 2.11 was believed to be one of the major problems in obtaining reproducible results. Hand-painting the silver paste onto the tubes leads to discrepancies in the quantity of silver painted to the steel tubes from one cell test to the next. Consistencies in size of gas inlet channels were also hard to obtain, due to the hand rolling of the fuel cells in their green state. It is also unlikely that the same tautness was achieved from one fuel cell to the next, changing the size of the gap between touching anode layers and touching cathode layers therefore changing the resistance to gas flow through the spirals (see figure 1.13, section 1.6). Gas channels down the length of the fuel cell (into which the steel tubes are inserted) were often not equal in size – the anode inlet being smaller than the cathode inlet, or vice-versa.

A combination of problems related to the quantity of silver paste and the size of the gas inlets channels would affect the material resistance. For a given inlet hole size, the greater quantity of silver paste would lead to lower material resistance both for electronic conductivity with time (due to corrosion of the silver tubes) and the contact area between steel tube and electrode. For a given silver quantity, smaller inlet holes would give a larger contact area between steel and electrode and hence the contact resistance would be reduced. Additionally, due to the difficulty in obtaining equal sized inlet holes for some fuel cells, some of the steel tubes had a smaller outer diameter at the end in order for them to fit into the inlet holes. This would lead to increased resistances to current flow down the length of the tubes.

All the above factors meant that a direct comparison between material resistances from one fuel cell to another to obtain useful information was difficult. For example, initial material resistances of a fuel cell (when similar open circuit voltages were achieved) varied between 0.23Ω and 0.49Ω at 800°C .

4.2.1.2 Deterioration with time

All the fuel cells tested showed increased material resistance during testing. An example is shown in figure 4.2, where the material resistances at 800°C increased from 0.25Ω to 0.29Ω after one temperature sweep to 925°C and then to 0.32Ω after the second sweep to 925°C . Generally three fuel cells were set up to be tested in one day, but if one broke during set-up or a short circuit was created only two cells were tested. When three fuel cells were tested in one day, the material resistance increased to a greater extent than when only two fuel cells were tested in one day. The most likely explanation for this is the corrosion of the steel inlet tubes at high temperature.

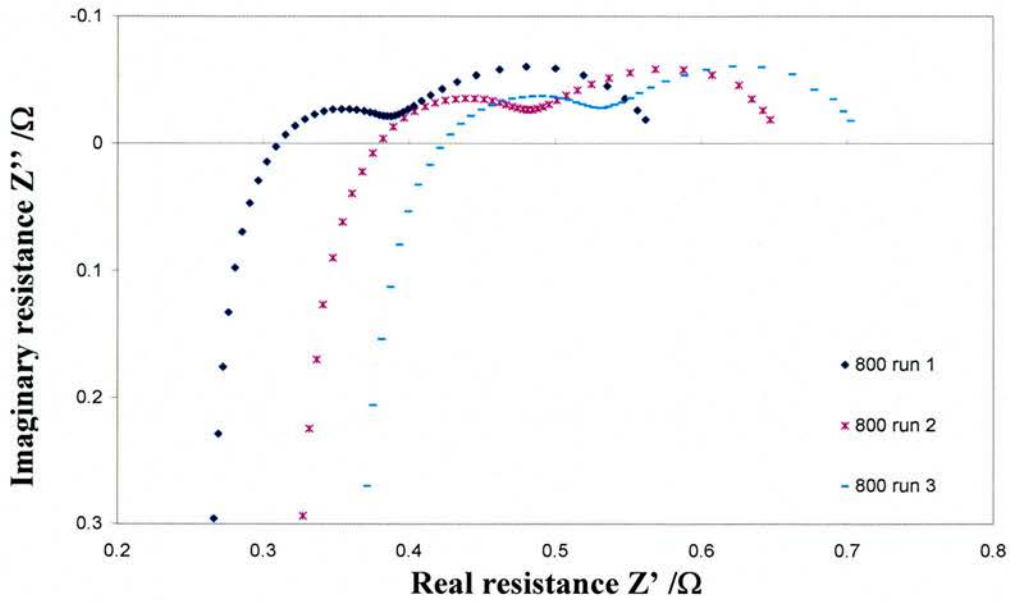


Figure 4.2: Nyquist plot showing increased material resistance at 800°C during testing

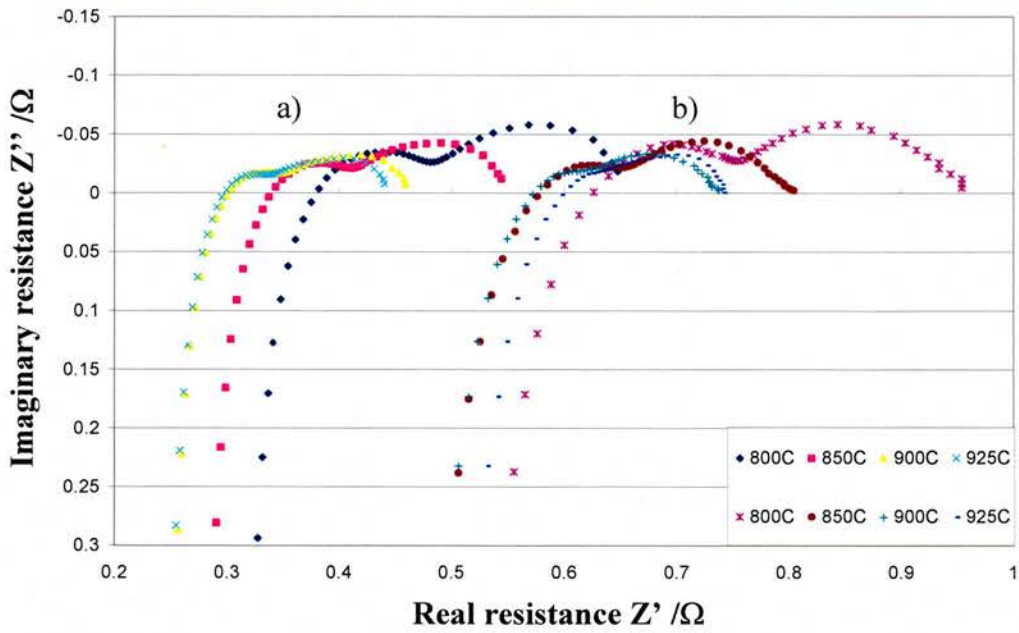


Figure 4.3: Nyquist plot showing a) decrease of material resistance with temperature (2 cells tested) and b) increase of material resistance from 900°C to 925°C (3 cells tested).

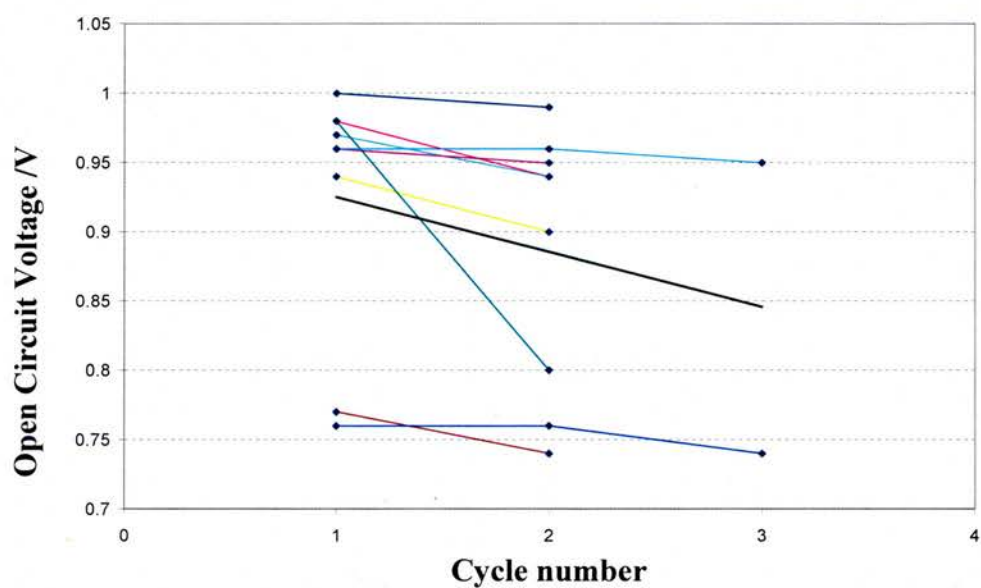


Figure 4.4: Graph showing the deterioration of open circuit voltage (OCV) at 800°C with thermal cycling between 800°C and 900°C (cycle number 1 was after initial heating to 800°C).

The fuel cells spent a greater length of time at high temperatures when more cells were tested in the same day. Figure 4.3 shows an example of where an increase in material resistance was seen when increasing from 900°C to 925°C when three cells were tested, whereas a decrease was seen when only two cells were tested. Additionally, since new steel tubes were not used for testing each fuel cell, the material resistance of the steel tubes would be different from one fuel cell to the next due to high temperature corrosion.

Open circuit voltages (also discussed in sections 4.2.2 and 4.3) decreased during testing for the majority of fuel cells tested due to thermal cycling or deterioration with time shown in figure 4.4. This suggests formation of cracks in electrolyte, propagation of existing cracks or deterioration of the seal. Where the open circuit voltage drop was associated with mixing of fuel and oxidant gases (cracked electrolyte or bad sealing at the anode inlet) it is possible that part of the anode was partially or fully oxidised (seen visually by the green colour of anodes in some cells after sample preparation for SEM analysis). Not only would this affect the electrochemical performance of the fuel cell, but also increase the anode contribution to material resistance.

4.2.2 Open circuit voltages

The thermodynamic factors affecting open circuit voltages (OCV) are discussed in section 1.2. Equation 4.1 shows the relationship between OCV (E), fuel (H_2) and oxidant (O_2) partial pressure, and temperature (T). Partial pressures are affected by gas flow rate, efficiency of sealing and formation of cracks in the electrolyte as discussed in the following sections.

$$E = E^0 - \frac{RT}{2F} \ln \left(\frac{P_{H_2} \cdot P_{O_2}^{1/2}}{P_{H_2O}} \right) \quad 4.1$$

4.2.2.1 Gas flow rate

As shown above in equation 4.1, the partial pressure and so gas flow rate of gases affect the open circuit voltage (OCV), with increased flow rate increasing the OCV. The gas flow meters fluctuated $\pm 5 \text{cm}^3 \text{min}^{-1}$ for a hydrogen flow of $\sim 55 \text{cm}^3 \text{min}^{-1}$ and so whilst attempts were made to keep the same flow rate from one fuel cell to the next, it is possible that errors originate from here. Additionally, the hydrogen was bubbled through water prior to passing through the flow meters, which could lead to the flow meters sticking, resulting in a higher real flow rate than that measured by the flow meter. Occasionally OCVs were seen to increase with temperature, the opposite to that expected by the Nernst equation (equation 4.1) and is most likely to be attributed to increased gas flow, although another possibility is the improvement of sealing at high temperatures.

4.2.2.2 Sealing

Once sealing had been performed (see section 2.11), the seals were not examined again until after testing had finished in order to minimising stresses involved in heating and cooling of the fuel cells, and so good seals could not be guaranteed. Generally speaking, the sealing of the fuel cells was good, however occasionally holes were clearly visible in the seals which would give decreased OCVs. Since the steel tubes could not be fired to high temperatures, the seal at the gas inlet end of the fuel cell was merely a close packed YSZ powder, so the seals could neither be gas tight or mechanically strong.

One particular example of a poor seal, probably due to the mechanically weak nature of the seal (which was evident during testing), was for a cell which clearly had an electrolyte crack due to the glow around the circumference (approximately 1.5cm from the opposite end to the inlet seal) seen when the cell was removed from the furnace after testing at approximately 350°C. The unsintered seal had a clear hole at the cathode side, possibly occurring when the fuel and oxidant gases were first introduced, burned at the electrolyte crack causing increased pressure, blowing a hole in the seal. In order to achieve the best OCV (0.763V at 800°C) for this cell at a H₂ flow rate of 55cm³min⁻¹, the O₂ flow rate had to be increased to 55cm³min⁻¹. If the low OCV was purely as a result of cracked electrolyte or hole in the anode side of the seal, increasing the oxygen flow rate would have resulted in a dilution of fuel and further reduced OCV. Positive results were obtained for successful sealing however, with the best measured open circuit voltage being 1.008V with gas flow rates of 55cm³min⁻¹ H₂ and 25cm³min⁻¹ O₂ at 800°C, deteriorating by only 0.018V to 0.99V by the end of testing.

4.2.3 SEM cross-sectional analysis

Whilst the cross-sectional analysis of the fuel cells after testing gave important information regarding the reasons for poor performance and areas for improvement, it is important to realise that the damage seen could have happened after testing as detailed in the following sections.

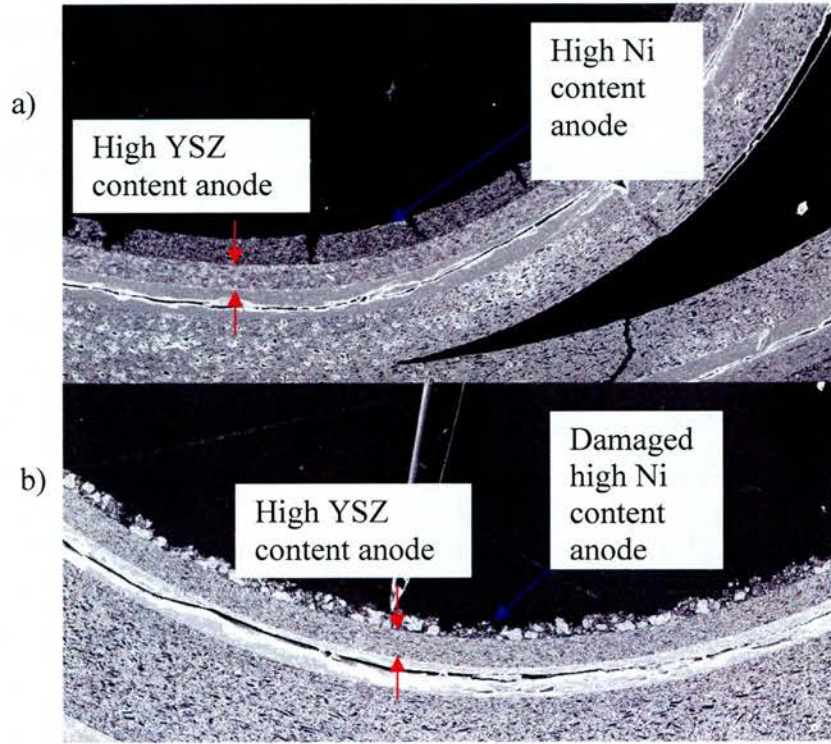


Figure 4.5: SEM image showing a) high Ni content anode half way up the cell undamaged when removing the steel tubes and b) the damage occurring to the high Ni content anode when removing the steel tubes.

4.2.3.1 Damage to cell after testing when removing tubes

Generally, the adhesion of the steel tubes to the electrodes with the silver paste was very good and as a result when removing the steel tubes after testing, damage occurred to the cells. Occasionally part of the electrode was removed, typically the the high nickel current collection layer as shown in figure 4.5. Additionally, cracking was commonly heard when removing the steel tubes, presumed to be due to the cracking of the thin central web as it was commonly missing at the gas-inlet end of the epoxied cell as shown in figure 4.6.

4.2.3.2 Damage to cell due to epoxy

Damage to the cell by the epoxy was believed to occur, due to the shrinkage of the epoxy during curing imposing stresses on the cell leading to cracks forming. Cracking along the length of the electrolyte was commonly seen, as denoted by the blue stars in figure 4.6. Other areas of damage seen in the cross-section were attributed to epoxy shrinkage during curing if the area of de-lamination or crack was not filled with epoxy, and deemed to have occurred prior to epoxy impregnation if the crack/de-lamination was filled with epoxy. Figure 4.6 shows various faults in the cell, which were routinely seen and have been identified as produced by the shrinkage of the epoxy, by removal of the steel tubes or by some other process. Figure 4.7 also shows a common phenomenon seen in the cross-sectional analysis, where large cracks occurred in the inlet holes, which frequently propagated to the central web.

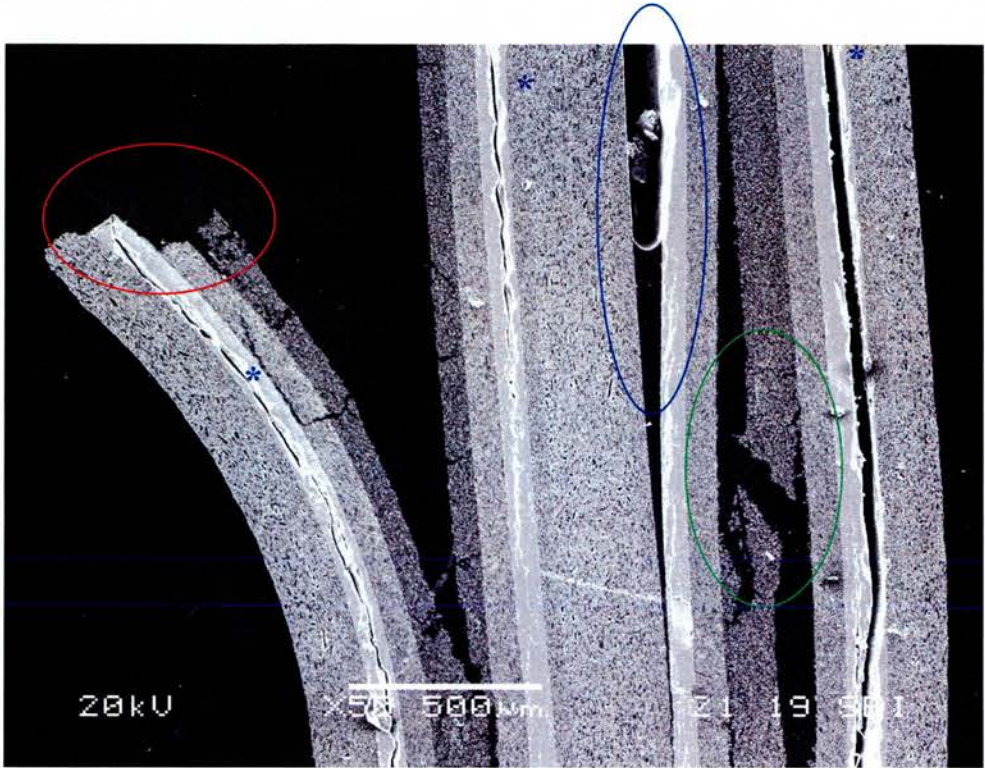


Figure 4.6: SEM image of a cross-section cut of the gas-inlet area of a fuel cell. Red circle shows breakage of central web, green circle crack and de-lamination of anode filled with epoxy, blue star showing cracks along length of electrolyte not filled with epoxy and the blue circle shows de-lamination partially filled with epoxy (likely de-lamination was present prior to impregnation, but worsened during epoxy cure).

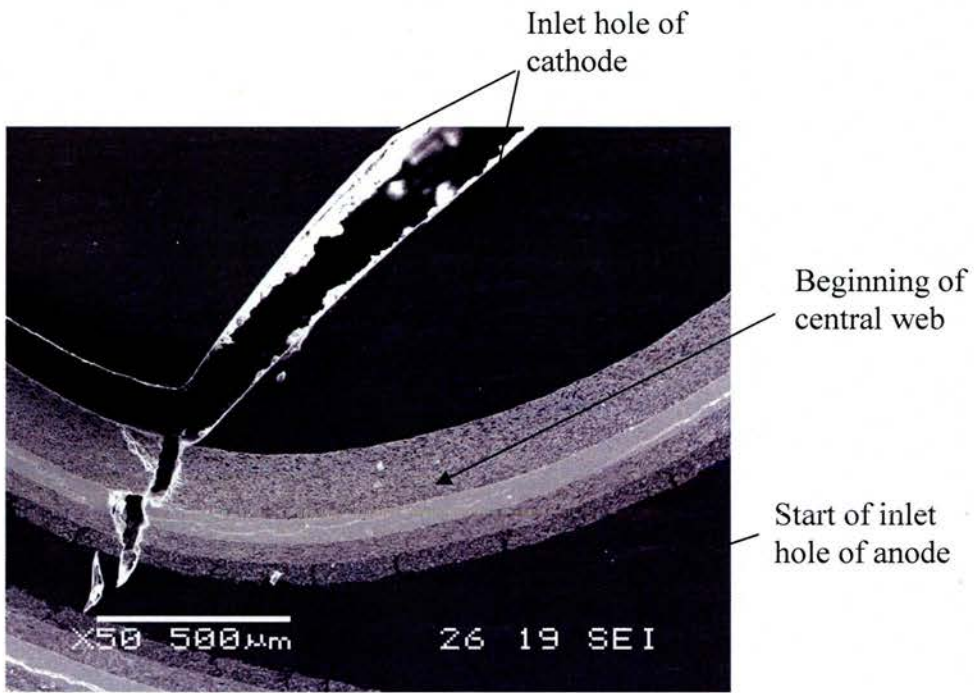


Figure 4.7: SEM image showing crack through cathode-electrolyte-anode caused by propagation of crack in the inlet holes formed during hardening of epoxy

4.3 Anode Current Collection

Initial cells produced had no separate anode current collector layer. These cells had very high resistances and poor electrical performances. The following sections describe the progression of SOFC development regarding the anode, investigating the following factors: increasing electrolyte thickness (improvement of open circuit voltages), increasing sintering temperature (reduction of electrode porosity) and addition of a high nickel current collection layer (reduction of electrode resistance) in order to improve performance.

4.3.1 Sintering temperature: 1300°C vs 1350°C

With the use of high A-site deficiency LSM, the higher sintering temperature of 1350°C could be used without production of the pyrochlore (see section 3.6.1). The higher sintering temperature is beneficial as it increases the extent of sintering in the electrolyte resulting in increased grain size and reduced thickness, thereby reducing ohmic resistance (see section 1.4.1). It decreases the quantity of nickel in the cermet required for percolation^[5] due to reduced porosity, thereby increasing the conductivity and altering the area of the triple phase boundary (tpb). Additionally, the cathode resistance should decrease with increased sintering temperature due to reduced porosity in the current collection layer and as with the anode, the tpb area of the intermediate layer will be changed. Due to the high porosity of both the anode and cathodes when sintered at 1300°C, it was thought that a small reduction in porosity would serve to increase the tpb area of both electrodes. At this stage of fuel cell production, one layer of electrolyte was used, resulting in electrolyte thicknesses of approximately 50µm.

Clearly increasing the sintering temperature by 50°C vastly reduces the cell resistances, evident from both the material resistance and electrochemical responses as shown in figure 4.8. Both plots clearly show evidence of 3 arcs and so the equivalent circuit shown in figure 4.1b was used to fit the data, giving material resistances (R_1) of 0.32 Ω and 3.84 Ω when sintered at 1350°C and 1300°C respectively. Referring back to section 4.2.1.1, a small decrease could be explained by a decrease in inlet hole size with increased sintering temperature, resulting in a better contact area between electrodes and steel tubes, however clearly the reduced resistance is more likely to be due to a change of the electrode microstructures, the predominant factor believed to be due to better Ni-Ni contact due to reduced anode porosity^[5]. EDS mapping of the cross-sections of fuel cell anodes shown in figure 4.9 show that the Ni-Ni connectivity is indeed much improved with increased sintering temperature. There is also a huge reduction in the size of the high frequency arc R_2 , from 12.06 Ω to 0.07 Ω and a decrease in the mid and low frequency arcs: R_3 from 1.31 Ω to 0.10 Ω and R_4 from 0.36 Ω to 0.22 Ω . It was thought that the reduced size in R_2 was due to an improved anode performance related to percolation of the nickel and resulting increased tpb area.

Figure 4.10 shows the maximum power obtained for the cell sintered at 1350°C (0.275W) was much greater than the cell sintered at 1300°C (0.072W). This again is due to the much lower anode resistances obtained when sintering at the higher temperature. A small decrease in cell voltage from 0.986V to 0.861V was observed with higher sintering temperatures, thought to be due to the increased cracking in the electrolyte from shrinkage mismatches at high temperatures (see section 4.3.2). However, both cells showed deterioration of cell voltage during the thermal cycling of

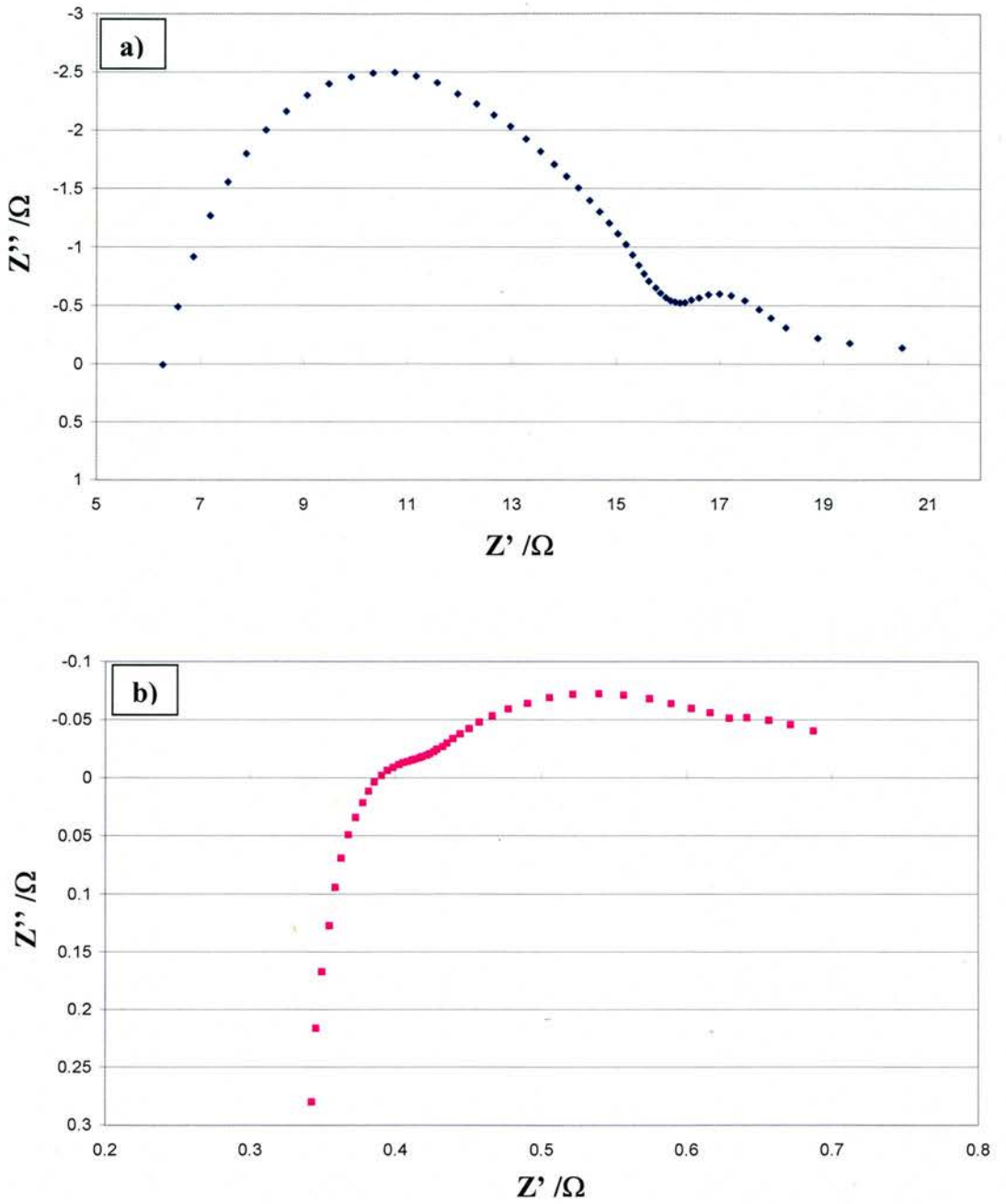


Figure 4.8: Nyquist plot of cells showing difference in impedance of cells with no anode current collection layer when sintered at a) 1300°C (note the difference in scale between the x and y axis) and b) 1350°C. Data obtained at 800°C.

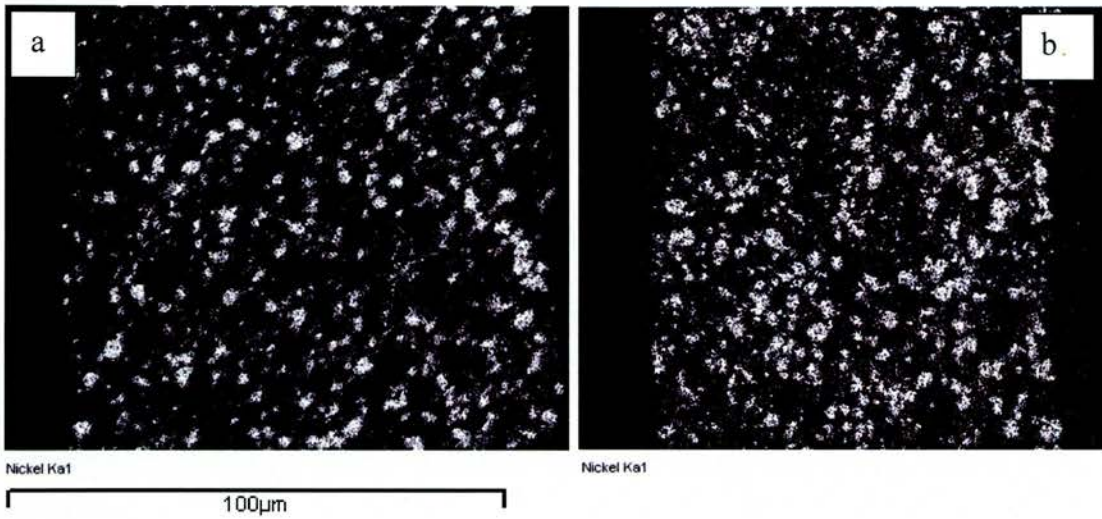


Figure 4.9: EDS map of nickel in the anode of cells when sintered at a) 1300°C and b) 1350°C

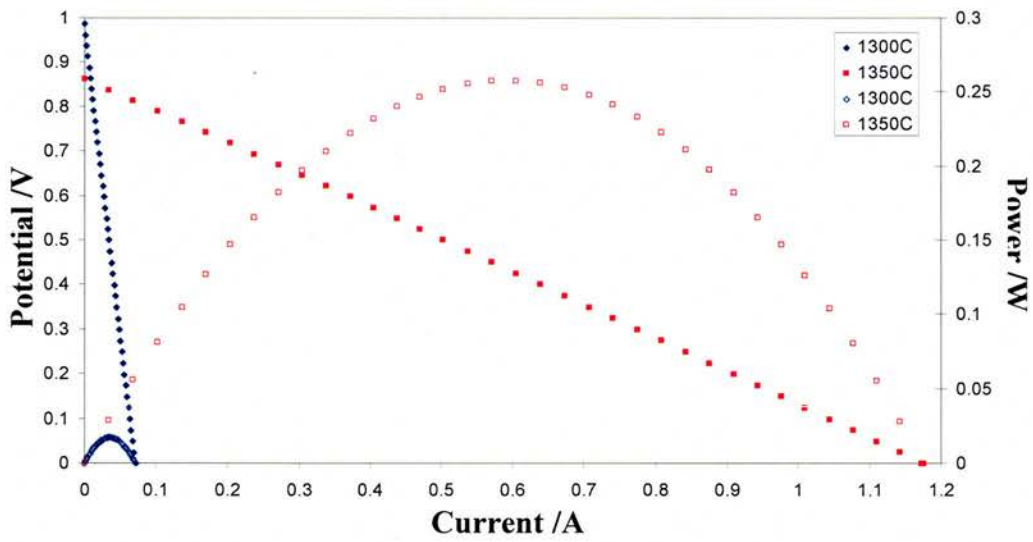


Figure 4.10: Power/Potential vs Current for cells with no anode current collection layer when sintered at 1300°C and 1350°C. Data obtained at 800°C.

the electrochemical tests thought to be due to the thermal expansion mismatches in the cell and propagation of existing electrolyte cracks.

4.3.2 Electrolyte thickness

Increasing the electrolyte thickness by using 2-layer laminates of electrolyte tape rather than one would have the effect of reducing the cracks in the electrolyte, both by eliminating pin holes and by increasing the thickness thereby increasing the influence of the electrolyte shrinkage to the cell shrinkage. This would result in an increased open circuit voltage (OCV), whilst increasing the cell resistance due to ohmic losses. Figure 4.11 shows that when sintering at 1300°C, the increased electrolyte thickness has little impact on the OCV, whereas it is greatly improved when sintering at 1350°C. The low OCV cluster (<0.9V) obtained when sintering at 1300°C with 2 layers of electrolyte was as a result of one cell being damaged prior to testing or having uneven gas flow (as the OCV showed no trend with time and temperature) or both, as seen by the large gap between measured potentials at 0.93V and 0.85V. Elimination of this cell showed a much narrower range of OCV, as expected when a thicker electrolyte is used.

4.3.3 Addition of high Ni content layer

The high nickel current collection layer added to the fuel cell to improve performance consisted of a Nickel to YSZ ratio (by volume) of 80:20, with a measured porosity when singularly fired at 1300°C of >60% after reduction (see figure 3.48, section 3.5.3). Having such a high nickel content layer in the fuel cell will cause problems as described in section 1.4.2, such as volume change upon

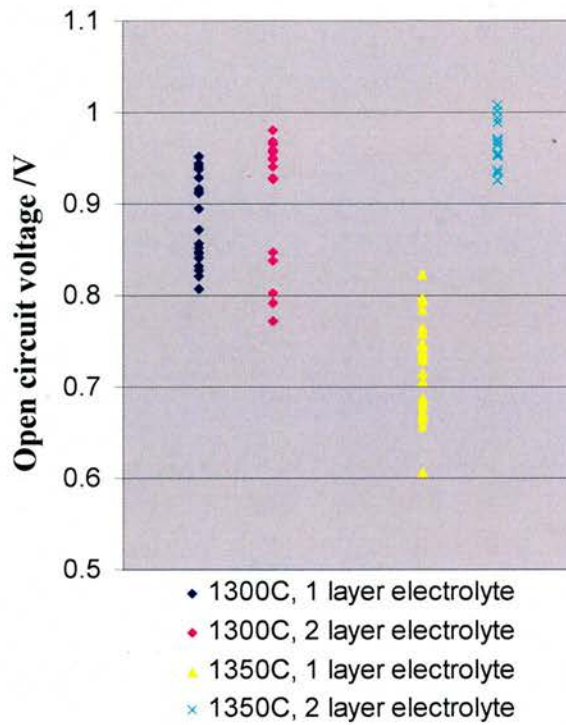


Figure 4.11: Variation of OCV with sintering temperature and number of layers of electrolyte

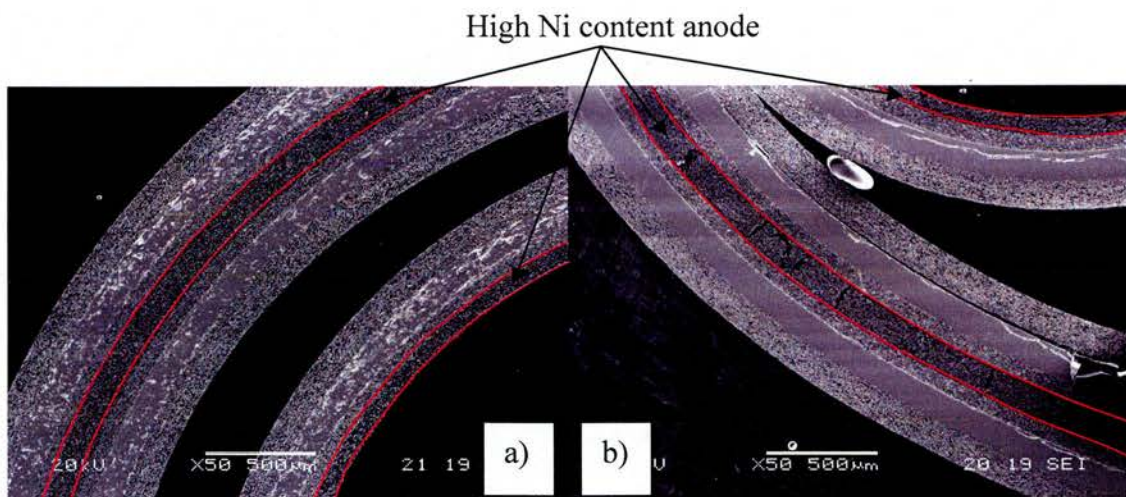


Figure 4.12: SEM image of cell with high nickel current collector a) un-tested cell (non-reduced anode) and b) tested cell (reduced anode)

reduction^[6], increased strain from thermal expansion mismatches^[7] and nickel particle sintering^[6]. The measured volume change of the anode current collector after reduction (see section 3.5.3) was ~20%, when fired singularly to 1300°C. It was this volume change that was attributed to be the cause of the copious cracking seen along the current collection layer, shown in figure 4.12. The performance of the cells however was much improved with a maximum power achieved of 0.18W and 0.58W for cells (at 925°C) fired at 1300°C and 1350°C respectively, as shown in figure 4.13.

Comparison of performances of cells with and without anode current collection layer (section 4.3.1, figure 4.10) at 800°C, shows that addition of the anode current collection layer increases the maximum power achieved by 0.156W (~900% increase) and 0.175W (~70% increase) when sintering at 1300°C and 1350°C respectively. Clearly the addition of the anode current collection layer improves the performance of the fuel cells at both firing temperatures.

As with the absence of an anode current collection layer, the higher firing temperature resulted in greatly improved performances. As described in section 4.3.1, the increased firing temperature was thought to improve the Ni-Ni particle connectivity, resulting in improved performances^[2,5]. This, together with the fact that the performance of the cell fired at 1300°C is increased to a much greater extent than the cell fired at 1350°C with the addition of an anode current collector, further supports the reasoning of improved nickel percolation and increased tpb area. The anode fired at 1300°C is clearly very close to the percolation threshold, with the addition of an anode current collector both improving the tpb area (at the interface of the two anodes) and reducing resistance to current flow.

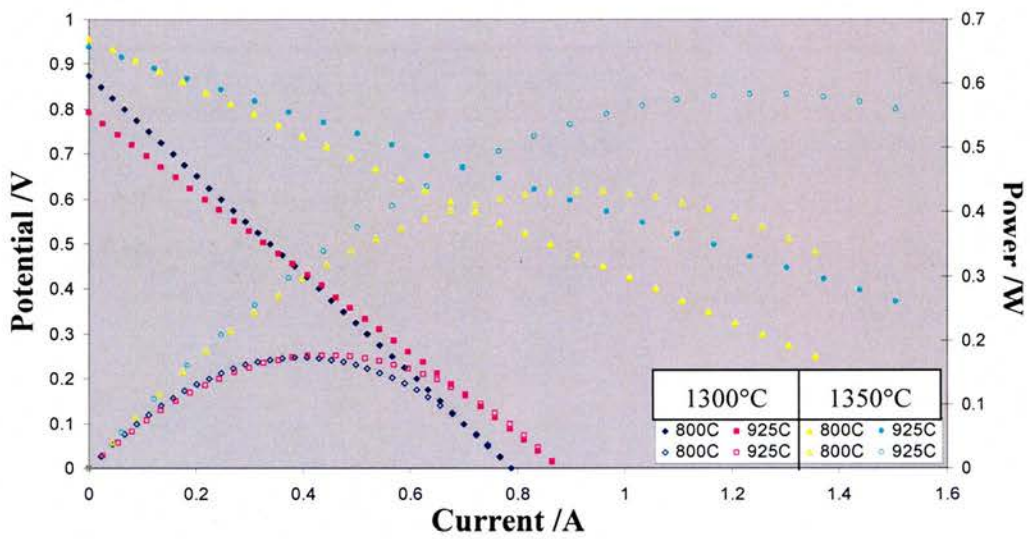


Figure 4.13: V-I and W-I responses for cells with high nickel anode current collector layer when sintered at 1300°C and 1350°C.

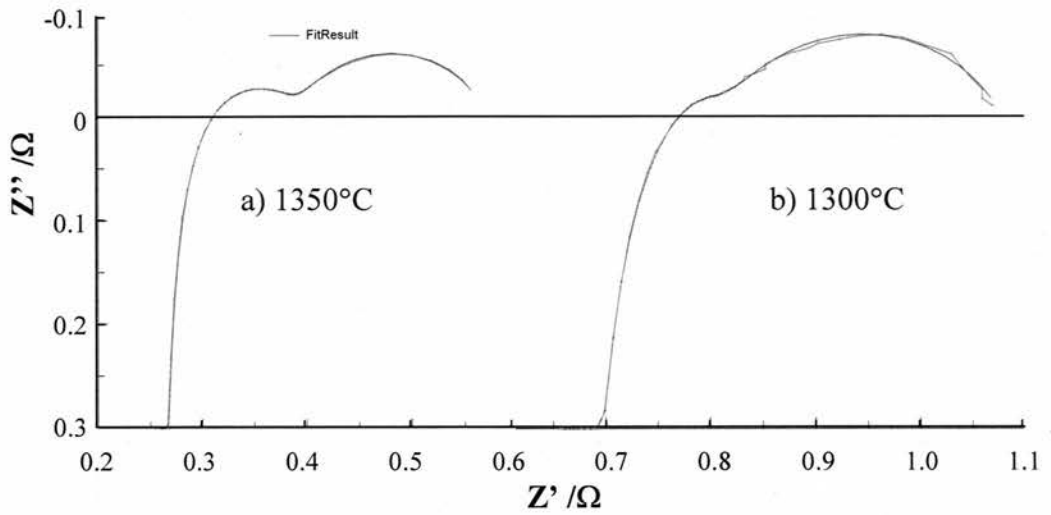


Figure 4.14: Nyquist plot of cells and fits showing difference in impedance of cells with anode current collection layer when sintered at 1300°C and 1350°C. Data obtained at 800°C.

	1300°C /3sf	Error /% 2sf	1350°C /3sf	Error /% 2sf
L /H	3.25E-06	0.15	3.11E-06	0.073
R1 /Ω	0.635	0.55	0.249	0.25
R2 /Ω	0.263	1.1	0.177	0.82
CPE-T	0.431	2.2	1.131	1.2
CPE-P	0.682	1.1	0.754	0.74
R3 /Ω	0.182	2.6	0.146	0.78
CPE-T	0.00561	11	0.0227	3.7
CPE-P	0.640	2.2	0.632	0.77

Table 4.1: Fitted data (obtained at 800°C) using equivalent circuit 4.1a for best performing cells produced at 1300°C and 1350°C with the anode current collection layer.

Figure 4.14 shows the difference in material resistance between the two cells to be much closer than that seen in the cells without a current collector layer (section 4.3.1) at 0.25Ω and 0.64Ω (table 4.1) when sintered at 1350°C and 1300°C respectively. The smaller material resistance of cells produced with an increased sintering temperature, can be attributed to both the lower porosity in the high YSZ layer anode, (as this layer is still relatively thick at $\sim 60\mu\text{m}$ and so will still contribute to the material resistance of the cell) and reduced porosity of the current collectors. Inspection of the cross-sectional images shown in figure 4.15 however, shows that the general condition of the best performing cell sintered at 1300°C to be much worse than the one sintered at 1350°C , with a higher degree of de-lamination and cell cracking giving additional reasons for the higher material resistance.

The a.c. impedance plots of figure 4.14 show only two arcs and so the equivalent circuit shown in figure 4.1a was used to fit the data, the values of which are shown in table 4.1. These resistance values show a reduction in all resistances with the higher sintering temperature which can be attributed to a reduction in porosity, which increases the tpb area without increasing the concentration polarisation due to the high level of porosity in the electrodes^[3]. The high frequency arc R2, shows a greater decrease in resistance with the higher sintering temperature than the low frequency arc (R3). Since the high frequency arc is thought to correspond to the tpb area^[1,2,4], this further supports the theory that the high YSZ content anode has too high a porosity and so the relative nickel content is too low when sintered at 1300°C , whilst increasing sintering temperature serves to reduce the porosity thereby increasing electronic conductivity of this layer and increasing the tpb area. Since research has taken the maximum tpb area to be obtained at a thickness of

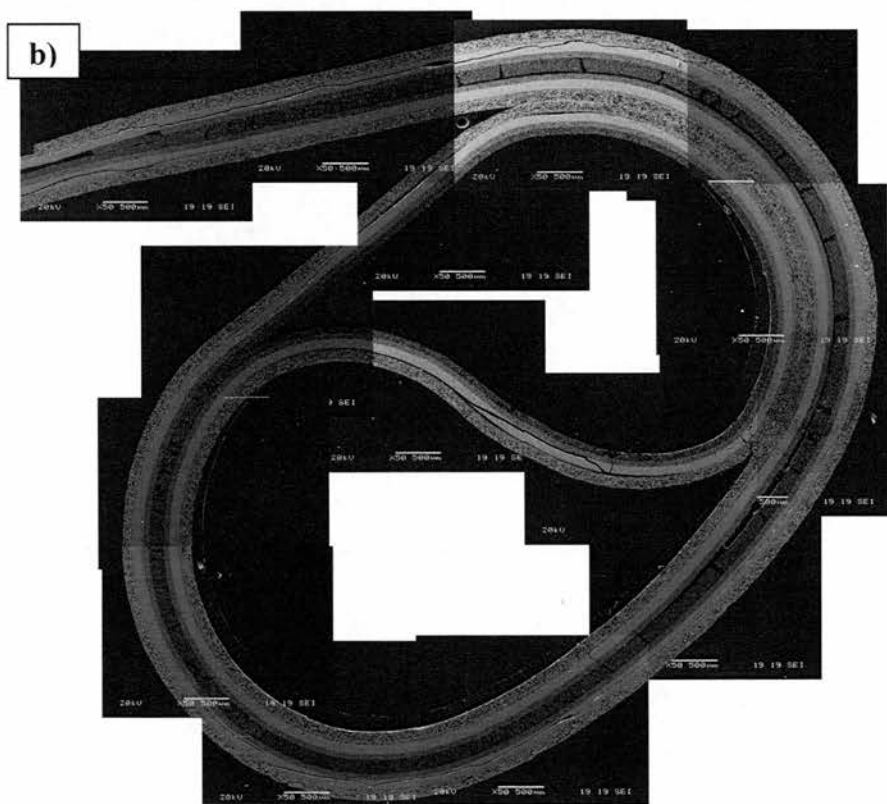
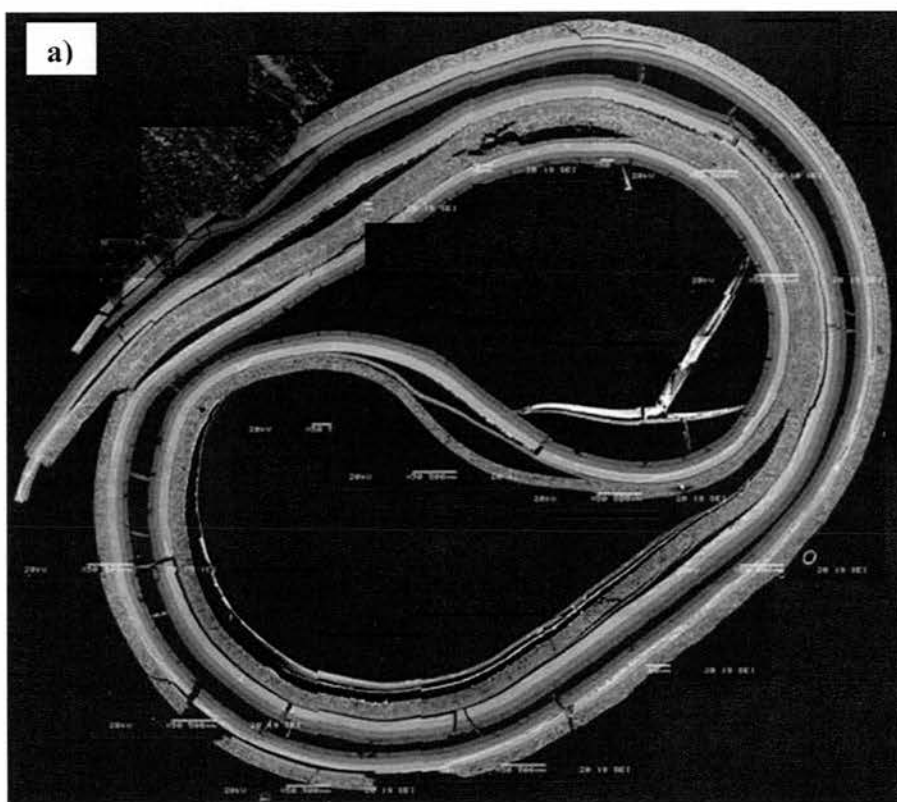


Figure 4.15: SEM image of a cross-section of the fuel cell with the best OCV and performance with a sintering temperature of a) 1300°C and b) 1350°C.

$10\mu\text{m}^{[8]}$, it is assumed that the performance of these cells should be improved by reducing the thickness of this layer, currently measuring $60\text{-}70\mu\text{m}$. Comparison with the cells with no anode current collector layer, the change in R2 with sintering temperature is much smaller, which can be attributed to an increase in tpb area at the interface between the two anode layers.

The reduction in resistance of the low frequency arc is probably also due to a reduction of porosity resulting in a higher tpb area, shortening the distance the oxide ions must diffuse along the LSM to the YSZ^[1], again without increasing the concentration polarisation due to the high porosity of this layer. Since the cathode layer has a slightly larger shrinkage at high temperatures than the electrolyte (see section 3.6 and 3.7), it could be beneficial to reduce the graphite content in this layer thereby further reducing porosity and high temperature shrinkage, reducing strains on the SOFCRoll geometry during firing and improving performance. Again, as with the anode a reduction of thickness from $\sim 30\mu\text{m}$ to $10\mu\text{m}$ should further improve performances^[8].

The cross-sectional analysis performed by SEM seen in figure 4.15 shows evidence of de-lamination and reasonable amount of cross-sectional cracking through the 3-component multi-layers. The cell sintered at 1300°C has a greater amount of cracking and de-lamination than the cell sintered at 1350°C , which suffered from a reasonable quantity of de-lamination of the anode current collector in the spiral and only a small amount of electrolyte cracking. These images show the condition of just one cross-section of the best performing cells. A cross-section of a poorer performing cell sintered at 1350°C is shown in figure 4.16, showing that (assuming damage was present prior to testing) a large variation in cell quality was present.

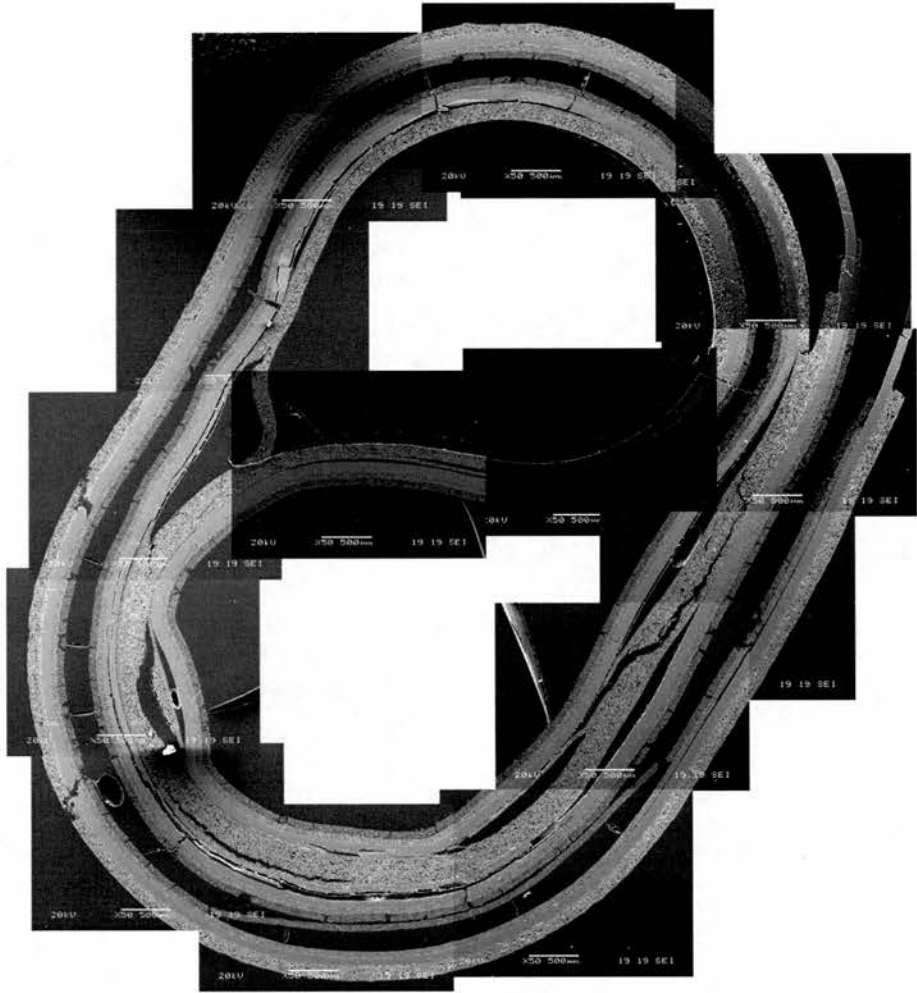


Figure 4.16: SEM image of a cross-section of a fuel cell sintered at 1350°C with a lower electrical performance.

4.4 Heating Rates

The addition of the high nickel content anode current collector layer, whilst improving the performance of the fuel cell, increases the strain in the fuel cell both from the thermal expansion mis-match (described in section 1.4.2) and shrinkage mismatch (described in section 3.5.3). Additionally, as seen by the variation in open circuit voltages (OCV) with sintering temperature and electrolyte thickness in section 4.3.2 more cracking in the electrolyte is present in the fuel cell when sintering at the higher temperature of 1350°C. The following section details the electrical performances and state of the fuel cells after testing when the heating rates were modified in order to minimise strains on the system during firing.

4.4.1 Sintering temperature of 1350°C

This section examines fuel cells with the following heating regimes:

- A 50-260°C; 360-650°C at 0.1°C/min⁻¹, 250-360°C; 650-1000°C at 0.5°Cmin⁻¹, 1000-1350°C at 2°Cmin⁻¹.
- B As A with the exception of 1000-1350°C at 5°Cmin⁻¹
- C 50-260°C; 360-650°C at 0.1°C/min⁻¹, 250-360°C; 650-1000°C at 2°Cmin⁻¹, 1000-1350°C at 2°Cmin⁻¹.
- D As C with the exception of 1000-1350°C at 5°Cmin⁻¹
- E 50-1000°C at 0.5°Cmin⁻¹, 1000-1350°Cmin⁻¹

Cooling rates used were 5°Cmin⁻¹, and dwell times at 1000°C and 1350°C were 300mins. The above heating regimes are listed in order with respect to time taken, with A taking the longest and E the shortest. E shows the heating rates used throughout the project for components detailed in chapter 3 and cells detailed in section 4.3 for completeness. The slow ramp rates between 50-260°C and 350-650°C

were chosen as these temperature ranges showed the greatest rate of shrinkage/expansion (see section 3.7) during the calcining stage to 1000°C. Heating regimes A and B kept the slow heating rate of 0.5°Cmin⁻¹ for the other temperature ranges up to 1000°C, whereas C and D had a faster heating rate of 2°Cmin⁻¹ in order to reduce the overall firing time. Heating regimes B and D made no attempt to reduce the shrinkage rate between 1000 and 1350°C, whereas A and C had a reduced heating rate to reduce the high rate of sintering shown in section 3.7.

Regarding maximum power obtained, figure 4.17b shows a clear gap in data points for C and E cells tested, showing variations between different cells produced. This is a result of variation of OCVs (figure 4.17a) caused either by cracking of the electrolyte or a damaged seal. This gap is reflected in the range of measured powers for C and E cells. Additionally, there is a gap in data points of the material resistance of E cells (figure 4.17c) further contributing to the gap seen for the maximum power obtained. The trend in maximum power obtained is mirrored by the material resistance (with the exception of the gap in data points seen in the power obtained from C cells, attributed to the variation in OCV), which suggests that this is the dominating factor for reduced power.

Considering the material resistance of the cells (figure 4.17c), a definite trend is visible for A-D cells – giving increased material resistance and increased variation of material resistance for cells produced with faster firing times, whereas E cells deviate from this trend, showing a lower resistance. Re-plotting this graph (figure 4.18) with respect to the order the cells were tested in shows an overall increase in material resistance. As detailed in section 4.2.1, the steel tubes were re-used from cell to cell, so this suggests the increase in material resistance could be due to the

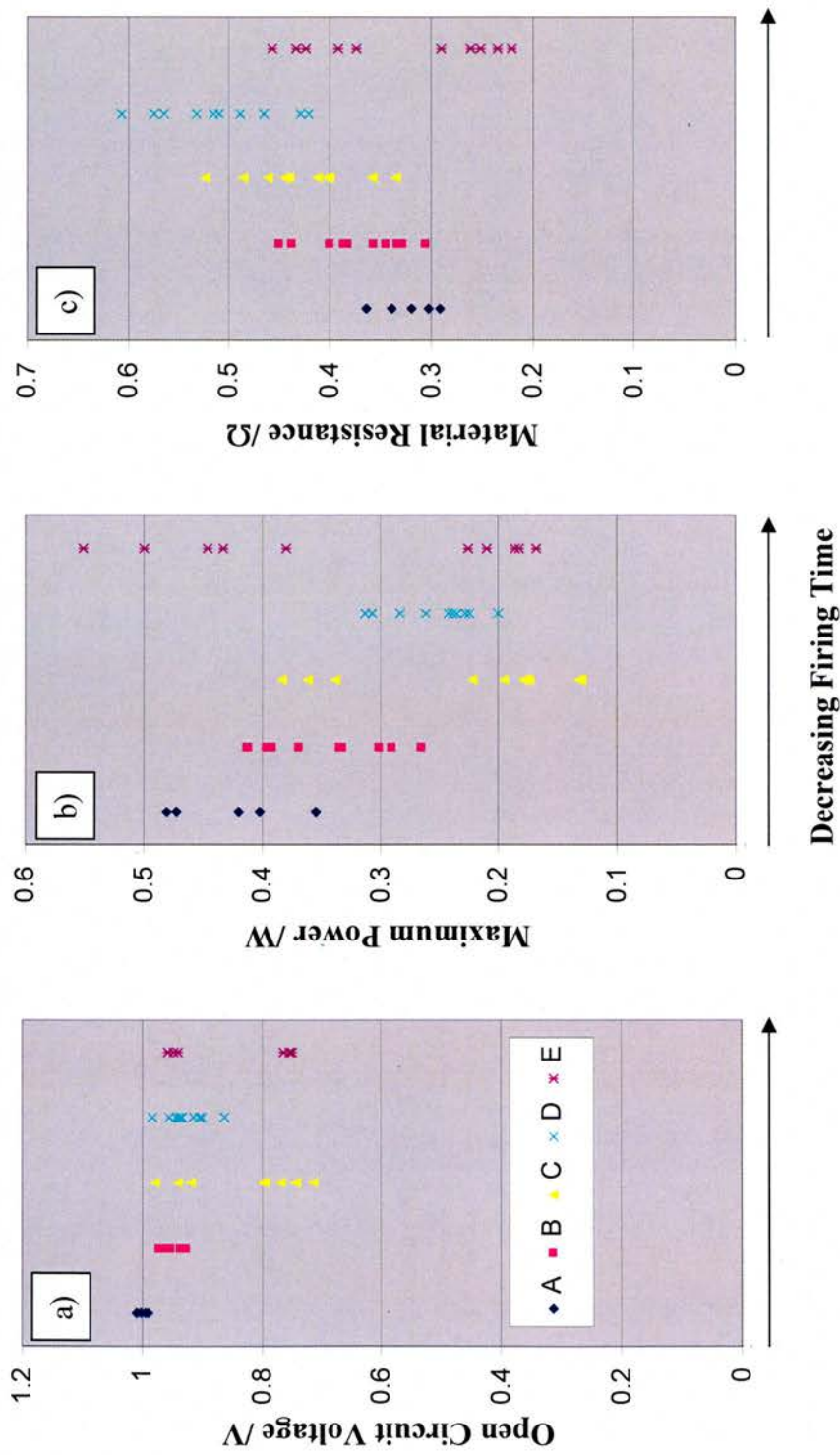


Figure 4.17: Graphs show how the heating regimes affect a) open circuit voltage, b) maximum power (calculated from I-V response) and c) material resistance (obtained from a.c. impedance response).

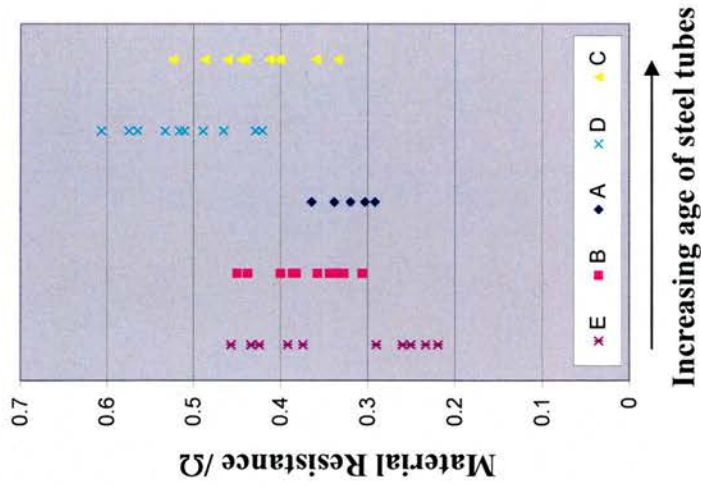


Figure 4.18: Graph showing how the order in which cells were tested and hence the age of the steel affects the measured material resistances of the cells A-E (with different heating rates) (re-plot of figure 4.17)

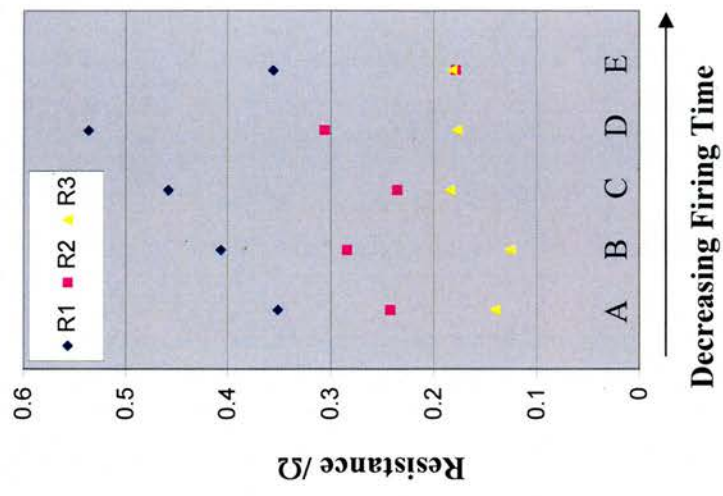


Figure 4.19: Graph showing the effect of firing regime on the cell resistances, where R1, R2 and R3 are as shown in figure 4.1a. R1 relates to the material resistance as shown in figure 4.17c. Data shows average resistances from cells tested at 800°C.

deterioration of the steel. This isn't the whole story however, as the trend isn't quite linear: A cells have a lower average material resistance than B cells despite being tested with older steel tubes. The same is seen with C and D cells – with C cells having a lower average material resistance than D cells. Both A and C cells were produced with the decreased heating rate between 1000°C and 1350°C, suggesting the slower high temperature heating rate reduces the material resistance of the cells.

Figure 4.19 shows the trend in resistances R1, R2 and R3 with the firing schedules obtained from fitting the data according to the model of figure 4.1a. The lowest R3 values were obtained with A and B cells (C-E cells all having similar R3 values). This suggests the slower heating rate between 50°C and 1000°C decreases the R3 resistances. Regarding the R2 values (corresponding to the tpb area and shown in section 4.3 to be dominated by the anode polarisation due to being close to the nickel percolation threshold), B and D cells had similar values to each other which were the highest of all the cells. A and C cells also had similar values to each other at a lower magnitude to B and D cells. This suggests that the anode performance is improved by a slower heating rate between 1000°C and 1350°C. E cells have a much reduced R2 resistance – lower than any of the other cells. This lower R2 value is also mirrored by the much smaller material resistance (R1) obtained with these cells, suggesting that the nature of the anode in E cells is different: an increased nickel percolation resulting in increased tpb area (lower R2 value) and improved conductivity (lower R1 value).

Examination of SEM images and EDS mapping analysis of the cathodes and anodes shown in figures 4.20 and 4.21 respectively explain some of the trends seen in cell resistances. Figure 4.20 shows the cathode containing YSZ is marginally thinner

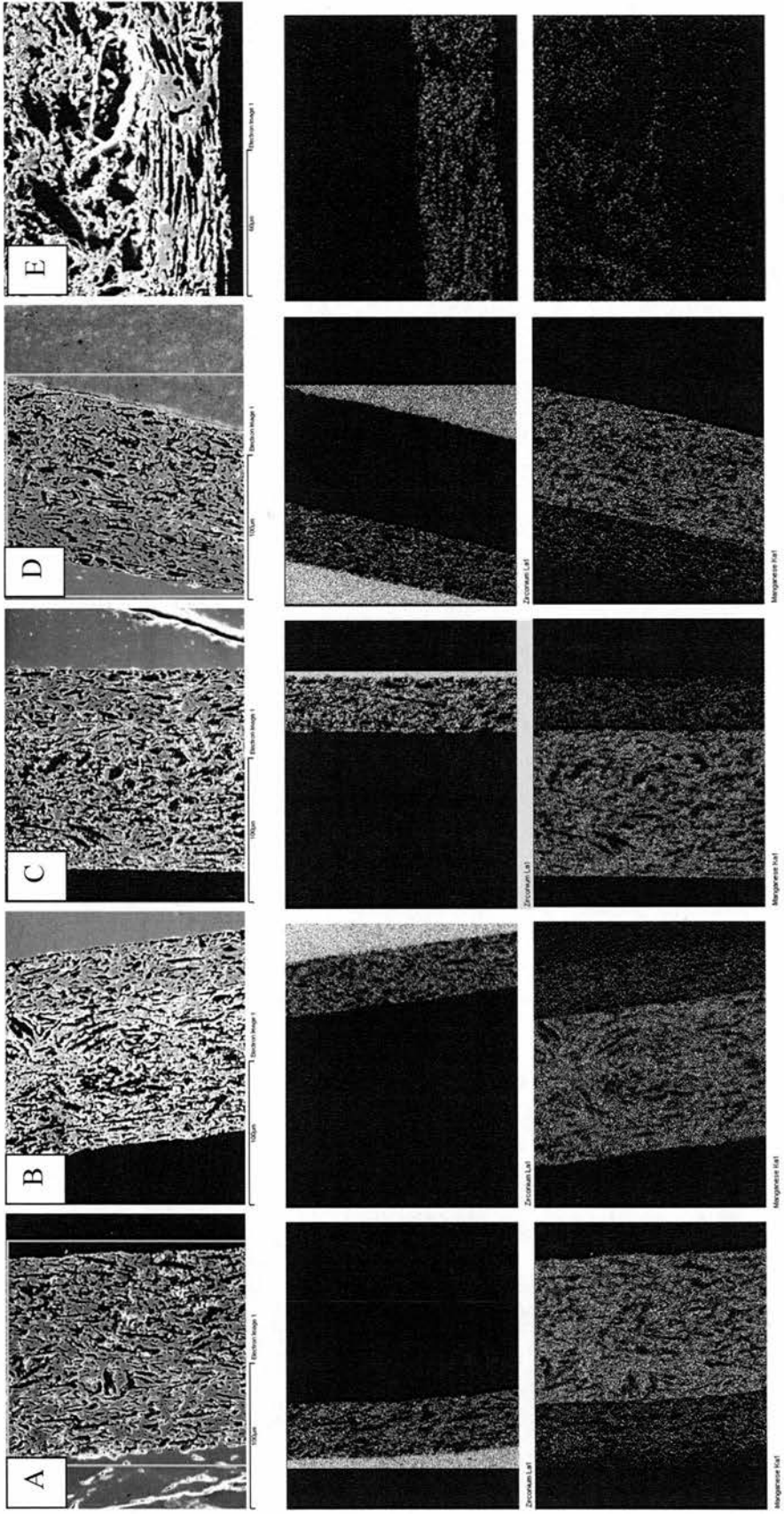


Figure 4.20: SEM image and EDS mapping of the cathodes fired at different heating regimes. From top to bottom shows the image, zirconium mapping and manganese elemental mapping. (Note different magnification for cell E)

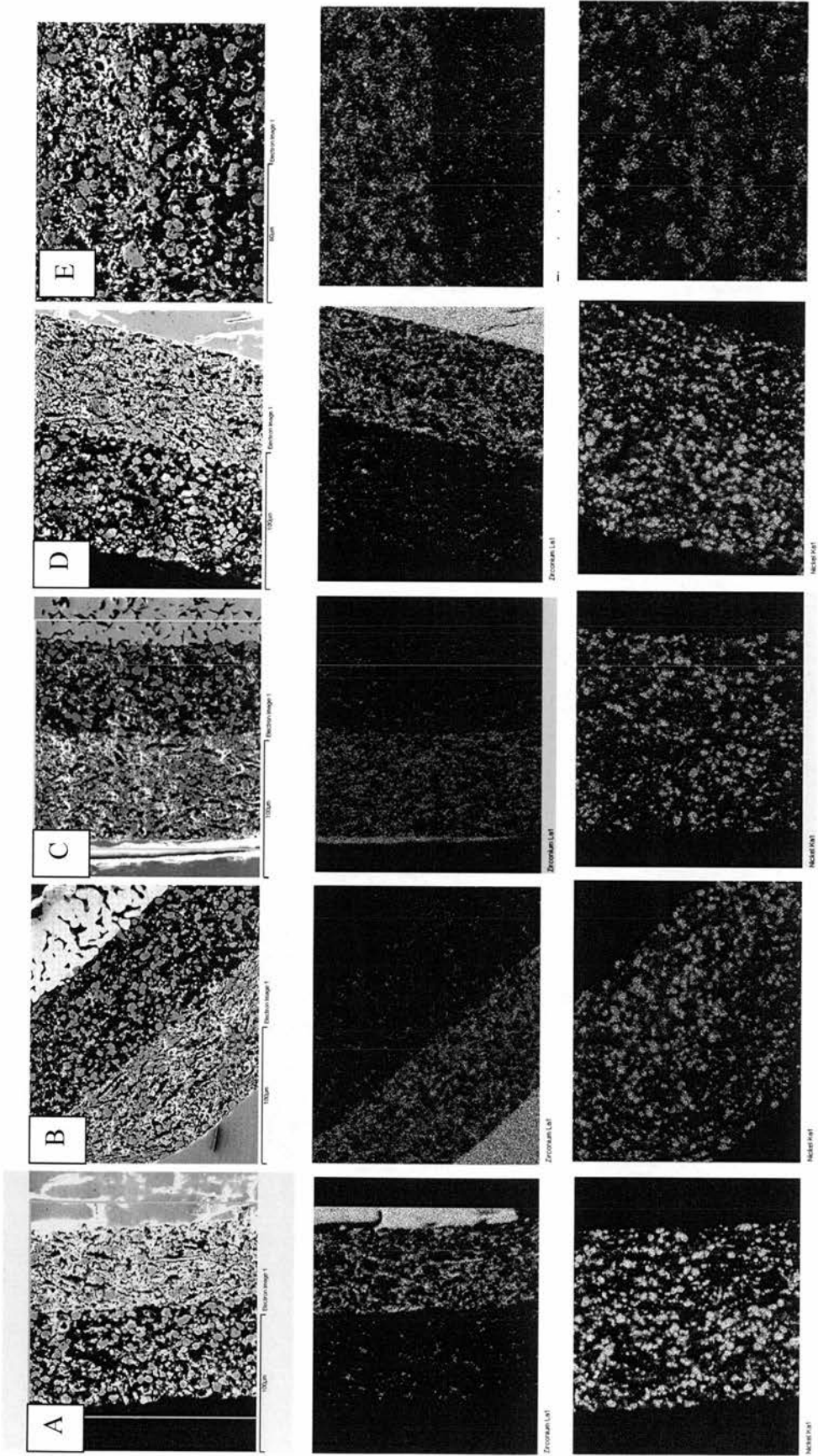
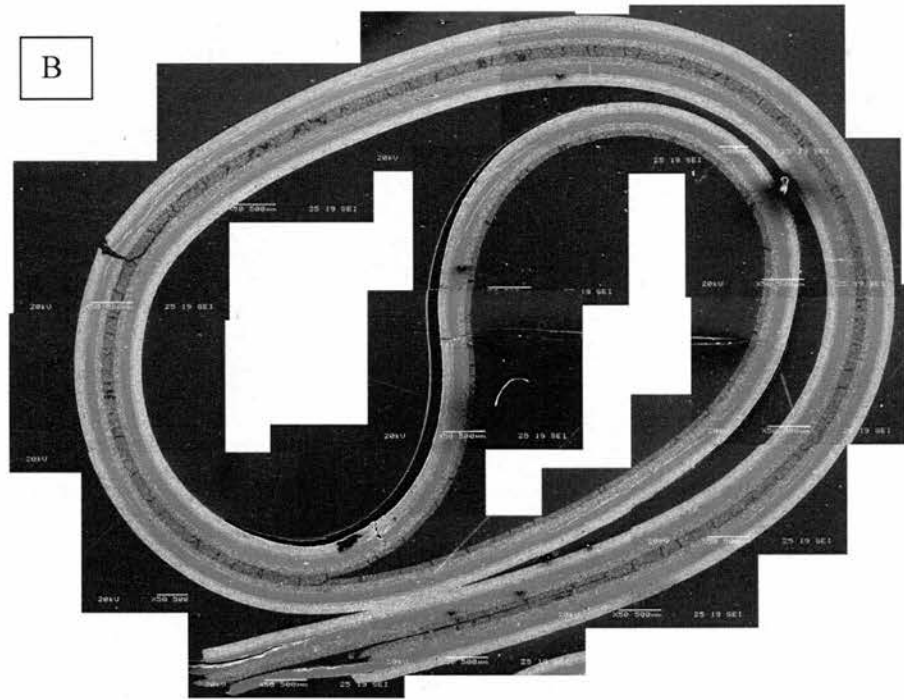
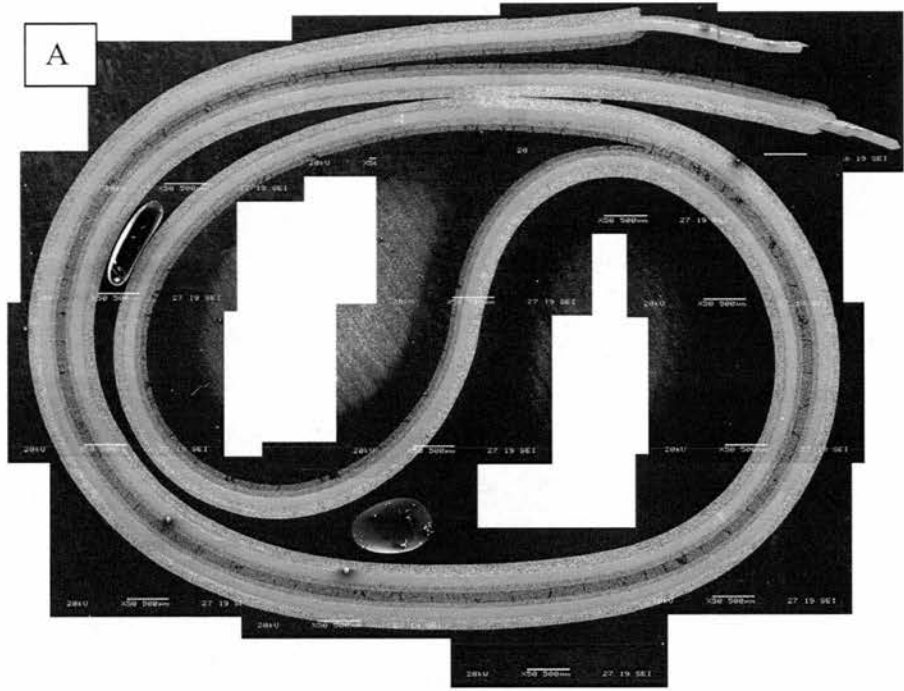


Figure 4.21: SEM image and EDS mapping of the anodes fired at different heating regimes. From top to bottom shows the image, zirconium mapping and nickel elemental mapping. (Note different magnification for cell E)



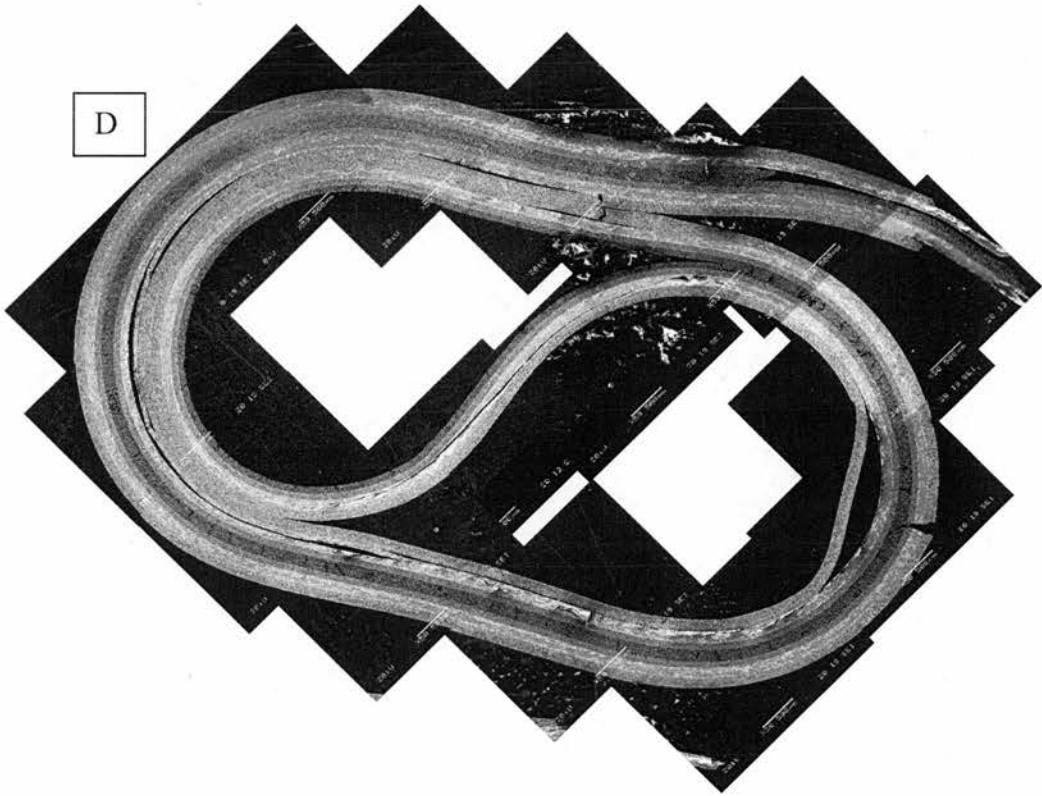
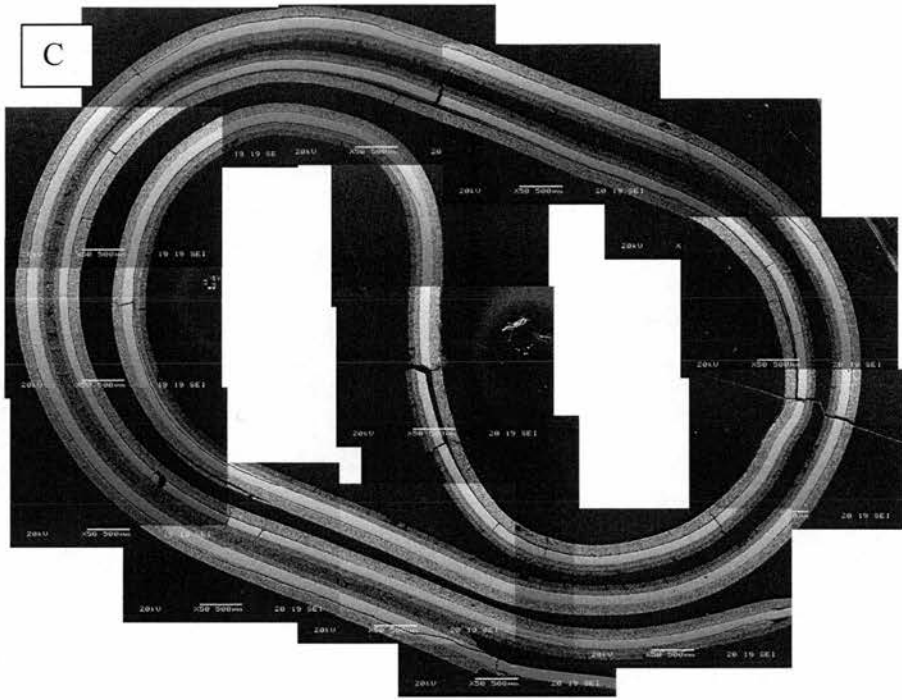


Figure 4.22: SEM images showing general condition of cells A-D after testing

for A&B cells (the cells with the smallest cathode polarisation resistances, R3) and the microstructure of cell E has longer pores and so will have a different tpb area than cells A-D. The thickness of the cathode current collector in this particular cell D is thinner, which would contribute to a higher material resistance as observed for these cells. The microstructure and elemental mapping, shown in figure 4.21 shows no obvious difference in porosity, tpb area or component thickness, offering no explanation for the difference in polarisation resistances. With the exception of one of the C cell anodes which had not been reduced at the end of the cell, and only part way up the mid-section of the cell (seen by the absence of cracking in the current collector layer), all anodes had been reduced.

All cells with the modified heating rates had a much better general condition than the E cells, ie with much less variation from cell to cell. Figure 4.22 gives a representation of the conditions of A-D cells (a cross-section of E cells is shown in figure 4.15, section 4.3.3). Some de-lamination was still evident, particularly with C and D cells ie cells produced with a faster heating rate between 50°C and 1000°C. Cells with a slower heating rate between 50°C and 1000°C (A and B cells) showed a general improvement in condition after testing, whilst the effect of the heating rates between 1000°C and 1350°C didn't seem to have a great effect on the general cell condition, although it is important to remember that only 3 cross-sectional images were taken and so the vast majority of the fuel cell was not examined.

4.4.2 Sintering temperature of 1300°C

This section examines the performance and general cell condition of the cells when the heating rates detailed in section 4.4.1 were used with a lower sintering temperature of 1300°C as follows:

- A' 50-260°C; 360-650°C at 0.1°C/min⁻¹, 250-360°C; 650-1000°C at 0.5°Cmin⁻¹, 1000-1300°C at 2°Cmin⁻¹.
- B' As A with the exception of 1000-1300°C at 5°Cmin⁻¹
- C' 50-260°C; 360-650°C at 0.1°C/min⁻¹, 250-360°C; 650-1000°C at 2°Cmin⁻¹, 1000-1300°C at 2°Cmin⁻¹.
- D' As C with the exception of 1000-1300°C at 5°Cmin⁻¹
- E' 50-1000°C at 0.5°Cmin⁻¹, 1000-1300°Cmin⁻¹

Cooling rates used were 5°Cmin⁻¹, and dwell times at 1000°C and 1300°C were 300mins. The above heating regimes are listed in order with respect to time taken, with A' taking the longest and E' the shortest. E' shows the heating rates used throughout the project for components detailed in chapter 3 and cells detailed in section 4.3 for completeness.

The OCVs of cells A'-D' (shown in figure 4.23a) show a general improvement over E' cells, but in terms of variation in OCVs between cells, the most impressive improvement occurs with A' cells which had the slowest heating rates with OCVs ranging from 0.95V to 0.981V. Cell A' also had the highest measured OCV of all the cells. The two lowest points shown in figure 4.23a obtained for B' and E' cells are believed to be due to variation in gas flow, as the OCV of these particular cells increased with temperature.

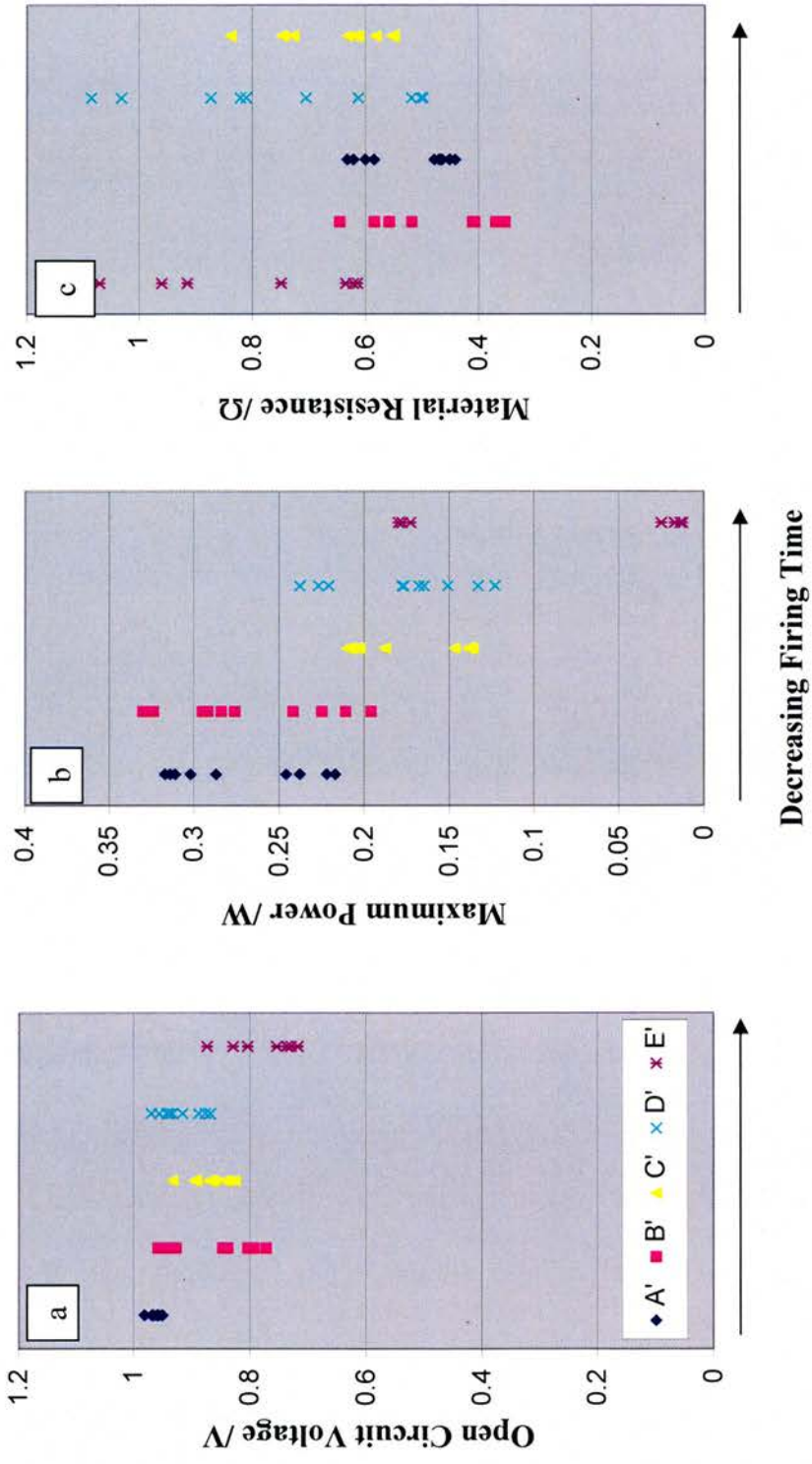


Figure 4.23: Graphs show how the heating regimes affect a) open circuit voltage, b) maximum power (calculated from I-V response) and c) material resistance (obtained from a.c. impedance response).

Regarding maximum powers obtained, figure 4.23b shows a general increase with decreasing firing times. The maximum power of A' and B' cells are similar to each other (both of these cells have the slowest heating rate between 50°C and 1000°C). C' and D' cells also have similar maximum powers to each other, suggesting that the decreased heating rate at low temperatures is beneficial to the cell performance. The range of maximum powers obtained is larger for B' and D' cells, suggesting that having a slower heating rate between 1000°C and 1300°C reduces the variation in performance from cell to cell. The variations between cell performances and relative power outputs of these cells are mirrored in the material resistance shown in figure 4.23c. This could suggest that the variation in power is not dominated by the cell microstructure but the electrode-steel contact for example (assuming this to be the dominating factor of the material resistance).

The large gap in data points seen in maximum powers achieved with E' cells is not explained either by the OCV or material resistance. One likely explanation is that some damage has occurred in some of these cells during firing to one or both of the electrodes. The OCV, maximum power and material resistance of cells A'-D' all show an improvement with respect to E' cells.

The material resistance of the cells was re-plotted as in section 4.4.1 in the order they were tested to see whether it is affected by the age of the steel. Figure 4.24 shows that considering the lowest material resistances measured for each cell there is a definite increase in material resistance with the age of the steel. The tubes used for E' cells were sacrificed for SEM analysis and so tubes used for these cells were different from cells A'-D'. There is however no trend observed for the highest measured material resistances for the cells.

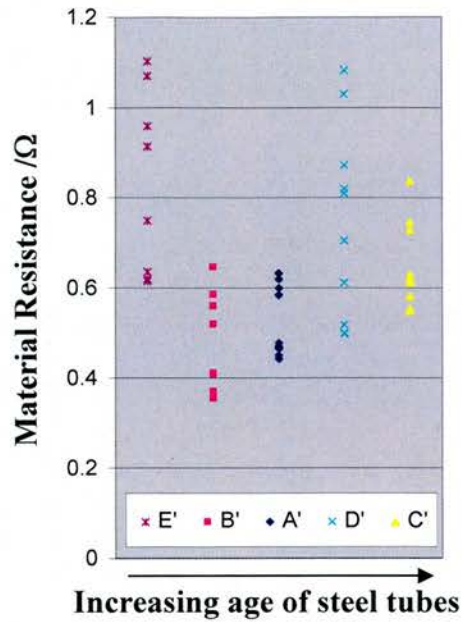


Figure 4.24: Graph showing how the age of the steel affects the measured material resistances of the cells (with different heating rates) (re-plot of figure 4.21)

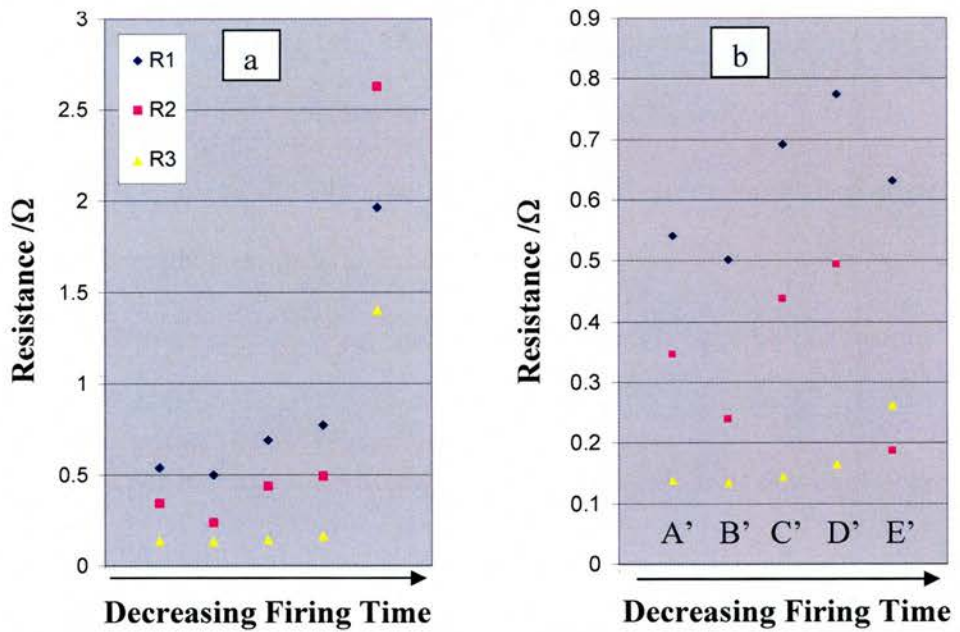


Figure 4.25: Graph showing the effect of firing regime on average cell resistances, where R1, R2 and R3 are as shown in figure 4.1a. a) shows the average of all E' cells, b) shows the average of E' when poor performers were eliminated.

R1 has been corrected for lead resistance. Data shows average resistances from cells tested at 800°C.

The fitted impedance data (shown in figure 4.25a) according to the equivalent circuit shown in figure 4.1a, showed the average polarisation resistances of E' cells to be much higher than cells A'-D', believed to be due to possible damaged electrodes. When the poor performer E' cell was removed and the average re-calculated as shown in figure 4.25b, interesting evaluations can be made. The cathode polarisation R3, changes only slightly with the different heating profiles, although cell E' has a notably higher R3 resistance. The polarisation resistance R2 (thought to be dominated by the interface between the anode and anode current collector – see section 4.3), show a similar trend to that of the material resistances, which suggests that this could be related to the tpb area of the high YSZ content anode. As already shown in section 4.3.1, material resistances and R2 resistances are notably higher with a sintering temperature of 1300°C as opposed to 1350°C. This relationship is therefore not surprising despite the addition of a high Ni content current collector. What is unclear however, is why the R2 resistances vary in the way they do, and why E' cells has relatively speaking, a much lower R2 value than the material resistance would suggest. The much lower R2 value of E' cells however, was also seen with E cells (same heating rates, but with a sintering temperature of 1350°C, described in section 4.4.1) again suggesting the nature of the anode to be different.

Figures 4.26 and 4.27 showing microstructures and elemental mapping of the cells give some indication as to the variation of resistance values. The anode current collector of cell E' is much denser than cells A'-D'. This could be due to the longer test times of these cells prior to microstructure analysis, since the nickel particle size seems larger, or different cell placement in the furnace causing the temperature the cells were tested at to be higher at the gas inlet part of the cell. However, higher

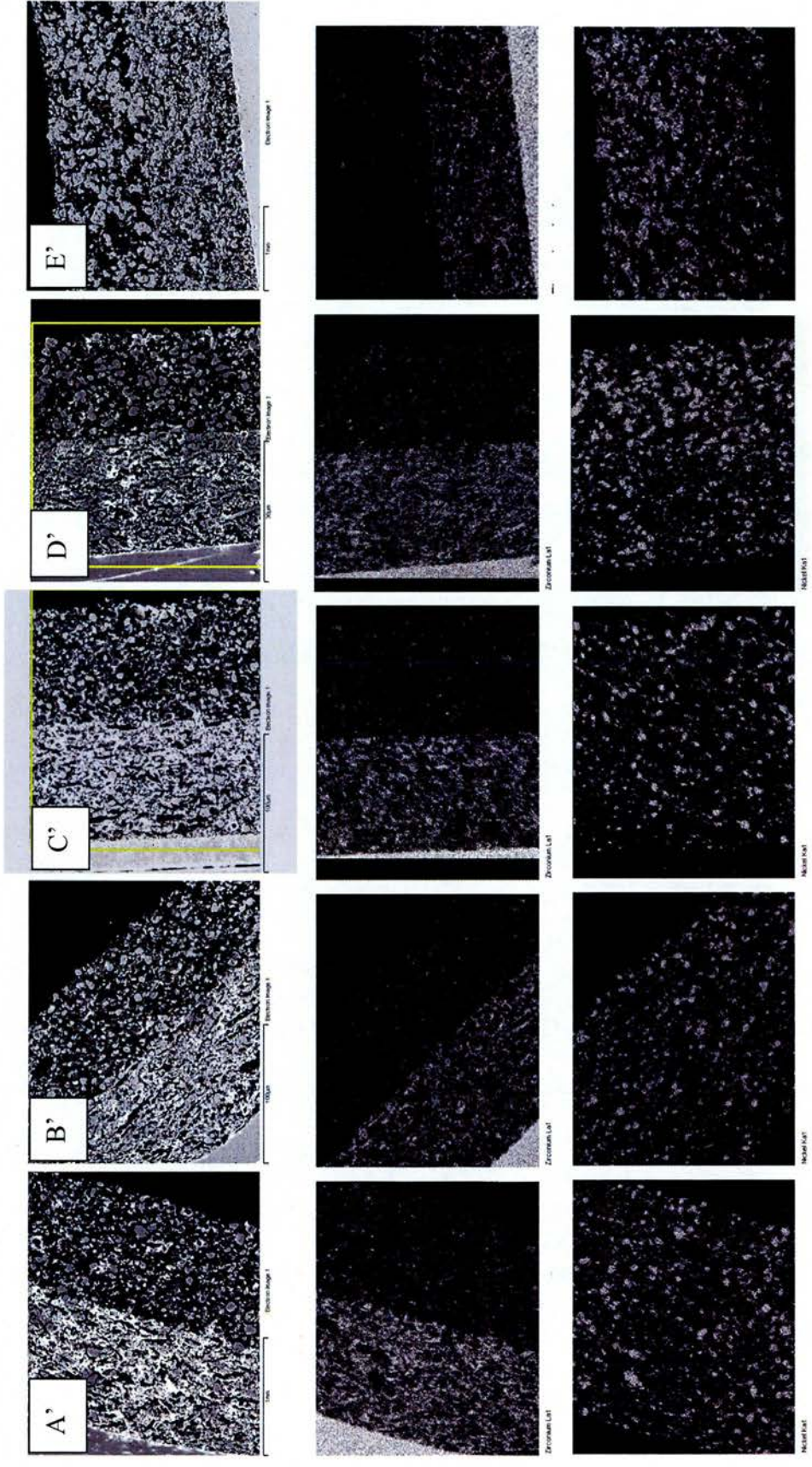


Figure 4.26: SEM image and EDS mapping of the anodes fired at different heating regimes. From top to bottom shows the image, zirconium mapping and nickel elemental mapping.

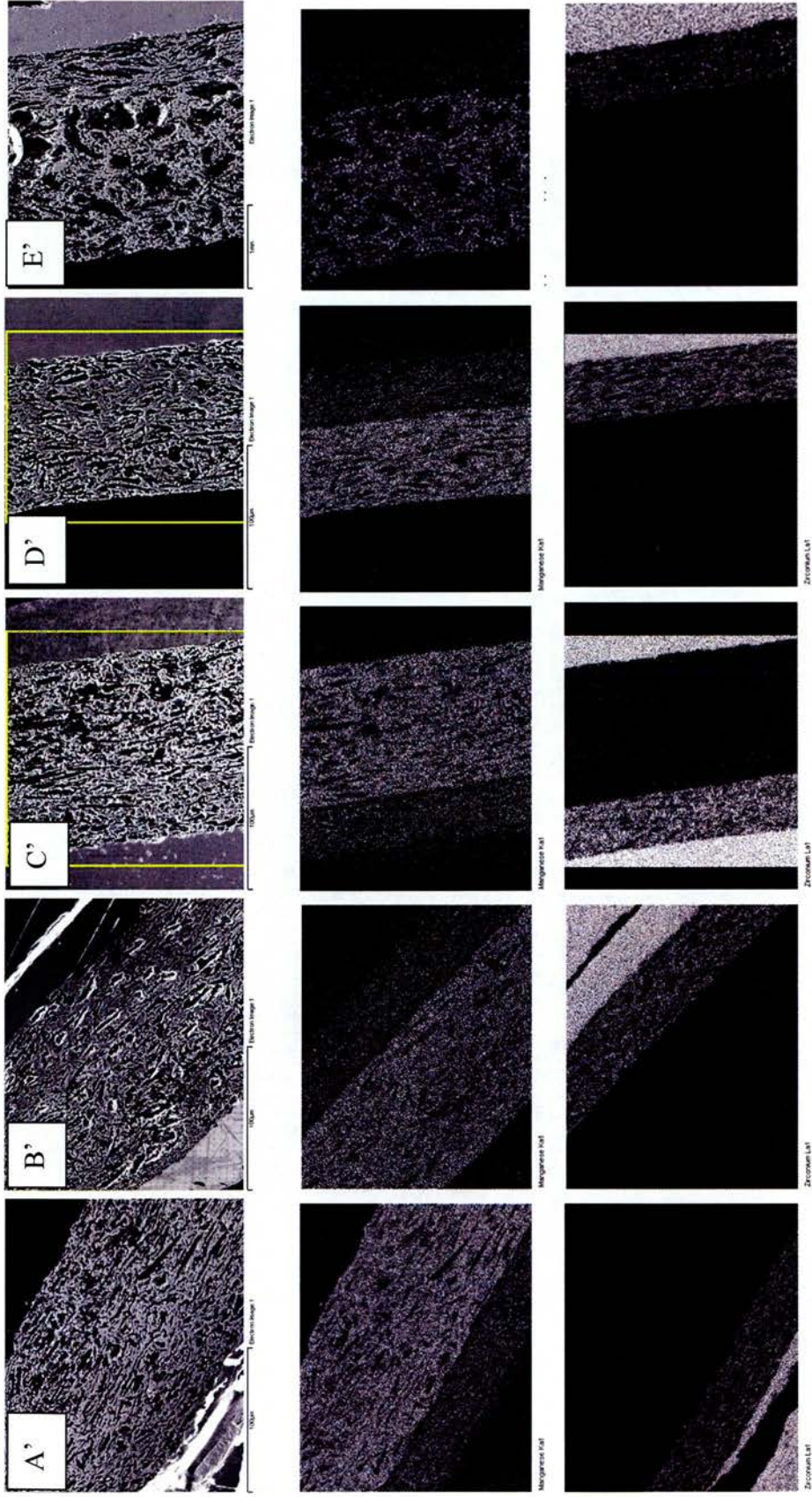
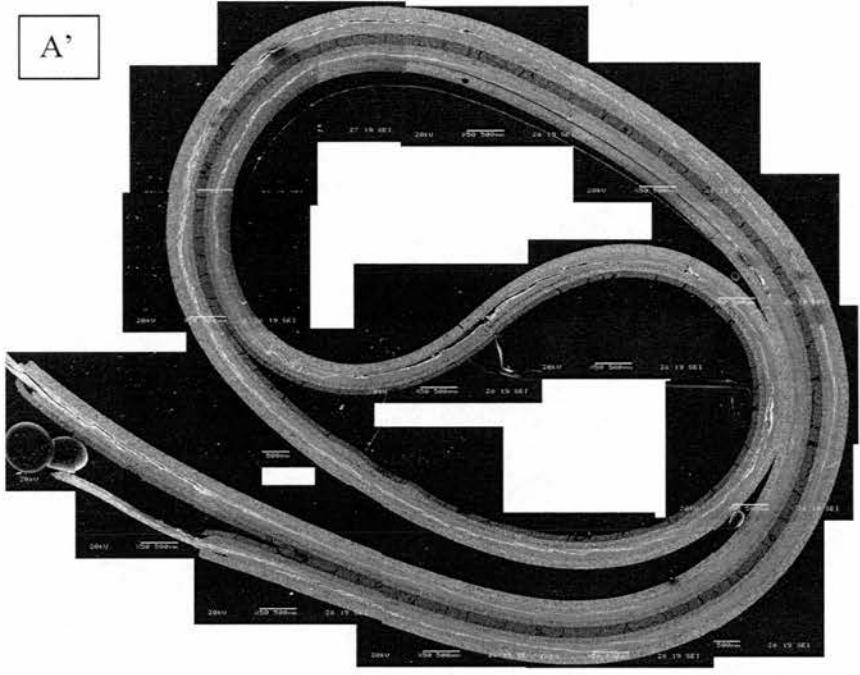
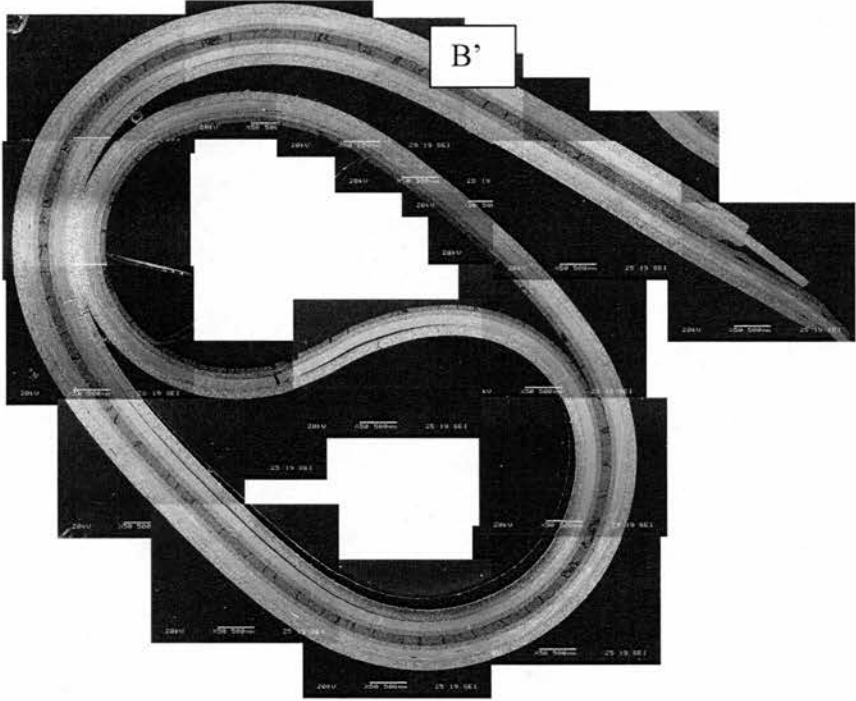


Figure 4.27: SEM image and EDS mapping of the cathodes fired at different heating regimes. From top to bottom shows the image, manganese mapping and zirconium elemental mapping.

A'



B'



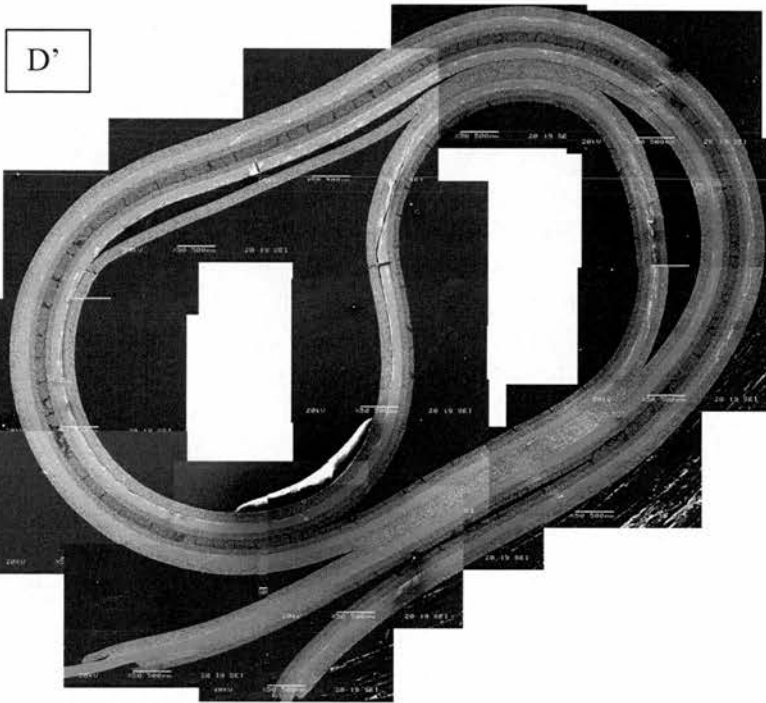
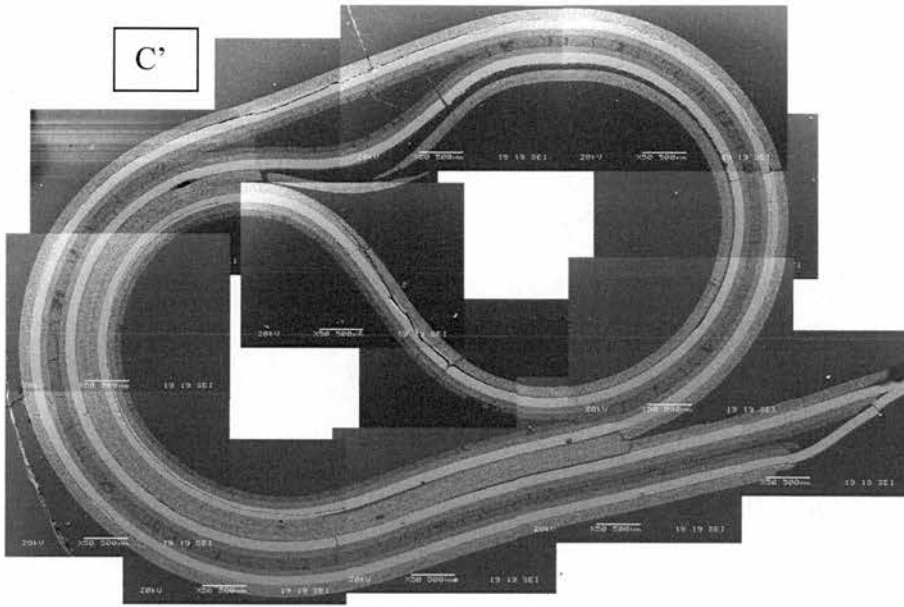


Figure 4.28: SEM images showing general condition of A'-D' cells after testing

densities will increase the tpb area at the interface of the two anodes and decrease polarisation, R2 (described previously in section 4.3.1). If in fact the densification was caused by misplacement of thermocouples in the testing furnace, resulting in a higher real temperature and nickel particle sintering, this could explain the larger relative gap between R2 and R1 values for A'-D' cells in comparison to E' cells, as the steel would deteriorate to a larger extent at higher temperatures (shown in section 4.2).

From the zirconia mapping of the anodes (figure 4.26), it could be argued that the YSZ content is lower for B' and E' cells, and although the nickel distribution looks similar for all cells, this could result in an increased nickel percolation, explaining the low R2 values for these cells. Again, as with E' cells sintered at 1350°C, the microstructure of the cathode is different, which could explain why the R3 value increased.

Figure 4.26 shows the anode current collector is thicker for A' and C' cells than B' and D' cells, whereas figure 4.27 shows the cathode current collector of D' cells to be thicker than A', B' and C' cells. Assuming the microstructures are similar irrespective of thickness, this would suggest A' and C' cells have lowest material resistance values (R1), with D' cells having the highest. Whilst D' cells do indeed have the highest R1 values, B' cells have the lowest R1 values, rather than A' & C' cells.

The general condition of cells A'-D' (figure 4.28) and E' cell (figure 4.15), show a large improvement to the cells has been made by the different heating rates. A larger amount of de-lamination is present in C' and D' cells which is reflected in the higher material resistance R1 values.

4.4.3 Summary

The variation of condition from cell to cell was reduced with the modified heating rates. All cells with the slower heating rates showed a reduced amount of delamination and cracking (not including the high Ni content current collector) throughout the cell, mirrored by the improved open circuit voltages and maximum achieved powers. When sintering at 1300°C, higher performances were achieved with all the modified heating rates. Conversely, when sintering at 1350°C, the maximum power achieved was with the original heating rate, explained by the excellent condition of this cell, however when considering average performances of cells the modified heating rates lead to improved results.

The cells with the slower heating rates between 50°C and 1000°C resulted in the best cell conditions (seen by SEM), irrespective of the heating rates to temperatures in excess of 1000°C. The slower heating rates at temperatures above 1000°C resulted in the smallest variation in performance when sintered at 1300°C irrespective of low temperature heating rates, whereas when sintering at 1350°C, this was only true with the slower low temperature heating rates.

Whilst the modification of the heating rates consistently reduced cracking and de-lamination, the consistency of layer thickness was not improved, neither was the reduction in cracking of the anode current collector layer. This is not surprising as the layer thickness is controlled in the tape casting and tape lamination processing stages and the cracking in anode current collector layer is a result of the volume reduction upon NiO reduction to Ni.

4.5 References

- 1 J.-D. Kim, G.-D. Kim, J.-W. Moon, Y.-i. Park, W.-H. Lee, K Kobayashi, M. Nagai, C.-E. Kim, "Characterisation of LSM-YSZ composite electrode by ac impedance spectroscopy" *Solid State Ionics*, *143*, **2001**, pp. 379-389
- 2 M. Guillodo, P. Vernoux, J. Fouletier, "Electrochemical properties of Ni-YSZ cermet in solid oxide fuel cells. Effect of current collecting", *Solid state ionics*, *127*, **2000**, pp. 99-107
- 3 S. P. Yoon, S. W. Nam, J. Han, T.-H. Lim, S.-A. Hong and S.-H. Hyun, "Effect of electrode microstructure on gas-phase diffusion in solid oxide fuel cells", *Solid State Ionics*, *166*, **2004**, pp.1-11
- 4 H. Orui, K. Watanabe, M. Arakawa, "Electrochemical characteristics of tubular flat-plate-SOFCs fabricated by co-firing cathode substrate and electrolyte", *J. Power Sources*, *112*, **2002**, pp. 90-97
- 5 W. Z. Zhu, S. C. Deevi, "A review on the status of anode materials for solid oxide fuel cells" *Mat. Sci. Eng. A362*, **2003**, pp. 228-239
- 6 M. Cassidy, G. Lindsay, K. Kendall, "The reduction of nickel-zirconia cermet anodes and the effects on supported thin electrolytes" *J. Power Sources*, *61*, **1996**, pp. 189-192
- 7 N. Q. Minh, "Ceramic Fuel Cells", *J. Am. Ceram. Soc.* *76 (6)*, **1993**, pp 563-88
- 8 P. Holtappels, C. Bagger, "Fabrication and performance of advanced multi-layer SOFC cathodes", *J. Euro. Ceram. Soc.*, *22*, **2002**, 41-48

5 Conclusions

The main challenge of this project was to co-fire the anode-electrolyte-cathode laminate to give a porous-dense-porous structure whilst avoiding any interfacial reactions which would decrease the electrical performance of the resulting fuel cell. Achieving a similar shrinkage profile of each component is essential in order to prevent de-lamination and cell cracking during the firing process.

The minimum temperature required for adequate density (>94% giving a gas tight ceramic with no continuous porosity) of the YSZ electrolyte in a reasonable time frame was 1300°C for a duration of 5hrs. The shrinkage profile of this component was measured and formed the target for all other components. A thicker electrolyte (a 2-layer laminate) of ~100µm resulted in a higher open circuit potential than when just one tape cast layer was used as the electrolyte resulting in a thickness of ~50µm. Possible reasons for the lower open circuit potential obtained with single layer electrolyte is that the shrinkage mismatch between electrolyte and electrodes causes cracking of the electrolyte, or the presence of pinholes in the tape. Lamination of two electrolyte layers would reduce the number of pinholes as the likelihood of two pinholes lining up is small, and the increased electrolyte thickness would increase its strength, reducing the cracking occurring from shrinkage mismatches.

Powder reactions between YSZ and varying A-site deficient LSM showed the pyrochlore $\text{La}_2\text{Zr}_2\text{O}_7$ (LZO) concentration to decrease with increasing A-site deficiency. At an A-site deficiency of 5%: $(\text{La}_{0.8}\text{Sr}_{0.2})_{0.95}\text{MnO}_3$ or more eliminated LZO formation even at sintering temperatures as high as 1350°C for a duration of 5hrs. As the A-site deficiency was increased, the shrinkage at high temperatures was also increased, and the on-set of shrinkage began at lower temperatures. The shrinkage of the stoichiometric LSM was similar to the electrolyte, and the shrinkage

of the 5% A-site deficient LSM was reduced by the addition of YSZ. A multi-layer cathode system was therefore used for the fuel cell: a thin composite cathode $(\text{La}_{0.8}\text{Sr}_{0.2})_{0.95}\text{MnO}_3$ with YSZ in a 1:1 (by weight) ratio for increased triple phase boundary, improved adhesion to the electrolyte, with no LZO formation, and a thicker $(\text{La}_{0.8}\text{Sr}_{0.2})\text{MnO}_3$ current collector used to improve the conductivity of the cathode.

When the anode was comprised of a nickel to YSZ ratio of 40:60 (by volume), the shrinkage at high temperature was much lower than that of the electrolyte, and the porosity too low for the SOFCRoll geometry. The shrinkage was matched to that of the electrolyte by the addition of graphite in the green tape, which also increased the porosity. However, the high porosity resulted in the effective nickel volume being below percolation threshold. Increasing the sintering temperature to 1350°C reduced the anode porosity and as a result the percolation of the nickel was greatly improved shown by a decrease in total fuel cell resistance by 95% to 0.7Ω and an increase in fuel cell maximum power by 1400% to 0.26W (with an electrolyte thickness of ~50μm and performance data recorded at 800°C).

When a current collector layer was added to the anode with a nickel to YSZ ratio of 4:1 (by volume), the fuel cell performance was further improved. Addition of this anode current collection layer decreased the total fuel cell resistance to 1.1Ω and 0.52Ω, and increased the maximum power to 0.17W and 0.43W at cell sintering temperatures of 1300°C and 1350°C respectively (with an electrolyte thickness of ~100μm and performance data recorded at 800°C). Due to the high NiO content in the current collector (prior to reduction in the fuel cell) the high temperature shrinkage was much lower than that of the electrolyte. Furthermore, the shrinkage of the current collector caused by the reduction of the NiO to Ni was much too high, resulting in crazing of the current collector. Additionally, this current collector was

very weak due to very high porosity upon reduction both due to the high Ni:YSZ ratio and the high graphite content required in the green tape for increased high temperature shrinkage (although the high temperature shrinkage of this anode was never optimised). Further work is therefore required to improve the shrinkage of any high Ni content anode, whilst decreasing the porosity. Decreasing the porosity of the anode current collector would also allow a lower Ni to YSZ ratio whilst achieving the same conductivity, which would in turn reduce the shrinkage upon reduction.

Modification of the heating rates for the fuel cells in order to minimise strains present from shrinkage mismatches resulted in improved fuel cell conditions after testing, with smaller variations between fuel cells of the same compositions. Further work on modifying the heating rates would be beneficial. The best fuel cell conditions, that is reduced delamination and cracking were achieved with the slowest heating rates, resulting in long heating times. Increasing production times is not ideal when considering scaling up for manufacture, therefore identifying temperature ranges where the heating rates could be increased in addition to temperature ranges where a dwell is required would improve the fuel cell performance whilst keeping the production time to a minimum.